

HIGH-SPIN STATES AND BAND STRUCTURES IN  $^{112,114,116}\text{Te}$

By

© VICTOR PAUL JANZEN

A Thesis

Submitted to the School of Graduate Studies  
in Partial Fulfilment of the Requirements

for the Degree

Doctor of Philosophy

McMaster University

July 1985

HIGH-SPIN STATES AND BAND STRUCTURES IN  $^{112,114,116}\text{Te}$

Doctor of Philosophy (1985)  
(Physics)

McMaster University  
Hamilton, Ontario

Title: High-spin States and Band Structures in  
112, 114, 116<sub>Te</sub>.

Author: Victor Paul Janzen, B.Sc. (Queen's University)

Supervisor: Dr. J.A. Cameron

Number of Pages: xiii, 232

### Abstract

Excited states in the neutron-deficient transitional nuclei  $^{112,114,116}\text{Te}$  have been studied by means of heavy-ion (H.I., xnypz $\alpha$ ) reactions. Levels up to spin  $22\hbar$  at excitation energies of up to 9 MeV were established using  $\gamma$ - $\gamma$  coincidence,  $\gamma$ -ray angular distribution,  $\gamma$ -ray excitation function and, in the case of  $^{112}\text{Te}$ ,  $\gamma$ - $\gamma$ -time measurements. In addition, the characteristics of a number of fusion-evaporation reactions leading to residual nuclei in this region have been analyzed and compared to theoretical predictions.

Positive-parity structures above spin  $4^+$ ,  $8^+$  and  $14^+$  in  $^{112}\text{Te}$ ,  $^{114}\text{Te}$  and  $^{116}\text{Te}$  respectively as well as negative-parity bands based on  $8^{(-)}$  and  $9^{(-)}$  states are reported for the first time. Positive- and negative-parity band structures up to spin  $16^+$  are compared to the predictions of a number of models usually applied to transitional nuclei, and interpreted in terms of valence single-particle plus collective vibrational degrees of freedom. At higher spins ( $12\hbar$  to  $22\hbar$ ) no strong evidence for rotational structure is seen.

As part of the data analysis for the present work, a numerical deconvolution method appropriate to  $\gamma$ -ray spectra is presented in the Appendix.

### Acknowledgements

Clearly there are many people who have made my stay at McMaster scientifically rewarding and just plain enjoyable as well, and although I cannot thank them all there are a number who deserve specific mention. First and foremost is my supervisor John Cameron, whose invariably good humour and sensible solutions to problems made many tasks easier. John and Frances' interest and friendship have also meant a great deal to me. To Jim Waddington I extend a special Thank You, not only for his "heavy-ion" expertise but also for his ongoing support and encouragement, not to mention the use of his canoe. I would also like to thank Henry Schwarcz, for readily agreeing to help out on the supervisory committee in the later stages.

The support staff at the Tandem Lab have been instrumental during this project, and I would be remiss not to mention the help of Jim Stark, Phil Ashbaugh and crew in obtaining a (normally) useful Na beam. Suzanna Wannamaker's help with letters and all that mysterious secretarial stuff has been invaluable as well.

In the course of obtaining a degree, I have also acquired many friends among the graduate student population who have greatly enriched my last, uh, few years in Hamilton. Ron Schubank's assistance on experiments, particularly on

those overnights, has been much appreciated; his unique brand of humour (probably no-name) seemed to be particularly suitable at four a.m. when nothing was working as it should. Arlene Larabee and Albert Lee, members of the "old guard", will always be thought of as good friends, as will Terry Kleven, whose views from the other side of campus I always found intriguing. Mike Vetterli and I have shared many experiences, including a stint as roommates, and I have really enjoyed his and Chris's friendship.

Heather, my fiancée, deserves a special mention for putting up with me during the last and most difficult year. That kind of patience and understanding will hopefully not be needed again! And finally, I owe a great deal to my parents, for their constant support and gracious example to me. This thesis is dedicated to them.

## Table of Contents

<u>Chapter</u>		<u>Page</u>
1	INTRODUCTION	1
2	THEORY	7
	Introduction	7
	2.1 Shell-Model Description	10
	2.2 The Vibrational Model	16
	2.3 Pairing-plus-Quadrupole Model	18
	2.4 Interacting Boson Approximation	23
	2.5 Variable Moment of Inertia and Variable Anharmonic Vibrator Models	31
	2.6 High-Spin States	37
3	EXPERIMENTAL METHODS	49
	3.1 Introduction to Heavy-Ion Fusion-Evaporation Reactions and Gamma-Ray Spectroscopy	49
	3.2 Experimental Procedures	60
	3.2.1 Ion Beam Production	63
	3.2.2 Target Preparation	67
	3.2.3 Multiplicity Filter	67
	3.2.4 Excitation Functions	73
	3.2.5 Gamma-Gamma Coincidence Measurements	76
	3.2.6 Angular Distributions	81
	3.2.7 $^{112}\text{Te}$ $\gamma$ - $\gamma$ -TAC Coincidence Experiment	85
4	EXPERIMENTAL RESULTS	89
	Introduction	89
	4.1 Excitation Functions	89
	4.1.1 Reactions Leading to $^{116}\text{Te}$	89
	4.1.2 Reactions Leading to $^{114}\text{Te}$	96
	4.1.3 The Reaction $^{92}\text{Mo}(^{23}\text{Na}, xnypz\alpha)$	97

Contents (cont'd)

4.2	Experimental Results for $^{116}\text{Te}$	98
4.3	Experimental Results for $^{114}\text{Te}$	112
4.4	Experimental Results for $^{112}\text{Te}$	126
5	DISCUSSION	153
	Introduction	153
5.1	Systematics of Even-Even $^{112-124}\text{Te}$ Isotopes	154
	5.1.2 Positive-Parity Levels	154
	5.1.3 Negative-Parity Levels	159
5.2	Shell-Model Description	161
5.3	The Vibrational Model	167
5.4	Pairing-plus-Quadrupole Model	169
5.5	Interacting Boson Approximation	177
5.6	Variable Moment of Inertia and Variable Anharmonic Vibrator Models	182
5.7	High-Spin States	187
6	SUMMARY	194
	APPENDIX - A Numerical Method for Gamma-ray Analysis	199
	REFERENCES	226

## List of Tables

<u>Table</u>	<u>Page</u>
2.1 Proton and neutron single-particle energies used in the S.D.I. shell-model calculation.	11
2.2 Pairing-plus-quadrupole parameters used by Lopac (Lo70).	24
3.1 (H.I., xnyp $\alpha$ ) reaction information.	61
3.2 Relative isotopic abundances of target materials.	68
3.3 Gamma-ray detector characteristics and typical count rates.	79
3.4 Comparison of filter-gated <u>vs.</u> singles gamma-ray angular distribution coefficients.	84
4.1 Results of analysis for $\gamma$ rays assigned to $^{116}\text{Te}$ .	105
4.2 Results of analysis for $\gamma$ rays assigned to $^{114}\text{Te}$ .	120
4.3 Results of analysis for $\gamma$ rays assigned to $^{112}\text{Te}$ .	133
4.4 $^{112}\text{Te}$ $\gamma$ - $\gamma$ time-peak centroid shifts.	136
5.1 Shell-model calculation of two-particle states of maximum spin in $^{116}\text{Te}$ .	166
5.2 Experimental <u>vs.</u> I.B.A. $\gamma$ -ray transition ratios.	181
5.3 V.M.I. and V.A.V.M. parameters for $^{112}\text{Te}$ , $^{114}\text{Te}$ , $^{116}\text{Te}$ and a number of comparison nuclei.	183
5.4 Moments of inertia extracted from Sn and Te yrast $8^+$ - $12^+$ level spacings.	188
A-1 Comparison of differences in centroids and relative differences in areas for the various fitting procedures.	212

Tables (cont.)

A-2	Comparison of peak intensities and centroids due to the various fitting procedures.	219
A-3	$\chi^2$ results from the analysis of channels 730 to 820 using the various fitting procedures.	221

## List of Figures

<u>Figure</u>		<u>Page</u>
2.1	Predicted spectra for a) harmonic and b) anharmonic vibrational excitations.	19
2.2a)	$E(2^+)$ for $Z=46$ (Pd), 48 (Cd), 50 (Sn), 52 (Te) and 54 (Xe) <u>vs.</u> neutron number $N$ .	34
2.2b)	$R_4 = E(4^+)/E(2^+)$ for the same nuclei.	34
2.3	Methods for generating high values of angular momentum.	39
2.4	Potential energy surface for $^{118}\text{Te}$ as a function of deformation at various angular momenta.	44
2.5	Nuclear deformations corresponding to calculated energy minima at different values of angular momentum, for $^{114}\text{Te}$ , $^{116}\text{Te}$ and $^{118}\text{Te}$ .	45
3.1	Schematic picture of neutron evaporation and subsequent de-excitation following a (H.I.,xn) reaction.	53
3.2	Neutron-deficient $Z=50$ region of the chart of the nuclides, illustrating the proton-neutron equal emission line.	56
3.3	Observed exit channels and subsequent decay modes for the $^{96}\text{Mo}(^{23}\text{Na},xyz)$ reaction.	59
3.4	Multiplicity filter gating probabilities.	72
3.5	Filter-gated <u>vs.</u> singles $\gamma$ -ray spectra from the $^{94}\text{Mo}(^{23}\text{Na},xyz)$ reaction.	74
3.6	Gamma-gamma coincidence electronics diagram.	80
3.7	$^{112}\text{Te}$ $\gamma$ - $\gamma$ -TAC electronics diagram.	86

Figures (cont.)

4.1	Production of residual nuclei from the $^{96}\text{Mo}(^{23}\text{Na}, \text{xnpz}\alpha)$ reaction.	90
4.2	Intensities of some $\gamma$ rays belonging to $^{116}\text{Te}$ as a function of bombarding energy.	92
4.3	Theoretical cross-sections for residual nuclei populated by the $^{96}\text{Mo}(^{23}\text{Na}, \text{xnpz}\alpha)$ reaction.	93
4.4	High-multiplicity xnp yields of residual nuclei following the $^{96}\text{Mo}(^{23}\text{Na}, \text{xnpz}\alpha)$ reaction.	95
4.5	$^{116}\text{Te}$ level scheme due to Chowdhury <u>et al.</u>	99
4.6	Total coincidence spectrum from the $^{96}\text{Mo}(^{23}\text{Na}, \text{xnpz}\alpha)$ reaction.	100
4.7	Coincidence gates from the $^{96}\text{Mo}(^{23}\text{Na}, \text{p2n})^{116}\text{Te}$ reaction.	101
4.8	Coincidence gates from the $^{96}\text{Mo}(^{23}\text{Na}, \text{p2n})^{116}\text{Te}$ reaction.	102
4.9	Some results from the $^{116}\text{Te}$ angular distribution analyses.	103
4.10	Proposed level scheme for $^{116}\text{Te}$ .	107
4.11	$^{114}\text{Te}$ level scheme due to Warner and Draper.	113
4.12	Total coincidence spectrum from the $^{94}\text{Mo}(^{23}\text{Na}, \text{xnpz}\alpha)$ reaction.	114
4.13	Coincidence gates from the $^{94}\text{Mo}(^{23}\text{Na}, \text{p2n})^{114}\text{Te}$ reaction.	115
4.14	Coincidence gates from the $^{94}\text{Mo}(^{23}\text{Na}, \text{p2n})^{114}\text{Te}$ reaction.	116
4.15	Some results from the $^{114}\text{Te}$ angular distribution analyses.	117
4.16	Proposed level scheme for $^{114}\text{Te}$ .	118
4.17	$^{112}\text{Te}$ level scheme due to Tidemand-Petersson <u>et al.</u>	128

Figures (cont.)

4.18	Total coincidence spectrum from the $^{92}\text{Mo}(^{23}\text{Na}, \text{xnp}\alpha)$ reaction.	129
4.19	Coincidence gates from the $^{92}\text{Mo}(^{23}\text{Na}, \text{p}2\text{n})^{112}\text{Te}$ reaction.	130
4.20	Coincidence gates from the $^{92}\text{Mo}(^{23}\text{Na}, \text{p}2\text{n})^{112}\text{Te}$ reaction.	131
4.21	Some results from the $^{112}\text{Te}$ angular distribution analyses.	132
4.22	Representative $\gamma_1$ - $\gamma_2$ time spectra for $^{112}\text{Te}$ .	135
4.23	Proposed level scheme for $^{112}\text{Te}$ .	137
4.24	Partial $^{112}\text{Te}$ level scheme determined from $\gamma$ - $\gamma$ coincidence data.	142
4.25	Partial $^{112}\text{Te}$ level scheme determined from $\gamma$ - $\gamma$ coincidence and angular distribution data.	151
5.1	Level systematics of even-even $112 < A < 126$ Te isotopes.	155
5.2	Excited-state energy ratios for $112 < A < 126$ Te isotopes.	157
5.3	Calculated shell-model states for $A \sim 114$ Te.	162
5.4	Two-quasiparticle states in $^{118}\text{Te}$ calculated by Van Ruyven <u>et al.</u>	164
5.5	Shell-model configurations in $^{148}\text{Gd}$ .	168
5.6	Vibrational-model predictions compared to the experimental $^{112}\text{Te}$ positive-parity level scheme.	170
5.7	Pairing-plus-quadrupole level scheme due to Lopac compared to experimental states up to $8^+$ in $^{114}\text{Te}$ .	173
5.8	Interpretation of $^{112}\text{Te}$ level scheme in terms of pairing-plus-quadrupole and neutron excitations.	176
5.9	Calculated I.B.A. level scheme for $^{112}\text{Te}$ compared to the experimental results.	178

Figures (cont.)

5.10	Calculated V.M.I. and V.A.V.M. ground-state bands for $^{112}\text{Te}$ , $^{114}\text{Te}$ and $^{116}\text{Te}$ .	185
5.11	Typical slightly-deformed rotor spectrum for even-even transitional $Z < 50$ nuclei.	186
5.12	Excitation energy vs. $J(J+1)$ for high-spin states in $^{112}\text{Te}$ , $^{114}\text{Te}$ and $^{116}\text{Te}$ .	191
A-1	Total $\gamma$ -ray coincidence spectrum from the $^{92}\text{Mo}(^{27}\text{Al}, \text{xnp}\gamma\alpha)$ reaction.	207
A-2	Relative singlet peak area differences <u>vs.</u> centroid differences for the various fitting procedures.	211
A-3	Correlation between relative area differences for SANDRA and SAMPOMIN (global background).	213
A-4	Expanded channels 730 to 820 of the spectrum showing the SAMPOMIN (internal background) fit.	215
A-5	Expanded region of the spectrum showing the SAMPOMIN (global background) fit.	216
A-6	Expanded region of the spectrum showing the SANDRA fit.	217
A-7	Expanded region of the spectrum with the SANDRA fit and generator groups shown.	218

## Chapter One - Introduction

Our understanding of nuclear structure is based on an extensive body of experimental evidence, spanning a wide range of nuclear systems containing from two all the way up to hundreds of nucleons. To a large extent the way in which we classify these systems is determined by models which have been formulated in attempts to explain observed behaviour. The nuclei in the vicinity of  $Z=50$  constitute an area of which our experimentally-obtained knowledge has increased substantially in recent years; in addition, they are examples of nuclear systems which do not fit neatly into convenient classifications. They therefore provide interesting tests of many aspects of nuclear structure physics.

A number of the neutron-deficient nuclei in this region have been examined using in-beam gamma-ray spectroscopy or mass-separated isotope decay studies. High spin states in  $^{102}\text{Cd}$  (ref. Tr82),  $^{106,108}\text{Sn}$  (An81,Au80),  $^{116-122}\text{Te}$  (Ch82,Va82) and  $^{116,118}\text{Xe}$  (Ja84,Ke84) have been studied in-beam using heavy-ion (H.I.) fusion-evaporation reactions, while the masses and/or unusual decay properties of very neutron-deficient nuclei such as  $^{106}\text{Te}$ ,  $^{110}\text{Xe}$  (Sc81) and  $^{114}\text{Cs}$  (Ro80) have been deduced by means of on-line mass

separation and beta-, proton-, and alpha-decay spectroscopy following H.I. reactions such as  $^{58}\text{Ni} + ^{58}\text{Ni}$ . Some of those properties have been used to infer the characteristics of nuclei nearer the postulated double shell closure at  $Z=N=50$ , i.e.  $^{100}\text{Sn}$ .

Concerning the neutron-deficient  $A < 116$  Te isotopes very little in the way of detailed nuclear structure information was known before this study. These nuclei, having  $Z=52$ , lie just outside the  $Z=50$  Sn closed proton shell and as such are considered to be "transitional", having neither overtly collective deformed structure nor purely spherical characteristics. There are indications, looking at nuclei in the close vicinity, of competition between a number of the elementary modes of excitation which give rise to nuclear spectra, in this case single-particle shell model, vibrational and rotational degrees of freedom. Firstly, low-lying levels in nearby even Sn isotopes display  $0^+ - 2^+ - 4^+ - 6^+$  sequences, the spacings of which have been interpreted as two valence neutrons outside the closed proton shell, coupled with a short-range interaction (eg.  $^{108}\text{Sn}$ ; An81). Positive-parity levels in  $^{134}\text{Te}$  exhibit similar behaviour, only in this case the interpretation considers two protons outside a  $Z=50$ ,  $N=82$  inert core. The presence of the  $g_{9/2}$  proton excitation across the  $Z=50$  closed shell, in the structure of odd- $A$  Sb ( $Z=51$ ) and I ( $Z=53$ ) isotopes, has been demonstrated by the Stony Brook group (eg. Sh79,82, Ga82), among others.

Secondly, the ratios of the energies of the first  $J^\pi=2^+$  and  $4^+$  excited states,  $R_4=E_{4^+}/E_{2^+}$ , in the even-even  $^{112-130}\text{Te}$  isotopes vary between 1.95 ( $A=130$ ) and 2.14 ( $A=112$ ), close to the value of 2.00 predicted by the simple harmonic vibrational model. The presence of other members of the two-phonon multiplet near the  $4^+$  level in  $^{118-130}\text{Te}$  is also indicative of the vibrational character of the low-lying excited states.

Finally, positive- and negative-parity level structures in transitional  $Z < 50$  Cd ( $Z=48$ ) and Pd ( $Z=46$ ) nuclides have been described (Si80) as rotational bands built on zero-quasiparticle ( $0^+$  ground state) and two-quasiparticle  $10^+$ ,  $8^-$  and  $9^-$  band-heads, leading to a slightly-deformed rotor interpretation of these nuclei.  $\Delta I=1$  level structures built on the previously-mentioned  $9/2^+$  states in odd-A nuclei have been interpreted (He76) as strongly-coupled bands resulting from a  $1g_{9/2}$  quasi-proton hole plus a rotor with prolate deformation. This evidence, as well as the discovery of rotational bands atop two-particle two-hole ( $2p-2h$ ) excited  $0^+$  states in the even Sn isotopes with  $A > 112$  (Br79) led Chowdhury *et al.* to search for similar  $4p-2h$  bands in  $^{116-122}\text{Te}$  (Ch82). Although no clear rotational structure was seen, a possible explanation of the  $8^+-12^+$  level spacings was advanced in terms of a prolate rotor. Certainly the  $^{116-128}\text{Xe}$  isotopes, with two more protons ( $Z=54$ ), display rotational bands starting at the ground state and extending

up to observed angular momenta  $18\hbar$  or so (eg. Ja84, Ke84, Ga84). Venturing further into the  $50 < Z < 82$  shell, Nolan et al. have followed a rotational band in  $^{132}\text{Ce}$  ( $Z=58$ ) up to  $42\hbar$  (No85), one of the highest spins yet observed.

Within a collective framework the possibilities of  $\beta$  and  $\gamma$  vibrations in "soft" transitional nuclei favour the use of a complete Bohr-Mottelson (BM69,75) description, of which the harmonic vibrator is a specific case, or something along the lines of an interacting boson phenomenology (eg. I.B.A.; Al75a,b, Ar77), both of which take into account those degrees of freedom. A full explanation of nuclei such as the Te isotopes would then include quasiparticle excitations based on shell-model orbitals as well, preferably coupled to the collective core. Van Ruyven et al. (Va82) have characterized the excited states in  $^{118,120}\text{Te}$  observed by them up to spin 14 as either collective quadrupole ( $0^+ - 2^+ - 4^+ - \dots$ ) or two-quasiparticle (eg.  $7^-$ ,  $8^-$ ) excitations described by the I.B.A.-2 (Ar77, Ot78a) and "broken-pair" (Va74) models respectively, but no coupling between the modes was considered.

Nearly-spherical nuclei may form states of very high angular momentum not by collective rotations about an axis perpendicular to the symmetry axis, as seen in  $^{132}\text{Ce}$ , but by lining up individual particle angular momenta parallel to a symmetry axis (BM74). This single-particle alignment results in irregular sequences of  $\gamma$  rays de-exciting the high spin

levels, and the possibility of long-lived states having high angular momentum, i.e. "yrast traps".

It is with the objective of extending the understanding of transitional nuclei in the  $Z > 50$  region, especially those neutron-deficient isotopes of which little was previously known, that this study was undertaken. As just outlined, the results must be considered within the context of competitive modes of nuclear excitation, particularly since the observed level structures extend from the ground states up to nearly 9 MeV in excitation energy.

Chapter Two deals in an elementary way with theoretical means of calculating nuclear state characteristics based on single-particle, vibrational, pairing-plus-quadrupole, phenomenological and rotational models. Chapter Three outlines the experimental methods used for heavy-ion reactions and in-beam  $\gamma$ -ray spectroscopy. The characteristics of H.I. fusion-evaporation reactions bear significantly on the measurements that have been made, to the extent of determining which nuclei may be reached and how well they may be studied. For example, the well-known tendency of the cascading  $\gamma$  rays to populate states of the highest angular momentum at a given excitation energy (the so-called "yrast" states) limits the observations to yrast or near-yrast levels. Therefore experimentally-determined properties of H.I. reactions will be considered, as well as the procedures used to acquire and analyze the data. Experimental results

drawn from the data for  $^{116}\text{Te}$ ,  $^{114}\text{Te}$  and  $^{112}\text{Te}$  are presented in Chapter Four, along with a description of the H.I. reaction characteristics deduced from excitation functions. A discussion of the spectroscopic results in the light of various theoretical nuclear structure models follows in Chapter Five, at which point comparisons will also be drawn between the  $^{112,114,116}\text{Te}$  nuclides under consideration, and nuclei belonging to other transitional regions. Chapter Six summarizes the present work.

A description of the deconvolution program SANDRA, developed to extract photopeak intensity and centroid information from many of the  $\gamma$ -ray spectra, is given in the Appendix.

## Chapter Two - Theory

### Introduction

Any discussion of transitional nuclei must of necessity deal with a number of differing perceptions of nuclear excitations and resulting model descriptions. The aim of this chapter is to provide a basic overview of a subset of what have come to be acknowledged as the more useful views, as well as to outline their chief predictions and important differences. Detailed descriptions of the theoretical approaches employed here are readily available in a number of higher-level textbooks (see, for example, Lawson (La80 - shell model), Ring and Schuck (RS80 - many-body problem) and Preston and Bhaduri (PB75)).

In principle a pure shell-model approach, described as a "microscopic" theory because of its dependence on single particles and individual nucleon-nucleon interactions, should be capable of producing a valid picture of the behaviour of any assemblage of nucleons, given a set of reasonable starting assumptions. An elementary calculation of this type is outlined in Section 2.1. However in many cases such an approach may be overly (or even impossibly) complicated and result in a picture which obscures some of the characteris-

tics displayed by a nucleus. As well, there are many excited states with features which do not fit into the shell model mold, even with the use of more sophisticated models such as Hartree-Fock (independent particles) or Hartree-Fock-Bogoliubov (independent quasiparticles) (RS80). It then becomes necessary to consider "collective" excitations, i.e. excitations caused by some form of coherent participation by many nucleons. The vibrational model considered in Section 2.2 is an example of such a mechanism. Section 2.3 describes the pairing-plus-quadrupole approach, termed "semi-microscopic" because of its inclusion of single-particle excitations and residual nucleon-nucleon interactions as well as vibrational degrees of freedom.

For many nuclei not very close to closed shells, it is reasonable that "phenomenological" representations would be favoured, which can simplify calculations enormously, but at the risk of an incomplete description of the available excitation modes. A number of models have been developed based on the use of boson expansions, which approximate the complicated particle (fermion) Hamiltonian by a small group of boson operators. The vibrational Hamiltonian lends itself quite easily to this approach, for example, since the quadrupole vibrational phonon is analogous to a so-called "d-boson". The inclusion of interactions among the various bosons led to the formulation of the Interacting Boson Approximation (I.B.A.) of Arima and Iachello (AI75a,b), which

is outlined in Section 2.4 for a limiting case involving weak boson-boson interactions.

Another phenomenological description of "bands" in even-even nuclei which has been widely applied is the Variable Moment of Inertia (V.M.I.) model of Mariscotti, Scharff-Goldhaber and Buck (Ma69), which was originally proposed as an explanation of the experimentally-observed deviation of "rotational" level spacings from the expected  $J(J+1)$  dependence. The extension (SG70) of this model to less-deformed nuclei provided a progression from "deformed" to "spherical" to "magic" regions of the chart of the nuclides, distinguished from each other by varying degrees of nuclear stiffness and initial resistance to "cranking" of the nucleus. Recently Klein has generalized (K180) this variable-parameter approach, and Bonatsos and Klein (BK84) have proposed a Variable Anharmonic Vibrator Model (V.A.V.M.) in the same vein as the V.M.I., but including one additional parameter. These models, as applied to the "spherical" Te isotopes, are discussed in Section 2.5.

Finally the excitation degrees of freedom capable of producing high-spin states in  $^{112,114,116}\text{Te}$  are touched upon in Section 2.6. In this instance a totally quantitative explanation of energy levels is not attempted, the emphasis instead being on an understanding of the most likely structural reasons for the observed high-spin characteristics.

## 2.1 Shell-model Description

The nuclear shell model, first proposed by Mayer and Jensen (MJ55), has been very successful at explaining level energies and characteristics, transition intensities etc. near closed neutron and proton shells. As well, it has provided a basis for understanding the behaviour of nuclei having more than one or two nucleons (or holes) outside a core which can be taken to be relatively inert. The  $^{112,114,116}\text{Te}$  isotopes which form the focus of this study have two protons and 10, 12 and 14 neutrons respectively more than the  $Z=50, N=50$  closed shell, and as such cannot be expected to display purely individual-particle behaviour. However an indication of possible single-particle influence may be obtained by considering the excited states produced by coupling two protons and also two neutrons in the appropriate shell-model orbitals, using a simple form of residual nucleon-nucleon interaction.

In the  $50 < Z, N < 82$  major shells, the  $1g_{7/2}$ ,  $2d_{5/2}$ ,  $1h_{11/2}$ ,  $2d_{3/2}$  and  $3s_{1/2}$  orbitals are available for both neutrons and protons. As indicated in Chapter One, the  $1g_{9/2}^{-1}$  proton hole orbital may also play a role. A calculation of the expected 2-proton and 2-neutron states was performed using the single-particle energies listed in Table 2.1 and a Surface Delta Interaction (S.D.I.). The full derivation of the general S.D.I. matrix elements may be found, for example, in Lawson (La80). In the absence of proton-neutron inter-

Table 2.1

Proton and neutron single-particle energies used in the S.D.I. calculation.

$\pi$ orbital	$\epsilon_{\pi}$ (MeV) <sup>a</sup>	$\nu$ orbital	$\epsilon_{\nu}$ (MeV) <sup>b</sup>
1g <sub>9/2</sub>	-1.8	2d <sub>5/2</sub>	-1.0
1g <sub>7/2</sub>	0.0	1g <sub>7/2</sub>	0.0
2d <sub>5/2</sub>	0.75	3s <sub>1/2</sub>	1.4
2d <sub>3/2</sub>	1.8	1h <sub>11/2</sub>	1.5
3s <sub>1/2</sub>	2.0	2d <sub>3/2</sub>	2.0
1h <sub>11/2</sub>	2.4		

The S.D.I. strength  $A_{SDI} = 0.50$  MeV

<sup>a</sup> Taken from Lo70.

<sup>b</sup> Taken from Sa83.

actions and configuration mixing, the matrix elements reduce to the form:

$$\langle j_1 j_2 | v_{SDI} | j_1 j_2 \rangle = \frac{-A_{SDI} (2j_1+1)(2j_2+1) *}{2(2J+1)(1+\delta_{j_1 j_2})} * [(j_1 - 1/2 j_2 - 1/2 J_0)^2 (1 - (-1)^{\ell_1 + \ell_2 + J + 1})] \quad [2.1]$$

where:  $j_i$  = angular momentum of  $i$ th particle,  
 $J$  = total angular momentum of coupled particles,  
 $\ell_i$  = orbital angular momentum of  $i$ th orbital occupied;

and  $A_{SDI}$  = interaction strength.

If both particles are in the same orbital ( $j_1 = j_2 = j$ ) and coupled to spin zero ( $J=0$ ) the expression becomes even simpler:

$$\langle j^2 | v_{SDI} | j^2 \rangle_0 = -A_{SDI} \frac{(2j+1)}{2} \quad [2.2]$$

This matrix element is the largest possible and indicates that the most important effect of the S.D.I. interaction for two particles in the same orbital is to lower the  $0^+$  energy by a significant amount.

The calculated energy of a level with spin  $J$  is given by:

$$E_{j_1 j_2 J} = \epsilon_1 + \epsilon_2 + \langle j_1 j_2 | V_{SDI} | j_1 j_2 \rangle_J \quad [2.3]$$

where  $\epsilon_i$  is the single-particle energy of the  $i$ 'th orbital. For protons, the  $1g_{7/2}$ ,  $2d_{5/2}$  and  $1g_{9/2}^{-1}$  (proton-hole) orbitals are expected to be important, while the neutron  $1g_{7/2}$ ,  $1h_{11/2}$ ,  $8s_{1/2}$ ,  $2d_{3/2}$  and  $2d_{5/2}^{-1}$  (neutron-hole) orbitals may contribute significantly for isotopes having  $N > 56$ . In the case of particle-hole coupling the Pandya transformation (Pa56) must be used to determine the correct particle hole excitation energy. In its simplest form this may be written as:

$$E_{j_1 j_2 J}^{-1} = -\frac{1}{K} (2K+1) W(j_1 j_2 j_2 j_1; JK) E_{j_1 j_2 K} \quad [2.4]$$

where  $J$  = angular momentum of particle-hole state,

$K$  = angular momentum of particle-hole state

used in Equation [2.3],

$W(j_1 j_2 j_2 j_1; JK)$  = Wigner coefficient (eg. Ro59),

and  $E_{j j K}$  = energy obtained from Equation [2.3].

For Te nuclei two extra-core nucleons in  $(1g_{7/2}^2)$  or  $(1g_{7/2}, 2d_{5/2})$  configurations can couple to a number of spins up to  $6^+$ . It is reasonable to expect that the low-lying

positive-parity levels will thus contain significant amounts of two-particle strength.

In order to generate higher spins, two  $h_{11/2}$  particles can couple to  $J < 10^+$ , and four nucleons in a  $(h_{11/2}^2, g_{7/2}^2)$  or  $(h_{11/2}^4)$  configuration can combine to produce spin  $16^+$  at most.

The energy of two-particle states corresponding to a maximum spin coupling configuration can also be estimated by using the empirical formula of Chan et al. (Ch79). In the case of two neutrons from the  $j_1$  and  $j_2$  orbitals coupling to form a state of maximum spin  $J$  in the even-even nucleus  ${}_{2Z}^A{}_{2N}$ :

$$E_x({}_{2Z}^A{}_{2N}; j_1 j_2 J) = E_x({}_{2Z}^A{}_{2N-1}; j_1) + E_x({}_{2Z}^A{}_{2N-1}; j_2) + E_{\text{pair}} \quad [2.5]$$

where  $E_x({}_{2Z}^A{}_{2N-1}; j_1)$  = excitation energy of the single-neutron state of spin  $j_1$  in nucleus  ${}_{2Z}^A{}_{2N-1}$ ,

$E_{\text{pair}}$  = pairing energy when two neutrons are identical, obtained from the binding energies (B.E.'s) by:

$$= 2 \times \text{B.E.}({}_{2Z}^A{}_{2N-1}) - \text{B.E.}({}_{2Z}^A{}_{2N+2}) - \text{B.E.}({}_{2Z}^A{}_{2N-2}) \quad [2.6]$$

Assuming that Equation [2.3], suitably normalized with respect to the energy of the ground state, and Equation [2.6] should give approximately the same result for states of maxi-

mum spin coupling, it can be seen that in this case the S.D.I. matrix element is closely related to the pairing energy.

A complete shell-model analysis of the possible excited states in  $^{112,114,116}\text{Te}$  would involve the diagonalization of quite large matrices including proper configuration mixing, proton-neutron interactions and the possibility of coupling more than two particles together. Such a calculation is not only beyond the scope of this work, where the aim is to indicate important shell-model contributions to the structure of these nuclides, but also beyond the capabilities of most computer codes.

An alternative to calculating all the possible combinations of particles, holes and angular momenta is to introduce the concept of quasiparticles, together with a continuous particle density distribution and a Fermi surface which shifts with particle number. Particle-like to an extent  $U^2$  and hole-like to an extent  $V^2$ , where  $U^2 + V^2 = 1$ , quasiparticle excitations can be described by the B.C.S. pairing formalism and their introduction can make certain calculations much easier. Simply put, the introduction of a pairing force transforms a particle-hole state into a two-quasiparticle state with a minimum energy of  $\sim 2\Delta$ , where  $\Delta$  is the pairing gap. Thus a configuration such as  $(h_{11/2}, d_{5/2}^{-1})$  which in strict shell-model terminology would be called particle-hole could also be referred to as a two-quasi-

particle configuration. The concept is not limited to obvious particle-hole combinations; in even-even nuclei the lowest-lying group of states connected by strong transitions is sometimes described as a zero-quasiparticle band, where the next excitation structure might be described as a two-quasiparticle band (c.f.  $^{108}_{48}\text{Cd}_{60}$  (Sa78)). Even when the B.C.S. functions are not used explicitly, as is the case here, this concept is often quite useful, and within the context of conventional shell-model descriptions a shifting Fermi level and adjustable pairing gap are often convenient. For a full description of the quasiparticle treatment the reader is referred to, for example, Ring and Schuck (RS80).

The Projected-B.C.S. (P.B.C.S.) model (Va74) uses the B.C.S. formalism in conjunction with number-projected two-quasiparticle diagonalization. Also known as the broken-pair model because the states involved do not have the two quasiparticles paired to spin zero, it has been used to calculate two-quasiparticle excitations in  $^{110-118}\text{Sn}$  and  $^{118,120}\text{Te}$  by Van Poelgeest et al. (Va80) and Van Ruyven et al. (Va82) respectively. A comparison of the latter results with experiment is shown in Section 5.2.

## 2.2 The Vibrational Model

For nearly-spherical nuclei, collective oscillations about an equilibrium shape (see, for example, Bohr and Mottelson (BM75)) may compete with single-particle exci-

tation. The simplest picture involving only quadrupole vibrational modes (i.e. quadrupole phonons) results in the familiar  $0^+, 2^+, (0^+, 2^+, 4^+), \dots$  sequence at energies of  $0, \hbar\omega_2, 2\hbar\omega_2, \dots$ , as shown in Figure 2.1a). The inclusion of octupole phonons gives the  $3^-, (0^+, 2^+, 4^+, 6^+), \dots$  levels shown in the same diagram, while coupling the two types together may give rise to further negative-parity states.

The harmonic oscillator assumption is an approximation and it can be expected that anharmonicities will occur in connection with vibrational motion in real nuclei. For the quadrupole mode the most important anharmonic terms arise from the phonon-phonon interaction, and the result is that the 2-phonon degenerate  $(0^+, 2^+, 4^+)$  triplet is split and the  $2^+_2 \rightarrow 0^+_1$  transition is no longer forbidden, effects that are often seen. The degeneracy of the higher n-phonon multiplets,  $n > 2$ , is also removed. As for the high-spin members of these multiplets, which are most likely to be yrast and therefore most likely to be populated in H.I. reactions, the energy spectrum is then given by (BM75):

$$\begin{aligned}
 E(n, J=2n) &= n(E(n=1)) + (n(n-1)/2)[E(n=2, J=4) - 2E(n=1)] \\
 &= J[E(n=1) - E(n=2, J=4)]/4 + \\
 &\quad + J^2[E(n=2, J=4) - 2E(n=1)]/8 \\
 &= J[E(2^+) - E(4^+)/4] + J^2[E(4^+) - 2E(2^+)]/8
 \end{aligned}$$

[2.7]

where  $E(n, J=2n)$  = energy of  $n$ -phonon level with spin  $J$ . The energies  $E(n=1) = E_2^+$  and  $E(n=2, J=4) = E_4^+$  are available experimentally and thus higher-spin vibrational levels may be predicted. A theoretical spectrum for the case of  $E_4^+/E_2^+ = 2.10$  appears in Figure 2.1b). It is interesting to note that Equation [2.7] is a straight line on a graph of  $2E(J)/J \cdot E(2^+)$  vs.  $J$ . On such a plot a harmonic vibrator should have a horizontal line with an intercept equal to one, an anharmonic vibrator would have a slope dependent on the degree of anharmonicity, and a rotor characterized by the semi-classical  $E(J) \propto J(J+1)$  would display a line with slope  $1/6$ . Within such a context the yrast spectra of transitional nuclei might be expected to display nearly-straight lines on this plot with slopes between 0 and  $1/6$ , the actual value depending on whether the particular nuclide can be considered more a vibrator or a rotor. For a group of nuclei in the region  $180 < A < 190$  this type of comparison can be seen in Bohr and Mottelson (BM75 p.537)..

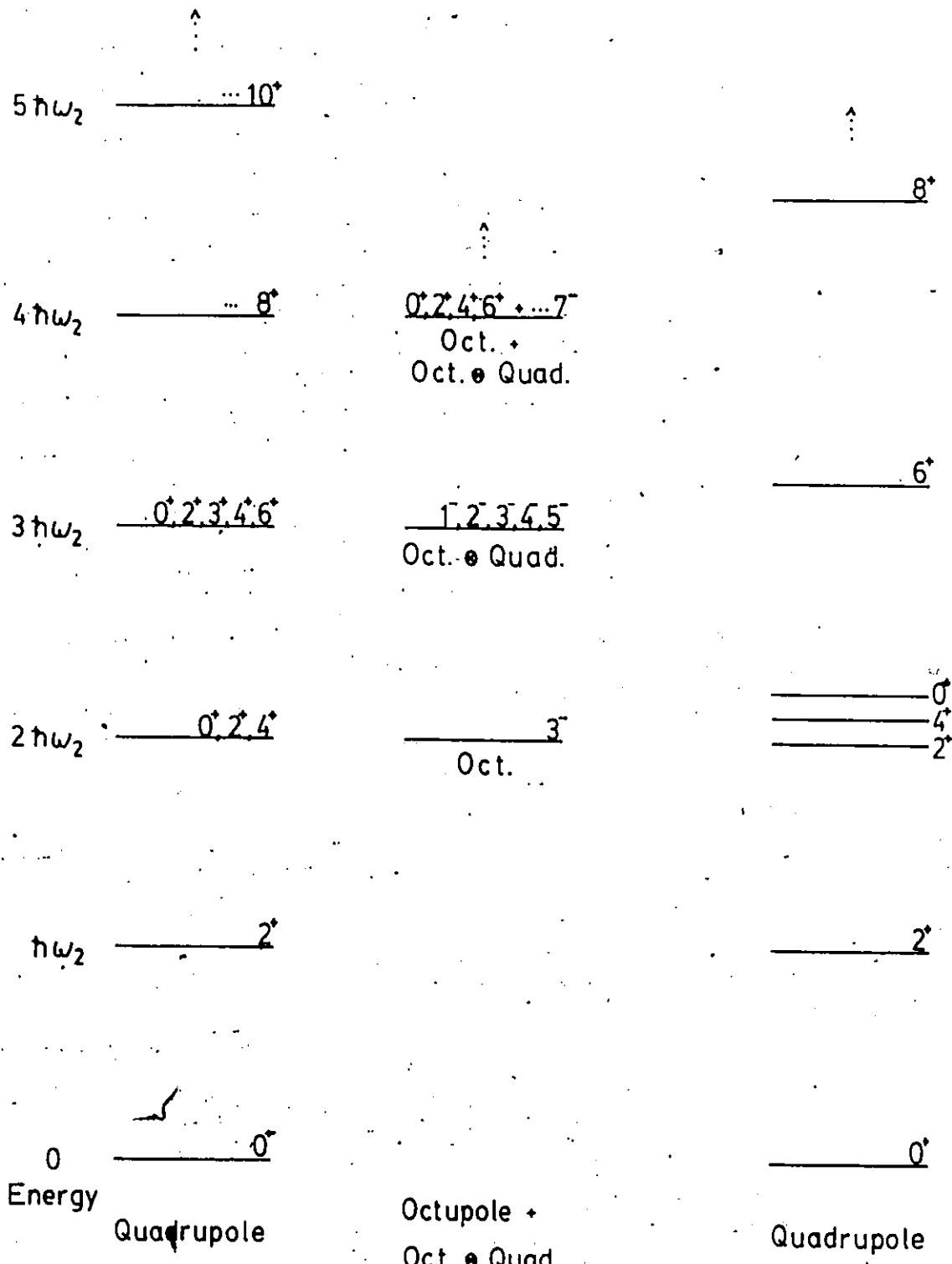
### 2.3 The Pairing-plus-Quadrupole Model

A description of nucleon-nucleon interactions can be summarized by the following three considerations:

a) to a first approximation the last few particles move in an average spherical potential, in discrete orbitals,

Figure 2.1

Harmonic (a) and anharmonic (b) spectra for vibrational excitations.



(a) Harmonic

(b) Anharmonic

b) short-range particle-particle correlations can be simulated by a residual interaction such as the S.D.I., and

c) long-range correlations, especially important in open-shell nuclei, can be treated by small time-dependent deformations of the nuclear surface, resulting in some form of collective motion.

The first two points have been addressed in Section 2.1 by the shell-model approach, the last by a separate discussion of the vibrational model in the previous Section. All three effects are taken into account by the pairing-plus-quadrupole model, wherein a) is handled by using single-particle energies as in Section 2.2, b) is approximated by a pairing force for two particles combining to  $J=0$ , shown to be the most important part of the S.D.I., and c) is taken care of by considering quadrupole deformations in the manner of Section 2.2. This model, which was first suggested by Bohr and Mottelson, has been reviewed by Bès and Sorensen (BS69).

A simple approach to Te considers the two valence protons in single-particle orbitals, modified by the residual pairing force, combined with the core quadrupole vibrations (due to the collective effect of the extra-core neutrons) and then perturbed by the proton-pair-quadrupole interaction. Besides satisfying the Pauli principle, a distinction between the two valence protons and the collective neutrons is indicated by factors discussed in Section 5.4.

The Hamiltonian used to calculate energies is:

$$H = H_0 + H_{\text{pair}} + H_{\text{p-core}} \quad [2.8]$$

where  $H_0$  describes the single-particle energies, added to the core vibrations,  $H_{\text{pair}}$  describes the residual pairing interaction, and  $H_{\text{p-core}}$  describes the particle-vibration interaction. For the first two terms in the Hamiltonian, simple expressions may be used resulting in diagonal matrix elements in the basis of states having the form  $|(j_1 j_2)_{J_p}^{nR}\rangle_J$ , where  $(j_1 j_2)_{J_p}$  is the state formed by coupling two particles of angular momenta  $j_1$  and  $j_2$  to a total spin  $J_p$ ,  $n$  is the phonon number,  $R$  is the phonon angular momentum, and  $J$  is the resultant spin from adding  $J_p$  and  $R$ . The energy of such a state is given by:

$$\langle (j_1 j_2)_{J_p}^{nR} | H_0 | (j_1 j_2)_{J_p}^{nR} \rangle = \epsilon_{j_1} + \epsilon_{j_2} + n\hbar\omega \quad [2.9]$$

where the  $\epsilon_j$  are single-particle shell-model energies, as in Section 2.1, and  $\hbar\omega$  is the phonon energy. An estimate of  $\hbar\omega$  may be obtained from the energy of the first excited  $2^+$  state in the nearby closed-shell Sn nuclei. The pairing term is simply:

$$\langle (j_1 j_2) | H_{\text{pair}} | (j_1 j_2) \rangle_J = -\frac{G}{2} [(2j_1+1)(2j_2+1)]^{1/2} \delta_{J,0} \quad [2.10]$$

where  $G$  is the pairing strength, which is closely related to the ~~S.D.I.~~ parameter  $A_{SDI}$ . The proton-pair vibration interaction has the form:

$$H_{int} = - \sum_{i=1}^2 k(r_i) \sum_{\mu} Y_2^{\mu*}(\theta_i, \phi_i) \alpha_2^{\mu} \quad [2.11]$$

where  $k(r)$  contains the radial dependence of the interaction,  $Y_2^{\mu}$  are the spherical harmonics and  $\alpha_2^{\mu}$  are the corresponding deformation parameters. The procedure then is to diagonalize the complete  $H$  matrix in order to obtain excited-state energies and wavefunctions, which depend on the coupling constant defined as:

$$a_2 = \frac{\langle k \rangle}{\sqrt{4\pi}} (\hbar\omega/2C)^{1/2} \quad [2.12]$$

where  $\langle k \rangle$  = radial matrix element of pair-phonon interaction, and  $C$  = vibrational restoring force constant. Such calculations have been performed for some even-even Te isotopes by Lopac (Lo70) and Degrieck and Vanden Berghe (DV74). In the latter case an S.D.I. residual interaction was used instead of a pairing force, and the parameters  $\epsilon_j$ ,  $\hbar\omega$ ,  $G$  and  $a_2$  were varied to fit the experimental energies for each nuclide considered. The results of Lopac's simpler calculation were used to compare the pairing-plus-quadrupole model to the experimental data obtained from this study. This calculation utilized parameters which generally fit the whole

group of A=122-130 isotopes best; these values are listed in Table 2.2. In order to allow comparisons for a number of isotopes the value of the particle-phonon coupling constant  $a_2$  was varied over a range  $0 < a_2 < 1$  MeV.

It is also possible to deduce electromagnetic properties such as quadrupole moments and some transition amplitudes (Lo70, DV74) as well as, for example, spectroscopic factors for stripping reactions (DV74). The spectroscopic factors are of course only comparable with experimental results for a few of the heavier Te isotopes.

#### 2.4 Interacting Boson Approximation

The underlying motivation for the development of boson representations is to replace the complicated many-fermion Hamiltonian in a large shell-model configuration space with spherical tensor (i.e. boson) operators working in a much smaller collective space. The Interacting Boson Approximation (I.B.A.) as put forward by Arima and Iachello (AI75a,b) is a phenomenological model wherein group theoretical techniques are used to provide simple analytical expressions for such properties as excited-state energies and transition amplitude ratios for a number of quite different limiting cases. For a nucleus composed of an inert core plus  $N_{\text{val}}$  valence particles,  $N=N_{\text{val}}/2$   $s^+$  bosons are used to construct the ground state while the replacement of these "pairing" bosons with successively more  $d_{\mu}^+$  bosons ( $\mu=-2,-1,0,1,2$ )

Table 2.2

Pairing-plus-quadrupole parameters used by Lopac (Lo70).

---

Single-proton energies (MeV):	$\epsilon(g_{7/2})$	=	0.0
	$\epsilon(d_{5/2})$	=	0.75
	$\epsilon(d_{3/2})$	=	1.8
	$\epsilon(s_{1/2})$	=	2.0
	$\epsilon(h_{11/2})$	=	2.4

Phonon energy (MeV):  $\hbar\omega = 1.0$

Pairing constant (MeV):  $G = 0.25$

Particle-phonon coupling constant:  $0.0 < a_2 < 1.0$  MeV

---

results in quadrupole excitations within the same nucleus. One consequence of this description is that one is limited to excitations up to spin  $2N^+$ , since at that point the available quadrupole bosons have been used up.

The general I.B.A. Hamiltonian is given by:

$$\begin{aligned}
 H = & \epsilon_s s^+ s + \epsilon_d [d^+ d]_0 + \sum_{L=0,2,4} c_L [d^+ d^+]_L [dd]_L + \\
 & + u s^+ s^+ s s + \{ v_2 [d^+ d^+]_2 [ds]_2 \}_0 + v_0 [d^+ d^+]_0 s s + \\
 & + u_2 [d^+ s^+]_2 [ds]_2 \}_0 + \text{h.c.} \quad [2.13]
 \end{aligned}$$

where the square brackets indicate coupling of angular momenta, and h.c. denotes higher-order contributions which are not considered. The  $\epsilon_2 = \epsilon_d - \epsilon_s$  parameter essentially sets the scale of excitation energies while the constants  $c_L$ ,  $v_L$  and  $u_L$  determine interaction strengths. In the absence of any interactions ( $c_L = v_L = u_L = 0$ ), the energy spectrum turns out to be just that of a purely harmonic quadrupole vibrator, as in Section 2.2, with  $\hbar\omega = \epsilon_2 = \epsilon_d - \epsilon_s$ . For a weak interaction ( $u_L = 0$ ;  $v_L, c_L \ll \epsilon_2$ ) the Hamiltonian [2.13] reduces to:

$$H = \sum_{\mu=-2,2} \epsilon_d d_{\mu}^+ d_{\mu} + \sum_{L=0,2,4} c_L [d^+ d^+]_L [dd]_L \quad [2.14]$$

The corresponding energy eigenvalues are given by (IA74):

$$E(n, v, J) = \epsilon_2 n + (\alpha/2)n(n-1) + \beta(n-v)(n+v+3) + \gamma(J(J+1)-6n) \quad n=0,1,2,\dots,N \quad [2.15]$$

where  $\epsilon_2$  = excitation energy of quadrupole boson  
(as defined earlier),

$n$  = boson number,

$v$  = seniority quantum number,

$J$  = angular momentum,

and  $\alpha$ ,  $\beta$  and  $\gamma$  are parameters which may be varied to suit individual cases.

For the ground-state band (g.s.b.),  $v=n$  and  $J=2n$  for  $n=0,1,2,\dots,N$ . Equation [2.15] can then be written:

$$E_{gsb}(J=2n) = (1/8)(4\epsilon_2 - 3C_4^{22})J + (C_4^{22}/8)J(J+1) \quad J=0,2,4,\dots,2N \quad [2.16]$$

Values for the two parameters  $\epsilon_2$  and  $C_4^{22}$  may be obtained by using the observed energies of the first  $2^+$  and  $4^+$  excited states in a nucleus, leading to:

$$\epsilon_2 = E_{2^+}$$

and:

$$C_4^{22} = E_{4^+} - 2E_{2^+} \quad [2.17]$$

indicating that a non-zero  $C_4^{22}$  is responsible for the deviation of this calculated g.s.b. from that of a purely harmonic vibrator. For a better overall fit to the data,  $\epsilon_2$  and  $C_4^{22}$  can be treated as adjustable parameters. Equations [2.16]

and [2.17] are equivalent to Equation [2.7], the expression for the high-spin yrast members of an anharmonic vibrator as given in Section 2.2, but with the additional boson-number limitation. In the case of  $^{112}\text{Te}$  there are 12 valence fermions available, resulting in a maximum spin of  $12^+$  within this framework.

The model can be extended (IA75a) to include octupole bosons, which may be coupled to one or more quadrupole bosons. Energy levels for a "totally-aligned" band are calculated by:

$$E_{\text{tab}}(J=2n+3) = E_{\text{gsb}}(J=2n) + \epsilon_3 + nC_5^{23} \quad n=0,1,2,\dots,N \quad [2.18]$$

where  $\epsilon_3$  is closely related to the energy of the octupole boson and  $C_5^{23}$  contains the coupling strength. This band would have spins of  $3^-$ ,  $5^-$ ,  $7^-$  etc. The octupole-quadrupole coupling also gives rise to a "totally-aligned minus one" band with spins of  $4^-$ ,  $6^-$ ,  $8^-$  etc., whose energies are given by:

$$E_{\text{tmb}}(J=2n+2) = E_{\text{gsb}}(J=2n) + \epsilon_3 + nC_5^{23} + (1/5)(2n+3)\Delta_4^{23} \quad n=1,2,\dots,N \quad [2.19]$$

where  $\Delta_4^{23}$  is another parameter which may be adjusted to fit observed spectra.

The comparison of  $\gamma$ -ray "in-band" to "out-of-band" transition rates in the I.B.A. model is quite straightforward. For transitions within the totally-aligned band (E2) vs. those proceeding out-of-band to the g.s.b. (E1):

$$\frac{B\{E1; (J=2n+3)^- \rightarrow (J'=2n+2)^+\}}{B\{E2; (J=2n+3)^- \rightarrow (J'=2n+1)^-\}} = \frac{(n+1)c}{n} \quad [2.20]$$

where  $c$  is a constant which depends on the nucleus and can be obtained experimentally from, say, the  $(9^- \rightarrow 8^+)$  vs.  $(9^- \rightarrow 7^-)$  branching ratio. A simple expression also results for transitions within the totally-aligned minus one band vs. those to the totally-aligned band.

The I.B.A. model certainly contains some attractive features in that it quite naturally embodies limiting cases which are often analytically solvable, and which correspond to important physical mechanisms in real nuclei. In group theoretical terms the model's  $SU(6)$  symmetry is broken down into subgroups  $SU(2)$  (equivalent to a seniority scheme in a single  $j$ -orbital shell model),  $SU(5)$  (the vibrational limit discussed in this section),  $SU(3)$  (axially symmetric rigid rotor limit) and  $O(6)$  (in one form equivalent to a deformed, completely  $\gamma$ -soft oscillator, sometimes applicable near the end of major shells). However it is worth remembering that this approach is equivalent to a substantial reduction in the available shell-model space (Ot78) and cannot be expected to

encompass all the possible single-particle (or quasiparticle) degrees of freedom. To a theorist, the absence of a general underlying microscopic justification (RS80) is of some concern. Efforts to show equivalence between the I.B.A. and shell model using more than one  $j$ -orbital (eg. Sc80) have so far relied on extrapolating to very large boson and fermion numbers. It has been shown (Mo80) that subject to some constraints the I.B.A. is mathematically equivalent to the Bohr-Mottelson collective model (BM69,75); the physical correspondence is less clear.

It is also interesting to note that, as Klein has pointed out (Kl80) the g.s.b. predictions of the I.B.A. for all the limiting cases can be summarized by the relation:

$$E(J) = aJ + bJ(J-2) \quad [2.22]$$

In the SU(5) vibrational case  $b \ll a$ , whereas at the SU(3) rotational limit  $b/a = 1/3$ .

The SU(5) limiting case discussed in this Section is a simplification, and a more realistic approach within the interacting boson model takes into account the neutron-proton distinction as well as configuration mixing and particle-hole excitations. Heyde et al. have calculated (He82) energy levels and decay properties in  $^{112,114}\text{Cd}$  using such an approach and found reasonable agreement with experiment.

However, the emphasis was on low-lying states and their decays.

The interacting proton-neutron boson model (Ar77, Ot78a), also known as I.B.A.-2, is an extension of the simple I.B.A. already discussed in this section. The underlying nucleon-nucleon interaction has a strong pairing component between identical particles together with a strong quadrupole component between unlike particles. As well, for nuclei with many more neutron than proton bosons, as is the case for Te isotopes, a neutron-neutron boson interaction is added, resulting in a Hamiltonian of the following type:

$$H = \epsilon_2(n_{d_\pi} + n_{d_\nu}) + \kappa_d Q_\pi \cdot Q_\nu + \sum_{L=0,2,4} c_L (1/2)(2L+1)^{1/2} * [[d_\nu^+ d_\nu^+]_L [d_\nu d_\nu]_0] \quad [2.22]$$

where  $\kappa_d$  is a parameter and  $Q_{\pi, \nu}$  are quadrupole operators in the boson representation, containing parameters  $\chi_{\pi, \nu}$ . Exact details may be obtained from Otsuka et al. (Ot78a). Using such a model Van Ruyven et al. have calculated (Va82) ground-state collective quadrupole excitations for  $^{118, 120}\text{Te}$ . Although this model should come closer to reality, it still is limited in spin to  $J=N_\pi+N_\nu=N$  (i.e.  $12^+$  for  $^{112}\text{Te}$ ).

Within a boson framework the analogous approach to a pairing-plus-quadrupole treatment would be to couple two quasiparticles to an I.B.A. core, as Morrison et al. have

done (Mo81). The Hg ( $Z=80$ ) transitional nuclei have been described (Fa82) in such a manner and it would be interesting to see results from a similar calculation for Te. Although the spin range should be somewhat less restrictive, due to the inclusion of two-quasiparticle degrees of freedom, one would still hesitate to apply the model at high spins.

### 2.5 Variable Moment of Inertia and Variable Anharmonic Vibrator Models

In an historical context the discovery of rotational bands in the atomic nucleus was followed almost immediately by the realization that the  $0^+ - 2^+ - 4^+ - \dots$  (in even-even cases) level spacings were not adhering quite properly to the semi-classical  $E_J = (\hbar^2/2\mathcal{J})J(J+1)$  relationship, in many instances as early as spin  $6^+$ . The original correction applied was an additional  $[J(J+1)]^2$  term, taken from the rotational-vibrational coupling observed in molecular spectra.

Such smooth deviations from rigid rotational behaviour are much better fit by the Variable Moment of Inertia (V.M.I.) model (Ma69), in which the nuclear moment of inertia is allowed to vary as a function of angular momentum within the framework given by:

$$E(J) = (C/2)(\mathcal{J} - \mathcal{J}_0)^2 + (1/2\mathcal{J})J(J+1) \quad [2.23]$$

with the minimization constraint:

$$(\partial E(J)/\partial \mathcal{J}) = 0 \quad [2.24]$$

which determines the moment of inertia  $\mathcal{J}_J$  for a state with spin  $J$ . (Note that for the sake of convenience  $\hbar^2=1$  in this discussion.) This again is a phenomenological model, with the constants  $C$  and  $\mathcal{J}_0$  representing the nuclear "stiffness" and ground-state (g.s.) moment of inertia respectively. Equations [2.23] and [2.24] may be combined:

$$\mathcal{J}_J^3 - \mathcal{J}_0 \mathcal{J}_J^2 = [J(J+1)]/2C \quad [2.25]$$

Given values of  $C$  and  $\mathcal{J}_0$ , experimentally obtained by solving [2.23] and [2.25] using the low-spin level energies, this equation can be used to calculate  $\mathcal{J}_J$  and therefore  $E(J)$  for the higher-spin levels.

The behaviour of the V.M.I. equations is often represented by considering the energy ratios  $R_J$  for a given nucleus, where:

$$R_J = E(J^+)/E(2^+) \quad [2.26]$$

The value of  $R_4$  turns out to be particularly meaningful. For a perfect rotor  $R_4=10/3$  and  $\mathcal{J}=\mathcal{J}_0$ . Although it is not immediately obvious,  $\mathcal{J}_0$  vanishes at  $R_J=[(1/6)J(J+1)]^{2/3}$  and therefore  $R_4=2.23$ , which was originally taken to indicate the limit of validity for this model. (A full description of the mathematical reasons for this behaviour can be found in Scharff-Goldhaber et al. (Sc76)). Within this purely rotational context the V.M.I. equations have been shown to be

equivalent to an expansion of the energy in terms of the angular velocity  $\omega$  (Harris cranking model) (Da70).

The V.M.I. representation is actually more general than this, in that it can be extended to cover nuclei not having such clear-cut rotational inclinations. For  $R_4 < 2.23$ ,  $\mathcal{J}_0$  becomes negative while  $\mathcal{J}_{J=0}=0$ . For large negative  $\mathcal{J}_0$ ,  $R_4 \rightarrow (20/6)^{1/2} = 1.82$ . This second range for which  $1.82 < R_4 < 2.23$  has been proposed (SG70) as indicating a "spherical region" within which  $\mathcal{J}_0$  represents a measure of the resistance to departure from spherical symmetry. The larger the negative value of  $\mathcal{J}_0$ , the more firmly the nucleus resists cranking. The  $^{112,114,116}\text{Te}$  nuclei lie within this "spherical" range, having  $R_4$  values of 2.14, 2.09 and 2.00 respectively.

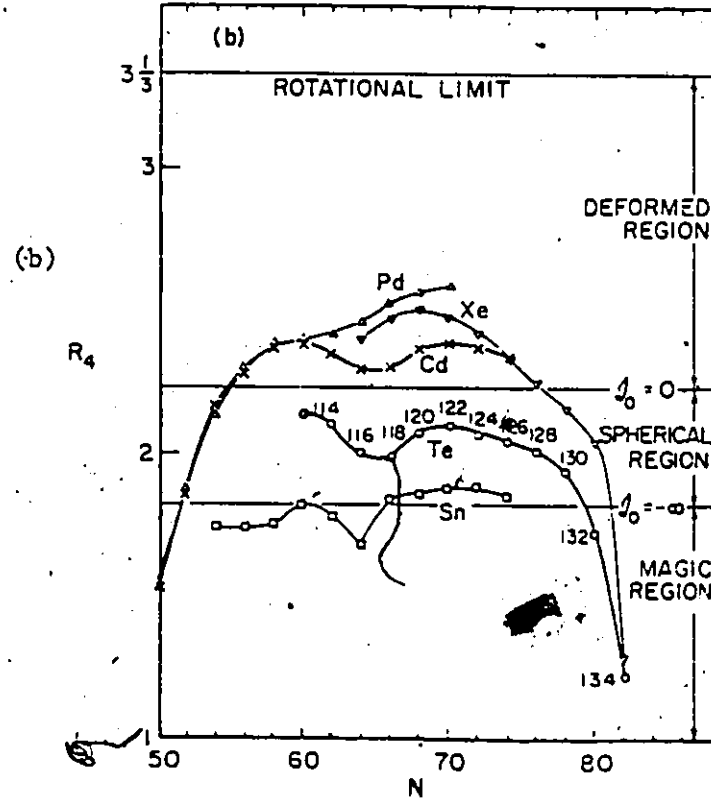
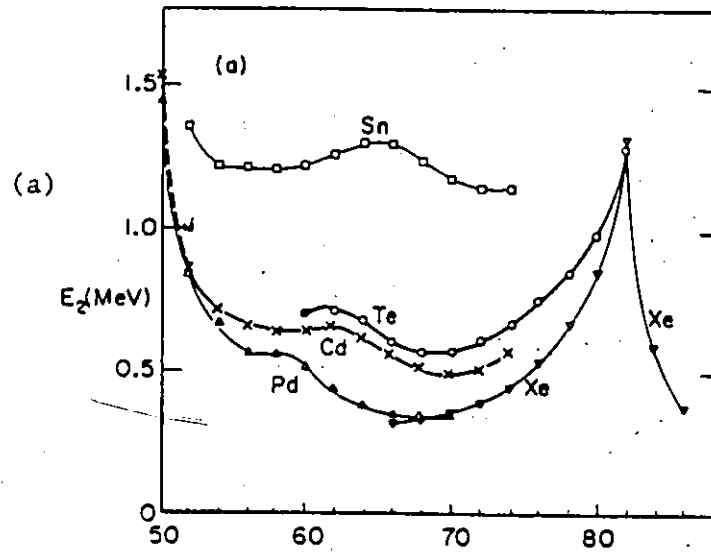
Those cases with  $R_4 < 1.82$ , of which  $^{132,134}\text{Te}$  are examples, are labelled as "magic" or "near-magic" nuclei.

Ground-state bands in even-even Cd ( $Z=48$ ) have been described quite well up to about spin 14 using the V.M.I. approach (Sa78,79). However, the Te nuclei, on the  $Z > 50$  side of the closed shell, do not exhibit quite the same behaviour, even though the  $E_2^+$  energies are similar. This particle-hole asymmetry is indicated in Figures 2.2a,b) where the Te  $R_4$  curve is significantly different from that of Cd. Scharff-Goldhaber has suggested (Sc74) that this is due to mixing of the proton  $g_{7/2}$  orbitals in Te with those higher orbitals which possess maximal overlap with the occupied

Figure 2.2

- a)  $E_{2^+}$  for  $Z=46(\text{Pd})$ ,  $48(\text{Cd})$ ,  $50(\text{Sn})$ ,  $52(\text{Te})$  and  $54(\text{Xe})$  vs. neutron number  $N$ .
- b)  $R_4 = E(4^+)/E(2^+)$  for the same nuclei.

Reproduced from Scharff-Goldhaber et al. (Sc76).



neutron orbitals i.e. a neutron-proton interaction. The possible significance of higher proton orbitals has also been mentioned by Lopac (Lo70), with reference to the negative static quadrupole moments observed in some Te nuclei. It has been found that for "spherical" nuclei the  $2^+ \rightarrow 0^+$  transition quadrupole moment  $Q_{02} = [4\pi B(E2:0^+ \rightarrow 2^+)]^{1/2}$  can be related to an "average" V.M.I. moment of inertia  $\mathcal{J}_{02}$  through the relation:

$$Q_{02} = k\mathcal{J}_{02} = k[\mathcal{J}(0) + \mathcal{J}(2)]/2 \quad [2.27]$$

where  $k$  is an empirical constant, determined by a least-squares fit to 49 nuclei having values of  $R_4$  in the "spherical" range, and found to be  $k = (39.4 \pm 2.6) \times 10^{-24} \text{ keV}^{1/2}$  (SG70). Such an approach estimates  $Q_{02}$  to within 20% for  $^{120-126}\text{Te}$  (DV74).

Both the V.M.I. model and the limiting cases of the I.B.A. model mentioned at the end of Section 2.4 are actually limits of a general energy formula proposed recently by Klein (K180):

$$E(J) = [J/\phi_1(J)] + [J(J-2)/\phi_2(J)] + \frac{1}{2} \sum_{i,j=1}^2 K_{ij}(\phi_i - \phi_{i0})(\phi_j - \phi_{j0}) \quad [2.28]$$

employing five fixed parameters and two "scaling functions"  $\phi_i(J)$  (c.f. V.M.I.  $\mathcal{J}(J)$ ) determined by:

$$\partial E(J)/\partial \phi_1(J)_J = 0 \quad i=1,2 \quad [2.29]$$

Bonatsos and Klein have defined (BK84) a "Variable Anharmonic Vibrator Model" (V.A.V.M.) by making  $\phi_1(J)$  a constant and retaining  $\phi_2(J)$  as a variable (usually relabelled  $\theta(J)$ ), resulting in:

$$E(J) = aJ + \frac{J(J-2)}{\theta(J)} + \frac{1}{2}C[\theta(J)-\theta_0]^2 \quad [2.30]$$

and:

$$\partial E(J)/\partial \theta(J)_J = 0 \quad [2.31]$$

This model has three parameters  $a$ ,  $C$  and  $\theta_0$ , and is valid for cases in which  $2 < R_4 < 10/3$ . Basically the constant  $a$  sets the energy scale, while  $C$ ,  $\theta(J)$  and  $\theta_0$  are interpreted in the same manner as  $C$ ,  $\mathcal{J}(J)$  and  $\mathcal{J}_0$  in the original V.M.I. setting. Bonatsos and Klein have applied the V.A.V.M. to a broad range of nuclei, and have concluded that for 45 cases belonging to the "spherical region" and "transitional region I", defined by them as  $2 < R_4 < 2.4$  and  $2.4 < R_4 < 2.7$  respectively, this model gives much better results.

Of the three Te isotopes under consideration in this work,  $^{112}\text{Te}$  is really the only case to which this model is applicable, as  $^{114}, ^{116}\text{Te}$  possess  $R_6$  values outside the range of validity for the V.A.V.M.

## 2.6 High Spin States

As was mentioned in Section 2.1,  $(g_{7/2}^2)$  or  $(g_{7/2}^2 d_{5/2}^1)$  valence configurations can lead to states of spin up to  $6^+$ , while two quasiparticles in the  $h_{11/2}$  orbital can combine to give spin  $10^+$  at the most. Four quasiparticles in  $(h_{11/2}^2, g_{7/2}^2)$  or  $(h_{11/2}^4)$  configurations can couple to a maximum spin of  $16^+$ . The  $h_{11/2}$  neutron orbital is expected to be more relevant to yrast or near-yrast levels than its proton counterpart, as indicated by the single-particle energies listed in Table 2.1.

In the nearby  $Z < 50$  transitional region, Cd ( $Z=48$ ) and Pd ( $Z=46$ ) excited levels up to spin ( $16^+$ ) have been successfully described (eg. Si80) as two-quasiparticle states coupled to slightly deformed rotors, with positive- and negative-parity band spacings following a V.M.I. pattern. Observed  $10^+$ ,  $8^-$  and  $9^-$  band-heads were assigned  $\nu(h_{11/2}^2)$ ,  $\nu(h_{11/2}, d_{5/2}^{-1})$  and  $\nu(h_{11/2}, g_{7/2})$  two-quasineutron configurations respectively.

The possibility of rotational bands built on deformed 4-particle 2-hole (4p-2h) excited  $0^+$  states in the Te nuclei, analogous to those based on 2p-2h  $0^+$  states in the Sn isotopes (Br79), has been raised by Chowdhury et al. (Ch82). They expected the  $J=2^+, 4^+, 6^+$  and  $J=10^+$  levels to be dominated by  $\pi(g_{7/2}^2)$  or  $\pi(g_{7/2}^0, d_{5/2}^1)$  and  $\nu(h_{11/2}^2)$  particle pair configurations respectively, and so they chose the yrast  $8^+$  and  $12^+$  levels as more likely to be rotational in nature, pre-

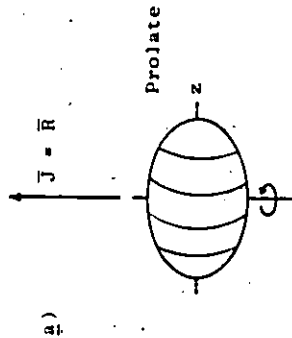
suming higher energies for  $8^+$  and  $12^+$  particle configurations. As well, several states below  $8^+$  in  $^{118,120,122}\text{Te}$  were identified as possibly containing 4p-2h band strength. No obvious rotational band structures were observed; however, moments of inertia extracted from the  $8^+$ - $12^+$  energy differences for  $^{116,118}\text{Te}$  were found to be consistent with those taken from Sn ( $Z=50$ ), Sb ( $Z=51$ ) and I ( $Z=53$ ) particle-hole bands.

In general there are two methods by which nuclei generate very high spins; collective rotation of a deformed nucleus, perpendicular to the symmetry axis, or alignment of single-particle angular momenta along a symmetry axis. The latter mechanism is expected to be important in spherical or near-spherical systems: These two modes are illustrated in Figure 2.3. The level energies of a rotor are quite regular and for the most part approximately follow the  $J(J+1)$  expression. The "backbending" observed in many rotational nuclei is caused by the alignment of two high- $j$  quasiparticles due to the Coriolis force, resulting in the modified collective picture of Figure 2.3b). A sequence of yrast levels due to single-particle alignment, on the other hand, is more irregular but, based on the Fermi gas model, on the average the yrast energies are expected (BM75) to follow:

Figure 2.3

Methods for generating high angular momentum in a) prolate deformed, b) prolate with aligned quasi-particles, c) spherical, and d) oblate deformed nuclei. After Khoo et al. (Kh79).

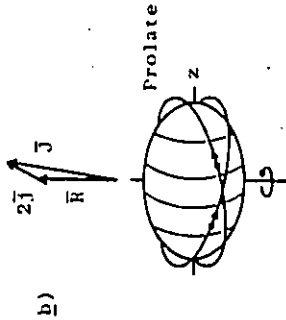
Collective Rotation



$$\vec{J} = \vec{R}$$

$$E = \frac{\hbar^2}{2I_{\text{pro}}} J(J+1)$$

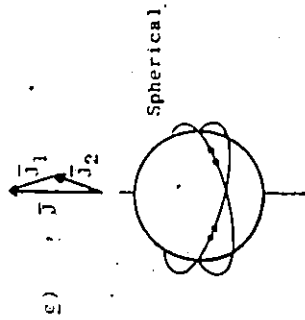
Collective Rotation + Rotation Alignment



$$\vec{J} = \vec{R} + 2\vec{J}_1$$

$$E = \frac{\hbar^2}{2I_{\text{pro}}} R(R+1) + E_{J_1}$$

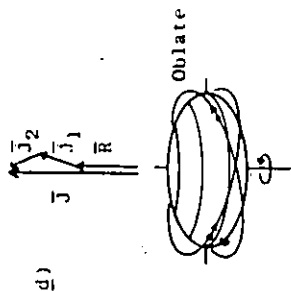
Particle Alignment



$$\vec{J} = \vec{J}_1 + \vec{J}_2$$

$$E_{\text{avgc}} = \frac{\hbar^2}{2I_{\text{sph}}} J(J+1)$$

- Moments of Inertia:
- $I_{\text{sph}} = (2/5)MR^2$  (R=radius)
  - $I_{\text{pro}} = (1+0.36)I_{\text{sph}}$
  - $I_{\text{obl}} = (1+0.66)I_{\text{sph}}$



$$\vec{J} = \vec{R} + \vec{J}_1$$

$$E_{\text{avgc}} = \frac{\hbar^2}{2I_{\text{obl}}} J(J+1)$$

1 c.f. Equation (2.40)

$$E_{\text{yrast}}^J = \frac{\hbar^2 J(J+1)}{2\mathcal{J}_{\text{sph}}} \quad [2.32]$$

where  $\mathcal{J}_{\text{sph}}$  is the spherical rigid-body moment of inertia given by:

$$\mathcal{J}_{\text{sph}} = (2/5)MR^2 \quad [2.33]$$

leading to:

$$(2\mathcal{J}_{\text{sph}}/\hbar^2) = 0.0277A^{5/3} \text{ MeV}^{-1} \quad [2.34]$$

using  $R = 1.2A^{1/3}$  Fm, where  $A$  is the number of nucleons. Te nuclei, close to the  $Z=50$  closed shell, are nearly spherical and so single-particle alignment may be expected to dominate the nuclear structure at high spins. This alignment of spins along the rotation axis means that the valence particle orbitals lie close to the equatorial plane, which may end up polarizing the core and result in a collective oblate shape as shown in Figure 2.3d). The yrast energies would then be given by:

$$E_{\text{yrast}}^J = \frac{\hbar^2 J(J+1)}{2\mathcal{J}_{\text{rig}}} \quad [2.35]$$

where  $\mathcal{J}_{\text{rig}}$  is the rigid-body moment of inertia for an oblate shape. The measured quadrupole moment of the 8.6 MeV  $49/2^+$

isomer in transitional  $^{147}\text{Gd}$  suggests an oblate deformation (Ha82).

It is possible to calculate theoretically the most likely shape for a nucleus as a function of angular momentum using the Liquid Drop Model (L.D.M.) and the Strutinsky shell-correction method (St68). A brief explanation of the procedure is given here.

The surface of a moderately-deformed body can to order  $\lambda=2$  in the spherical harmonic functions be expressed as:

$$R(\epsilon, \phi) = R_0 \left\{ 1 + \beta \sqrt{5/16\pi} (\cos\gamma (3\cos^2\theta - 1) + \sqrt{3}\sin\gamma \sin^2\theta \cos 2\theta) \right\} \quad [2.36]$$

where the deformation parameters  $\beta$  and  $\gamma$  are chosen so that:

$$\begin{aligned} \beta=0 & \quad \text{corresponds to a spherical shape,} \\ \beta \neq 0, \gamma=0^\circ & \quad \text{" " " prolate spheroid,} \\ \beta \neq 0, \gamma=60^\circ & \quad \text{" " an oblate spheroid,} \\ \text{and } \beta \neq 0, 0^\circ < \gamma < 60^\circ & \quad \text{" " a triaxial shape.} \end{aligned} \quad [2.37]$$

As it turns out  $0^\circ < \gamma < 60^\circ$  encompasses all ellipsoidal ( $\lambda=2$ ) shapes.

The total energy in the liquid drop model is given by:

$$E_{\text{LDM}} = E_{\text{surf}}(\beta, \gamma) + E_{\text{coul}}(\beta, \gamma) + E_{\text{rot}}(\beta, \gamma) + \text{deformation-independent terms} \quad [2.38]$$

where  $E_{\text{surf}}$  and  $E_{\text{coul}}$  are the nuclear surface and Coulomb energies respectively (see Appendix 6A of Bohr and Mottelson (BM75) for derivations of  $E_{\text{surf}}$ ,  $E_{\text{coul}}$  and  $E_{\text{rot}}$ ). The rotational energy is obtained using:

$$E_{\text{rot}} = (\hbar^2/2\mathcal{I}_{\text{rig}})J(J+1) \quad [2.39]$$

The rigid-body moment of inertia for rotation about the principal 1-axis (the axis of the largest moment of inertia) is given by:

$$\mathcal{I}_{\text{rig}} = \mathcal{I}_{\text{sph}} \{1 - (5/4\pi)^{1/2} \beta \cos(\gamma + 120^\circ)\} \quad [2.40]$$

where  $\mathcal{I}_{\text{sph}}$  can be obtained using Equations [2.33] and [2.34].

The L.D.M. is designed to reproduce smoothly-varying "bulk" features of nuclei, but does not contain the microscopic details of the shell model which are necessary to calculate the characteristics of a given nucleus at a specified angular momentum. As such  $E_{\text{LDM}}$  contains the smooth part  $\bar{E}_{\text{sh}}$  of the shell model energy  $E_{\text{sh}}$ , but not the oscillating part  $E_{\text{osc}}$ . Therefore the total energy should be calculated as:

$$\begin{aligned} E(\beta, \gamma, J) &= E_{\text{LDM}} + E_{\text{osc}} \\ &= E_{\text{LDM}} + E_{\text{sh}} - \bar{E}_{\text{sh}} \end{aligned} \quad [2.41]$$

where  $E_{sh}$  is obtained by summing single-particle shell model energies and  $\bar{E}_{sh}$  is calculated using the Strutinsky shell-correction method (see, for example, Ring and Schuck (RS80)).

Pairing correlations can be treated in a similar manner using the B.C.S. model, although this should not be as important at high spins where the pairing energy  $P_{BCS}$  is less than the rotational and shell-model energies.

The total energy as a function of deformation and angular momentum can then be expressed as:

$$E(\beta, \gamma, J) = E_{LDM} + E_{sh} - \bar{E}_{sh} + P_{BCS} - \bar{P}_{BCS} \quad (2.42)$$

Such calculations have been performed for  $^{114,116,118}\text{Te}$  by Andersson et al. (An76), who included pairing effects for the  $J=0$  case only. Figure 2.4 illustrates their calculated  $^{118}\text{Te}$  energy surfaces as a function of  $\beta$  and  $\gamma$  deformation for different values of  $J$ , while in Figure 2.5 the energy minima corresponding to various angular momenta, representing shapes along the yrast line, are plotted for  $^{114,116,118}\text{Te}$ . It can be seen that at low spin slightly-deformed prolate ( $\gamma < 10^\circ$ ) shapes are preferred, while approaching spin 20 small oblate deformations have the lowest energy. In a later calculation  $^{112}\text{Te}$  was predicted (An78) to become triaxial at spin 20. Because of this tendency toward a change in  $\gamma$  the Te nuclei have been categorized as " $\gamma$ -soft". To detect such possible shape changes then, the observation of yrast states having  $J \sim 20$  or greater is necessary, and a comparison of  $E_{yrast}^J$  at

Figure 2.4

Potential energy surfaces for  $^{118}\text{Te}$  as a function of deformation at various angular momenta. The minima are not sharply-defined, especially in the  $\gamma$  direction, and so the Te isotopes have been described as "soft" against  $\gamma$  deformation. The deformation parameter  $\epsilon = 0.953$ . Reproduced from Andersson et al. (An76).

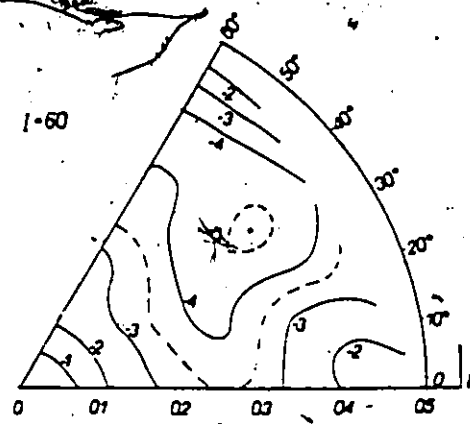
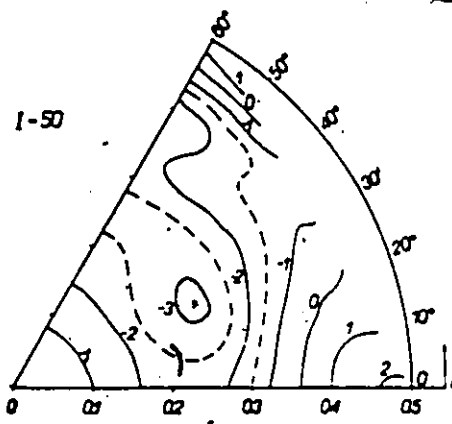
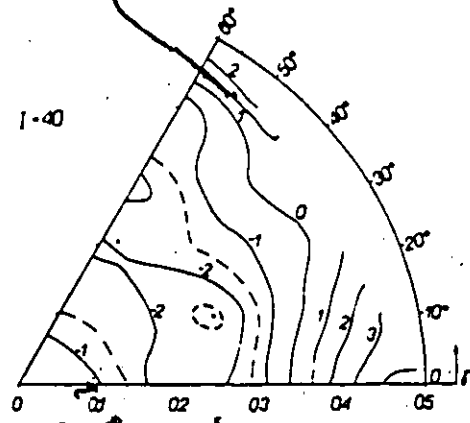
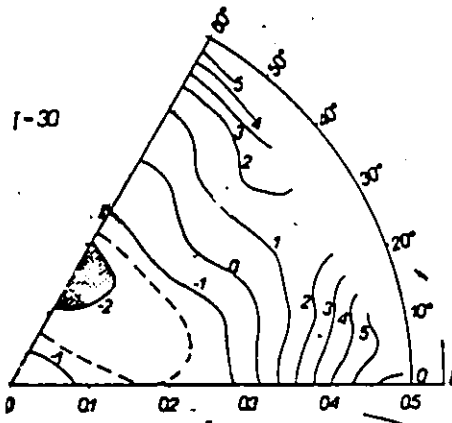
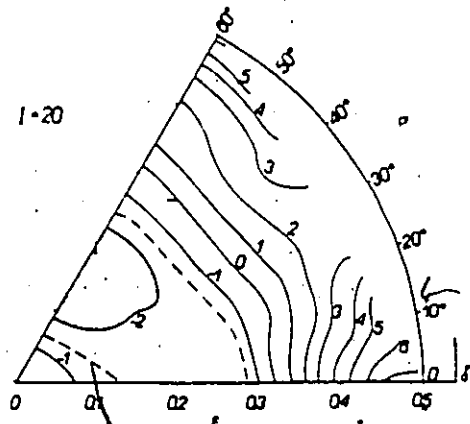
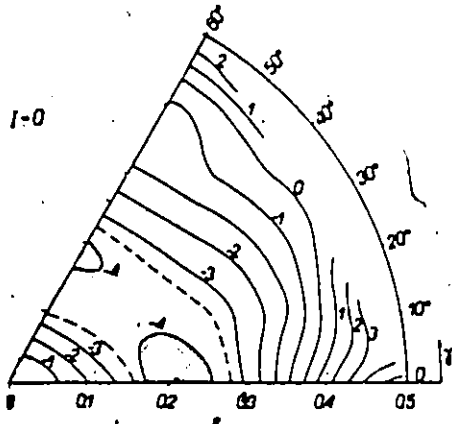
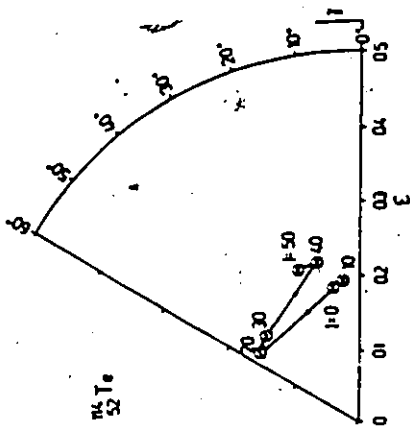
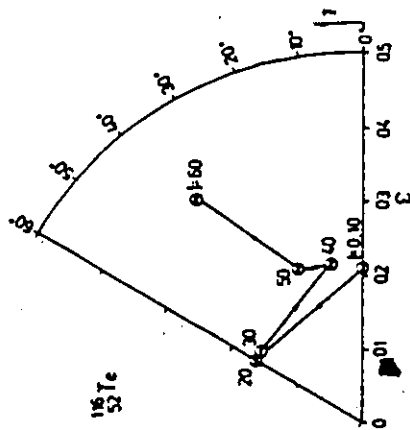
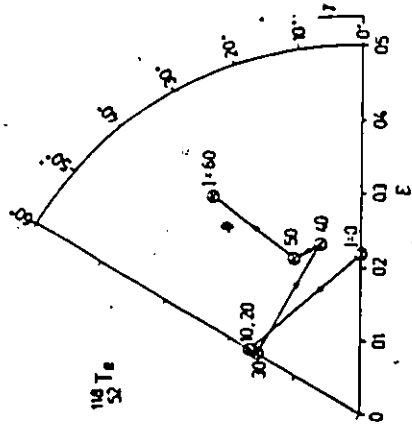


Figure 2.5

Nuclear deformations corresponding to calculated potential energy minima at different values of angular momentum, for  $^{114,116,118}\text{Te}$ . Reproduced from Andersson et al. (An76).



*[Handwritten scribble]*

*[Handwritten mark]*

high spin with Equations [2.35] and [2.40] leads to a determination of  $J_{rig}$  and gives an indication of the nuclear deformation. However it should be remarked that an unambiguous classification of the yrast structure is dependent on observations over a wide range of high spins.

Quite recently Bengtsson and Ragnarsson have calculated (BR85) the characteristics of high spin states in  $^{118}\text{Te}$  within the cranking model, using Nilsson single-particle orbitals with Strutinsky shell corrections, and minimizing the potential energy with respect to deformation parameters  $\epsilon$  (essentially equivalent to  $\beta$ ),  $\gamma$  and also  $\epsilon_4$ , the higher-order hexadecapole deformation term. Although pairing effects were again not included, single-particle orbital crossings or virtual crossings were considered in detail. The results show a change in yrast structure from oblate deformation for  $20 < J < 30$ , to collective prolate deformation ( $\beta \sim 0.24$ ,  $\gamma \sim 8^\circ$ ) from spin 30 to 45 approximately. This agrees qualitatively with the results of Andersson et al. in the range  $20 < J < 30$  but not at the higher spins, where Andersson et al. show  $^{118}\text{Te}$  as being triaxial.

As well as the irregular spacing of yrast energy levels and possible high spin oblate deformations, the building up of angular momentum by single-particle alignment may produce long-lived states resulting from de-excitation transitions requiring awkward rearrangements of the nuclear valence structure. These "yrast traps" were predicted by

Bohr and Mottelson (BM74), and high-spin isomers have been observed (Pe77, Bo80) in the transitional region  $64 < Z < 71$ ,  $82 < N < 90$ . The question arises as to whether isomers should be expected to occur for  $Z > 50$ ,  $50 < N < 82$ , and the answer seems to be negative, at least in the vicinity of  $N=64$ , for the following reasons:

1) Isomers due to very pure shell-model single-particle j-j coupling combined with a short-range interaction (c.f. S.D.I.), as observed in  $^{210}_{84}\text{Po}_{126}$  ( $J=8^+$ ,  $T_{1/2}=115$  ns),  $^{144}_{62}\text{Sm}_{82}$  ( $J=6^+$ ,  $T_{1/2}=880$  ns),  $^{116}_{50}\text{Sn}_{66}$  ( $J=10^+$ ,  $T_{1/2}=900$  ns) and  $^{134}_{52}\text{Te}_{82}$  ( $J=6^+$ ,  $T_{1/2}=162$  ns) only occur very close to neutron plus proton shell or sub-shell closures, which is ruled out for  $^{52}\text{Te}$  nuclei with  $N=64$ .

2) Many of the isomers in the previously-mentioned  $64 < Z < 71$ ,  $82 < N < 90$  region have been assigned fairly pure single-particle configurations based on spherical shell-model considerations which depend heavily on the proton shell near-closure at  $Z=64$  (K179). Thus although the  $64 < N < 71$ ,  $50 < Z < 58$  area in which  $^{52}\text{Te}$  nuclei reside may be somewhat analogous to that region, the lack of a definite neutron  $N=64$  closure precludes identical shell-model arguments. The other yrast isomers detected in the vicinity of  $Z > 64$  are de-excited by slow transitions of lower energy than those observed in the yrast cascades of  $^{112-116}\text{Te}$ . Apart from the low-lying  $11/2^-$  single-particle states found in some of the odd nuclei, for example the 0.279 MeV 7.5- $\mu$ sec isomer in  $^{115}\text{Te}$ , no yrast

traps have been found so far in the light Te-Xe-Ba ( $Z=52-56$ ) region (Sz83).

## Chapter Three - Experimental Methods

### 3.1 Introduction to Heavy-Ion Fusion-Evaporation Reactions and Gamma-ray Spectroscopic Methods

Various types of reactions can occur in collisions between complex nuclei: elastic and inelastic scattering, Coulomb excitation of target or beam nuclei, and fusion of the projectile + target nuclei resulting in compound nucleus formation. This last process, followed by particle and  $\gamma$  emission, is capable of producing residual nuclei which are otherwise very difficult or impossible to reach.

The ability of compound nucleus fusion-evaporation reactions to gain access to isotopes well removed from the "valley of stability" has been increasingly exploited in the last few years. Although much of the standard literature, for example the review by Newton (Ne69), refers to heavy-ion induced fusion reactions followed by multiple neutron emission, also known as (H.I.,xn) reactions, for neutron-deficient compound nuclei charged-particle emission is quite likely as well, giving rise to (H.I.,xnypza) reactions. By and large the underlying principles and the techniques used are identical for (H.I.,xn) and (H.I.,xnypza) reactions, and where differences do exist they will be pointed out.

Heavy-ion induced fusion reactions possess a number of unique characteristics, some of which make them particularly suited to the study of high-spin states in neutron-deficient nuclei.

1) The fusion of a projectile such as  $^{23}\text{Na}$  with a moderately neutron-deficient target produces a much more neutron-deficient compound nucleus. The subsequent neutron emission obviously enhances this effect, although proton and/or alpha emission counteract it somewhat. In the case of  $^{92}\text{Mo}({}^{23}\text{Na}, p2n){}^{112}\text{Te}$  the residual nucleus is 8 neutrons removed from the lightest stable tellurium isotope.

2) At beam energies of a few MeV per nucleon, compound nuclei with very high excitation energies, in the range of 40-80 MeV, are produced. (The  $^{115}\text{I}$  compound nucleus formed by the bombardment of 90 MeV  $^{23}\text{Na}$  ions on  $^{92}\text{Mo}$  has  $E_x = 53$  MeV.) To reach the same excitation energies with a proton-induced reaction would require beam energies of 30-70 MeV, but most of the cross-section would go into so-called "knock-on" single particle processes, not compound nucleus events.

3) Heavy ions as projectiles bring in large amounts of angular momentum. In the 90 MeV  $^{23}\text{Na} + {}^{92}\text{Mo}$  compound system  $l_{\text{max}} = 37\hbar$ ,  $l_{\text{rms}} = 26\hbar$ , after allowing for Coulomb effects. Moreover this orbital angular momentum is perpendicular to the beam direction. The evaporated particles carry off only a small fraction of that (eg.  $\approx 1\hbar$  per neu-

tron). The residual nuclei thus have high spins and, just as importantly, are strongly aligned, leading to pronounced anisotropies in the  $\gamma$ -ray angular distributions. This feature is a powerful spectroscopic tool, as was pointed out by Diamond et al. (Di66).

4) (H.I.,xnypz) cross-sections are reasonably high, of the order of 100 millibarns (mb), and have maxima at beam energies which depend on  $x+y+z$ , the number of particles emitted after compound nucleus formation. The separation of these maxima allows the selection of a subset of the possible residual nuclei, although a particular final nucleus is not selected as uniquely as in (HI,xn) reactions proceeding to nuclei which are not so neutron deficient.

The H.I. fusion-evaporation mechanism and subsequent  $\gamma$ -ray de-excitation have been frequently discussed (eg. Ne69, St72, Ba80); nevertheless, a brief description is instructive. Initially only neutron emission will be considered.

Fusion of  $^{23}\text{Na} + ^{92}\text{Mo}$  at a beam energy of 90 MeV leaves the ( $A=115, Z=53$ )  $^{115}\text{I}$  compound nucleus with approximately 53 MeV of excitation energy. Since the average binding energy of a neutron is about 10 MeV, a neutron is easily evaporated off to form the nucleus ( $A-1, Z$ ). The average kinetic energy of an emitted neutron being  $\approx 2.5$  MeV, the excitation energy of ( $A-1, Z$ ) is roughly 40 MeV, still high enough for another two neutrons to boil off, forming ( $A-3, Z$ ). This residual nucleus will be much more stable to

neutron emission and so will likely decay to its ground state by  $\gamma$  emission. It can be seen that if the compound nucleus had been formed with an excitation energy  $\approx 12.5$  MeV higher, the emission of four neutrons would have been much more probable, preferentially populating  $(A-4, Z)$ . This type of mechanism gives rise to the different cross-section maxima mentioned previously. Spread in the evaporation neutron kinetic energy spectrum and differences in  $\gamma$  decay lead to some overlap in the excitation functions for different residual nuclei, and so total separation of those maxima is not observed.

Figure 3.1 illustrates the neutron evaporation and subsequent  $\gamma$  emission occurring following a  $(H.I., xn)$  reaction.

Near the valley of stability the binding energies of charged particles are not too different from those of neutrons, and so the Coulomb barrier strongly inhibits their emission. As the compound nucleus becomes more and more neutron deficient however, the proton (and alpha) binding energies decrease while those of the neutron increase. At some point the sum of the proton binding energy and kinetic energy ( $K.E. \sim$  Coulomb barrier energy) will be roughly equal to the sum of the neutron binding energy and its kinetic energy, i.e.:

$$B_p + E_c = B_n + KE_n \quad [3.1]$$

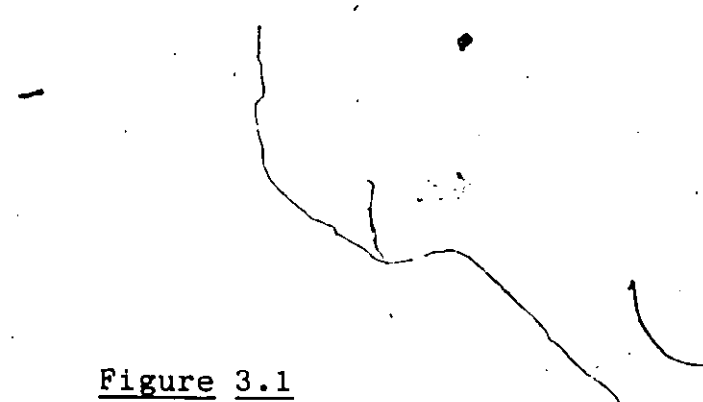
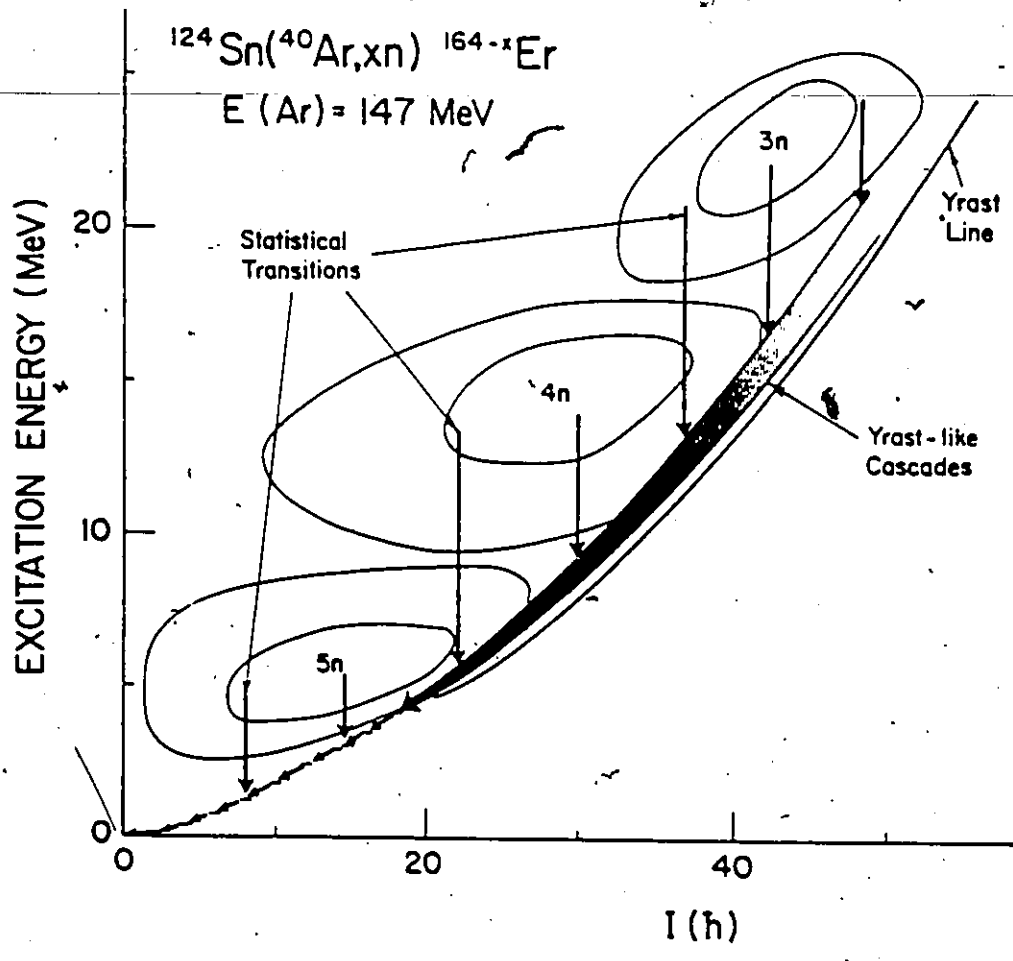


Figure 3.1

Schematic picture of neutron evaporation and subsequent  $\gamma$ -ray de-excitation following a (H.I., xn) reaction. Reproduced from GH79.



This means that neutron and proton emission would populate states with similar excitation energies and therefore similar level densities in their respective residual nuclei. Since the relative probability of neutron and proton emission depends on the barrier transmission coefficients and the available phase space, neutron and proton evaporation should be about equally likely. Under those conditions, and considering three-particle emission as a three-step process with equal probabilities at each step, the following simple exit channel comparison can be made.

$$\begin{aligned} \sigma_{3n} : \sigma_{p2n} : \sigma_{2pn} : \sigma_{3p} &= (1/2)^3 : 3(1/2)^3 : 3(1/2)^3 : (1/2)^3 \\ &= 1 : 3 : 3 : 1 \end{aligned} \quad [3.2]$$

i.e. the cross-sections for the p2n and 2pn modes are significantly higher than for 3n. Not only that, but the total cross-section has been fragmented, reducing the cross-section for a particular residual nucleus and complicating the de-excitation  $\gamma$ -ray spectrum significantly. As well, due to the diffuseness of the Coulomb barrier the proton energy spectrum has more spread in it than the neutron spectrum, resulting in a greater overlap between the excitation functions for different numbers of particles emitted.

An estimate for the line of equal emission probability was made by calculating the energies in Equation [3.1]. Using the Myers-Swiiatecki/Lysekil mass formula (MS67)

and a standard Coulomb barrier formula, this limit is reached at  $A=118$  for  $Z=53$  compound nuclei. As a result, exit channels involving at least one proton can be expected to dominate for  $^{23}\text{Na} + ^{92,94,96}\text{Mo}$  reactions. A similar calculation for alpha vs. neutron emission results in an equal-probability limit at  $A=113$ . At this point the protons are much easier to evaporate, but the ability of the alpha particle to carry off more angular momentum due to its greater mass will be important, especially if the compound nucleus has been formed with extremely high angular momentum.

Figure 3.2 shows the proton-neutron equal emission line for the relevant section of the neutron deficient side of the chart of the nuclides, calculated as described above. Also indicated is the limit at which estimated heavy-ion induced fusion reaction cross sections drop below 1 mb (eg. Re79), relating to the earlier discussion of total cross-section fragmentation.

The different exit channels all produce residual nuclei with roughly the same high excitation energies. For the fusion of 90 MeV  $^{23}\text{Na} + \text{Mo}$  followed by the emission of three particles,  $E_x=17$  MeV. At this energy the level density is extremely high, providing many pathways for  $\gamma$ -ray de-excitation and resulting in a continuum type of spectrum. Calculated level densities and widths do not point to any significant overlap between levels however, so this is referred to as the quasicontinuum spectrum (qcs). The qcs

Figure 3.2

Neutron-deficient  $Z=50$  region of the chart of the nuclides, illustrating the proton-neutron equal emission line ( $\Gamma_p = \Gamma_n$ ). Stable nuclei have the lower half shaded in, while the Te isotopes studied in the present work are cross-hatched. Nuclides labelled with an  $\alpha$  or p are known  $\alpha$ - or proton-emitters; parentheses indicate the emission is  $\beta$ -delayed. Also shown are the proton-drip line, on the n-deficient side of which nuclei are expected to be basically proton-unstable, and a calculated 1-mb production cross-section limit (eg. Re79).



has been found to contain a significant contribution from electric dipole (E1) transitions, which may carry off a fair amount of the excitation energy but little angular momentum. Quasicontinuum  $\gamma$ -ray studies are a fairly new area and have been used mainly to ascertain bulk properties of rapidly rotating nuclei. For a brief overview of qcs findings the reader is referred to the review by de Voigt et al. (de83).

In the region where the level density is no longer so high, the  $\gamma$  rays cascade down populating identifiable levels only on or near the yrast line, which is made up of the states of lowest energy for a given angular momentum. The discrete  $\gamma$  lines observed from these transitions are more likely to be stretched quadrupole, specifically E2, in nature, and so carry off larger amounts of angular momentum. Studies of yrast and near-yrast bands have established the high spin structure in nuclei up to  $\approx 40\hbar$  in some cases.

Due to the statistical nature of the level population process there is no unique point at which the qcs ends and discrete "in-band" transitions begin, and so many levels higher up are bound to be fed from the side as well as from directly above in the band. One can expect, therefore, that high-spin transitions will be less intense than those at the bottom of the level scheme.

Having reached their ground state, neutron deficient nuclei such as  $^{112,114,116}\text{Te}$  decay by  $\beta^+$ -emission and/or electron capture (EC), with half-lives in the range of 2.0

min. ( $^{112}\text{Te}$ ) to 2.5 hrs. ( $^{116}\text{Te}$ ). The decay of the different possible reaction products can further obscure the  $\gamma$ -ray spectra. Figure 3.3 shows the observed exit channels and  $\beta$ -decay modes for the  $^{96}\text{Mo}(\text{Na}, \alpha)$  reaction.

For very neutron deficient nuclei the behaviour of the ground state decay can be quite complex. Beta-delayed proton and/or alpha emission have been observed from a number of isotopes in this region including  $^{113}\text{Xe}$  ( $Z=54$ ),  $^{112}\text{I}$  ( $Z=53$ ), and  $^{108,109,111}\text{Te}$  ( $Z=52$ ) (Ti80, Bo74, Ki77). If the neutron number is small enough, ground state alpha decay and proton emission may be expected to compete.  $^{114}\text{Cs}$  ( $Z=55$ ) has been observed (Ro80) to exhibit all of the above-mentioned modes of decay, with the exception of ground state proton emission, which is energetically unfavourable.

Thus beyond a certain neutron deficiency the large number of open reaction exit channels and the more complex decay modes preclude conventional in-beam and  $\beta$ -decay  $\gamma$ -ray techniques and necessitate the adoption of mass/elemental separation together with decay particle- $\gamma$  coincidence methods. A description of those methods is beyond the scope of this work; however, it should be noted that the unambiguous in-beam identification of  $^{112}\text{Te}$  was made possible by determination of the  $^{113}\text{Xe}$   $\beta$ -delayed proton decay to  $^{112}\text{Te}$  (Ti80).

Figure 3.3

Observed exit channels and subsequent decay modes corresponding to the  $^{96}\text{Mo}(^{23}\text{Na}, xnypz\alpha)$  reaction at 90 MeV. The compound nucleus is  $^{119}\text{I}$ . Nuclei populated in-beam are labelled by exit channel (eg.  $^{116}\text{I}, 3n$ ). Arrows indicate E.C./ $\beta^+$ -decay.

Z = 53

	$^{116}\text{I}$ 3n			$^{119}\text{I}$ Cmpd. Nucl.
52	$^{115}\text{Te}$ p3n	$^{116}\text{Te}$ p2n		
51	$^{113}\text{Sb}$ $\alpha 2n$	$^{115}\text{Sb}$	$^{116}\text{Sb}$	
50	$^{112}\text{Sn}$ $\alpha p 2n$ stable	$^{113}\text{Sn}$	$^{114}\text{Sn}$ 3p2n stable	$^{115}\text{Sn}$ stable
49			$^{116}\text{In}$ stable	
	N = 62	63	64	65
				66

### 3.2 Experimental Procedures

In order to obtain information on the excited states of the chosen even Te nuclei, the nuclear reactions listed in Table 3.1 were initiated.  $^{23}\text{Na}$ ,  $^{27}\text{Al}$  and  $^{28}\text{Si}$  beams were provided by the McMaster FN Tandem Van de Graaff accelerator.

Detection of the  $\gamma$  rays was accomplished using coaxial Ge and Ge(Li) detectors with energy resolutions of 2.0 to 3.0 keV full width at half maximum (FWHM) @ 1.33 MeV under experimental conditions, and crystal volumes of 50 cc. to 130 cc. Data were acquired on a dedicated on-line PDP-9 computer or the on-line facility of a VAX 11/750. Intensities and centroids of peaks in spectra were extracted either by simple integration following a local background fit, or using a more complicated deconvolution method which was capable of unfolding the entire spectrum, after having stripped away a spectrum-wide background. A description of this latter process and of the program developed during the course of this work to implement the deconvolution procedure is given in the Appendix.

Detector energy and relative efficiency calibrations were carried out using standard calibrated sources of known  $\gamma$ -rays. The ADC's were found to be linear to  $\pm 2$  channels and so a first-order energy calibration was usually suitable.

Throughout these experiments the Ge detectors were used in conjunction with a 6-element array of large NaI scintillation counters. The relatively high efficiency of

Table 3.1

Nuclear reaction information.

Nucleus	Reaction	Beam Energy (MeV)	Avge. Beam Energy in Target (MeV) <sub>a</sub>
$^{112}\text{Te}$	$^{92}\text{Mo}(^{23}\text{Na}, p2n)$	90	84
$^{114}\text{Te}$	$^{94}\text{Mo}(^{23}\text{Na}, p2n)$	85 <sup>b</sup> , 90	79, 84
	$^{92}\text{Mo}(^{28}\text{Si}, \alpha 2p)$	125	115
$^{116}\text{Te}$	$^{96}\text{Mo}(^{23}\text{Na}, p2n)$	90	84
	$^{92}\text{Mo}(^{27}\text{Al}, 3p)$	114	105

<sup>a</sup> For a target thickness of 3.0 mg/cm<sup>2</sup>.

<sup>b</sup> The  $^{114}\text{Te}$   $\gamma$ - $\gamma$  coincidence experiment was performed at this lower energy due to FN limitations, before an accelerator upgrade was undertaken.

this "multiplicity filter" enabled events from the de-excitation of fusion reaction residual nuclei to be selectively chosen over competing processes such as Coulomb excitation and  $\beta$ -decay, without suffering an unreasonable loss in count rate. This capability proved not only to be extremely beneficial in enhancing high spin data, which was the filter's original purpose, but sometimes essential to recovering information about transitions which would otherwise have been masked by  $\gamma$  rays due to those unwanted events. Filter characteristics and illustrations of its effectiveness will be given in Section 3.2.3.

The following measurements were undertaken:

- 1)  $\gamma$ -ray excitation functions
- 2)  $\gamma$ - $\gamma$  coincidence experiments
- 3)  $\gamma$ -ray angular distributions.

The excitation functions served to determine the optimum beam energy at which to run the experiments, as well as to identify groups of  $\gamma$  rays as belonging to different subsets of residual nuclei. When used in conjunction with information available from the literature, as well as out-of-beam  $\beta$ -decay measurements, definite assignments of  $\gamma$  rays to specific nuclei could usually be made.

$\gamma$ - $\gamma$  coincidence experiments were used to determine the  $\gamma$ -ray decay schemes, and thus the energy levels for the nuclei of interest. The quoted transition intensities in the residual nuclei were based largely on coincidence measure-

ments. Ordering of the various  $\gamma$  rays was accomplished using both those quoted intensities and intensities extracted from relevant  $\gamma$ - $\gamma$  coincidence gate spectra.

Angular distributions yielded absolute intensities as well as the angular intensity patterns of the transitions. The intensity information was used to supplement that available from the  $\gamma$ - $\gamma$  measurements. Spins and parities ( $J^\pi$ ) of excited states were deduced from the angular distribution patterns.

Full descriptions of the techniques used in this work are given below. In those instances where an elaborate explanation of standard methods or equipment is not felt to be necessary, reference is made to the appropriate literature.

### 3.2.1 Ion Beam Production

Beams of  $^{27}\text{Al}$  and  $^{28}\text{Si}$  negative ions were produced routinely by a reflected cesium sputter source for injection into the FN Tandem accelerator. Because of their extremely low electron affinity and low sputtering yield,  $\text{Na}^-$  ions, however, are much more difficult to produce. Charge exchange of a  $\text{Na}^+$  beam in a sodium vapour canal has been attempted elsewhere with an observed efficiency of only 0.4% (He77). The McMaster lab did not have an ion source capable of producing a  $\text{Na}^+$  beam of the required intensity.

$\text{Li}^-$  ions have been produced by injecting intense proton beams from the duoplasmatron source into a canal filled with Li vapour, and then extracting the lithium ions from the canal region. The mechanism which causes this procedure to work is not well understood. It could be that the positive source beam is reflected or stopped near the extraction point due to the positive potential, ionizing a small region of the lithium vapour, from which  $\text{Li}^-$  ions can be extracted (As83). After considerable experimentation with Na vapour in the source,  $\text{Na}^-$  beams of useful intensity were produced in a similar manner.

The use of sodium vapour in the charge exchange canal introduced some complications, however, as Na is much more reactive than Li. As well, the vapour pressure of Na is quite high and varies strongly as a function of temperature, with the result that the negative ion beam intensity was not always steady, and the source parameters, especially the canal temperature, had to be carefully monitored. It was not uncommon for sodium vapour to condense in a cooler area of the canal region, and thus eventually block the canal completely. This happened less frequently after experience resulted in some reliable operating conditions and a canal with an improved electrode design and increased boiler cooling capacity was installed by the operations staff. Using positive hydrogen or deuterium ions from the duoplasmatron,  $\text{Na}^-$  beams were eventually obtained with some



consistency. After passing through the stripper foil in the central high voltage terminal of the accelerator, 5-20 nA of  $^{23}\text{Na}^{9+}$  could be focussed and selected by the analyzing magnet for use in the experiment. The use of the 9+ charge state meant that the 90 MeV beam energy necessary for the  $\text{Mo}(^{23}\text{Na}, xnyp)$  reactions was attainable at a reliable terminal potential. Later on in this series of experiments 10 MV was attainable and so the more convenient 8+ charge state was used with a less intense beam from the ion source.

As an interesting side-effect of this procedure, it was found that beams of some other negative ions could be produced with more intensity using Na vapour as a charge exchange medium. As an example 15  $\mu\text{A}$  of  $^4\text{He}^{2+}$  have been analyzed, compared with the previous maximum of 3  $\mu\text{A}$  obtained with Li. For many light ion and nitrogen beams the charge exchange is now carried out using sodium.

One complication of using heavy-ion beams is that ions of different combinations of mass and charge state may be accelerated and end up with very similar values of magnetic rigidity, in which case the feedback stabilizing system may select the wrong beam. This was quite possible in the case of the Na beam from the duoplasmatron, since when that source was operated at the higher temperatures necessary to extract a Na beam of sufficient intensity it usually produced "messy" beams containing a mixture of ion species, which the low energy magnet could not filter effectively. Fortunately

the strong characteristic  $^{23}\text{Na}$   $\gamma$ -ray transition at 440 keV, caused by Coulomb excitation at the target, could be used to make a quick definite identification.

Various compounds containing Na have been investigated in sputter sources, with generally quite poor results. For example, Middleton reported a  $\text{Na}^-$  yield of only 13 nA from a  $\text{Na}_{1.0}\text{Bi}_{1.8}$  cone, although the  $\text{Bi}^-$  yield was 800 nA, and the consensus seems to be that "alkali metals (except for  $\text{Li}^-$ ) are difficult to obtain from a sputter source" (Mi77). At the beginning of this study cones containing samples of  $\text{NaNH}_2$ ,  $\text{NaNO}_3$ ,  $\text{Na}_2\text{O}_2$ , Na, and NaOH were loaded into the McMaster sputter source, but no consistent  $\text{Na}^-$  beams of any useful intensity were observed.

However after the main series of experiments had been completed, it was found that a cone containing  $\text{NaCl} + \text{Ag}$  ( $\text{NaCl}:\text{Ag} \sim 1:1$  by volume) did produce a Na beam of sufficient intensity, but only for  $\sim 1$  hour, after which the intensity steadily dropped off. By keeping the Cs ionizer fairly hot but the rest of the source at a normal temperature a steady  $\text{Na}^-$  beam was obtained for 2-3 hours, after which a new cone could be used. Furthermore, a used cone could be re-used, if left untouched for a while. This procedure was used for the  $^{92}\text{Mo}(^{23}\text{Na}, p2n)^{112}\text{Te}$   $\gamma$ - $\gamma$ -TAC experiment, in which six cones were used over a twenty-hour period. The beams produced during this run were quite "clean" and the accelerator was not loaded appreciably and could be operated at high voltages

quite easily, in contrast to the beam characteristics using the duoplasmatron source.

### 3.2.2 Target Preparation

The enriched Mo isotopes were obtained from Oak Ridge National Laboratory in metallic powder form, then melted down and rolled into foils. A thickness of  $\sim 3 \text{ mg/cm}^2$  was chosen as a reasonable compromise between  $\gamma$ -ray production and beam energy loss considerations.  $^{208}\text{Pb}$  was then evaporated onto the Mo to a thickness of  $\sim 6 \text{ mg/cm}^2$ , sufficient to stop the reaction product recoils. Table 3.2 contains a list of the targets used and their isotopic purities.

### 3.2.3 Multiplicity Filter

The de-excitation of a residual nucleus after particle emission is characterized by high  $\gamma$ -ray multiplicity  $M_\gamma$ : it is not uncommon for 20 or more  $\gamma$  rays to be given off during this process. On the other hand, the usual "non-reaction" events result in multiplicities of two or so for Coulomb excitation (Coulomb) in this mass region (as observed in singles  $\gamma$ -ray spectra) and normally only three or four in the case of  $\beta^+$ -decay. Thus the capacity to differentiate between high and low-multiplicity events can not only enhance high-spin transitions, but also discriminate against those non-reaction events. The apparatus described here was built

Table 3.2

Relative isotopic abundances of target materials.

Mass Number	$^{92}\text{Mo}$	$^{94}\text{Mo}$	$^{96}\text{Mo}$
92	97.37	0.73	0.18
94	0.68	91.59	0.20
95	0.52	5.35	0.93
96	0.37	1.11	96.76
97	0.18	0.37	0.96
98	0.40	0.65	0.80

by Larabee and Waddington (LW80) with the former function in mind.

The multiplicity filter consists of five 5"x6" and one 3"x3" NaI scintillation counters, together with electronic modules to produce appropriate logic gates for the Ge detector signals. The beam passes through a hole in the centre of one of the 5"x6" crystals, minimizing the loss of solid angle at  $180^\circ$  due to the beam tube. All the NaI detector faces were covered with graded Pb, Cd, and Cu shields, while those surfaces not pointing towards the target had a 1/2" thick layer of Pb as well, to reduce the effect of Compton scattering between detectors. Normally only the beam-through crystal and the unit directly below the target chamber were constrained to remain in fixed locations. The remaining detectors were mounted on large arms and could be adjusted to optimize the geometry once the Ge detectors were in place.

Two logic pulses of 100 ns width are available from a fast coincidence module designed and built by the electronics group, either of which pulses may be used to determine the acceptance of a Ge or Ge-Ge event. The first is produced if at least one NaI is triggered, and the second if two or more NaI's register  $\gamma$  rays within 200 ns of each other.

The NaI array was employed in two configurations. For Ge-Ge coincidence experiments the adjustable elements were located to maximize the solid angle, after the Ge

detectors had been manoeuvred into position. The total efficiency times solid angle ( $\Sigma \epsilon_i$ ) was previously measured to be 0.225 for 660 keV  $\gamma$  rays in this mode (LW80). A Ge-Ge event was recorded only if it coincided with a filter gate. Five coaxial Ge units were mounted at angles of roughly  $\pm 100^\circ$ ,  $\pm 50^\circ$ , and  $0^\circ$  with respect to the beam axis, close to the horizontal plane, at distances of between 8 and 9 cm. from the target.

Angular distributions were performed using the filter in a symmetric mode with the detectors at back angles or straight above and below the target, so as to allow a Ge detector to be positioned at any forward angle from  $0^\circ$  to  $90^\circ$  with respect to the beam axis and to minimize possible angular correlation effects. Another monitor Ge detector was placed at  $-90^\circ$ . For this configuration  $\Sigma \epsilon_i = 0.176$  for the NaI filter. A Ge singles event was considered valid if it was coincident with a filter gate. Data acquired in this fashion were labelled as "gated singles" spectra.

Assuming an event has  $M_\gamma$   $\gamma$  rays associated with it, and that  $M_d$  of those  $\gamma$  rays have been detected by the Ge detector(s) ( $M_d=1$  or  $2$ ), the probability of at least one NaI being triggered and thus gating that event is given by:

$$P_{\text{gate}} = 1 - (1 - \Sigma \epsilon_i)^{M_\gamma M_d} \quad [3.3]$$

where  $(1 - \Sigma \epsilon_i)^{M_\gamma M_d}$  is just the probability that none of the

available  $\gamma$  rays were detected by the filter. If two or more NaI's are required for a gate:

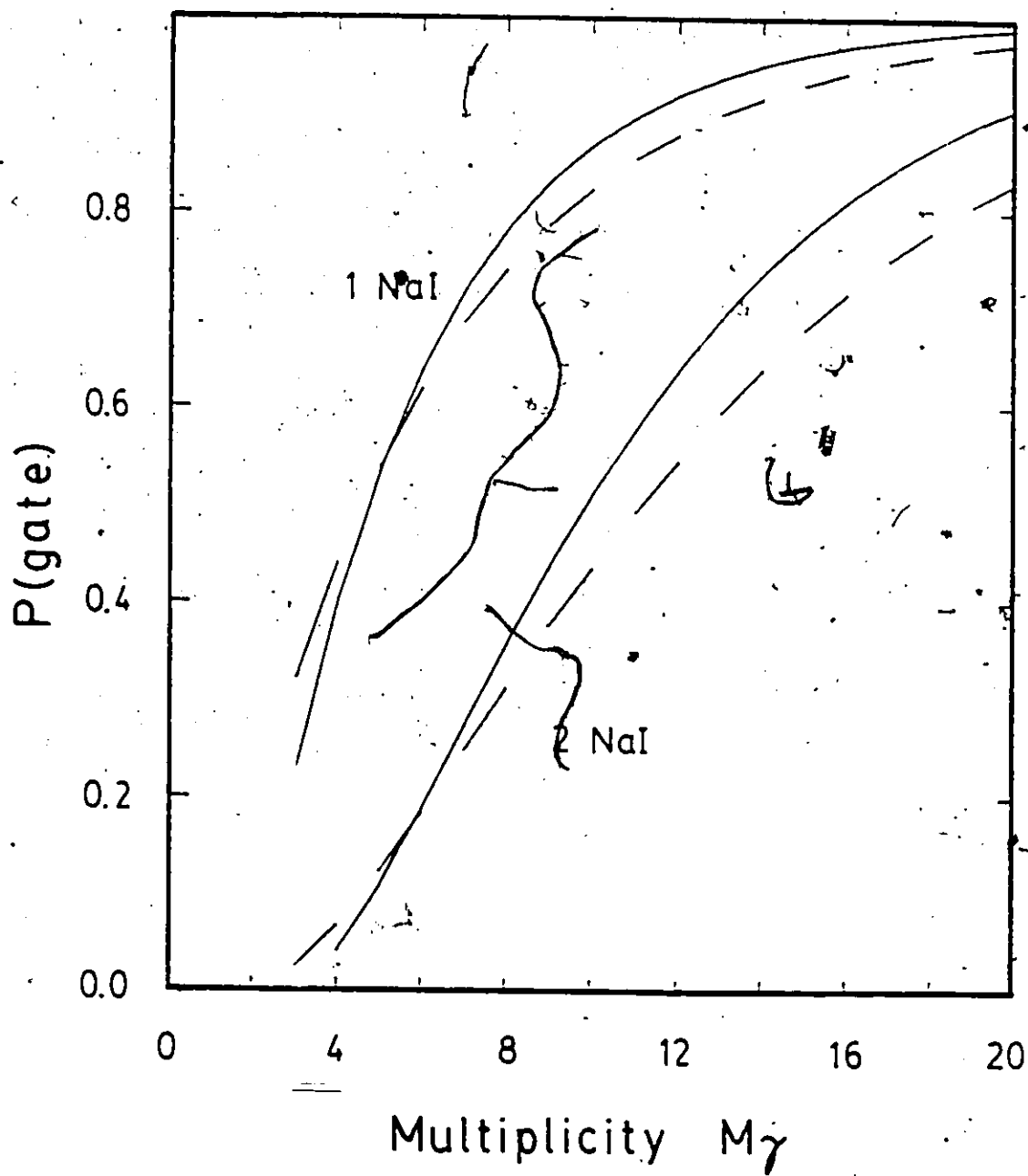
$$P_{\text{gate}} = 1 - (1 - \sum_i \epsilon_i)^{M_Y - M_d} - \sum_{N=1}^{M_Y - M_d} \binom{M_Y - M_d}{N} [\sum_i \epsilon_i]^N (1 - \sum_i \epsilon_i)^{M_Y - M_d - N} \quad [3.4]$$

The results of these calculations are shown in Figure 3.4. For  $M_d=2$  (Ge-Ge coincidence experiments), an  $M_Y=4$  cascade will be gated due to a coincidence in the filter only 4% of the time, while an  $M_Y=10$  cascade will be accepted 51% of the time. Thus the lower multiplicity events tend to be discriminated out quite drastically, with an acceptable loss in overall efficiency for the high multiplicity events. Coulomb excitation events, identified in singles spectra as overwhelmingly one- or two- $\gamma$  events, have a gating rate which is determined solely by the singles total count rates and the resolving time of 200 ns. With average count rates of  $<7,000$  counts/sec in the Ge detectors, and a total of  $<80,000$  counts/sec in the filter, this was negligible.

For Ge "singles" angular distributions ( $M_d=1$ ), again considering only coincidences in the filter, an  $M_Y=4$  cascade will be gated 7% of the time, while an  $M_Y=10$  event will be accepted 44% of the time. Based on these considerations the discrimination is not as severe, but again the Coulex multiplicity is less than the event requirement, so the

Figure 3.4

Multiplicity filter gating probabilities. Solid and dashed lines correspond to the coincidence ( $M_d=2$ ) and gated singles ( $M_d=1$ ) modes respectively, requiring one NaI (upper curves) or two (lower curves). In all of the measurements described here two NaI detectors were used to gate the data, with the exception of the  $^{112}\text{Te}$   $\gamma$ - $\gamma$ -TAC experiment (see Section 3.2.7).



acceptance rate is purely random and those events are effectively eliminated.

Figure 3.5 compares the  $\gamma$ -ray spectra, obtained with and without the multiplicity filter, from the  $^{94}\text{Mo}(^{23}\text{Na},xyz)$  reaction at 85 MeV. The reduction in intensity of the Coulex and  $\beta$ -decay lines relative to reaction  $\gamma$  rays is quite evident.

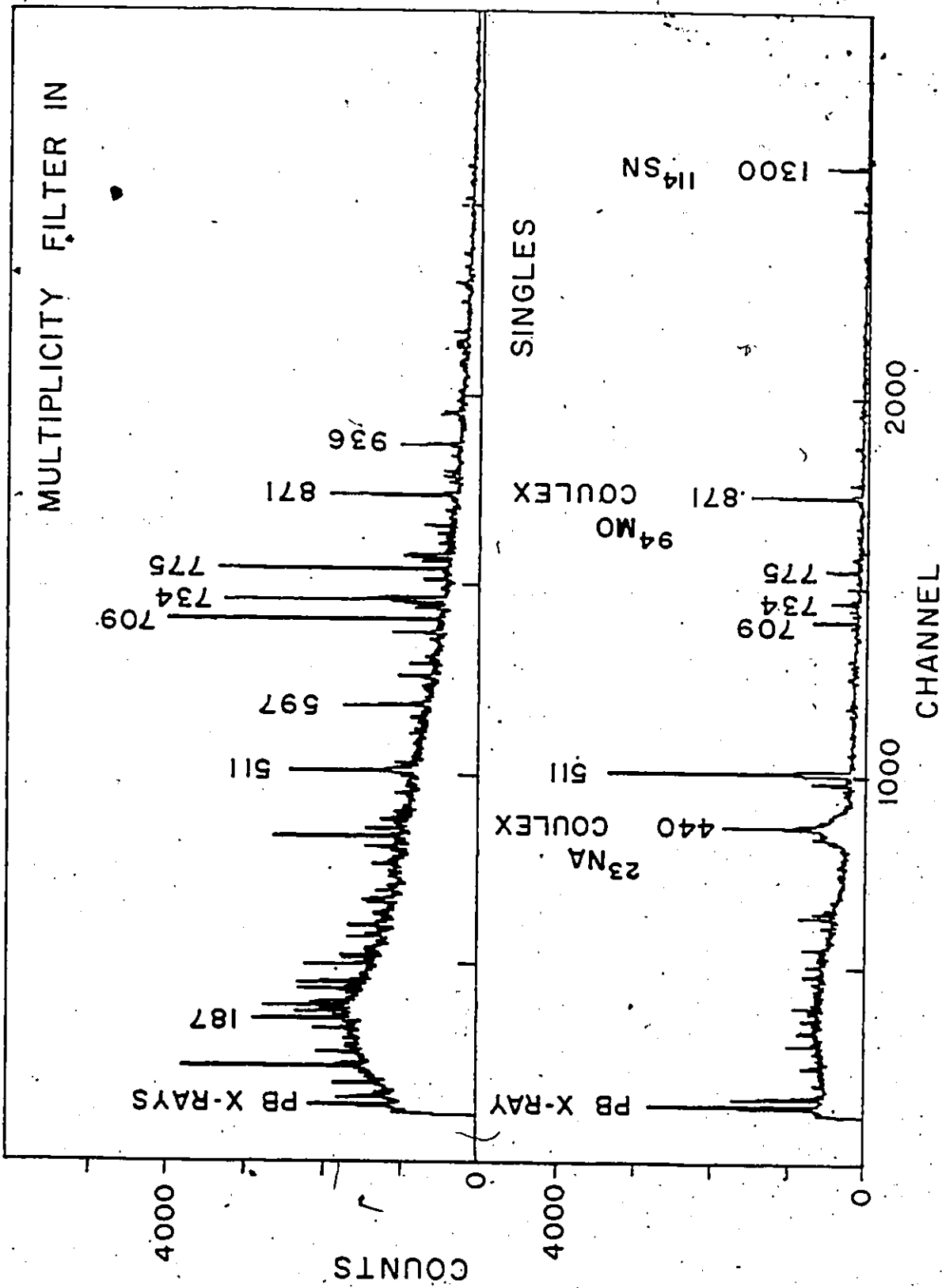
#### 3.2.4 Excitation Functions

For the reactions involving  $^{23}\text{Na}$  beams,  $\gamma$ -ray spectra, both singles and gated by a coincidence in the NaI filter, were acquired using a Ge detector at  $90^\circ$  to the beam direction at various beam energies. The integrated target current was used to normalize the  $\gamma$ -ray intensities, which were corrected for detector efficiency, angular distribution effects, and absorption by the target chamber. The  $^{23}\text{Na}$  beam energies ranged from 75 MeV (near the Coulomb barrier) to approximately 100 MeV, which was the upper limit of the accelerator for that beam.

Relative yields of residual nuclei from the (H.I., xyz) reactions, as functions of bombarding energy, were obtained first of all from singles  $\gamma$ -ray intensities. In most cases the intensity of the strongest  $\gamma$  ray identified as de-exciting medium to high-spin states in each particular nucleus was used. For even-even nuclei the  $2^+ \rightarrow 0^+$  g.s. transition was taken as representing the total de-excitation

Figure 3.5

Comparison of filter-gated and singles  $\gamma$ -ray spectra from the  $^{94}\text{Mo}(^{23}\text{Na},xyz)$  reaction at 85 MeV.



strength. In other cases wherever possible corrections were made as needed for reported branching ratios and/or multiple de-excitation paths. Where applicable the intensities were also adjusted for estimated  $\beta$ -decay strength from other nuclei in the same A-chain populated by the reaction. Gamma-ray identifications obtained solely from in-beam work may be ambiguous for some of the less-studied nuclei, and so not all of the necessary information was available to obtain accurate excitation measurements for some of the more neutron-deficient residual nuclei.

Statistical model fusion-evaporation cross-section calculations were carried out using the code ALICE/LIVERMORE 82 (a.k.a. ALICE; BB82) and compared with the observed excitation functions. Standard input parameters were used with the exception of the level density parameter, which was decreased from the usual  $\sim A_{CN}/10$  to  $A_{CN}/30$  in an attempt to produce closer agreement with the observed functions. Further changes in this parameter were less effective.

As a measure of the relative amount of  $\gamma$ -ray information available from the different nuclei, excitation functions for transitions gated by the multiplicity filter are more useful and can be quite different from singles intensities (c.f. Figures 4.2 and 4.4). One reason for this difference is that for these heavy-ion reactions the highest spin states, which give rise to high-multiplicity events, are

populated when the number of particles emitted is least (see Figure 3.1).

$^{92,96}\text{Mo}(^{23}\text{Na},\text{p}2\text{n})^{112,116}\text{Te}$   $\gamma$ - $\gamma$  coincidence measurements and  $^{92,94,96}\text{Mo}(^{23}\text{Na},\text{p}2\text{n})^{112,114,116}\text{Te}$  angular distributions were performed at 90 MeV, since this was the maximum energy at which a steady beam of sufficient intensity could be obtained for extended periods of time. However the  $^{114}\text{Te}$  coincidence experiment was completed before the latest accelerator upgrade, and only 85 MeV was attainable at that time. For these  $^{23}\text{Na}$ -induced reactions the excitation functions indicated that the accelerator limitations determined the choice of beam energy and served to identify groups of  $\gamma$  rays belonging to different exit channels. The p2n channel generally had the highest cross section at 85-90 MeV.

### 3.2.5 $\gamma$ - $\gamma$ Coincidence Measurements

For these experiments the target was mounted on a titanium ring inside a small cylindrical plastic chamber, and was situated about 2 cm in front of a lead beam stop. A single aperture 30 cm in front of the target was sufficient to ensure collimation of the beam.

As mentioned previously, five Ge co-axial detectors were used, placed at roughly  $\pm 100^\circ$ ,  $\pm 50^\circ$ , and  $0^\circ$  with respect to the beam direction, close to the horizontal plane. The crystal-to-target distances were 8-9 cm. The choice of a multi-detector array at this distance was shown by Larabee

and Waddington (LW80) to satisfy the requirement of a reasonable detection efficiency while minimizing the effect of true coincident summing. Lead shields and cones were placed around the crystals to reduce the number of Compton scattering events. Amplifier gains were adjusted so that peak positions in the five projection spectra were no more than a channel apart. Coincidences between any two detectors, within a resolving time of 200 ns, were accepted only if a coincident gating signal resulting from two or more  $\gamma$ -rays in the NaI filter was received. With five detectors there are  $\binom{5}{2} = 10$  possible combinations for a  $\gamma$ - $\gamma$  coincidence. Triple Ge coincidences were observed  $\sim 10\%$  as frequently as double coincidences, but were considered as valid as the usual 2-Ge + 2-NaI events, given the relative efficiencies, and so they made up  $\sim 20\%$  of the events that were finally accepted. The triples are also valuable because each event actually provides the same information as is contained in three  $\gamma$ - $\gamma$  coincidences. Quadruple Ge coincidences were also observed, but very infrequently (eg.  $\sim 0.4\%$  of the time for one experiment). Table 3.3 lists the characteristics of some typical detectors used for the coincidence experiments, as well as representative count rates for the Ge and NaI arrays. The coincidence electronics set-up is shown in Figure 3.6.

The data, labelled by detector, were written onto magnetic tape on an event-by-event basis. Approximately 20

million  $\gamma$ - $\gamma$  coincidences were acquired during each experiment. Off-line sorting programs allowed up to 250 digital windows to be set, and the backgrounds for the resulting 1024-channel gate spectra were subtracted using windows set on either side of the peak window. ADC gains were recorded frequently, and reasonable shifts could be accommodated by the sorting programs.

It was found that in the  $^{112}\text{Te}$   $\gamma$ - $\gamma$  experiment the detector array coincidence efficiency showed a serious roll-off at energies below 150 keV. The presence of an important 92 keV transition in the level scheme necessitated a second  $\gamma$ - $\gamma$  experiment, using two planar plus three large co-axial Ge detectors instead of the usual five large Ge units. As well, the shielding normally placed in front of the detector crystals to cut down on the Pb x-ray flux was removed.

For this experiment the same electronics and on-line acquisition system on the VAX 11/750 was used, but the data were sorted off-line into a 1024 x 1024-channel coincidence matrix. After corrections for detector efficiency had been made the matrix background was removed using the universal background method of Palametta and Waddington (PW85), and gate spectra projected out, as a result of which the coincidence relationships involving low-energy transitions did become clearer.

Table 3.3Typical  $\gamma$ -ray detector characteristics.

Detector	Resolution @ 1.257 MeV
25%	2.3 keV
11%	1.9 "
50cc	2.6 "
65cc	3.5 "
26%	2.4 "

Representative detector count rates: (counts/second)

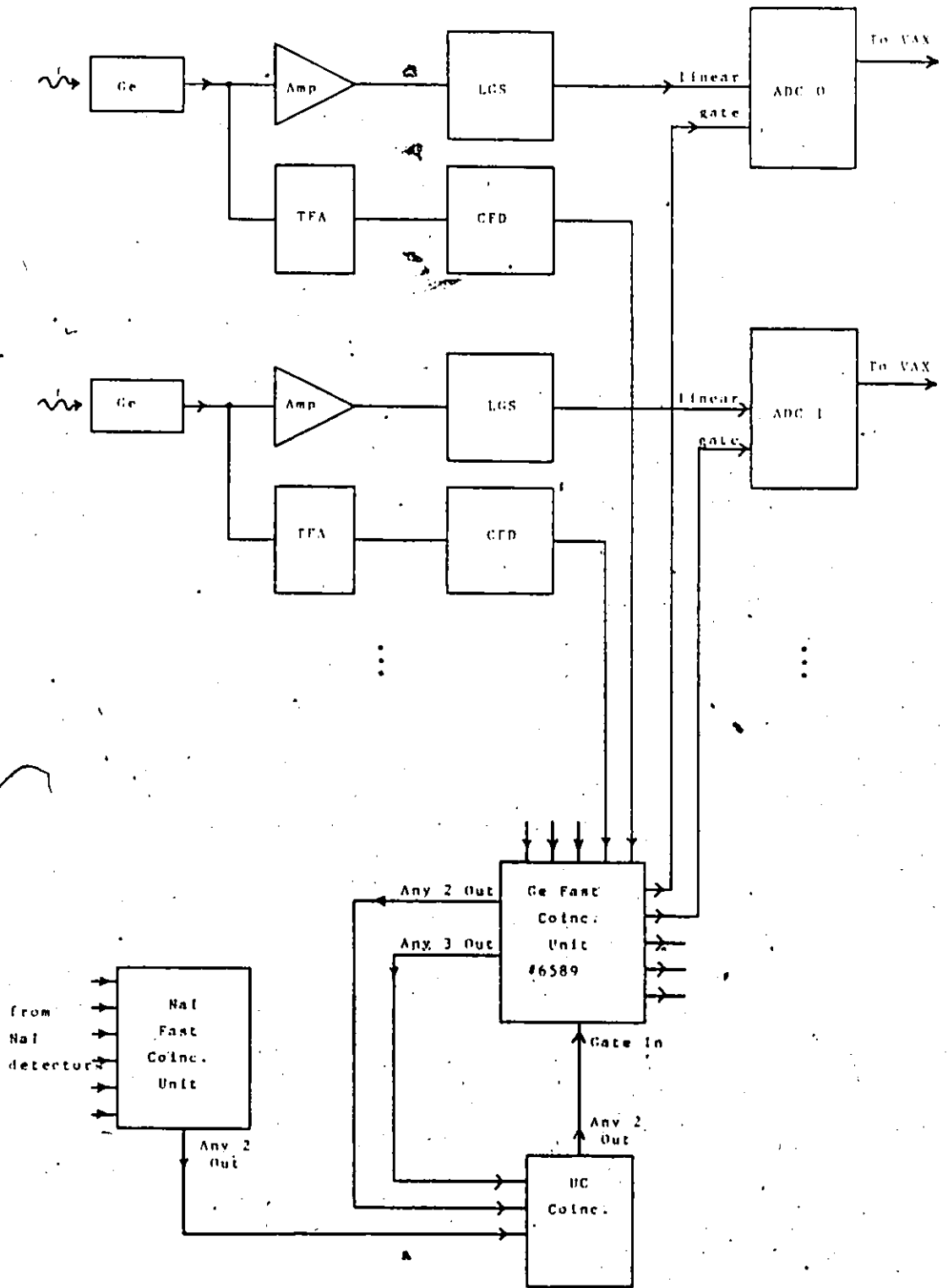
Ge singles (avge.)	6,000
Ge-Ge coincidences	3,000
Triple-Ge coincidences	300
Quadruple Ge coincidences	12
Any one NaI	60,000
Any two NaI	11,000
Overall event rate	1,200

Figure 3.6

Gamma-gamma coincidence electronics diagram. The module designations are as follows:

Ge Germanium  $\gamma$ -ray detector  
Amp Linear amplifier  
TFA Timing filter amplifier  
CFD Constant-fraction discriminator  
LGS Linear gate & stretcher<sup>c</sup>  
ADC Analogue to digital converter  
UC Universal coincidence module

Only two of the five Ge detector set-ups are shown.



### 3.2.6 Angular Distributions

For these measurements an aluminum chamber was used, with the target mounted on a  $64 \text{ mg/cm}^2$  lead beam stop against the  $1/32''$  Al end face, at  $45^\circ$  to the beam direction. A second collimator 6 cm from the target was used to keep the beam spot on the target to 2 mm or less in size and its position stable.

A single Ge detector was placed 9-11 cm from the target at angles of  $0^\circ$ ,  $30^\circ$ ,  $45^\circ$ ,  $60^\circ$  and  $90^\circ$  with respect to the beam direction. Spectra gated by a coincidence in the multiplicity filter, as well as in singles mode were acquired. A monitor counter at  $-90^\circ$  was used for normalization, while the intensities of out-of-beam  $\beta$ -decay lines provided geometrical corrections. Absorption of the  $\gamma$  rays by the lead beam stop was calculated and corrections made. ADC livetimes were monitored and when necessary taken into account.

The angular distributions for the extracted peak intensities were fitted to the usual function of Legendre polynomials  $P_k$ :

$$W(\theta) = I_\gamma [1 + A_2 Q_2 P_2(\cos\theta) + A_4 Q_4 P_4(\cos\theta)] \quad [3.4]$$

to obtain values of  $I_\gamma$ ,  $A_2$  and  $A_4$ . The  $Q_k$ 's (attenuation coefficients) were calculated from the detector geometry using the procedure given by Krane (Kr72). Typical values

for a 700 keV  $\gamma$  ray were  $Q_2 = 0.96$  and  $Q_4 = 0.89$ . The  $A_k$  coefficients depend on the  $\gamma$ -ray multipolarity ( $L$ ), the spins of the initial and final states ( $J_i$  and  $J_f$ ), and the magnetic substate population parameters. In some cases more than one  $L$  is possible and a mixing ratio  $\delta$  is necessary where:

$$\delta \equiv \frac{\langle J_f | L_2 | J_i \rangle}{\langle J_f | L_1 | J_i \rangle} \quad [3.5]$$

Using Gaussian substate populations (c.f. Di66) of various widths ( $\sigma = 1.0-4.0$ ) theoretical distributions were calculated for a range of mixing ratios, as well as different spin and multipolarity assumptions, and compared with the fits to experimental data by examining  $\chi^2$  values.

Spin and parity assignments were made using the following arguments:

1) Owing to the very large difference in transition rates for pure M2 vs. pure E1 radiation, substantially mixed M2/E1 transitions are highly unlikely. Therefore a mixing ratio for any  $\Delta J = 0$  or  $\Delta J = \pm 1$  transition was interpreted as indicative of an M1/E2 admixture, meaning that the two levels involved must have identical parity.

2) Angular distribution measurements usually allow a unique  $\Delta J$  determination but are not as sensitive to the sign of  $\Delta J$ . However, since following (H.I.,xyz) reactions the state with highest angular momentum at a given energy is

preferentially populated, it was assumed that high spin states are much more likely to decay to states with lower spin (see, for example, KW76).

3) Unless there was some reason to question the accuracy of the data (eg. very weak or unresolved doublet  $\gamma$  rays) only  $\Delta J$  results giving a  $\chi^2$  value below the 99.9% confidence limit were accepted. In some instances more than one possibility for  $\Delta J$  met this condition, and in most of these cases the option with the highest magnitude of  $\delta$  could be discarded based on reasonable upper limits for mixing ratios.

The angular distribution coefficients were in general extracted from the data gated by the multiplicity filter. In order to ensure that this gating condition was not imparting a significant bias to the distributions a comparison was made between singles and gated  $A_k$  coefficients for the  $^{94}\text{Mo}(^{23}\text{Na}, p2n)^{114}\text{Te}$  reaction spectra. The results, presented in Table 3.4, show no such bias. It is worth pointing out that some of the angular distributions were difficult or impossible to obtain using the singles data alone. A substantial number of angular distributions were extracted using programs, written as part of this project, which automatically unfold spectra (see Appendix) and then search output files for chosen  $\gamma$  rays and produce fits to Equation [3.4] as well as files for plotting those fits. Any necessary corrections as outlined earlier are made by the programs, which also look for centroid, width and intensity anomalies as a function of

Table 3.4

Comparison of filter-gated vs. singles  $\gamma$ -ray angular distribution coefficients from the  $^{94}\text{Mo}(^{23}\text{Na}, p2n)^{114}\text{Te}$  reaction. The higher values of gated  $A_2$ 's for E2 transitions are likely due to increased alignment of the residual nuclei.

$E_\gamma$ (keV)	$I_\gamma(^{114}\text{Te})$	Gated		Singles	
		$A_2$	$A_4$	$A_2$	$A_4$
125.2	15	0.05(6)	-0.20(7)	0.01(6) <sup>a</sup>	-0.04(7)
425.0	20	-0.28(4)	-0.03(4)	b	
596.1 <sup>c</sup>	29	0.30(3)	-0.16(4)	0.28(3)	-0.11(4)
691.7	17	0.32(4)	-0.13(5)	0.34(4)	-0.10(4)
708.8	100	0.28(2)	-0.10(3)	0.23(2)	-0.08(3)
733.7	93	0.32(2)	-0.11(3)	0.25(2)	-0.12(3)
775.0	100	0.29(2)	-0.11(3)	0.22(2)	-0.09(3)
790.2	19	0.19(5)	-0.09(6)	d	
831.4	14	0.38(5)	-0.13(6)	0.31(5)	-0.13(5)
871.3	57	0.26(3)	-0.08(3)	e	
936.2	21	-0.30(4)	-0.05(4)	-0.34(3)	-0.01(3)

<sup>a</sup> Part of a partially unresolved doublet in singles. The intensity of the second component is ~10% that of the major component.

<sup>b</sup> Unable to extract due to large 440-keV beam Coulomb excitation  $\gamma$ -ray background.

<sup>c</sup> Part of an unresolved doublet.

<sup>d</sup> Part of a multiplet unresolved at some angles in singles.

<sup>e</sup> Unable to extract due to presence of intense 871-keV target Coulomb excitation line.

angle and flag those transitions accordingly. For a number of transitions the results of this fairly automatic method were compared with those of more standard techniques. No discrepancies, which would have changed spin assignments were observed, and in the large majority of cases agreement among the  $A_k$ 's was quite good.

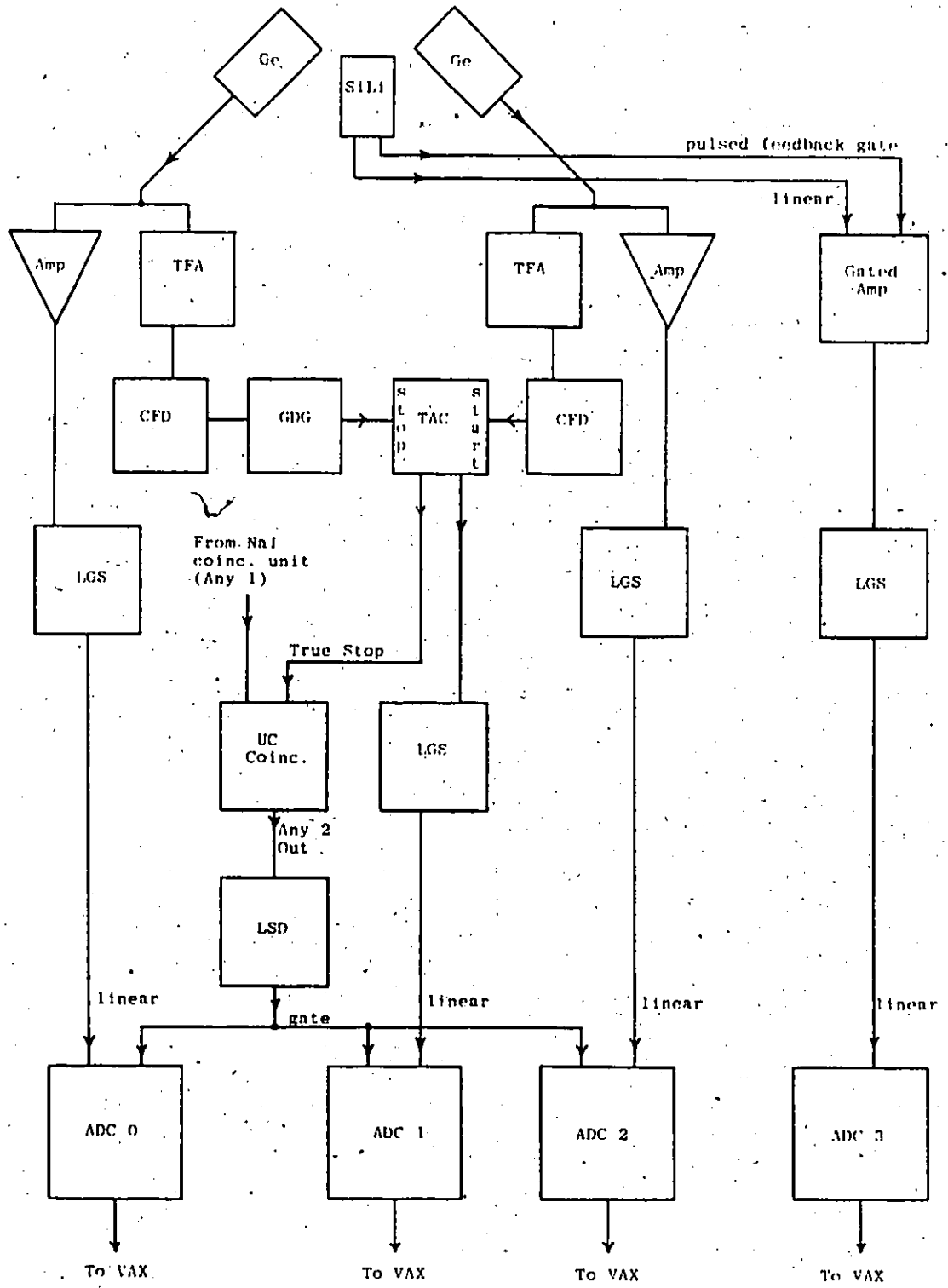
### 3.2.7 $^{112}\text{Te}$ $\gamma$ - $\gamma$ -TAC Coincidence Experiment

Analysis of the  $^{112}\text{Te}$  data, carried out in the manner described in the previous two sections, revealed a number of unusual  $\gamma$ -ray angular distributions and coincidence features which raised the question of possible excited state lifetimes in the nanosecond range. Therefore a separate  $\gamma$ - $\gamma$ -TAC coincidence experiment was performed using two 25%-efficiency Ge detectors and standard fast-slow coincidence techniques. The experimental set-up is shown in Figure 3.7. Data were gated by the multiplicity filter in this case as well. The two  $\gamma$ -ray energies plus time information for each event were written onto magnetic tape and analysed off-line at a later date. Gates could be set on different combinations of energy words and/or the time word to produce either  $\gamma$ - $\gamma$  coincidence spectra or specific  $\gamma_1$ - $\gamma_2$  time spectra. Coincidence spectra extracted corresponding to a 200 ns time gate agreed with those from the usual procedure as described in Section 3.2.5. Time spectra for 68  $\gamma_1$ - $\gamma_2$  combinations were also extracted,

Figure 3.7

$^{112}\text{Te}$   $\gamma$ - $\gamma$ -TAC electronics diagram. The module designations are identical to those in Figure 3.6, with the following additions:

SiLi	Si(Li) planar $\gamma$ -ray detector
GDG	Gate and delay generator
TAC	Time-to-amplitude converter
LSD	Logic shaper and delay



and for such spectra background under both  $\gamma_1$  and  $\gamma_2$  peaks required the following coincidence correction:

$$\begin{aligned}
 \gamma_1 \otimes \gamma_2 (\text{measured}) &= (\gamma_1 + \gamma_{1B}) \otimes (\gamma_2 + \gamma_{2B}) \\
 &= \gamma_1 \otimes \gamma_2 (\text{true}) + [(\gamma_1 \otimes \gamma_{2B}) + (\gamma_{1B} \otimes \gamma_2) + \\
 &\quad + (\gamma_{1B} \otimes \gamma_{2B})] \\
 &= \gamma_1 \otimes \gamma_2 (\text{true}) + \text{Bgnd} \quad [3.6]
 \end{aligned}$$

where  $\gamma_1$  refers to peak events,  $\gamma_{1B}$  stands for background events, and  $\otimes \equiv$  "in coincidence with". The background term, Bgnd, was estimated by taking background windows  $\gamma_{1B'}$  and  $\gamma_{2B'}$  nearby to each peak:

$$\text{Bgnd} = \frac{\gamma_{1B'} \otimes \gamma_2}{k_1} + \frac{\gamma_1 \otimes \gamma_{2B'}}{k_2} + \frac{\gamma_{1B'} \otimes \gamma_{2B'}}{k_1 k_2} \quad [3.7]$$

where  $k_1 = \text{Counts in } 1B' / \text{Counts in } 1B$ , and

$k_2 = \text{Counts in } 2B' / \text{Counts in } 2B$ .

Centroids and widths of the corrected spectra were calculated. For time peaks corresponding to  $\gamma$ -rays bracketting a state having a lifetime greater than the experimental time resolution, which was typically about 12 ns, an obvious departure from the usual prompt peak shape can be expected. If however the lifetime is less than but close to 12 ns, the centroid of the time peak should shift perceptibly. By comparing  $\gamma_1 \otimes \gamma_2$  vs.  $\gamma_2 \otimes \gamma_1$  centroids, which should shift in

opposite directions relative to the prompt peak, lifetimes of greater than approximately 2 ns could be revealed.

Although the experiment was not able to measure accurately  $\gamma_1 @ \gamma_2$  time characteristics for  $\gamma_1$  or  $\gamma_2$  energies less than about 300 keV, due to the large size of the detectors involved, this was circumvented by extracting time spectra for cases where  $\gamma_1$  is above while  $\gamma_2$  is below the level of interest, and the  $\gamma$ -ray energies involved are greater than 300 keV.

To investigate the possibility of very low-energy transitions in  $^{112}\text{Te}$  which may have been missed during experiments involving the larger Ge detectors, a 500 mm<sup>2</sup> Si(Li) detector was positioned close to the target during this last experiment, and singles data gated by the filter were acquired.

## Chapter Four - Experimental Results

### Introduction

This chapter deals with experimental  $\gamma$ -ray results from the heavy-ion reactions populating  $^{112,114,116}\text{Te}$ , while Chapter Five provides an interpretation of those results according to various nuclear models.

Excitation functions are presented in Section 4.1. Since for nuclei having  $Z=52$  the isotopes with  $A=116$  are better known than those more neutron deficient, a comprehensive comparison was made between fusion-evaporation code predictions and observed cross-sections for the  $^{96}\text{Mo}(^{23}\text{Na}, \text{xnpz}\alpha)$  reaction alone.

Sections 4.2 to 4.4 contain the analysed information condensed from the coincidence and angular distribution data collected for the  $^{116}\text{Te}$ ,  $^{114}\text{Te}$  and  $^{112}\text{Te}$  isotopes respectively.

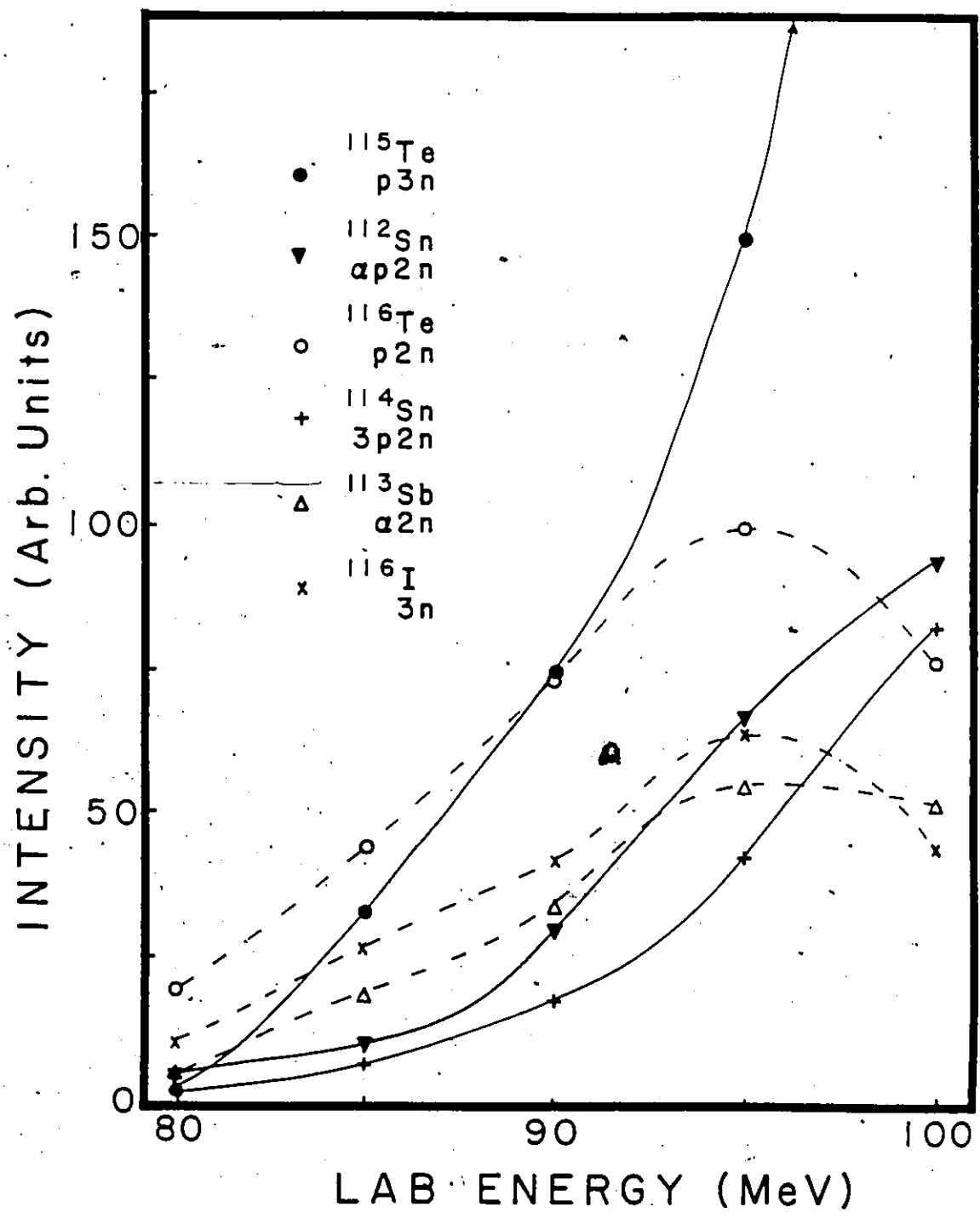
### 4.1 Excitation Functions

#### 4.1.1 Reactions Leading to $^{116}\text{Te}$

Figure 4.1 shows the relative yields of residual nuclei from the reaction  $^{96}\text{Mo}(^{23}\text{Na}, \text{xnpz}\alpha)$  as a function of bombarding energy, obtained from singles  $\gamma$ -ray intensities as

Figure 4.1

Production of residual nuclei from the  $^{96}\text{Mo}(^{23}\text{Na}, \text{xnypz}\alpha)$  reaction as a function of bombarding energy. The yields were deduced from observed ground-state transition intensities in the various nuclei, as outlined in Section 2.2.4. Experimental uncertainties are  $\leq \pm 5$ .



described in Section 3.2.4. Representative excitation curves for  $\gamma$  rays identified as belonging to  $^{116}\text{Te}$  are shown in Figure 4.2. At a beam energy of 90 MeV the ratio of three-particle xnyp cross-sections was determined to be:

$$\sigma_{3n} : \sigma_{p2n} : \sigma_{2pn} = 42 : 100 : < 5 \quad [4.1]$$

A short excitation function was also carried out for the  $^{92}\text{Mo}(^{27}\text{Al}, \text{xnyp}\alpha)$  reaction, in which the 3p exit channel populates  $^{116}\text{Te}$ . This revealed that cross-sections for  $^{116}\text{Xe}$  (p2n exit channel),  $^{116}\text{I}$  (2pn) and  $^{116}\text{Te}$  (3p) were all still rising at the accelerator operating limit of 114 MeV  $^{27}\text{Al}$ . For that beam energy the ratio of xnyp cross-sections was found to be:

$$\sigma_{p2n} : \sigma_{2pn} : \sigma_{3p} = 60 : 100 : 25 \quad [4.2]$$

Gamma rays belonging to  $^{116}\text{Cs}$ , corresponding to the 3n exit channel, were not identified. Interestingly enough, with the addition of just two neutrons, i.e. the reaction  $^{94}\text{Mo}(^{27}\text{Al}, \text{xnyp}\alpha)$ , the p2n channel completely dominates (Ja85).

Results of the statistical model fusion-evaporation calculations for the  $^{23}\text{Na} + ^{96}\text{Mo}$  reaction, carried out with the ALICE code, are shown in Figure 4.3. In general the three-particle exit channels, for example  $\alpha 2n$  ( $^{113}\text{Sb}$  residual nucleus) and p2n ( $^{116}\text{Te}$ ) are distinguished from the four-particle channels such as  $\alpha p 2n$  ( $^{112}\text{Sn}$ ) and p3n ( $^{115}\text{Te}$ ), as is seen in the measured excitation functions. Certainly the

Figure 4.2

Intensities of representative  $\gamma$  rays belonging to  $^{116}\text{Te}$ , as functions of bombarding energy.

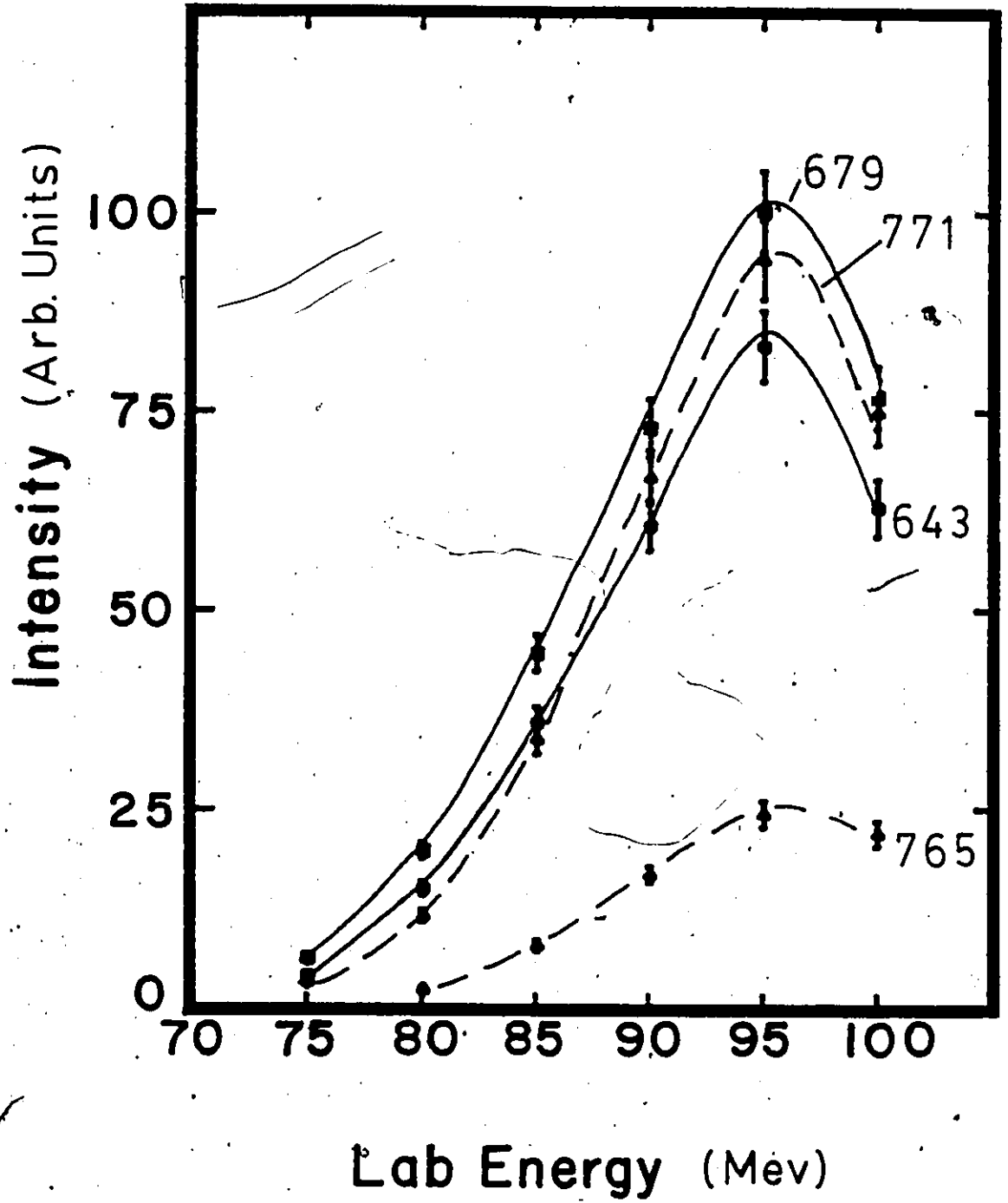
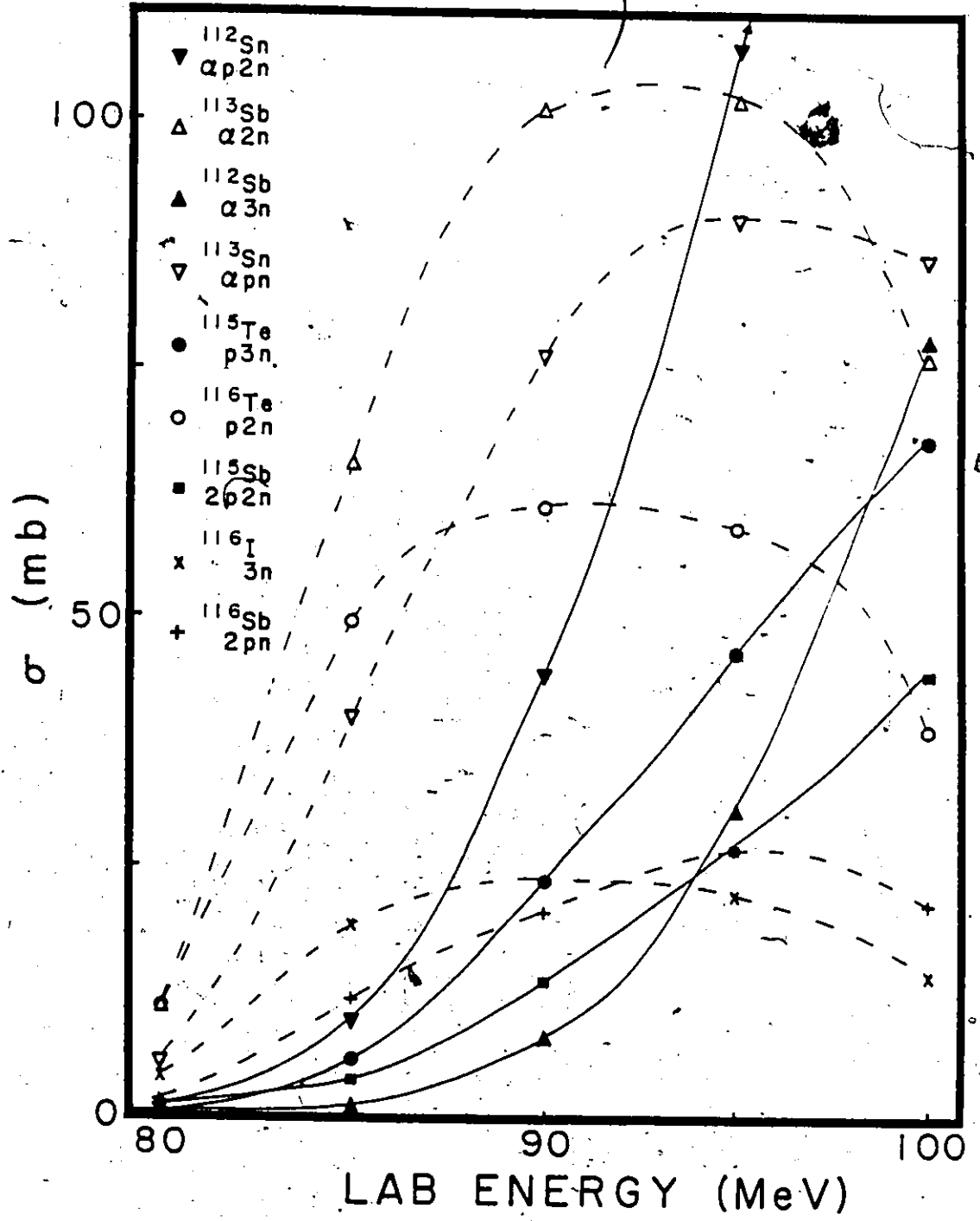


Figure 4.3

Theoretical cross-sections for residual nuclei populated by the  $^{96}\text{Mo}(^{23}\text{Na}, \text{znypza})$  reaction, calculated with the code ALICE.

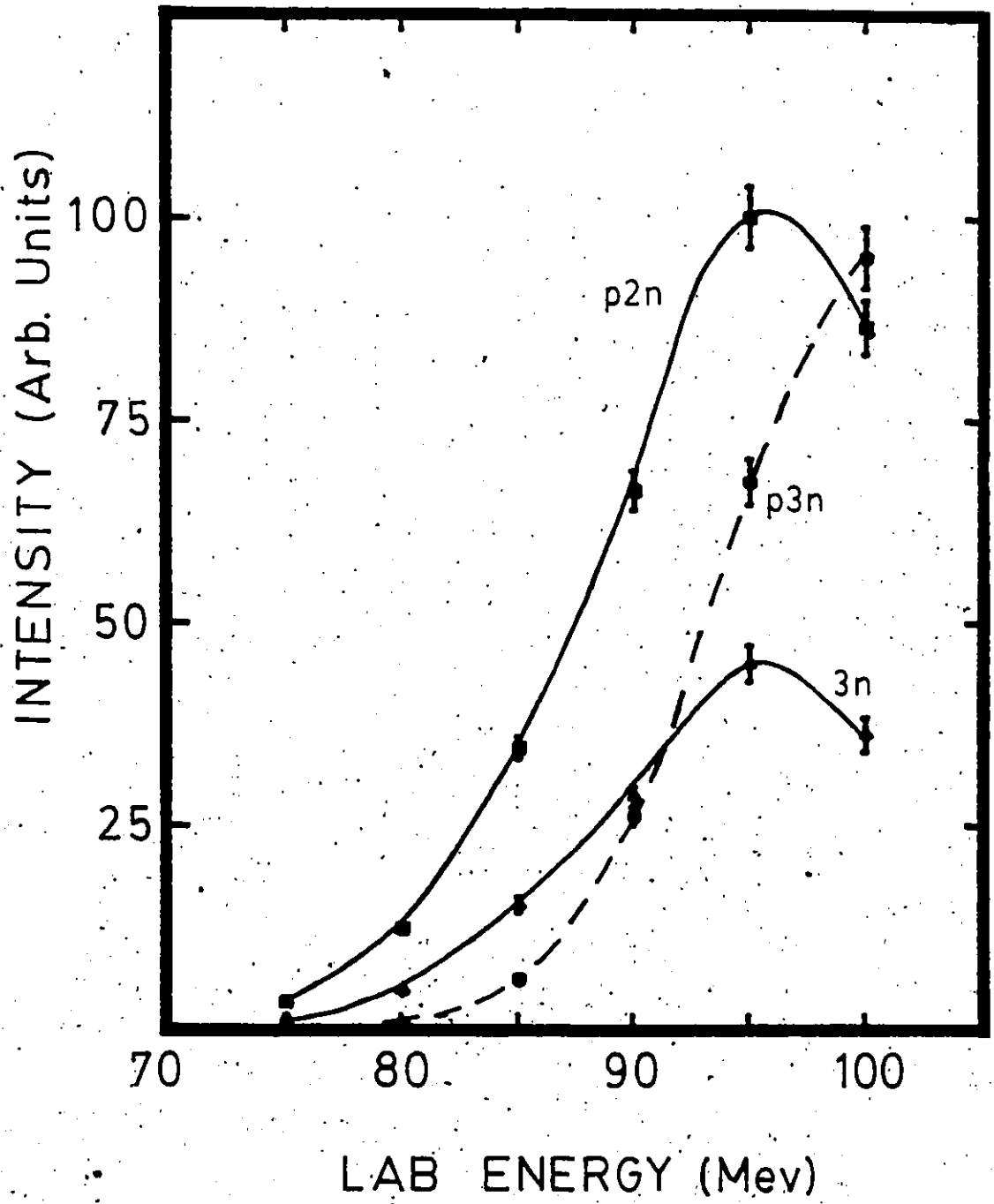


inclination of the  $^{119}\text{I}$  compound nucleus to emit at least one charged particle is predicted. However the relative intensities do not match very well, especially for channels involving  $\alpha$  emission, and the observed cross-section maxima are still not reproduced at the correct energy, even with the large adjustment of the level density parameter from the usual value of  $A_{\text{CN}}/10$  to  $A_{\text{CN}}/30$ . Further changes in the level density parameter were less effective. This tendency to predict cross-section maxima at too low a beam energy has been observed by others (eg. Lh79). The end result is that the ALICE predictions were taken as only a guide to the residual nuclei one would expect to populate in this range of beam energies, and the cross-sections for channels involving  $\alpha$  emission were assumed to possess a high degree of uncertainty.

Excitation functions gated by the multiplicity filter are more indicative of the  $\gamma$ -ray information available from a given nucleus than those deduced from singles intensities. Figure 4.4 shows, for example, that the p2n ( $^{116}\text{Te}$ ) channel has a higher combination of intensity and  $\gamma$  ray multiplicity than any other exit channel over most of the energy range scanned. This is in contrast to the singles excitation functions in Figure 4.1, where the p3n ( $^{115}\text{Te}$ ) channel dominates for energies greater than  $\sim 90$  MeV. At the practical beam energy of 90 MeV chosen for the experiments, high-multi-

Figure 4.4

High-multiplicity xnyp yields of residual nuclei following the  $^{96}\text{Mo}(^{23}\text{Na}, \text{xnyp}\alpha)$  reaction, as a function of bombarding energy. In this case the yields were deduced from multiplicity-filter-Ge  $\gamma$ -ray intensities, as outlined in Section 2.2.4.



plicity transitions from the p2n ( $^{116}\text{Te}$ ) channel were favoured over those from the other xnyp channels by:

$$I_{\gamma}^{3n} : I_{\gamma}^{p2n} : I_{\gamma}^{p3n} = 43 : 100 : 39 \quad [4.3]$$

### 3.1.2 Reactions Leading to $^{114}\text{Te}$

The p2n ( $^{114}\text{Te}$ ) exit channel dominated the  $\gamma$ -ray spectra from the  $^{94}\text{Mo}(^{23}\text{Na}, \text{xnyp}\alpha)$  reaction at beam energies up to 100 MeV. The 2pn ( $^{114}\text{Sb}$ ) channel was also identified, but information on  $\gamma$  rays belonging to  $^{114}\text{I}$  is not available and so cross-sections for the 3n channel were not determined. There is a 204-187-etc. unassigned group of transitions which may belong to  $^{114}\text{I}$ , since some 3n strength is expected. Assuming the 204 keV peak contains the significant de-excitation intensity in the unknown nucleus, at 90 MeV the strongest observed cross-sections were in the ratio:

$$\sigma_{p2n} : \sigma_{2pn} : \sigma_{\text{unknown}} = 100 : 23 : 9 \quad [4.4]$$

$^{114}\text{Te}$  is also clearly populated by the  $^{92}\text{Mo}(^{28}\text{Si}, \alpha 2p)^{114}\text{Te}$  reaction. In this case the cross-sections corresponding to three-particle emission are still rising at the maximum beam energy available, 125 MeV, and charged-particle emission is highly favoured.

For  $^{23}\text{Na} + ^{94}\text{Mo}$  ALICE overestimated the probability of  $\alpha$  emission, as it did for  $^{23}\text{Na} + ^{96}\text{Mo}$ . The  $\alpha$ p2n ( $^{110}\text{Sn}$  residual nucleus),  $\alpha$ pn ( $^{111}\text{Sn}$ ),  $\alpha$ 2n ( $^{111}\text{Sb}$ ) and 2 $\alpha$ n ( $^{108}\text{In}$ ) channels were all predicted to have higher cross-sections

than the p2n ( $^{114}\text{Te}$ ) channel. Some  $\gamma$  rays corresponding to nuclei with  $A=110$ , 111 and 113 were observed, but had very low intensities compared to those originating from  $A=114$  nuclei.

#### 4.1.3 The Reaction $^{92}\text{Mo}(^{23}\text{Na}, \text{xnpz}\alpha)$

Of the reactions attempted in this study using  $^{23}\text{Na}$ ,  $^{24}\text{Mg}$ ,  $^{27}\text{Al}$  and  $^{28}\text{Si}$  beams on Mo targets only  $^{92}\text{Mo}(^{23}\text{Na}, \text{xnpz}\alpha)$  was found to populate  $^{112}\text{Te}$ . Two groups of transitions in the spectra are clearly most intense: the 689, 787 etc. keV group in  $^{112}\text{Te}$ , corresponding to the p2n exit channel, and a 202, 325, 353, 380 etc. keV group, with which it was not possible to identify a known isotope in this mass region. Assuming the strong 325 keV  $\gamma$  ray contains most of the total de-excitation intensity of the unknown nucleus, at a beam energy of 90 MeV the cross-sections were in the ratio:

$$\sigma_{\text{p2n}} : \sigma_{\text{unknown}} = 100 : 73 \quad [4.5]$$

Both groups displayed similar excitation functions, with their intensities still rising at 96 MeV. Although  $\gamma$  rays from this latter unknown group do not match any of the transitions observed in the  $^{112}\text{Sn}(p, n\gamma)^{112}\text{Sb}$  and  $^{115}\text{In}(^3\text{He}, 6n\gamma)^{112}\text{Sb}$  reactions (Ka76), it could be that the heavy-ion ( $^{23}\text{Na}, 2\text{pn}$ ) reaction populates completely different states of higher spin than those reached in the reactions involving very light projectiles. Therefore the possibility that the

202 keV group of transitions does belong to  $^{112}\text{Sb}$ , corresponding to the usually-observed 2pn exit channel, cannot be ruled out. This is especially interesting since one would expect to observe a) the 2pn:p2n cross-section ratio to be increasing with decreasing neutron number, which is the case for the unknown group and b) strong low-energy  $\gamma$  rays similar to the 202 keV group in an odd-odd nucleus such as  $^{112}\text{Sb}$ .

#### 4.2 Experimental Results for $^{116}\text{Te}$

The nucleus  $^{116}\text{Te}$  had been investigated somewhat before this work. Most recently Chowdhury et al. (Ch82) populated yrast levels up to  $(14^+)$  using the  $^{106}\text{Pd}(^{12}\text{C},2n)$  and  $^{114}\text{Sn}(\alpha,2n)$  reactions, and reported a probable negative-parity state at 3028 keV (see Figure 4.5). Both the  $^{96}\text{Mo}(^{23}\text{Na},p2n)$  and  $^{92}\text{Mo}(^{27}\text{Al},3p)$  reactions, at beam energies of 90 and 114 MeV respectively, were found to populate  $^{116}\text{Te}$ . The data obtained from the  $(^{23}\text{Na},p2n)$  reaction was of much better quality and therefore the  $(^{27}\text{Al},3p)$  results were not used extensively. Coincidence gates extracted from the  $(^{27}\text{Al},3p)$  data were in agreement with those from the  $(^{23}\text{Na},p2n)$  reaction. The total coincidence spectrum for  $^{96}\text{Mo} + ^{23}\text{Na}$  is shown in Figure 4.6, and representative efficiency-corrected and background-subtracted gate spectra appear in Figures 4.7 and 4.8. Figure 4.9 shows some results from the least-squares analysis of the angular distributions. Gamma-ray intensities, distribution coefficients and resulting

Figure 4.5

$^{116}\text{Te}$  level scheme due to Chowdhury et al. (Ch82).  
Levels up to spin  $8^+$  had been previously reported  
by Warner and Draper (WD70).

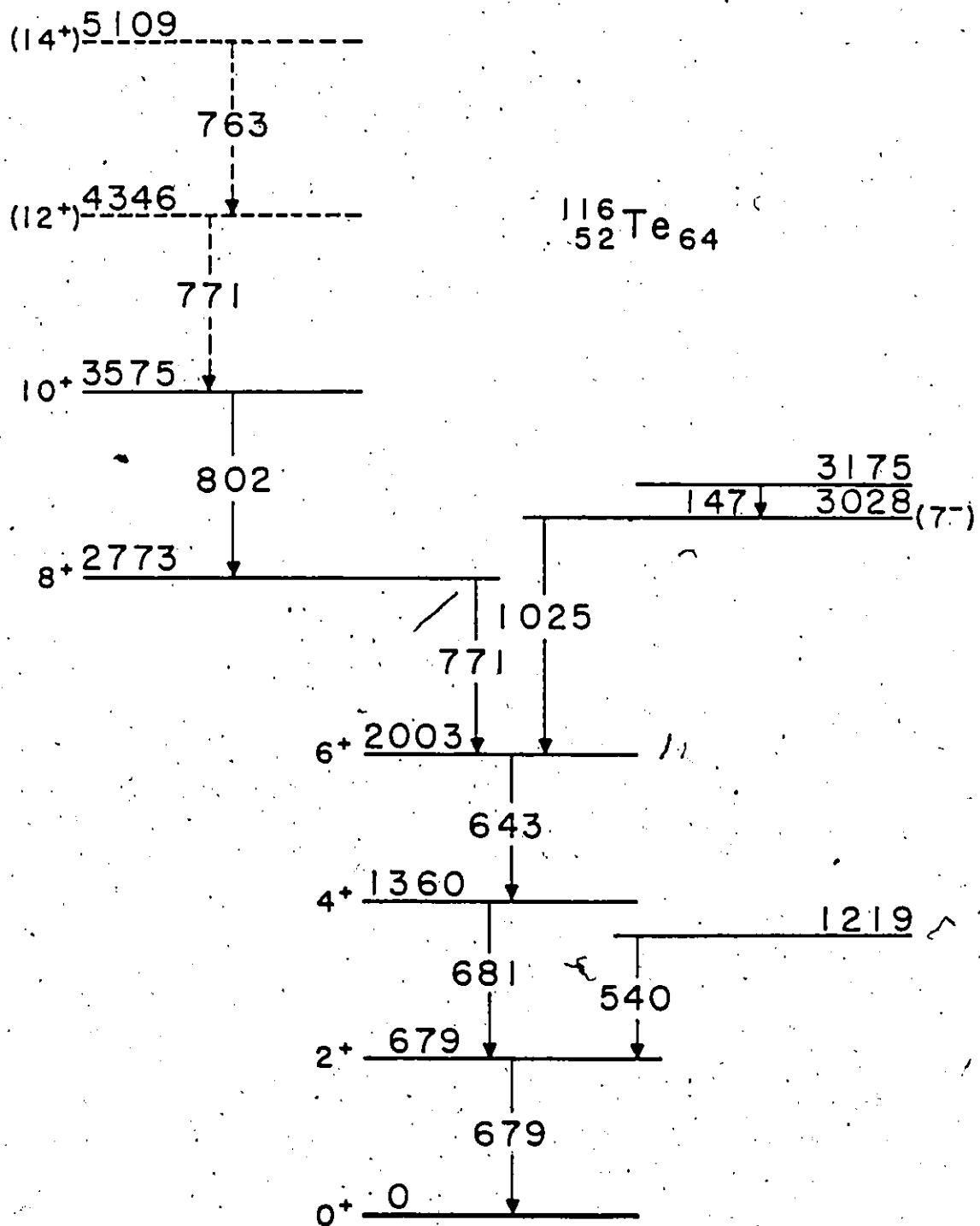


Figure 4.6

Total coincidence spectrum from the  $^{96}\text{Mo}(^{23}\text{Na}, \text{xnpza})$  reaction at 90 MeV. Strong transitions in  $^{116}\text{Te}$  are labelled by their energies in keV. Peaks marked with a \* belong in  $^{116}\text{I}$  (3n exit channel), while unresolved doublets in  $^{116}\text{Te}$  are indicated by a letter d.

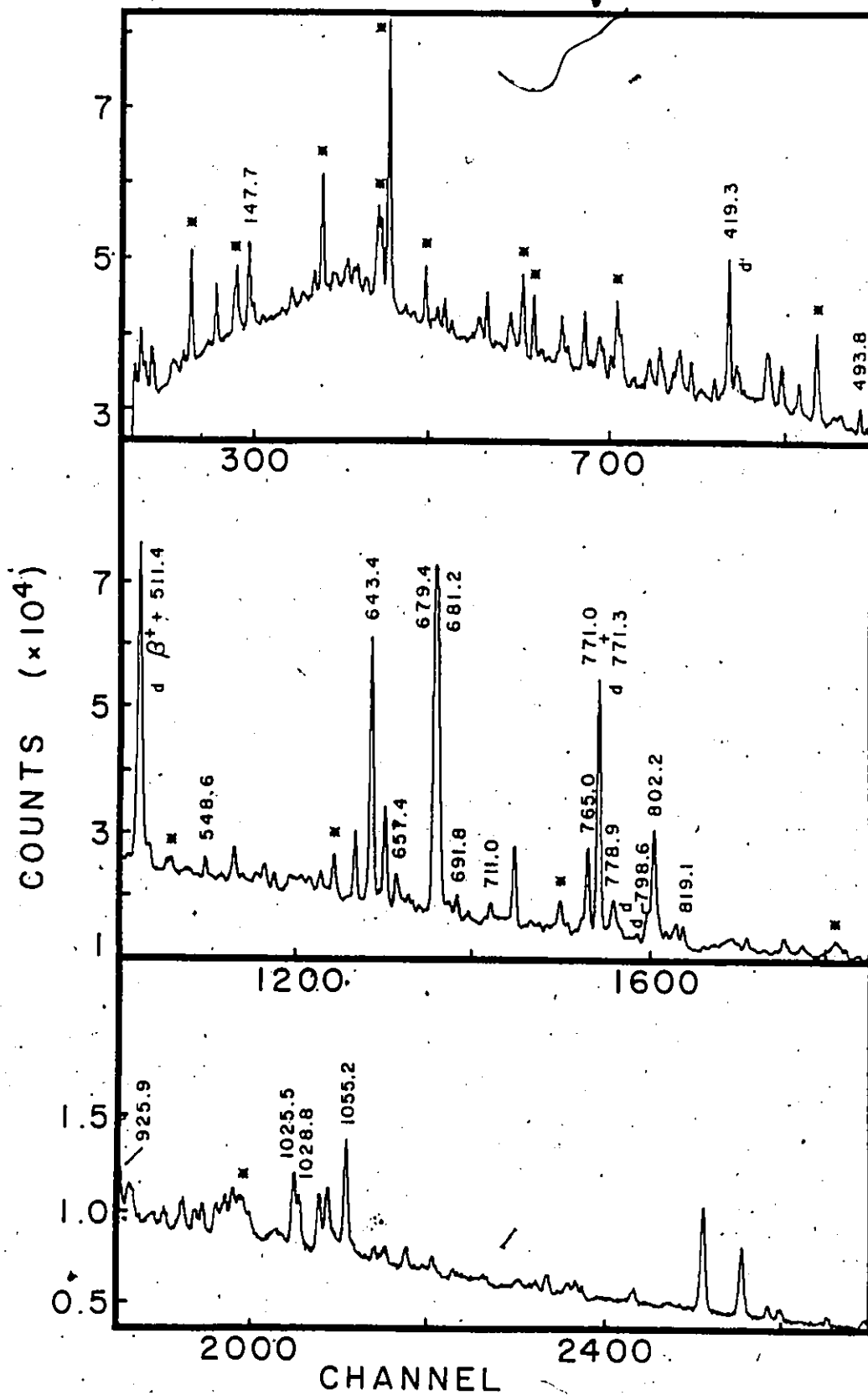


Figure 4.7

Coincidence gates from the  $^{96}\text{Mo}(^{23}\text{Na}, p2n)^{116}\text{Te}$  reaction. The data have been background-subtracted and corrected for detector efficiency. Peaks marked with a  $\nabla$  in the 1025.5 keV gate are impurities due to the nearby 1028.8 keV transition.

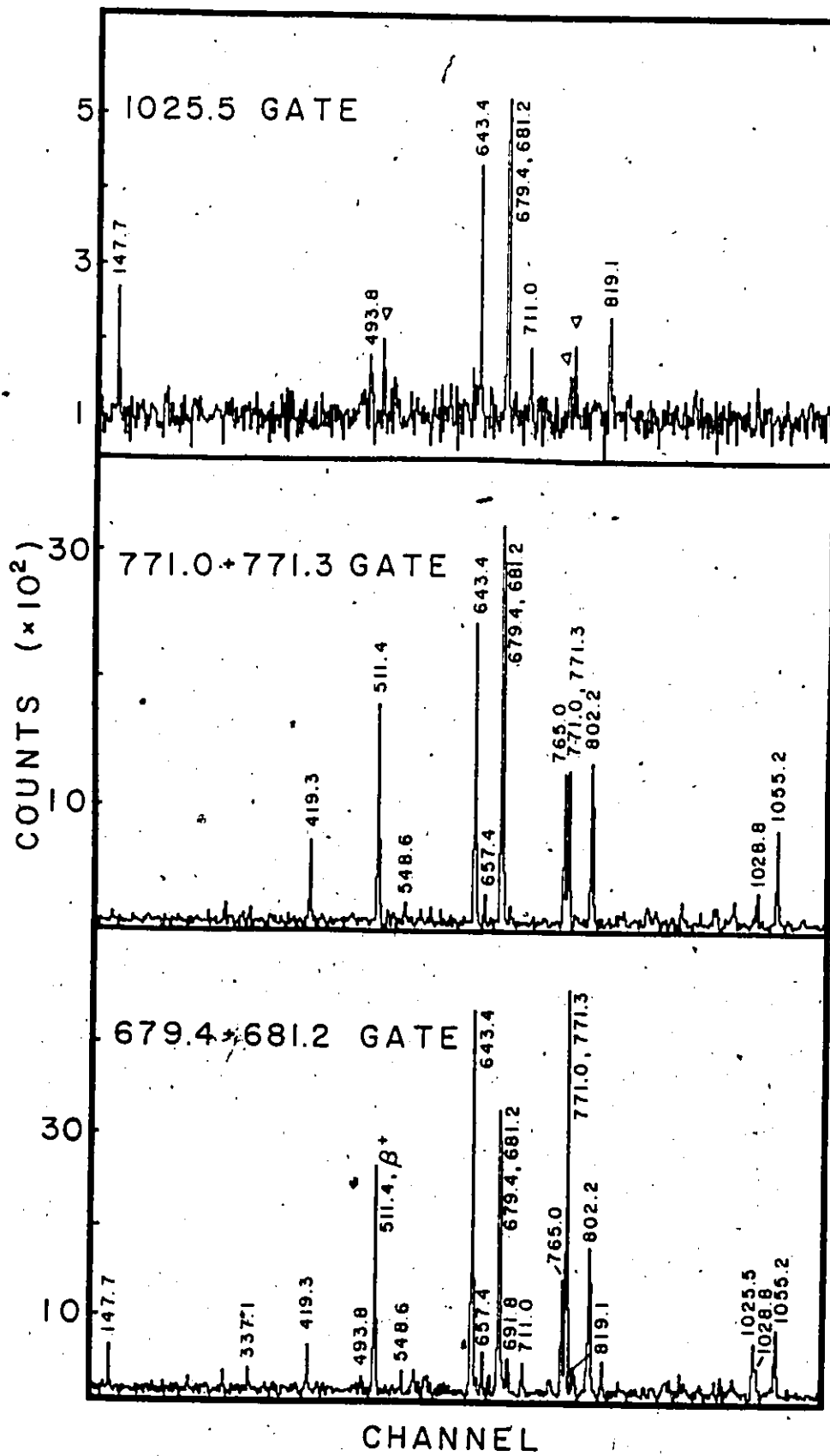


Figure 4.8

Coincidence gates from the  $^{96}\text{Mo}(^{23}\text{Na}, p2n)^{116}\text{Te}$  reaction. The data have been background-subtracted and corrected for detector efficiency. Peaks marked with a  $\nabla$  in the top gate are due to the strong 511.0 keV  $\beta^+$  component in the gating transition.

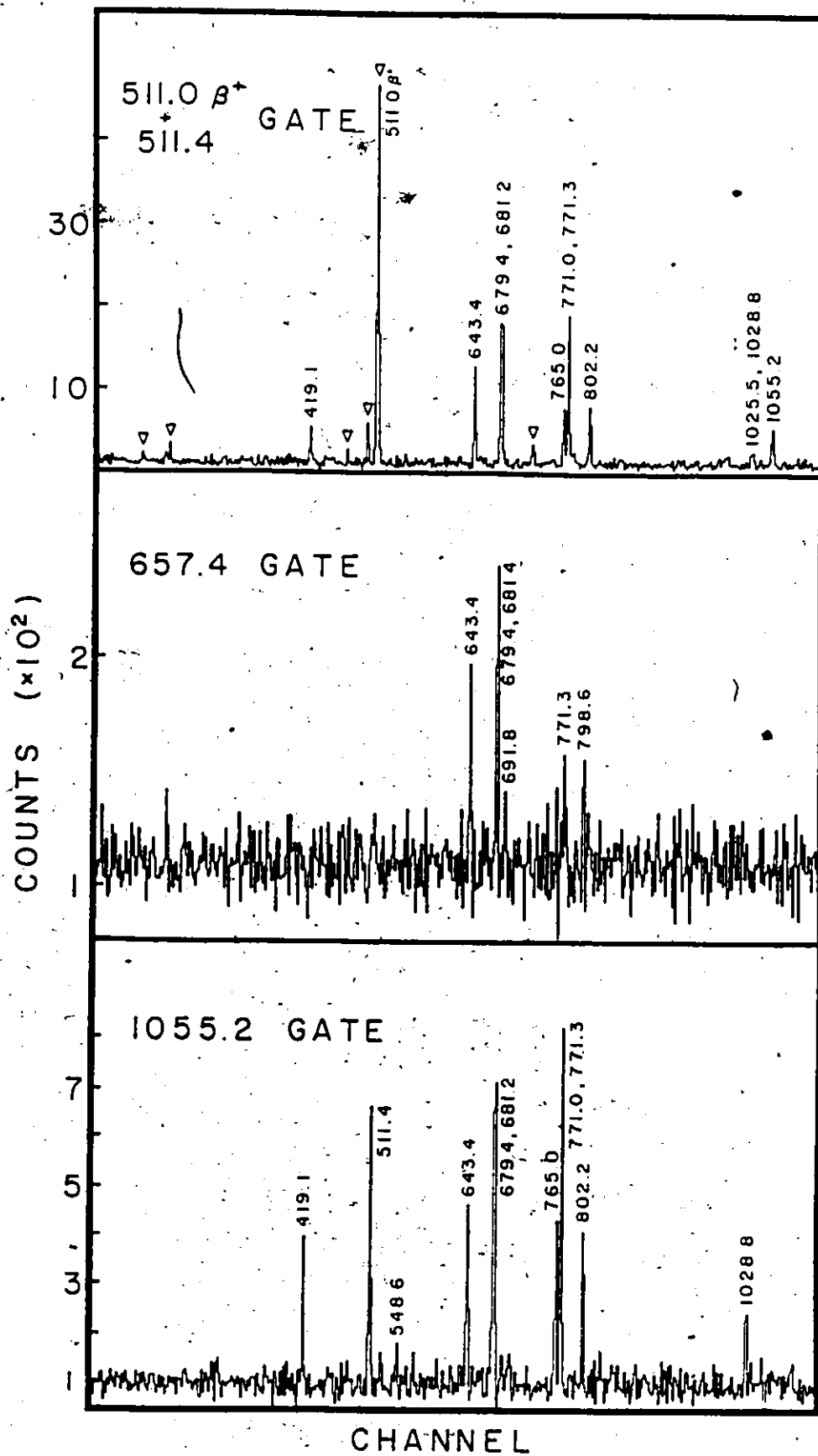
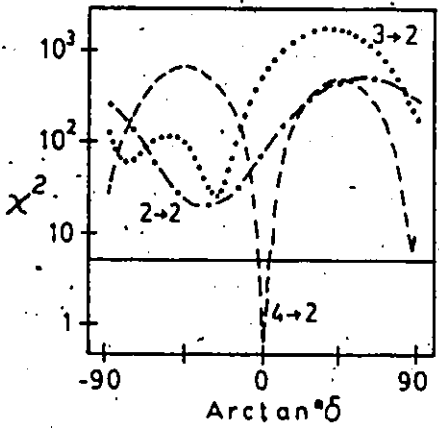
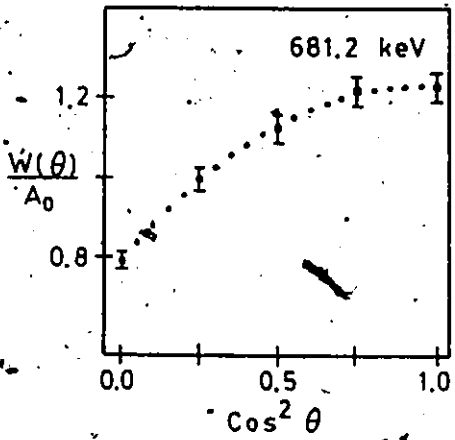
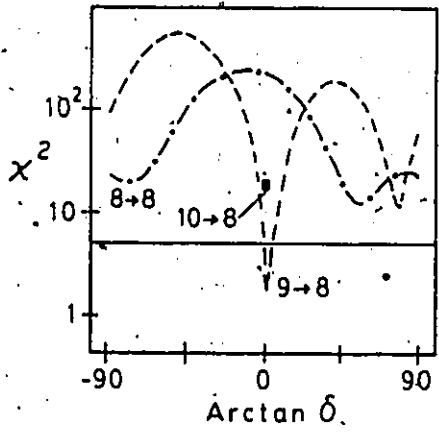
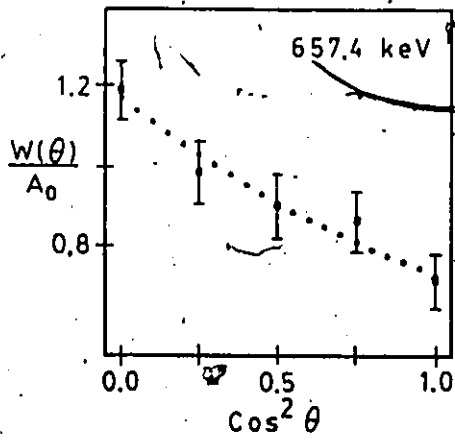
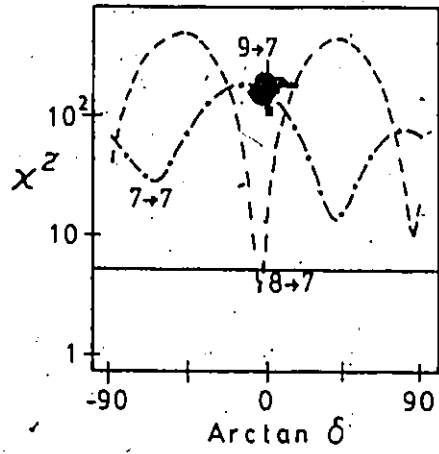
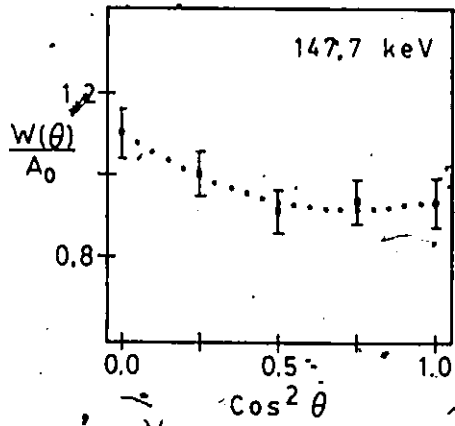


Figure 4.9

Some results from the  $^{116}\text{Te}$  angular distribution least-squares analyses: A  $\chi^2$  of 5.42, marked with a horizontal line in the right-hand panels, corresponds to a 99.9% confidence limit.



transition assignments are listed in Table 4.1. The level scheme constructed from the coincidence relations and angular distribution information is shown in Figure 4.10.

The strong 679.4-681.2-643.4-771.3-...-548.6 keV yrast cascade exhausts most of the  $\gamma$ -ray intensity assigned to  $^{116}\text{Te}$ . All of these transitions are seen to be in coincidence with each other. In addition, the 771 keV coincidence gate clearly shows a second 771 keV transition. The placement of the two members of this doublet is based on coincidence intensity considerations. Looking at first the 657.4, 691.8 and 788.6 keV, and then the yrast group coincidence gates a slight difference in 771 energies is indicated, as shown in the level scheme. The 925.9 and 647.6 keV coincidence gates show the yrast group with the exception of the 802.2 keV transition, and the 771 keV peak is weaker than in the yrast gates. The parallel placement of this pair with the 771.0 + 802.2 keV pair thus seems certain, especially since the energy sums match. The ordering of the 925.9 and 647.6 keV transitions is indicated by a small difference in intensities, and possibly could be reversed.

The measured angular distribution coefficients ( $A_k$  coefficients) for most of the yrast cascade  $\gamma$ -rays are characteristic of stretched  $L=2$ , presumably  $E2$  (see section 2.2.7) transitions (see Table 4.1). The  $E2$  nature of the four transitions de-exciting the  $8^+$  level is also supported by the electron conversion measurements of Wyckoff and Draper

Table 4.1

Results of analysis for  $\gamma$  rays assigned to  $^{116}\text{Te}$ .

$E_{\gamma}$ (keV) <sup>a</sup>	$I_{\gamma}$ <sup>b</sup>	$A_2$	$A_4$	Multipolarity	$J_i^{\pi} + J_f^{\pi}$
147.7	11 <sup>c</sup>	-0.15(4)	0.09(5)	M1/E2	8 <sup>(-)</sup> + 7 <sup>(-)</sup>
254.4	3	> 0			9 <sup>(-)</sup> + 8 <sup>(-)</sup>
278.4 <sup>d</sup>	4				(14 <sup>-</sup> ) + 13 <sup>(-)</sup>
302.7 <sup>d,e</sup>	5				
337.1 <sup>d,e</sup>	5				
419.3 <sup>d</sup>	10	-0.09(2)	0.01(3)	(M1/E2)	(19 <sup>+</sup> ) + (18 <sup>+</sup> )
493.8	5	0.29(10)	0.00(11)	E2	(14 <sup>-</sup> ) + (12 <sup>-</sup> )
511.4 <sup>d</sup>	4 <sup>f</sup>			(E2)	(14 <sup>+</sup> ) + 12 <sup>+</sup>
548.6	4	-0.54(14)	-0.20(16)	M1/E2	(22 <sup>+</sup> ) + (21 <sup>+</sup> )
643.4	94	0.32(2)	-0.10(3)	E2	6 <sup>+</sup> + 4 <sup>+</sup>
647.6	4				12 <sub>1</sub> <sup>+</sup> + 10 <sub>2</sub> <sup>+</sup>
657.4	9	-0.32(4)	0.04(5)	E1	9 <sup>(-)</sup> + 8 <sup>+</sup>
667.1 <sup>e</sup>	5				
679.4	≅ 100	0.28(2)	-0.08(3)	E2	2 <sup>+</sup> + 0 <sup>+</sup>
681.2	100	0.35(2)	-0.12(3)	E2	4 <sup>+</sup> + 2 <sup>+</sup>
691.8	10	0.30(7)	-0.04(3)	E2	11 <sup>(-)</sup> + 9 <sup>(-)</sup>
711.0	8	0.19(8)	-0.07(9)	E2	(12 <sup>-</sup> ) + 10 <sup>(-)</sup>
749.4 <sup>e</sup>	6				
765.0	27	0.34(3)	-0.13(3)	E2	(16 <sup>+</sup> ) + (14 <sup>+</sup> )
771.0	38			E2	12 <sup>+</sup> + 10 <sub>1</sub> <sup>+</sup>
771.3	63	0.32(2)	-0.09(3)	E2	8 <sup>+</sup> + 6 <sup>+</sup>

Table 4.1 (cont'd)

$E_Y^a$ (keV)	$I_Y^b$	$A_2$	$A_4$	Multipolarity	$J_i^\pi + J_f^\pi$
778.9 <sup>d</sup>	4				(5,6) + 4 <sup>+</sup>
798.6 <sup>d</sup>	8	0.34(5)	-0.14(7)	E2	13 <sup>(-)</sup> + 11 <sup>(-)</sup>
802.2	47	0.36(2)	-0.12(3)	E2	10 <sub>1</sub> <sup>+</sup> + 8 <sup>+</sup>
819.1	8	0.36(6)	-0.09(7)	E2	10 <sup>(-)</sup> + 8 <sup>(-)</sup>
925.9	4	0.32(8)	-0.02(10)	E2	10 <sub>2</sub> <sup>+</sup> + 8 <sup>+</sup>
1025.5	14	-0.32(5)	0.05(5)	E1	7 <sup>(-)</sup> + 6 <sup>+</sup>
1028.8	8	0.36(7)	-0.09(8)	E2	(21 <sup>+</sup> ) + (19 <sup>+</sup> )
1055.2	20	0.35(3)	-0.15(4)	E2	(18 <sup>+</sup> ) + (16 <sup>+</sup> )

<sup>a</sup> Energies of the  $\gamma$  rays are typically accurate to  $\pm 0.3$  keV.

<sup>b</sup> Where possible deduced from coincidence intensities in the  $2^+ \rightarrow 0^+$  and  $4^+ \rightarrow 2^+$  gates. The ratio of the  $4^+ \rightarrow 2^+$  to  $2^+ \rightarrow 0^+$  transition intensities was obtained from the gated angular distribution  $A_0$  coefficients. The quoted intensities are accurate to  $\pm 10\%$  or less for the stronger lines, or  $\pm 1$  for transitions having  $I_Y < 10$ .

<sup>c</sup> Corrected for internal conversion.

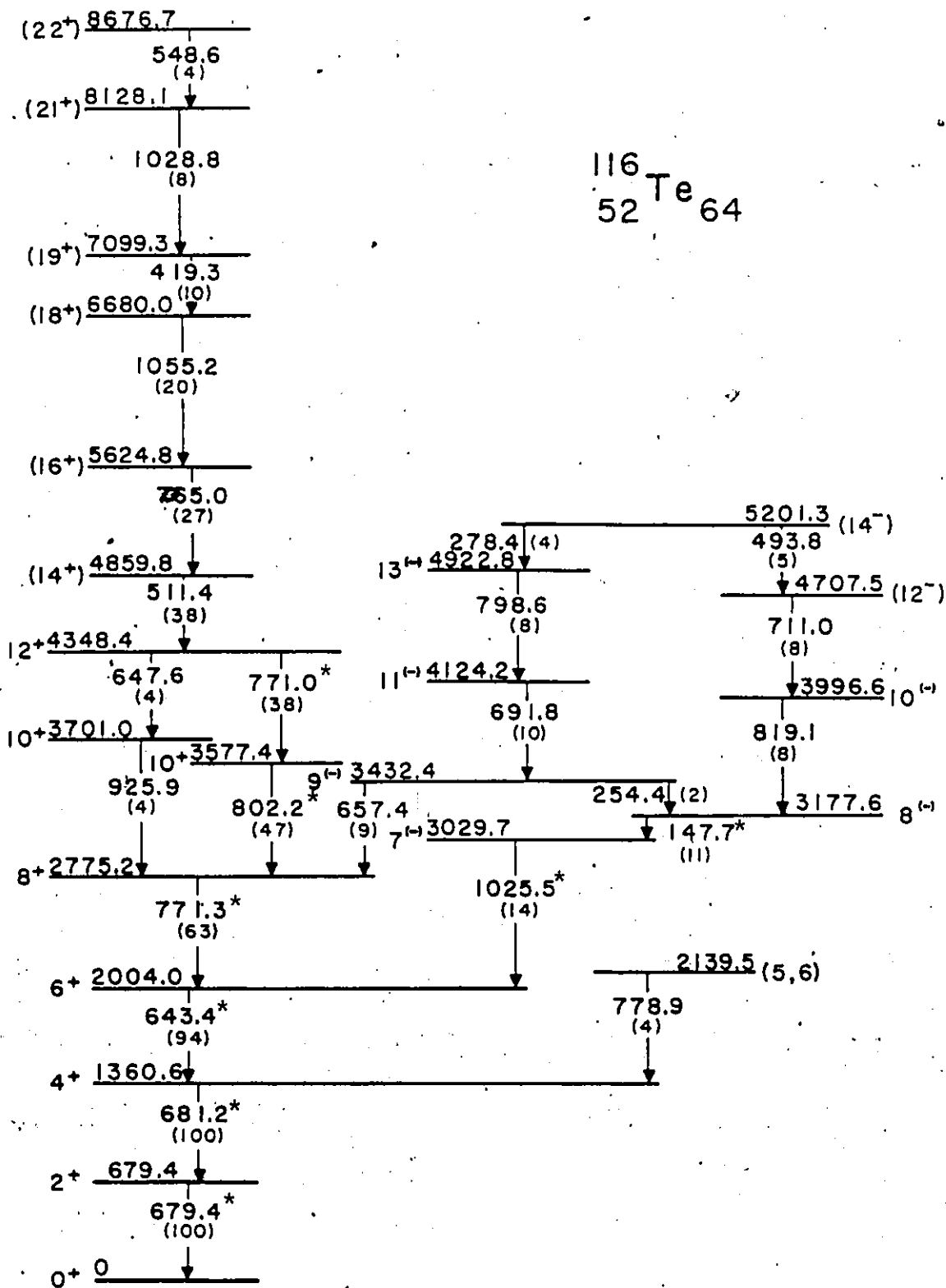
<sup>d</sup> Part of an unresolved multiplet. See text for specific cases.

<sup>e</sup> Not placed in level scheme.

When not quoted  $A_k$  coefficients could not be determined due to low intensities and/or interfering peaks.

Figure 4.10

Proposed level scheme for  $^{116}\text{Te}$ . All energies are in keV. Gamma-ray transitions marked with a \* have been reported previously (see Figure 4.5) in agreement with the present work.



(WD73), and by systematics of other Te isotopes. Since both members of the 771 keV doublet are fairly strong, the  $A_k$  coefficients for the sum of the two indicate stretched E2 character for both the 771.3 and 771.0 components. Although the 647.6 keV angular distribution was difficult to extract due to interfering stronger  $\gamma$  rays, the 925.9 keV transition appears to be E2, leaving  $10^+$  as the only reasonable spin assignment for the 3701.1 level.

Above the  $12^+$  level the spins and parities cannot be determined as precisely. It was not possible to measure the angular distribution for the 511.4 keV transition due to the presence of the much stronger 511.0 keV  $\beta^+$  annihilation  $\gamma$  ray peak. Using the 511 keV coincidence gate a comparison of yrast group intensities and centroids with those of non-yrast transitions resulted in the intensity and energy shown in the level scheme. The placement just above the  $12^+$  level is based on its deduced intensity, which is less certain than those of the adjacent  $\gamma$  rays, and so there is some chance of it being higher in the scheme. To place it lower would be to disrupt the 802.2 + 771.0 and 925.9 + 647.6 keV parallel combination, which seems to be firmly established. Based on the systematics of other Te isotopes the level at 4859.9 keV probably has spin and parity  $14^+$ ; however, a definite assignment cannot be made and hence spins and parities of that and higher levels are placed in parentheses.

The 765.0, 1055.2 and 1028.8 keV transitions appear to be E2 in nature, but  $A_k$  coefficients for the 419.3 and 548.6 keV  $\gamma$  rays are indicative of mixed M1/E2 transitions. The 419.3 keV transition is not completely resolved, but the effect of  $\sim 25\%$  contamination due to a transition in  $^{113}\text{Sb}$  ( $\alpha 2n$  exit channel) having a known anisotropy was taken into account.

The yrast level energies and spin assignments as outlined concur with those of Chowdhury et al. (Ch82) up to spin  $12^+$ , with the addition of a second  $10^+$  level at 3701.1 keV. However, the previous work reported no 511 keV transition, and listed a weak 763 keV  $\gamma$  ray as de-exciting a tentative 5109 keV ( $14^+$ ) level. Given the ubiquitous nature of the 511 keV  $\beta^+$  annihilation  $\gamma$  ray and the much weaker population of high spin states in that work, this discrepancy is understandable. Gizon et al. (Gi81) have also populated yrast states in  $^{116}\text{Te}$  via the  $^{106}\text{Pd}(^{12}\text{C}, 2n)^{116}\text{Te}$  reaction, and deduced a partial level scheme consistent with Figures 4.5 and 4.10 up to spin  $10^+$ . A weak 837 keV  $\gamma$  ray tentatively assigned as the  $(12^+) \rightarrow 10^+$  transition by them was not observed in the present work. Other results up to spin  $10^+$  have been reported (KC83), agreeing with the level scheme presented here.

Turning to the non-yrast states on the right hand side of Figure 4.10, the 3029.7 keV level is de-excited by a 1025.5 keV  $\gamma$  ray having  $A_k$  coefficients characteristic of a

stretched  $L=1$  transition. Although the possibility of an  $M1$  transition cannot be completely ruled out, in that case there would very likely be  $E2$  competition and therefore a significant mixing ratio. Since this was not observed the 1025.5 keV  $\gamma$  ray is shown as  $E1$  in Table 4.1, and so the 3029.5 keV level was determined to have spin 7 and negative parity. Although this parity assignment is clearly supported by the data it cannot be regarded as definitive, which has been indicated by labelling the 3029.7 keV state as  $7^{(-)}$ . This assignment agrees with tentative assignments made in previous reports (Ch82, KC83). Definite  $7^-$  levels have also been observed at similar excitation energies in  $^{118-132}\text{Te}$  (c.f. Figure 5.1); in those cases the parity was pinned down by measuring  $\gamma$ -ray linear polarizations and/or internal conversion coefficients.

In the same manner the level at 3432.4 keV was assigned spin and parity  $9^{(-)}$ , based on the 657.4 keV angular distribution. Since the 691.8 and 798.6 keV transitions exhibit stretched  $E2$  character, the 4124.3 and 4922.8 keV levels were deduced to have spin  $11^{(-)}$  and  $13^{(-)}$  respectively. The 798.6 keV  $\gamma$  ray is an unresolved doublet, but the contamination as deduced from the coincidence gate is approximately 16%, considered too low to affect its  $E2$  assignment. The order of the transitions involved is based on intensity considerations.

Angular distribution coefficients for the 147.7 keV  $\gamma$  ray indicate mixed L=1,2 multipolarity. In accordance with the considerations presented in section 2.2.7, this was taken to show M1/E2 character, and in combination with the least-squares analysis resulted in an  $8^{(-)}$  assignment for the 3177.4 keV level. A 254.4 keV  $\gamma$  ray was observed, and appears to connect the  $9^{(-)}$  and  $8^{(-)}$  levels. Although it is fairly weak and part of a doublet the  $A_2$  coefficient was determined to be slightly positive, indicating a mixed M1/E2 transition and supporting the  $8^{(-)}$  assignment. Since the 819.1, 711.0 and 493.8 keV  $\gamma$  rays all display stretched E2 angular distributions, the 3996.6, 4707.5 and 5201.3 keV levels were given spins of  $10^{(-)}$ ,  $(12^-)$  and  $(14^-)$  respectively. Parentheses enclosing the  $(12^-)$  and  $(14^-)$  spin assignments reflect the lower-than-normal 711.0 keV  $(12^-) + 10^{(-)}$   $A_2$  coefficient, although the value is still within two standard deviations of an average result.

It should be noted that the parities for these  $7^{(-)}$ ,  $8^{(-)}$ ,  $9^{(-)}$ ,  $10^{(-)}$  etc. states are either all negative or all positive, depending on the assigned characters of the 1025.5 and 657.4 keV transitions. The positive-parity option results in a series of even-J levels which are not seen to decay at all to the yrast J-2 states, a very unusual situation. Together with the factors mentioned previously the evidence strongly favours a choice of negative parity for the J=7,8,9 etc. structure, which interpretation will be assumed

to be correct during the discussion in Chapter Five. These comments also apply to the other  $^{112,114}\text{Te}$  isotopes under consideration in the present work.

#### 4.3 Experimental Results for $^{114}\text{Te}$

The nucleus  $^{114}\text{Te}$  had been populated before this study, via the  $^{112}\text{Sn}(\alpha, 2n)^{114}\text{Te}$  and  $^{114}\text{Sn}(\alpha, 4n)^{114}\text{Te}$  reactions, by Warner and Draper (WD70), who observed excited states up to spin  $8^+$  at 3087 keV (see Figure 4.11). Spins and parities of the yrast  $2^+-4^+-6^+-8^+$  levels were determined by  $\gamma$ -ray angular distribution measurements and electron conversion coefficients.

In the present work both the  $^{94}\text{Mo}(^{23}\text{Na}, p2n)$  and  $^{92}\text{Mo}(^{28}\text{Si}, \alpha 2p)$  reactions, at beam energies of 90 and 125 MeV respectively, were observed to populate  $^{114}\text{Te}$ . However, the  $^{94}\text{Mo} + ^{23}\text{Na}$   $^{114}\text{Te}$  cross-section was higher and the  $\gamma$ -ray spectra much cleaner than those of the more complicated  $^{92}\text{Mo} + ^{28}\text{Si}$  reaction, and therefore only data from the former were used.

A total coincidence spectrum for  $^{94}\text{Mo} + ^{23}\text{Na}$  is shown in Figure 4.12, and representative efficiency-corrected and background-subtracted gate spectra appear in Figures 4.13 and 4.14. Figure 4.16 shows some results from the least-squares analysis of the angular distributions. Gamma-ray intensities, angular distribution coefficients and resulting tran-

Figure 4.11

$^{114}\text{Te}$  level scheme due to Warner and Draper (WD70).

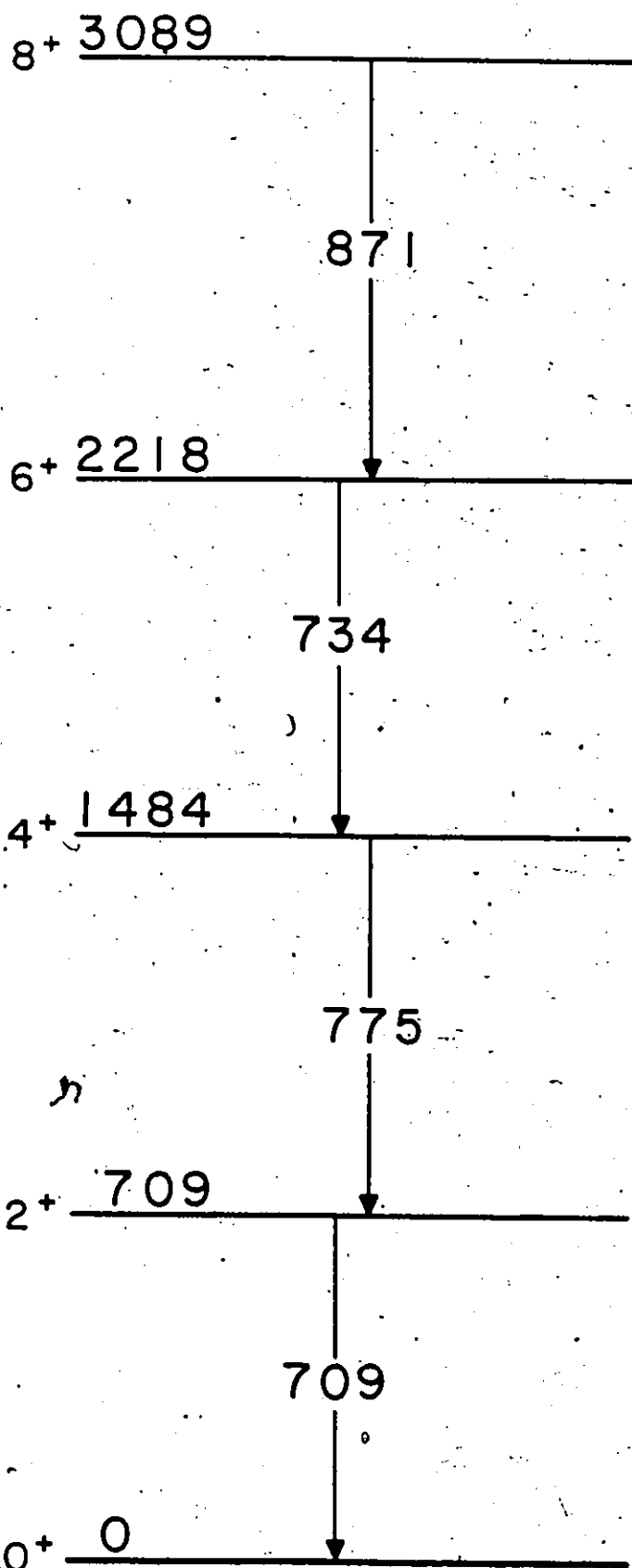
 $^{114}_{52}\text{Te}_{62}$

Figure 4.12

y Total coincidence spectrum from the  $^{94}\text{Mo}(^{23}\text{Na}, \text{xnpza})$  reaction at 90 MeV. Strong transitions in  $^{114}\text{Te}$  are labelled by their energies in keV. Peaks marked with a \* belong in  $^{114}\text{Sb}$  (2pn exit channel), while those marked by a  $\nabla$  are in the 204-187-etc. keV unknown group (see Section 4.1.2). Unresolved doublets in  $^{114}\text{Te}$  are indicated by a letter d.

7

16

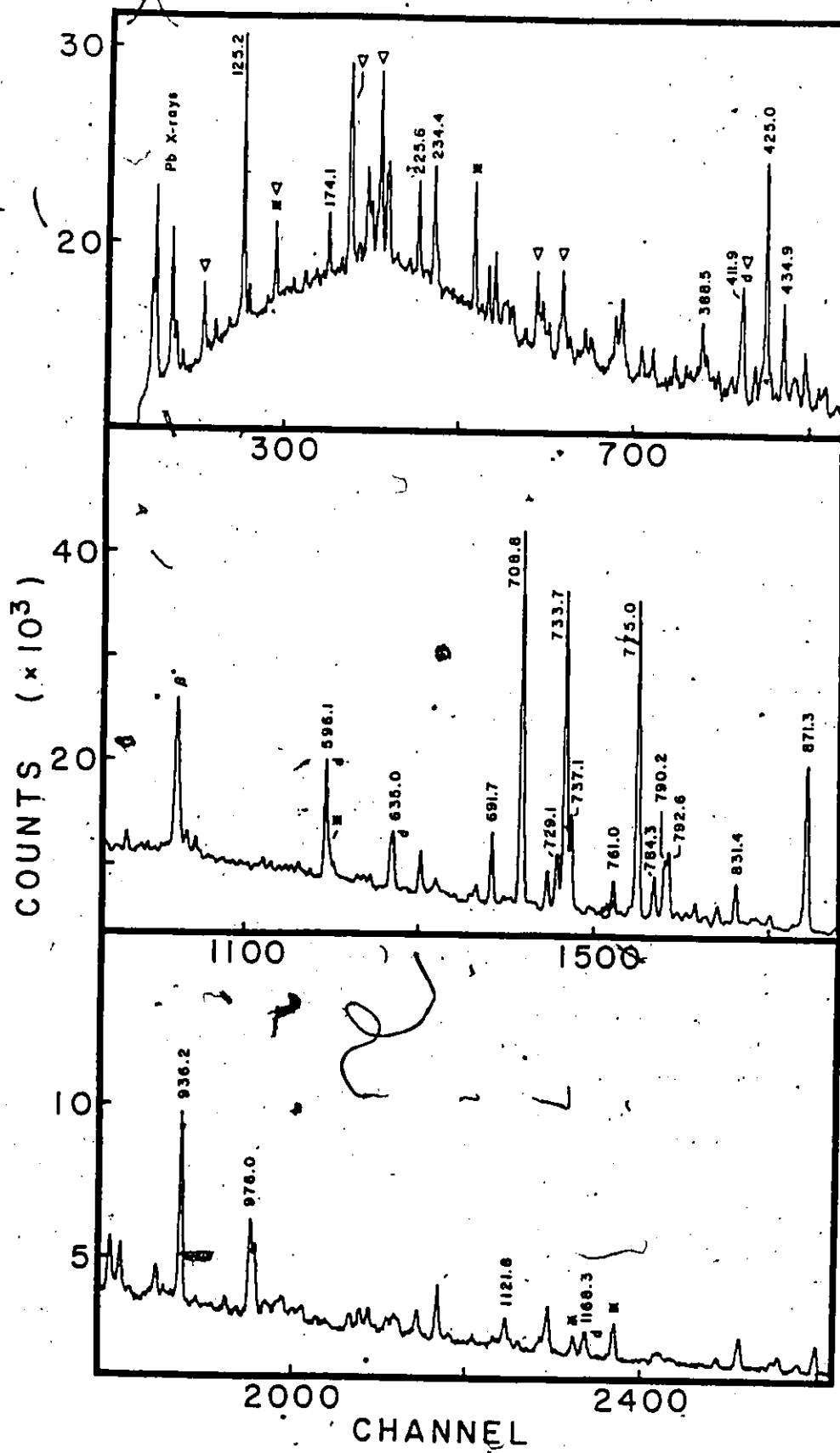


Figure 4.13

Coincidence gates from the  $^{94}\text{Mo}(^{23}\text{Na}, p2n)^{114}\text{Te}$  reaction. The data have been background-subtracted and corrected for detector efficiency.

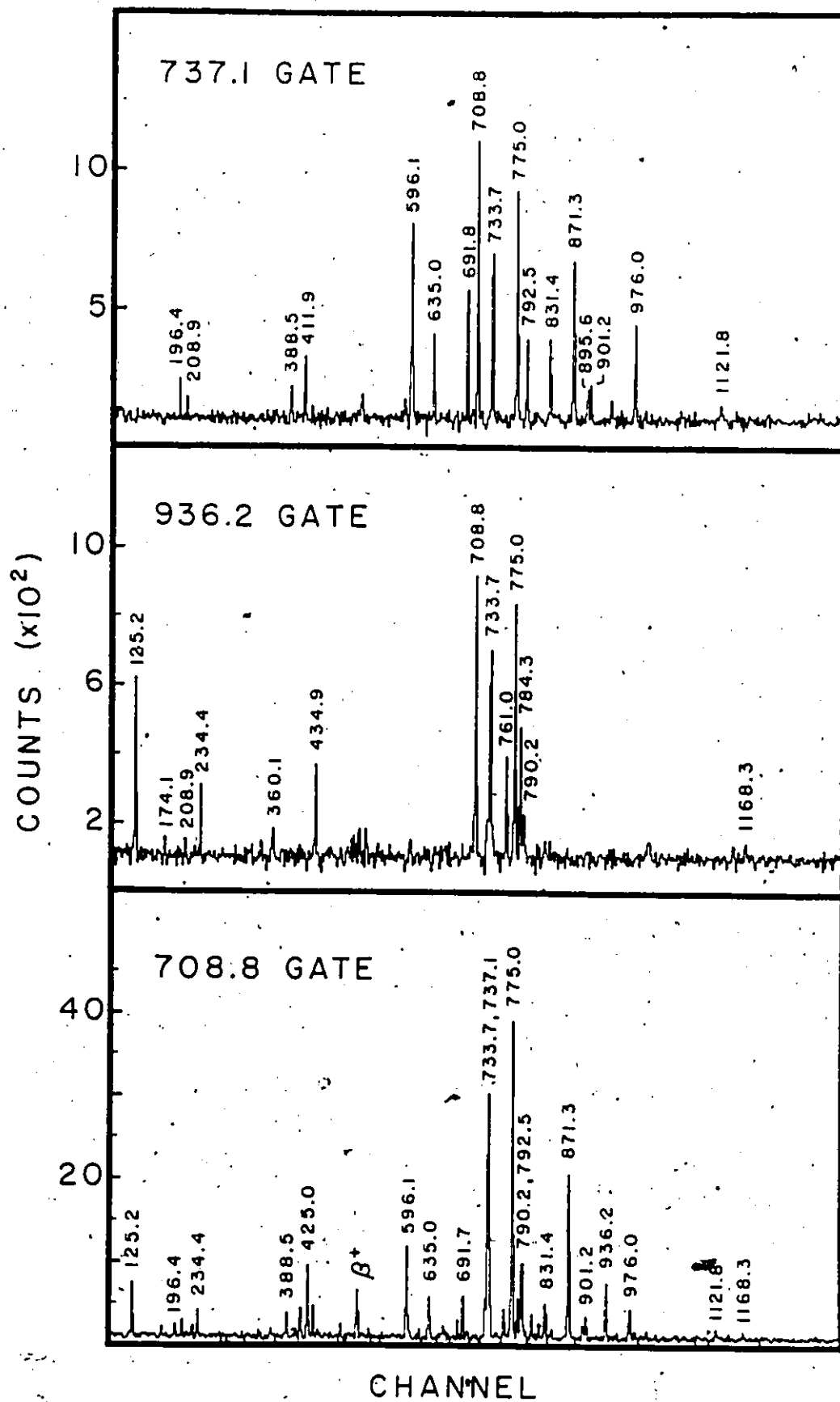


Figure 4.14

Coincidence gates from the  $^{94}\text{Mo}(^{23}\text{Na}, p2n)^{114}\text{Te}$  reaction. The data have been background-subtracted and corrected for detector efficiency.

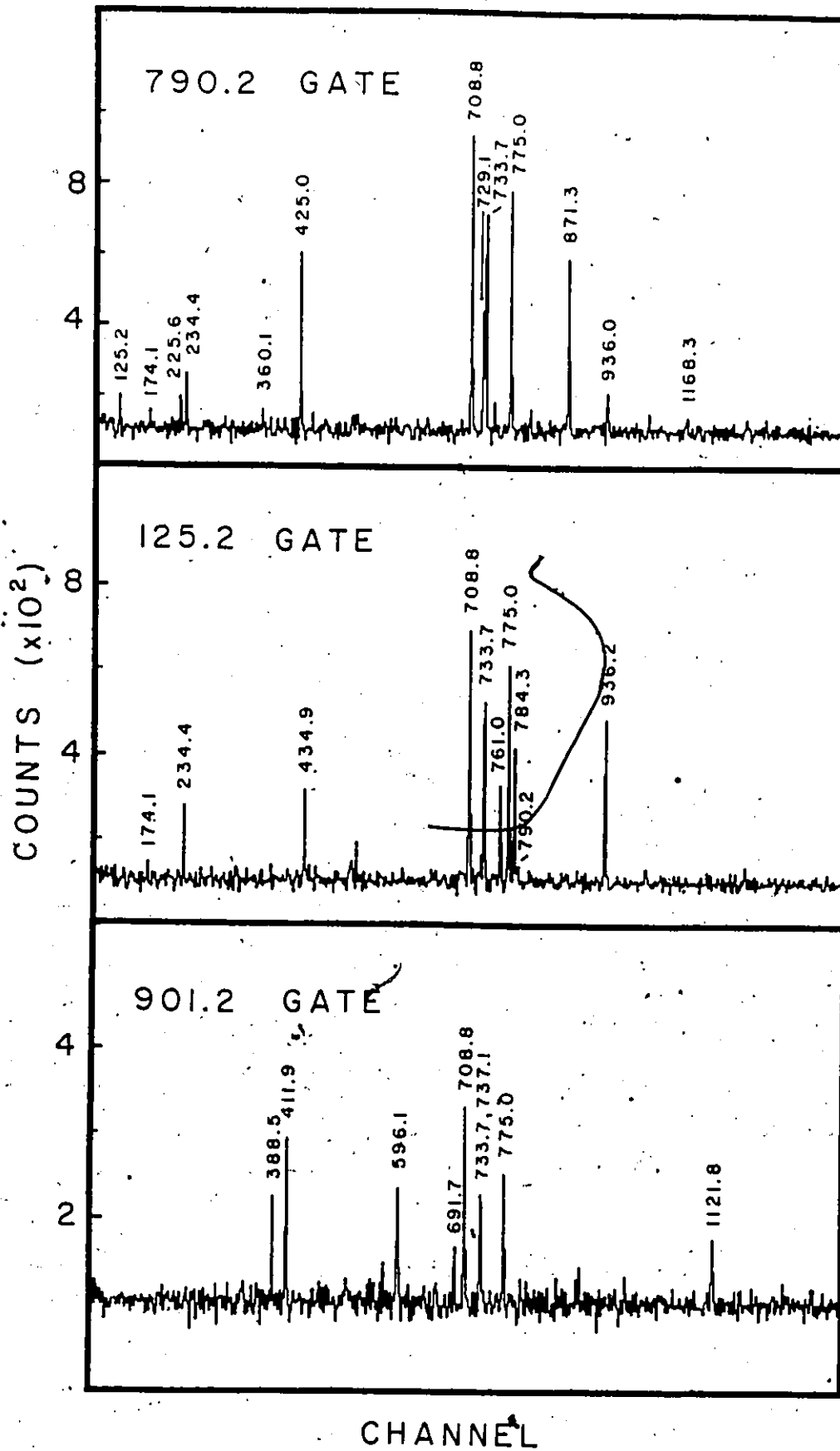


Figure 4.15

Some results from the  $^{114}\text{Te}$  angular distribution least-squares analyses. A  $\chi^2$  of 5.42, marked with a horizontal line in the right-hand panels, corresponds to the 99.9% confidence limit.

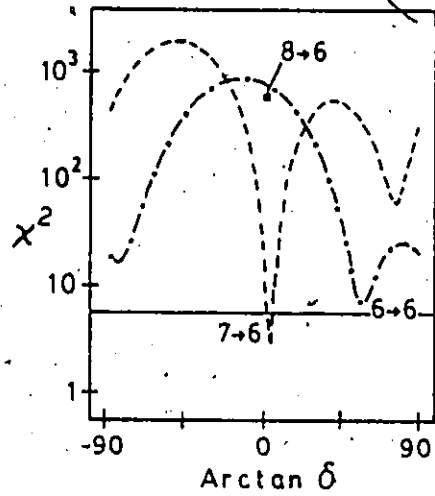
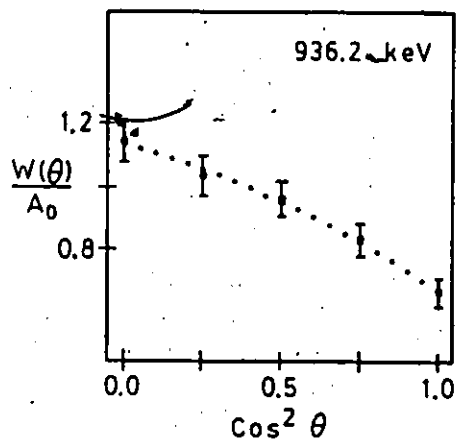
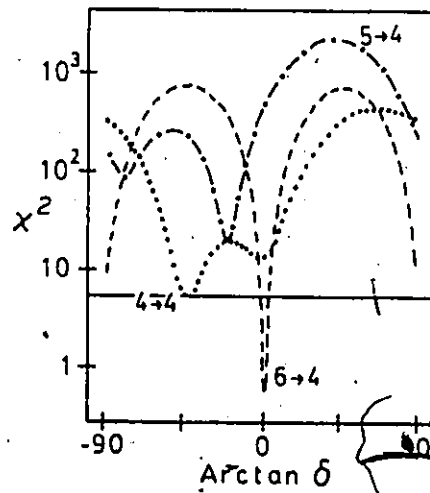
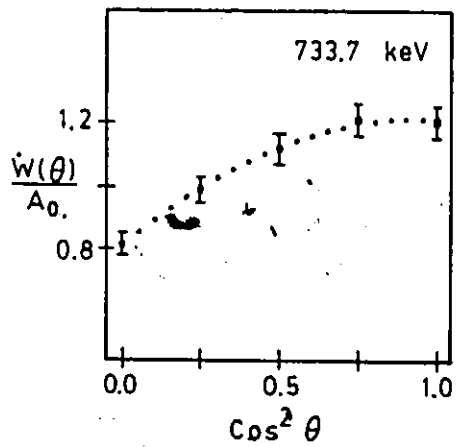
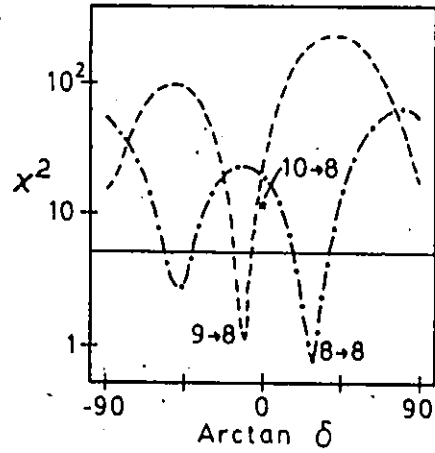
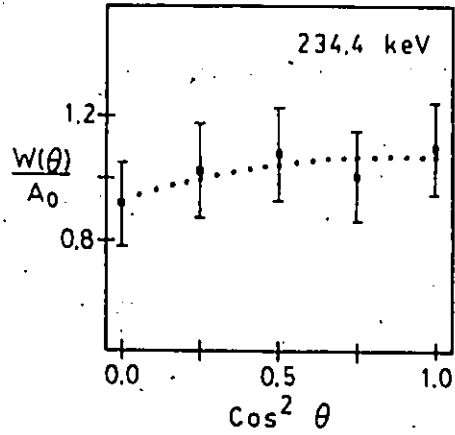
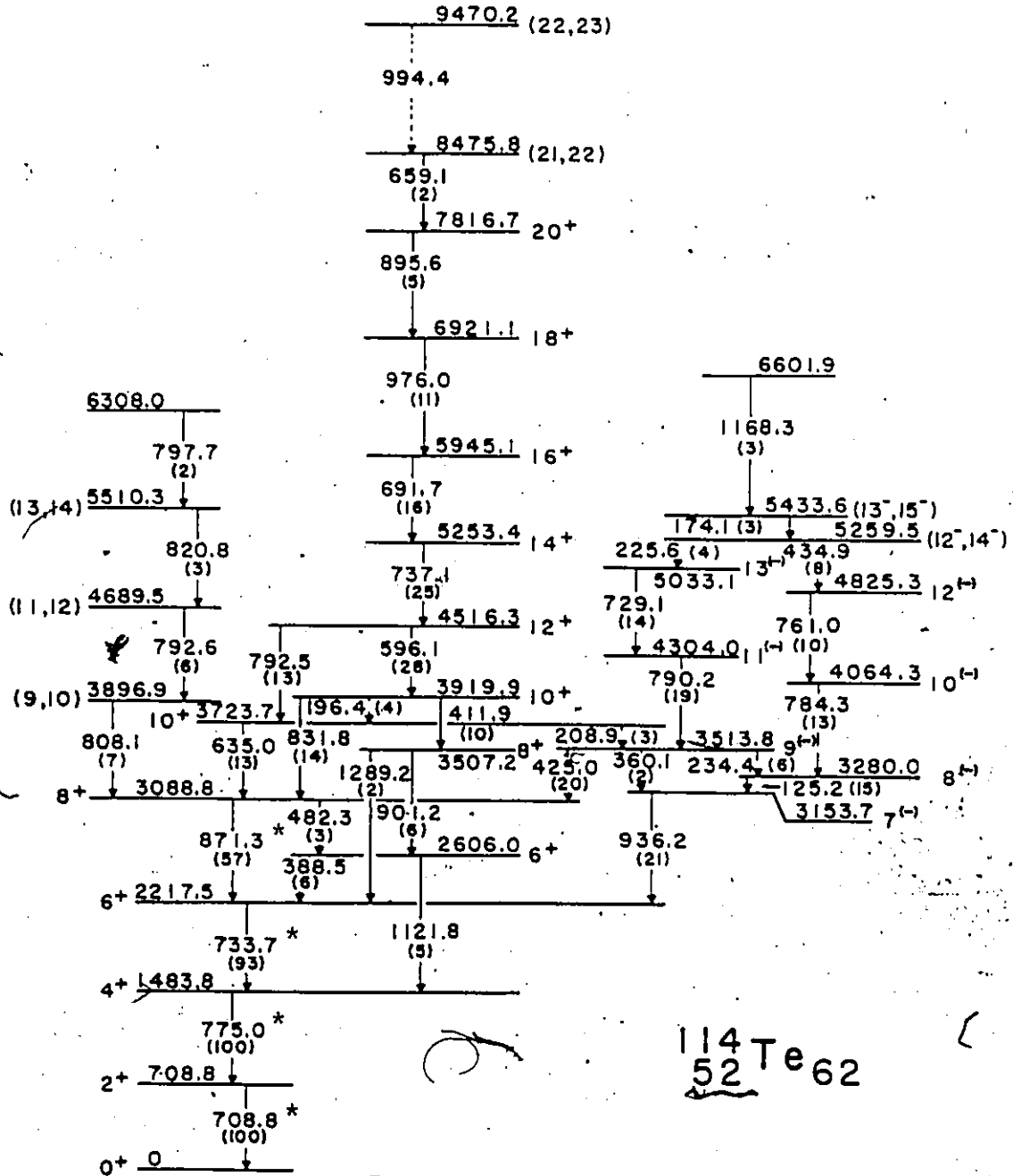


Figure 4:16

Proposed level scheme for  $^{144}\text{Te}$ . All energies are in keV. Gamma-ray transitions marked with a \* have been reported previously (see Figure 4.11).



sition assignments are listed in Table 4.2. The level scheme constructed from this information is shown in Figure 4.16.

A strong cascade of stretched E2 transitions (see Table 4.2) is observed to de-excite the highest spin states. The strongest  $12^+ \rightarrow 10^+ \rightarrow 8^+ \rightarrow 6^+ \rightarrow 4^+$  sequence, a 596.1-831.8-871.3-733.7 keV group, is paralleled by a number of other interconnecting decay chains made possible by duplicate  $6^+$ ,  $8^+$  and  $10^+$  states. The existence of the 3723.7 keV  $10_1^+$  level is clearly shown by the difference between the 635.0-792.5 keV and 831.8-596.1 keV pairs of coincidence gates. The former pair are in coincidence with the  $(24^+) \rightarrow 22^+ \dots 12^+$  and  $8^+ \rightarrow 6^+ \dots 0^+$  E2 transitions quite strongly but, except for a weak 596.1 keV peak in the 635.0 keV gate (due, as it turns out, to the presence of a 196.4 keV  $10_2^+ \rightarrow 10_1^+$  transition) are not in coincidence with the 831.8-596.1 keV pair. Conversely this latter pair are in coincidence with the other strong E2 transitions above spin  $12^+$  and below spin  $8^+$  but not, other than a similar weak exception, with the 635.0-792.5 keV pair. Since the  $\gamma$ -ray energy sums also match within error the placement of the two  $10^+$  levels seems certain.

The order of the clear 411.9-901.2-1121.8 keV  $10_2^+ \rightarrow 4^+$  cascade is constrained by a number of coincidence relationships. Both the 388.5 and the 482.3 keV gates contain strong transitions above spin  $8_1^+$  and below spin  $6_1^+$ , as well as each other, but not an 871 keV peak. Secondly, the 482.3 keV gate contains an 1122 keV peak and no 901 keV peak, while the

Table 4.2

Results of analysis for  $\gamma$  rays assigned to  $^{114}\text{Te}$ .

$E_{\gamma}^a$ (keV)	$I_{\gamma}^b$	$A_2$	$A_4$	Multipolarity	$J_{i.}^{\pi} + J_{f.}^{\pi}$
125.2	15 <sup>c</sup>	0.05(6)	-0.20(7)	M1/E2	$8(-) + 7(-)$
174.1	3	-0.20(17)	-0.07(26)	M1/E2	$(13^-, 15^-) + (12^-, 14^-)$
196.4	4	0.00(11)	-0.15(13)	M1/E2	$10_2^+ + 10_1^+$
208.9 <sup>d</sup>	3				$10_2^+ + 9(-)$
225.6	4	-0.46(11)	-0.08(11)	M1/E2	$(12^-, 14^-) + 13(-)$
234.4	6	0.11(8)	-0.05(9)	M1/E2	$9(-) + 8(-)$
310.4 <sup>d, e</sup>	1				
360.1	2	> 0			$9(-) + 7(-)$
388.5	6	-0.10(27)	0.17(31)	M1/E2	$6_2^+ + 6_1^+$
411.9 <sup>f</sup>	10	> 0			$10_2^+ + 8_2^+$
425.0	20	-0.28(4)	-0.03(4)	E1	$9(-) + 8_1^+$
434.9	8	0.11(8)	-0.03(9)		$(12^-, 14^-) + 12(-)$
443.5 <sup>e</sup>	2				
482.3 <sup>d</sup>	3	> 0			$8_1^+ + 6_2^+$
596.1 <sup>d</sup>	28	0.30(3)	-0.16(4)	E2	$12^+ + 10_2^+$
635.0 <sup>f</sup>	13	> 0			$10_1^+ + 8_1^+$
659.1 <sup>d</sup>	2				$(21, 22) + 20^+$
691.7	16	0.32(4)	-0.13(5)	E2	$16^+ + 14^+$
698.0 <sup>e</sup>	4				
708.8	$\approx 100$	0.28(2)	-0.10(3)	E2	$2^+ + 0^+$
729.1	14	0.23(5)	-0.05(6)	E2	$13(-) + 11(-)$

Table 4.2 (cont'd)

$E_{\gamma}^a$ (keV)	$I_{\gamma}^b$	$A_2$	$A_4$	Multipolarity	$J_i^{\pi} \rightarrow J_f^{\pi}$
733.7	93	0.32(2)	-0.11(3)	E2	$6_1^+ \rightarrow 4^+$
737.1	25	0.37(4)	-0.17(7)	E2	$14^+ \rightarrow 12^+$
747.3 <sup>e</sup>	3				
761.0	10	0.33(6)	-0.17(7)	E2	$12^{(-)} \rightarrow 10^{(-)}$
775.0	100	0.29(2)	-0.11(3)	E2	$4^+ \rightarrow 2^+$
784.3	13	0.29(5)	0.05(6)	E2	$10^{(-)} \rightarrow 8^{(-)}$
790.2	19	0.19(5)	-0.09(6)	E2	$11^{(-)} \rightarrow 9^{(-)}$
792.5	13	0.36(4)	-0.08(5)	E2	$12^+ \rightarrow 10_2^+$
792.6	6			E2	$(11,12) \rightarrow (9,10)$
797.7	2				$\rightarrow (13,14)$
808.1	7	0.16(12)	0.04(13)		$(9,10) \rightarrow 8_1^+$
820.8	3	0.27(11)	-0.17(13)	E2	$(13,14) \rightarrow (11,12)$
831.4	14	0.38(5)	-0.13(6)	E2	$10_2^+ \rightarrow 8_1^+$
844.3 <sup>e</sup>	2				
871.3	57	0.26(3)	-0.08(3)	E2	$8_1^+ \rightarrow 6_1^+$
895.6 <sup>f</sup>	5	0.28(13)	0.37(14)	E2	$20^+ \rightarrow 18^+$
901.2	6	0.38(9)	-0.22(12)	E2	$8_2^+ \rightarrow 6_2^+$
936.2	21	-0.30(4)	-0.05(4)	E1	$7^{(-)} \rightarrow 6_1^+$
976.0	11	0.17(6)	-0.17(7)	E2	$18^+ \rightarrow 16^+$
994.4	2	< 0			$(22,23) \rightarrow (21,22)$
1121.8	5	0.50(14)	-0.14(15)	E2	$6_2^+ \rightarrow 4^+$
1168.3 <sup>d</sup>	3			M1/E2	$\rightarrow (13^-, 15^-)$
1289.2	< 2				$8_2^+ \rightarrow 6_1^+$

Table 4.2 (cont'd)

- a Energies are typically accurate to  $\pm 0.3$  keV.
- b Deduced from coincidence intensities in the  $2^+ + 0^+$  and  $4^+ + 2^+$  gates, corrected for detector efficiencies. The ratio of the  $4^+ + 2^+$  to  $2^+ + 0^+$  transition intensities is obtained from the gated angular distribution  $A_0$  coefficients. The quoted intensities are accurate to  $\pm 10\%$  or less for the stronger lines, or  $\pm 1$  for transitions having  $I_\gamma < 10$ .
- c Corrected for internal conversion.
- d Part of an unresolved multiplet.
- e Not placed in level scheme.
- f Part of an unresolved multiplet at some or all angles. Sign of anisotropy agrees with assigned multipolarity. See text for specific cases.

When not quoted  $A_k$  coefficients could not be determined due to low intensities and/or interfering peaks.

388.5 keV gate shows the converse. Together with the matching of appropriate energy sums, plus the existence of a weak 1289.2 keV transition feeding the  $6_1^+$  level, these clear relationships establish the position of the 2606.0 keV  $6_2^+$  and 3507.2 keV  $8_2^+$  levels.

With the exception of the 196.4 keV  $10_2^+ \rightarrow 10_1^+$  and 388.4 keV  $8_2^+ \rightarrow 8_1^+$  transitions, all of the  $\gamma$  rays described so far should exhibit angular distributions characteristic of stretched E2's. Where the  $A_k$  coefficients could be measured unambiguously this is observed to be true. For the 411.9, 482.9 and 635.0 keV transitions a positive sign for  $A_2$  was measured, in agreement with but not exclusive to quadrupole character. Spin assignments for levels involving those transitions were made based on the analysis of angular distributions of other, clearer transitions.

The ordering of the transitions above spin  $12^+$  was determined mainly by coincidence intensities in the low spin gates. It was not possible to determine  $A_k$  coefficients for the 659.1 keV  $\gamma$  ray, but the 994.4 keV transition appears to have an  $A_2 < 0$ , favouring a spin change of one and resulting in a (22,23) spin assignment for the tentative 9470.2 keV level.

As in the case of  $^{116}\text{Te}$ , two stretched E1 transitions are observed. The 936.2 keV  $\gamma$  ray feeds the 2217.5 keV  $6_1^+$  level, while the 425.0 keV transition enters the positive parity group of states at the 3153.8 keV  $8_1^+$  level. Therefore the two levels at 3153.7 and 3114.0 keV, with spin and parity

$7^{(-)}$  and  $9^{(-)}$  respectively, are established. A weak 360.1 keV  $\gamma$  ray is seen to connect those two states, and while its angular distribution was difficult to extract the sign of  $A_2$  agrees with an expected quadrupole nature.

The 234.4 and 425.0 keV coincidence gates are quite similar, and since the 125.2 keV gate contains a 234 keV peak, plus the  $\gamma$  rays seen in the 234.4 keV gate, as well as additional transitions, the 125.2 + 234.4 keV combination was placed parallel to the 360.1 keV  $\gamma$  ray, connecting the  $9^{(-)}$  and  $7^{(-)}$  states. Both the 125.2 and 234.4 keV angular distributions show mixed  $M1/E2$  character leading to an  $8^{(-)}$  spin assignment for the 3279.0 keV level.

Both the 234.4 and 425.0 gates show the 790.2 and 729.1 keV peaks as well as weaker 225.6, 174.1 and 1168.3 keV  $\gamma$  rays, while the 936.2 and 125.2 keV coincidence gates clearly show a 784.3-761.0-434.9 keV combination, and also a weaker 790.2-729.1-225.6-174.1-1168.3 keV cascade. Looking at the 174.1 and 1168.3 keV gates, both the 790.2-761.0-434.9 and the 784.3-761.0-434.9 keV cascades as well as the strong lower spin transitions are seen, placing the 174.1 and 1168.3 keV  $\gamma$  rays entering a level common to both cascades at 5259.5 keV. The order of transitions comprising the two cascades is based on coincidence intensities taken from low-spin gates.

Spins and parities of the  $10^{(-)}$ ,  $11^{(-)}$ ,  $12^{(-)}$  and  $13^{(-)}$  levels are indicated by the stretched E2 nature of the de-exciting transitions, however the spin of the 5259.5 keV

state is more ambiguous. Spin 13 is ruled out completely by the 225.6 keV angular distribution ( $A_2 = -0.46(11)$ ,  $A_4 = -0.08(11)$ ), while a spin of 14 fits that distribution well but the 434.9 keV data poorly. The  $\chi^2$  value for a  $12^+12^-$  434.9 keV distribution is quite acceptable, while that for a  $12^+13^-$  225.6 keV distribution is marginally so. Although this last option does go against the so-called "yrast argument", whereby the spin should increase as one goes higher in excitation energy, it cannot be ruled out. Therefore the 5259.5 keV level was assigned spin and parity ( $12^-, 14^-$ ), with the latter choice favoured. The angular distribution for the 174.1 keV transition indicates M1/E2 character, leading to a ( $13^-, 15^-$ ) assignment for the level at 5433.6 keV. As for the 6601.9 keV level a number of spins greater than  $12^{(-)}$  (probably greater than  $14^{(-)}$ ) would be appropriate.

It should be noted that as in  $^{116}\text{Te}$  the parities of the close-lying spin 7, 8 and 9 states and of the structures built on them are undoubtedly all identical, and again the choice of negative parity is clearly favoured.

Besides those  $\gamma$  rays de-exciting the strongly-populated positive-parity states, and those de-exciting the non-yrast negative-parity group of levels, a weaker 808.1-792.6-820.8-797.7 keV cascade is observed entering the  $8_1^+$  level. The doublet nature of the 793 keV  $\gamma$  ray is evidenced by the fact that coincidence gates for the 808.1, 820.8 and 797.7 keV members of the cascade contain a 793 but no 635 keV peak,

which they should if the cascade involved the  $12^+$  level de-excited by the established 792.5 keV transition. The intensities and centroids of the two 793 keV  $\gamma$  rays were determined by comparing gates from cascades involving the two components. Due to the less-than-certain nature of the 808.1 keV angular distribution, and the absence of a  $12^+$ -4516.3 keV + 3896.9 keV transition, the latter level was assigned spin and parity  $(9,10)^+$ . This led to  $(11,12)^+$  and  $(13,14)^+$  assignments for the 4689.5 and 5510.3 keV levels respectively. It was not possible to extract an angular distribution for the 797.7 keV  $\gamma$  ray; however, a spin of other than  $(14,15,16)$  seems highly unlikely.

#### 4.4 Experimental Results for $^{112}\text{Te}$

In a survey of  $(\alpha, xn)$  reactions leading to nuclei in this region Warner and Draper (WD70) reported a weak 720 keV  $\gamma$  ray tentatively assigned as the  $2^+ \rightarrow 0^+$  transition in  $^{112}\text{Te}$ , reached by the  $^{112}\text{Sn}(\alpha, 4n)^{112}\text{Te}$  reaction. A 720 keV  $\gamma$  ray was observed by others working in this mass region, and sometimes assumed to indicate population of excited states in  $^{112}\text{Te}$ . However this was shown to be incorrect by Tidemand-Petersson et al. (Ti80), who conclusively determined the first few levels in this nucleus following the on-line mass separation of  $A=113$  nuclei, produced in the  $^{58}\text{Ni}(^{58}\text{Ni}, xnypz\alpha)$  reaction, and the subsequent  $\beta$ -delayed proton decay of  $^{113}\text{Xe}$ . The observation of a 787-689 keV  $4^+ \rightarrow 2^+ \rightarrow 0^+$  cascade,

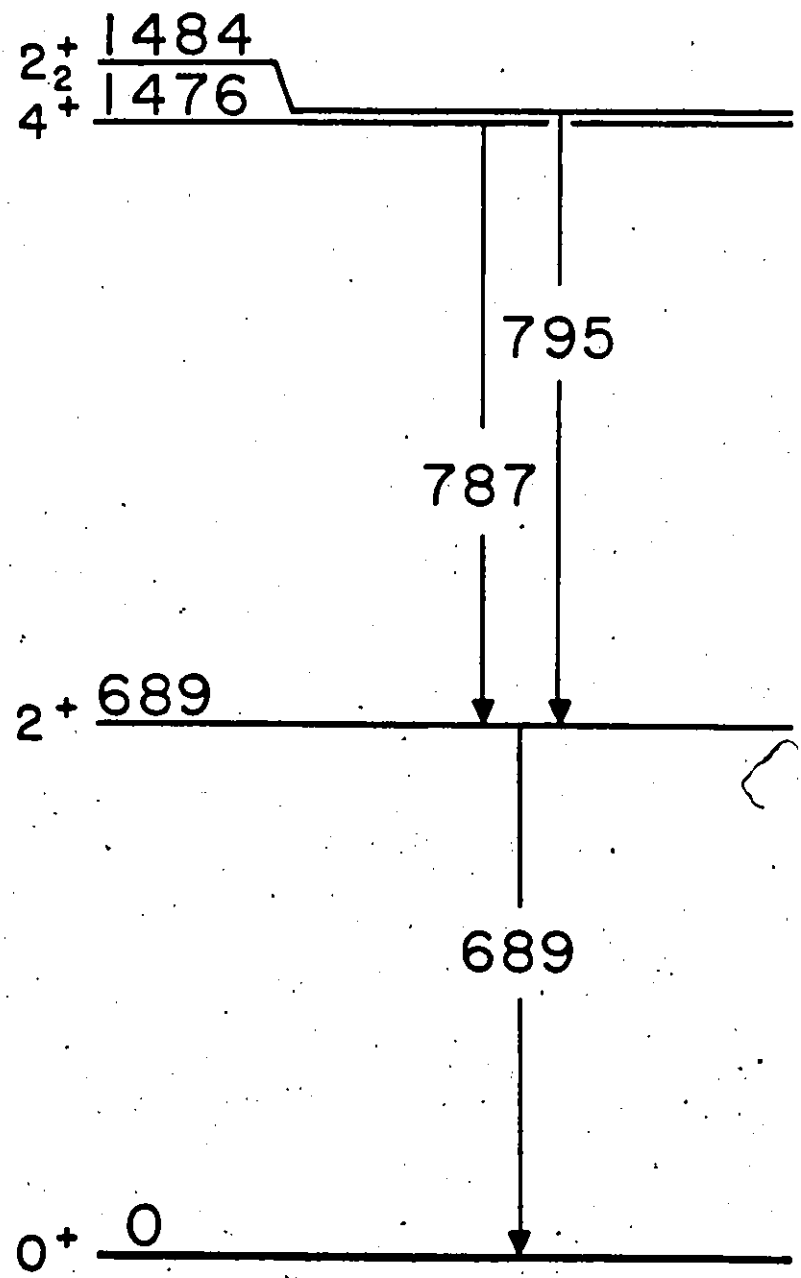
as shown in Figure 4.17, made possible the unambiguous identification of  $^{112}\text{Te}$  in the present work. The only reaction seen to populate  $^{112}\text{Te}$  in this study was  $^{92}\text{Mo}(^{23}\text{Na}, p2n)^{112}\text{Te}$ . The total coincidence spectrum appears in Figure 4.18, and some typical efficiency-corrected and background-subtracted gate spectra are shown in Figures 4.19 and 4.20. Figure 4.21 shows some results from the angular distribution analysis, while the  $\gamma$ -ray intensities, distribution coefficients and resulting transition assignments appear in Table 4.3. During the initial stages of analysis the possibility of excited state lifetimes in the nanosecond range was considered important enough to perform a separate  $\gamma$ - $\gamma$ -TAC experiment, as outlined in Section 3.2.7. Some typical time spectra are shown in Figure 4.22, and calculated centroid shifts appear in Table 4.4. No definite lifetimes greater than the experimental limit of detection, estimated at 2 ns, were observed. In addition, the low-energy  $\gamma$ -ray spectrum acquired by a Si(Li) detector during this experiment, failed to reveal any strong peaks other than x-rays between 30 and 85 keV.

The proposed level scheme constructed from the coincidence plus angular distribution information, based on the following analysis, is shown in Figure 4.23.

Initially this discussion will concentrate on the  $\gamma$ - $\gamma$  coincidence relationships which determine the level structure, and spin and parity assignments will be outlined subsequently.

Figure 4.17

$^{112}\text{Te}$  level scheme due to Tidemand-Petersson et al.  
(Ti80), from the  $\beta$ -delayed proton decay of  $^{113}\text{Xe}$ .



$^{112}_{52}\text{Te}_{60}$

Figure 4.18

Total coincidence spectrum from the  $^{92}\text{Mo}(^{23}\text{Na}, \text{xnypza})$  reaction at a beam energy of 90 MeV. Strong transitions in  $^{112}\text{Te}$  are labelled by their energies in keV. Peaks marked with a \* belong to the 202-325-ets. group (see Section 4.1.3), while unresolved doublets in  $^{112}\text{Te}$  are indicated by a letter d.

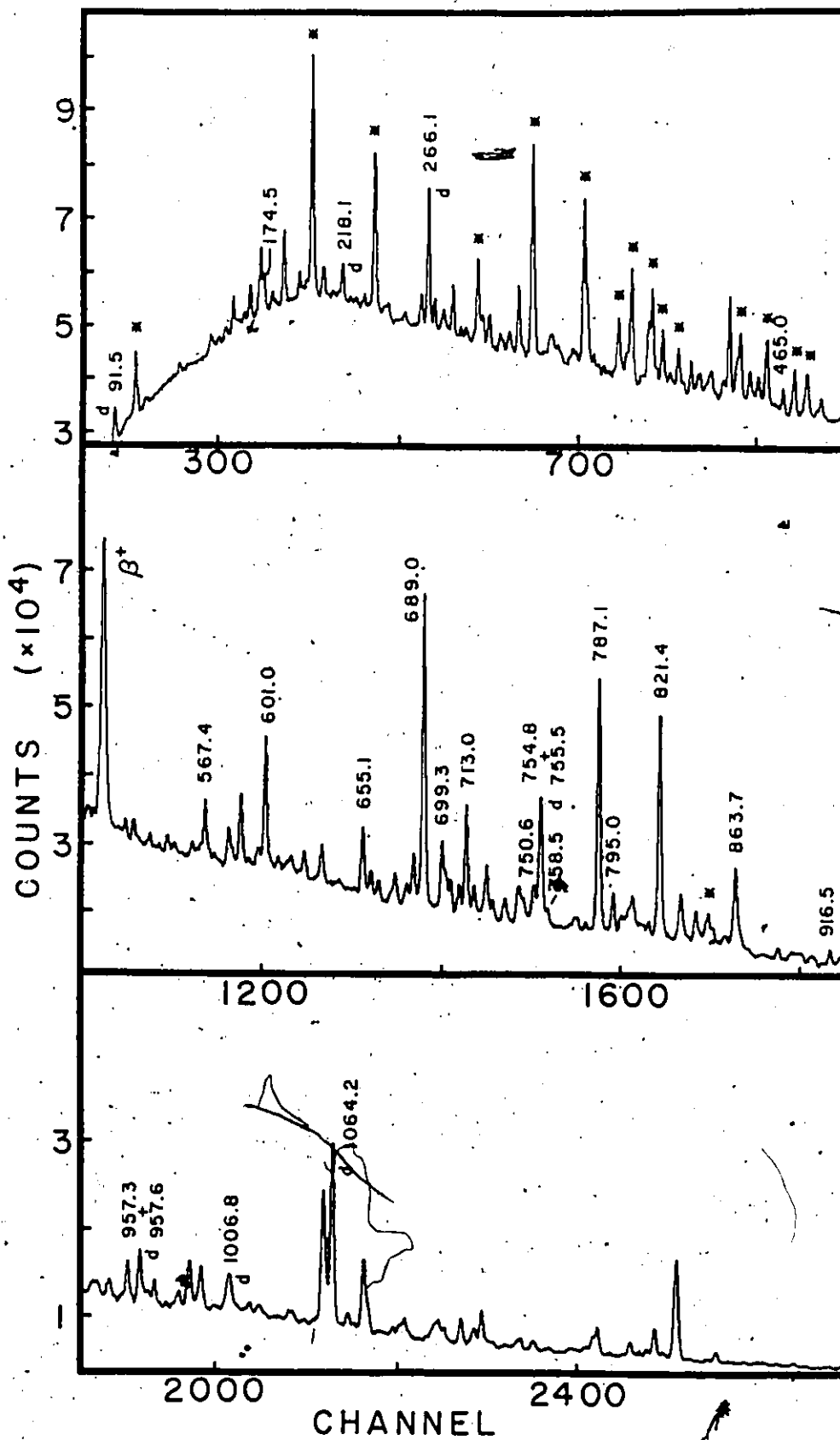


Figure 4.19

Coincidence gates from the  $^{92}\text{Mo}(^{23}\text{Na}, p2n)^{112}\text{Te}$  reaction. The data have been background-subtracted and corrected for detector efficiency. Gamma rays marked with a  $\nabla$  in the 266.1 keV gate are due to an impurity component in the gate peak.

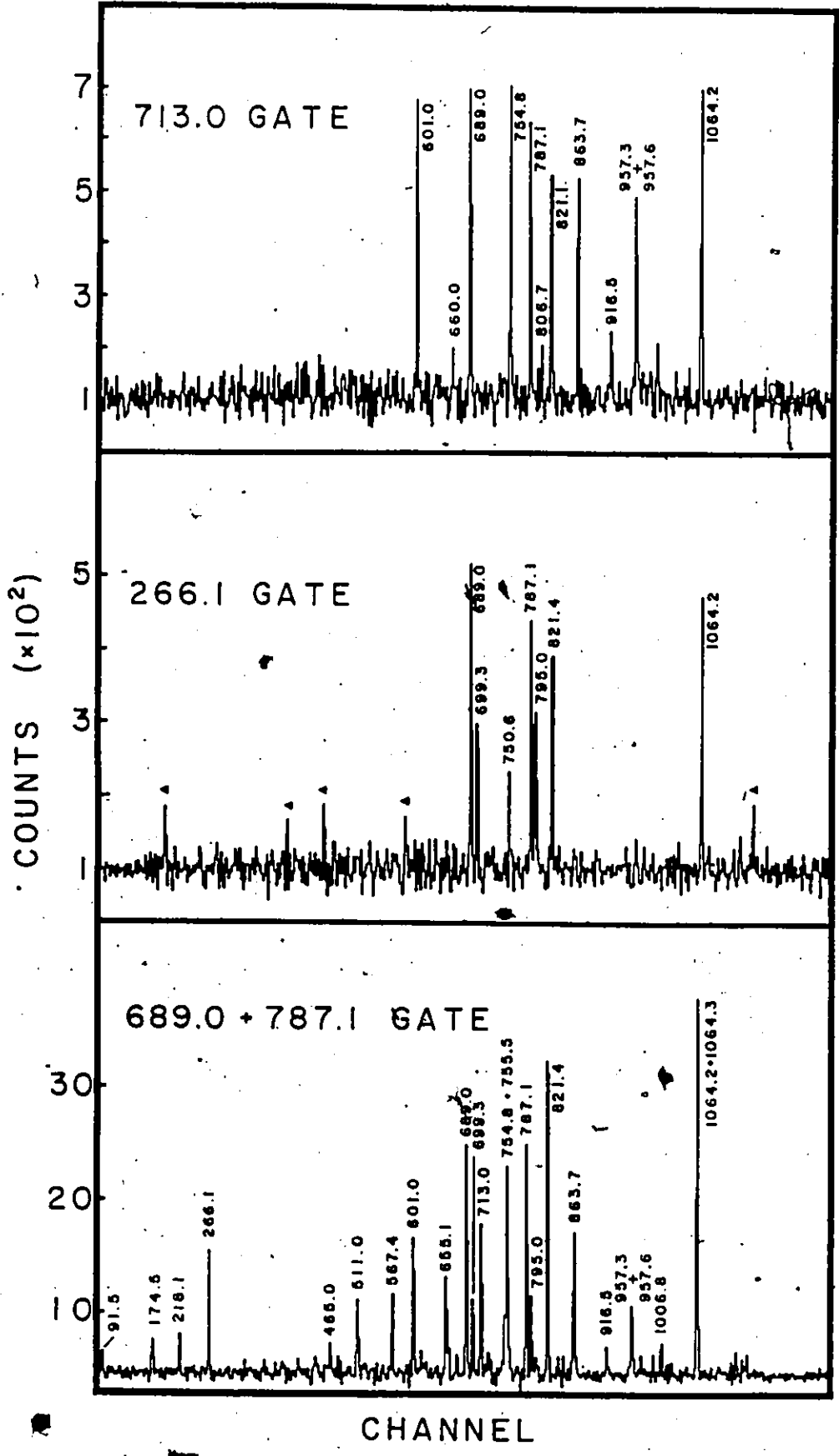


Figure 4.20

Coincidence gates from the  $^{92}\text{Mo}(^{23}\text{Na}, p2n)^{112}\text{Te}$  reaction. The data have been background-subtracted and corrected for detector efficiency.

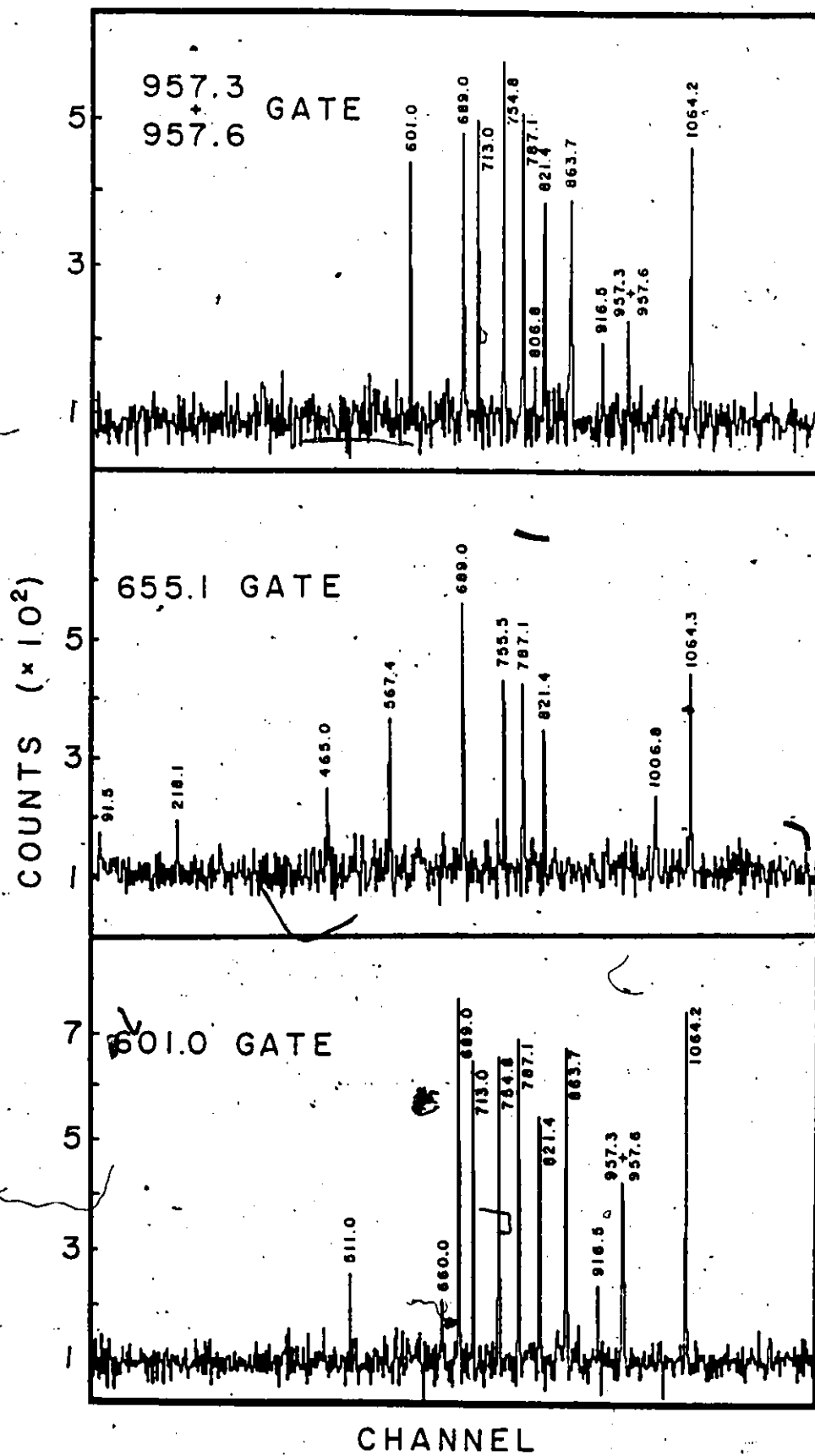


Figure 4.21

Some results from the  $^{112}\text{Te}$  angular distribution least-squares analyses. A  $\chi^2$  of 5.42, marked with a horizontal line in the right-hand panels, corresponds to the 99.9% confidence limit.

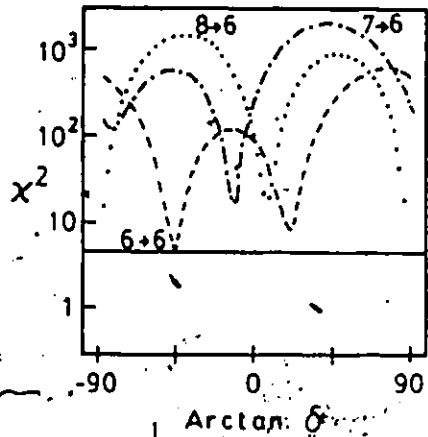
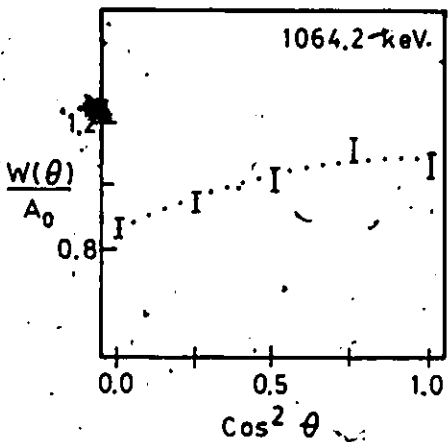
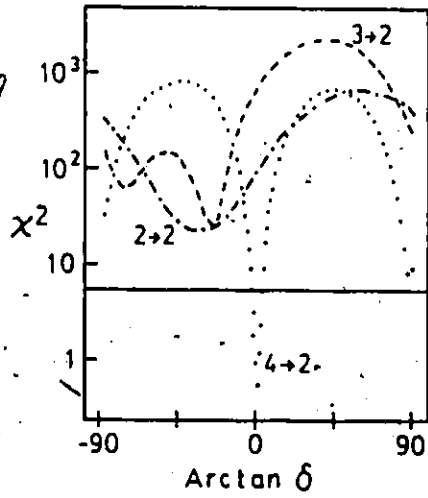
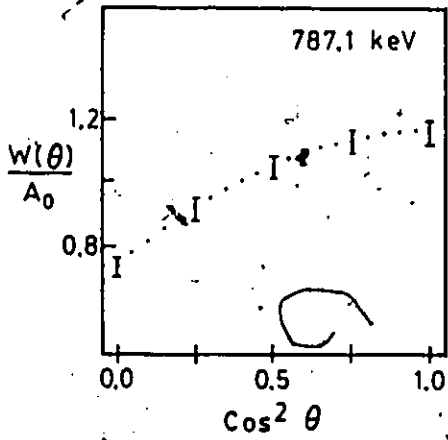
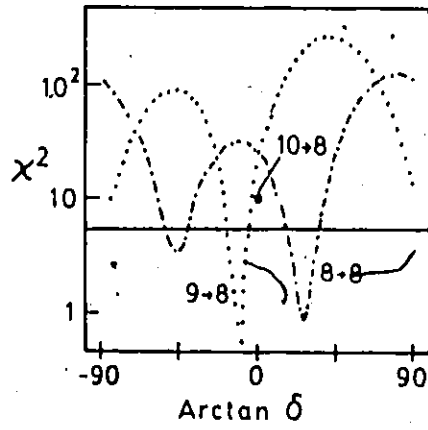
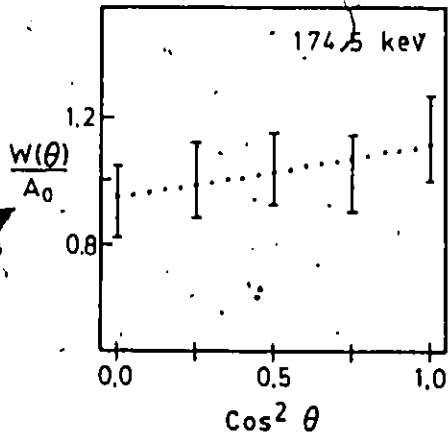


Table 4.3

Results of analysis for  $\gamma$  rays assigned to  $^{112}\text{Te}$ .

$E_{\gamma}^a$ (keV)	$I_{\gamma}^b$	$A_2$	$A_4$	Multipolarity	$J_i^{\pi} + J_f^{\pi}$
91.5 <sup>c</sup>	19 <sup>d</sup>	-0.03(7)	-0.08(8)		8 <sup>(-)</sup> + 7 <sup>(-)</sup>
174.5	7 <sup>d</sup>	0.11(7)	0.00(8)	M1/E2	9 <sup>(-)</sup> + 8 <sup>(-)</sup>
218.1 <sup>c</sup>	6	0.32(9)	-0.05(10)		8 <sup>(-)</sup> + 6 <sup>(-)</sup>
266.1 <sup>c</sup>	17	-0.40(2)	0.00(2)	E1	9 <sup>(-)</sup> + 8 <sup>+</sup>
439.5 <sup>c,e</sup>	2				
465.0	5	-0.22(15)	-0.03(18)	M1/E2	17 <sup>(-)</sup> + 16 <sup>(-)</sup>
567.4	14	0.45(6)	-0.12(7)	E2	14 <sup>(-)</sup> + 12 <sup>(-)</sup>
601.0 <sup>c</sup>	31	0.36(3)	-0.07(4)	E2	14 <sup>+</sup> + 12 <sup>+</sup>
614.9	5	0.24(16)	-0.07(15)		+ 4 <sup>+</sup>
655.1	20	0.36(4)	-0.07(5)	E2	10 <sup>(-)</sup> + 8 <sup>(-)</sup>
660.0	6				12 <sup>+</sup> + 10 <sub>2</sub> <sup>+</sup>
673.1 <sup>e</sup>	4				
689.0	≡ 100	0.35(2)	-0.08(2)	E2	2 <sup>+</sup> + 0 <sup>+</sup>
699.3	20	0.41(5)	-0.06(6)	E2	11 <sup>(-)</sup> + 9 <sup>(-)</sup>
713.0	31	0.36(3)	-0.11(4)	E2	16 <sup>+</sup> + 14 <sup>+</sup>
724.3 <sup>e</sup>	3				
750.6	12	0.26(9)	-0.05(11)	E2	15 <sup>(-)</sup> + 13 <sup>(-)</sup>
751.8 <sup>c</sup>	3				(11,12) + (10 <sup>+</sup> )
754.8 <sup>c</sup>	30			E2	10 <sub>1</sub> <sup>+</sup> + 8 <sup>+</sup>
755.5 <sup>c</sup>	14	0.31(3)	-0.08(3)	E2	12 <sup>(-)</sup> + 10 <sup>(-)</sup>
758.5	4	0.33(18)	-0.05(20)	(E2)	(10 <sup>+</sup> ) + 8 <sup>+</sup>

Table 4.3 (cont'd)

$E_Y^a$ (keV)	$I_Y^b$	$A_2$	$A_4$	Multipolarity	$J_i^\pi + J_f^\pi$
787.1	98	0.36(2)	-0.11(2)	E2	$4^+ + 2^+$
795.0	14	0.38(7)	-0.05(9)	E2	$13^{(-)} + 11^{(-)}$
802.9 <sup>e</sup>	3				
806.7 <sup>c</sup>	2				$(21,22) + 20^+$
821.4	86	0.36(2)	-0.07(3)	E2	$6^+ + 4^+$
863.7	31	0.34(3)	-0.04(4)	E2	$12^+ + 10_1^+$
916.5	4	0.30(15)	-0.07(20)	E2	$20^+ + 18^+$
957.3 <sup>c</sup>	10	0.49(6)	-0.20(7)	E2	$18^+ + 16^+$
957.6 <sup>c</sup>	6			E2	$10_2^+ + 8^+$
1006.8 <sup>c</sup>	8	0.52(8)	-0.02(9)	E2	$16^{(-)} + 14^{(-)}$
1064.2 <sup>c</sup>	52	0.18(2)	-0.06(3)	E2	$8^+ + 6^+$
1064.3 <sup>c</sup>	22			E1	$7^{(-)} + 6^+$
1076.2	3				$(16,17) + 15^{(-)}$
1127.0 <sup>e</sup>	4				
1144.2 <sup>c</sup>	4	0.17(5)	-0.03(6)		$6^{(-)} +$

<sup>a</sup> Energies are typically accurate to  $\pm 0.3$  keV.

<sup>b</sup> Deduced from coincidence intensities in the  $2^+ \rightarrow 0^+$  and  $4^+ \rightarrow 2^+$  gates, corrected for detector efficiencies. The ratio of the  $4^+ \rightarrow 2^+$  to  $2^+ \rightarrow 0^+$  transition intensities is obtained from the gated angular distribution  $A_0$  coefficients. The quoted intensities are accurate to  $\pm 10\%$  or less for the stronger lines, or  $\pm 1$  for transitions having  $I_Y < 10$ .

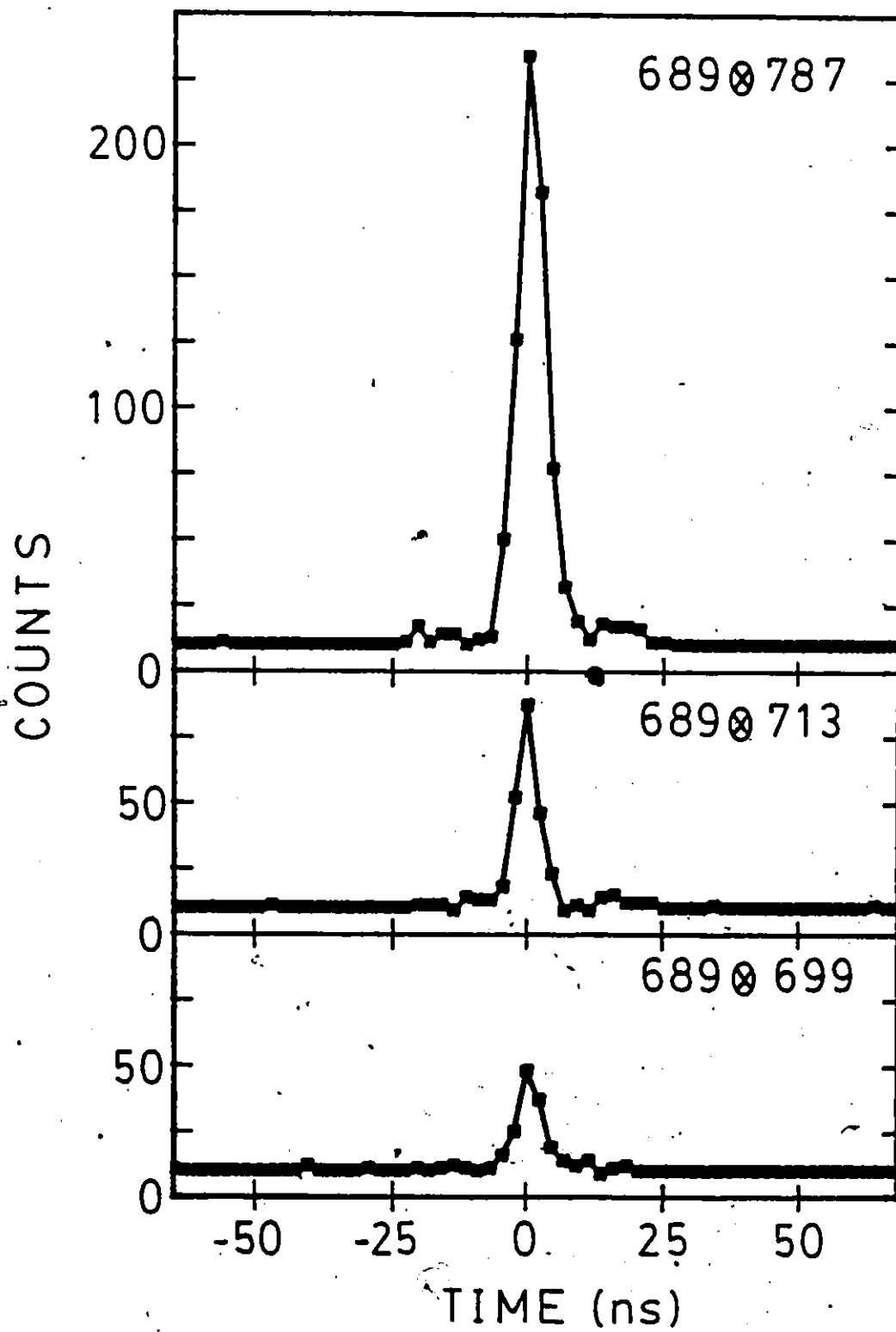
<sup>c</sup> Part of an unresolved multiplet.

<sup>d</sup> Corrected for internal conversion.

<sup>e</sup> Not placed in level scheme.

Figure 4.22

Representative  $\gamma_1$ - $\gamma_2$  time spectra for  $^{112}\text{Te}$ . The dispersion is 2.3 nanoseconds/channel.



Handwritten signature or initials.

Table 4.4

 $^{112}\text{Te}$   $\gamma_1$ ⊗ $\gamma_2$ <sup>a</sup> vs.  $\gamma_2$ ⊗ $\gamma_1$  time-peak centroid shifts

$E_\gamma$ (keV)	(689⊗ $\gamma$ ) vs. ( $\gamma$ ⊗689) Centroid Shift (ns)	(787⊗ $\gamma$ ) vs. ( $\gamma$ ⊗787) Centroid Shift (ns)
567	-0.4	1.0
601	0.1	-1.1
655	1.2	-1.3
689		-0.6
699	0.2	0.9
713	-1.4	-0.9
751	2.0 <sup>b</sup>	2.5 <sup>b</sup>
755	0.5	-0.8
756	-0.5	0.9
787	0.2	
795	0.1	-0.6
1064	0.5	0.2

<sup>a</sup> ⊗ = in coincidence with

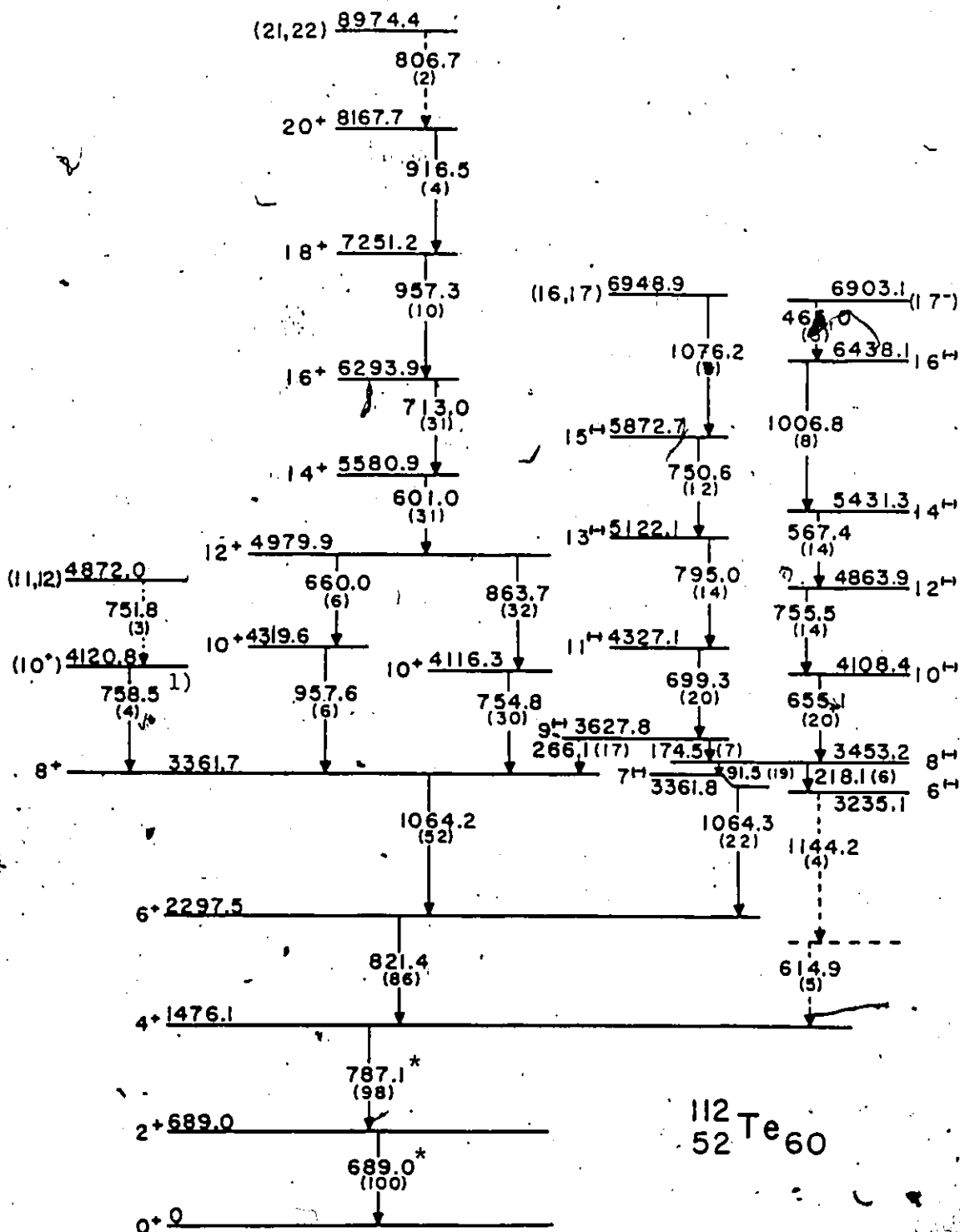
<sup>b</sup> These values indicate a possible lifetime for the  $15^{-}$  level at the limit of experimental resolution, but were not substantiated by other  $\gamma$ - $\gamma$  combinations.

The uncertainty in time-peak shifts is typically  $\pm 1.0$  nanoseconds.

Figure 4.23

Proposed level scheme for  $^{112}\text{Te}$ . All energies are in keV. Gamma-ray transitions marked with a \* have been reported previously, although they were not seen in-beam (see Figure 4.17).

- 1) Placement of the 758.5-(751.8) keV pair of rays is uncertain: they could feed the  $7^{(-)}$  instead of the  $8^{+}$  level (see text).



Coincidence gate spectra for the 689.0, 787.1, 821.4, 1064.2, 755, 863.7, 601.0, 713.0 and 957 keV transitions are quite clear, and they are all seen to be in coincidence with each other, establishing the strongest cascade group. For now this subset will be tentatively labelled as the "E2 group" or "E2 cascade", for reasons which will become clear. The only complications are caused by the presence of two obvious doublets. The 754.8-755.5 keV case is just barely resolved by the unfolding process, and so although energies and intensities of the two members were obtained the consistent separation necessary for independent angular distributions was not possible. In the coincidence spectra resolution of the two is out of the question, and so the 755 keV gate shows the E2 group as well as another set of transitions. However upon comparison of the two sets of gates a clear energy centroid shift is seen.

The 957 keV gate contains another 957 peak, as shown in Figure 4.20. The presence of a 660 keV  $\gamma$  ray in that gate, together with the absence in the 660 keV gate of an 864 or 755 keV peak and the match in energy sums place the 957.6-660.0 keV combination parallel to the 863.7-754.8 keV part of the E2 cascade. A slight centroid shift was determined by comparing 957 keV peaks in the 863.7 and 754.8 keV gates to those peaks in other gates seeing both components of the doublet.

A weak 807 keV peak was observed in the E2 group coincidence gates. It is the weaker member of an unresolved doublet and a clear gate could not be extracted, resulting in a tentative assignment at the top of the E2 cascade. Intensities for the 754.8, 863.7, 601.0 and 713.0 keV  $\gamma$  rays are quite uniform, and are actually all within experimental uncertainty of each other. The singles intensities taken at lower beam energies showed less similarity and so were used to determine the order of these transitions. A 758.5-(751.8) keV pair of  $\gamma$  rays enter the main scheme above the 1064.2-821.4-787.1-689.0 keV group, and appear to be in coincidence with each other. The latter transition is weak and in a complicated part of the gates, so has been marked as tentative.

Two weaker groups of  $\gamma$  rays are clearly distinguished in the gate spectra, both of which groups are in coincidence with the strong 1064.2-821.4-787.1-689.0 keV cascade. A 655.1-755.5-567.4-1006.8-465.0 keV group are all in coincidence with each other; as well, they possess gate spectra in which peaks at 91.5 and 218.1 keV are evident. The 699.3-795.0-750.6-1076.2 keV group are in coincidence with each other; as well, their gates contain 91.5, 174.5, 218.1 and 266.1 keV peaks. The 174.5 and 266.1 keV gate spectra are quite similar, in that both see the 1076.2-750.6-795.0-699.3 keV cascade, with the same intensity pattern, however the 174.5 keV gate also contains the 91.5 and 218.1 keV transi-

tions. Therefore the 174.5 and 266.1 keV  $\gamma$  rays seem to de-excite the same level, upon which is built a 699.3-795.0-750.6-1076.2 keV sequence.

The 91.5 keV gate contains the 655.1-...-465.0 keV chain and, more weakly, the 174.5-699.3-795.0-750.6 keV chain, as well as the strong 1064.2-821.4-787.1-689.0 keV cascade. Given the relative intensities, the 91.5 keV  $\gamma$  ray must be placed above the 1064.2 keV but below the 174.5 keV transition. This puts the 91.5-174.5 keV pair of  $\gamma$  rays parallel to the 266.1 keV transition, especially since the 266.1 keV gate does not see either of that pair. Furthermore, the similarities between these low energy gates and the match of energy sums forces the 91.5-174.5 keV combination to be placed between the same two energy levels as the 266.1 keV  $\gamma$  ray. Since coincidence gates for the  $\gamma$  rays mentioned to this point do not consistently show any transitions which might come between the 91.5, 174.5, 266.1, 655.3, 699.3-... keV group and the 1064.2-821.4-787.1-689.0 keV cascade, the 91.5 ... group was placed directly above the 1064.2 keV transition.

The 218.1 keV gate is very similar to the 91.5 gate spectrum, with the exception of the 821.4 and 1064.2 keV  $\gamma$  rays. The 218.1 keV transition, then, appears to de-excite the same level as does the 91.5 keV  $\gamma$  ray. A probable 218.1-1144.2-614.9 keV cascade was observed.

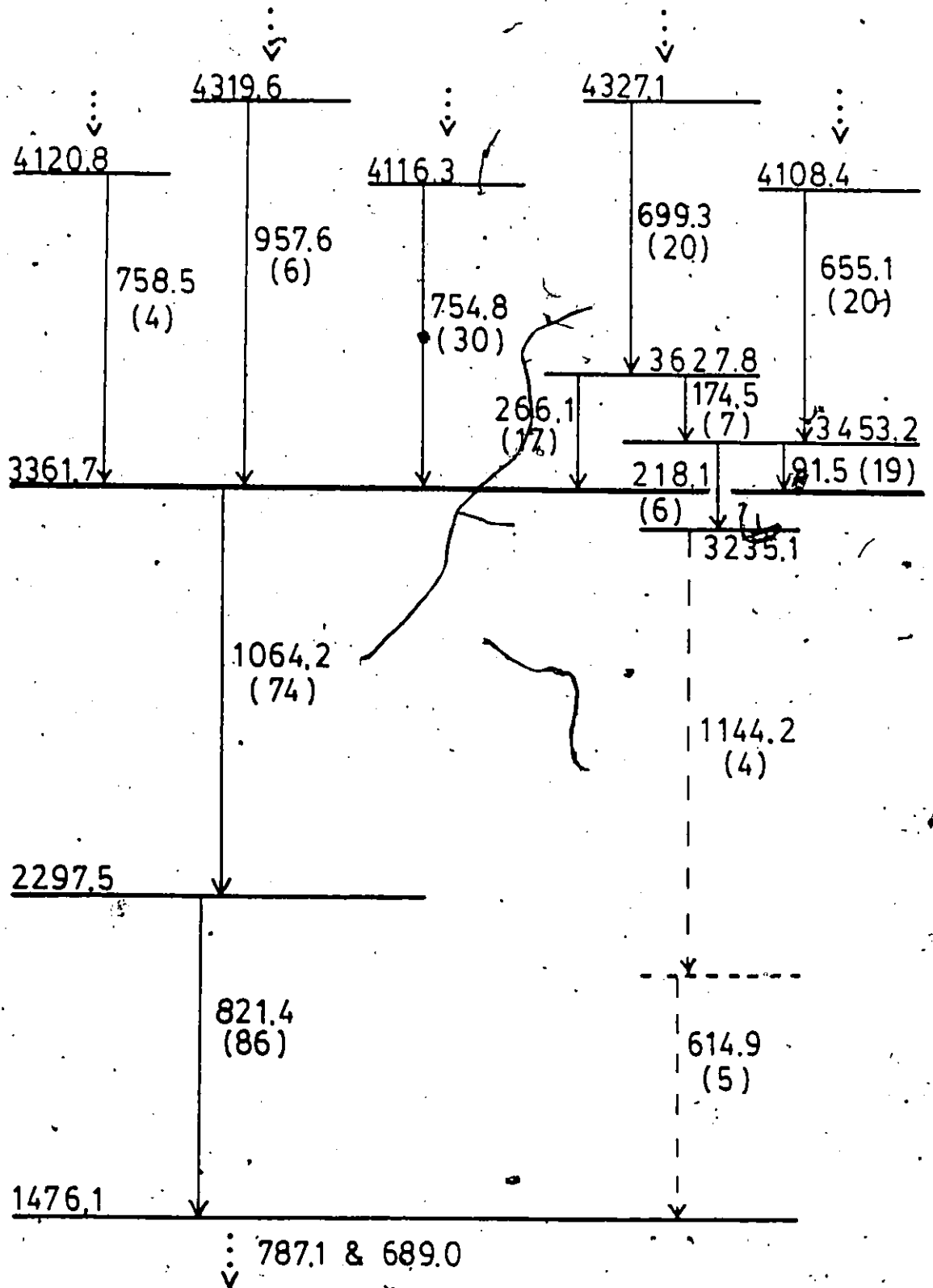
A partial level scheme summarizing this coincidence information is presented in Figure 4.24.

The strong 689.0 and 787.1 keV  $\gamma$  rays have angular distribution coefficients indicative of stretched E2 transitions, in accordance with the  $2^+$  and  $4^+$  spin assignments to the 689.0 and 1476.1 keV levels respectively made by Tidemand-Petersson et al. (Ti80). The 821.4 keV  $\gamma$  ray is also seen to be a stretched E2, and so the 2297.5 keV level is assigned spin  $6^+$ . Apart from the very weak 806.7 keV transition, the remaining members of the "yrast" group of  $\gamma$  rays exhibit angular distributions characteristic of stretched E2 transitions, with the lone exception of the 1064.2 keV  $\gamma$  ray. From Table 4.3, the strong transitions up to spin  $16^+$  show typical values for  $A_2$  and  $A_4$  coefficients of 0.35(2) and -0.08(2) respectively. However, the 1064.2 keV  $\gamma$  ray has an  $A_2$  of 0.18(2) and an  $A_4$  of -0.06(2). Since this transition is low in the level scheme and therefore crucial to many higher spin assignments, its angular distribution is quite important. As Figure 4.21 shows,  $8^+6$ ,  $7^+6$ , and  $6^+6$  assignments for the 1064 keV distribution can be rejected with 99.9% confidence.

There are a number of possible causes of such an abnormal distribution:

Figure 4.24

Partial  $^{112}\text{Te}$  level scheme determined from  $\gamma$ - $\gamma$   
coincidence data alone.



- 1) faulty analysis of the angular distribution data,
- 2) attenuation of anisotropy due to an excited state lifetime; or
- 3) the 1064 keV  $\gamma$  ray is an unresolved doublet.

In order to eliminate the first possibility a few points must be made. The nearest obvious peak in the spectrum is a 1059.4 keV  $\gamma$  ray which overlaps so little with the 1064.2 keV peak that a simple linear background fit and channel counts summation could be performed, resulting in  $A_k$  coefficients within the stated uncertainty of the quoted  $A_2$  and  $A_4$ .

Doppler shifting, or more usually Doppler broadening of  $\gamma$  rays has been observed in some heavy-ion reactions, although this effect usually can be detected quite easily by measuring peak centroids and widths. Certainly no such small shifts were observed; in fact, the peak position as a function of angle was stable to less than 0.1 keV. Using identical target-backing thicknesses and analysis techniques, angular distributions of weaker 1025.5, 1028.8 and 1055.2 keV transitions in  $^{116}\text{Te}$  were measured and quite clearly showed E1, E2 and E2 character respectively (c.f. Table 4.1).

An excited state lifetime in the  $> 10$  ns range could result in an E2 transition with attenuated  $A_k$  coefficients; however, a 1 MeV E2  $\gamma$  ray with such a lifetime is extremely unlikely. Its strength in relation to the Weisskopf single-particle estimates (BW52) would be about  $10^{-3}$  Weisskopf units.

(W.u.). More importantly, such an attenuation would be seen in the distributions of  $\gamma$  rays lower in the scheme, and this is definitely not the case. Certainly any lifetimes greater than 2 ns are precluded by the negative results of the  $\gamma$ - $\gamma$ -TAC experiment (see Table 4.4).

If the 1064 keV peak were to consist of a  $^{112}\text{Te}$  E2 transition in conjunction with an unresolved  $\beta$ -decay  $\gamma$  ray, the  $A_2$  could be attenuated to the value given in Table 4.3. However, no  $\gamma$  rays of that energy were detected in spectra taken with the beam off. Furthermore, using singles data with no multiplicity filtering the 1064 keV angular distribution shows the same values of  $A_2$  and  $A_4$ , within experimental uncertainty, as do the gated data.

The possibility remains that the 1064 keV  $\gamma$  ray is an unresolved doublet in  $^{112}\text{Te}$ , with the two components displaying different  $A_k$  coefficients, linear combinations of which produce the measured  $A_2$  and  $A_4$ . From the coincidence relationships no clue as to a doublet nature for this transition is seen, indicating that the two components must be parallel to each other in the level scheme and must proceed between levels quite close to if not identical in energy. In fact, as indicated in Figure 4.24, if there are two 1064 keV transitions, they seem to proceed from two degenerate (within instrumental resolution) 3362 keV levels to the  $6^+$  yrast state at 2297.5 keV. There are a number of multipolarity

possibilities for the two members of this doublet, involving various combinations of E1, M1/E2 and E2 transitions:

- 1) mixed M1/E2 + E1
- 2) mixed M1/E2 + mixed M1/E2
- 3) mixed M1/E2 + E2
- 4) E1 + E2

With the constraints of a) matching  $A_2$  and  $A_4$  to the measured values plus b) reasonable M1/E2 mixing ratios, options 1) and 2) may be discarded. An M1/E2 ( $J+J-1$ ) + E2 ( $J'+J'-2$ ) combination is able to fit the data, resulting in spin assignments of  $7^+$  and  $8^+$  to subsequent degenerate levels at approximately 3362 keV excitation energy. The E1 ( $J+J-1$ ) + E2 ( $J'+J'-2$ ) option fits the data as well, leading to degenerate  $7^-$  and  $8^+$  3361.7 keV levels. In either case the  $8^+$  level is yrast and thus the strong 754.8, 863.7, 601.0 ... keV set of E2 transitions were placed above it in the level scheme, forming an even-spin positive-parity "band" similar to those found in 114, 116, 118, ... Te. The transitions within this band comprise the "E2 group" referred to previously.

The two weaker 655.1-755.5-... and 699.3-795.0-... keV groups are connected to the E2 cascade by the 91.5-174.5-266.1 keV trio, the multipolarities of which determine the higher spins. On purely spectroscopic grounds, definitive spin and parity assignments cannot be made. There are considerations which will indicate the most likely alternative, however.

The angular distribution for the 174.5 keV  $\gamma$  ray definitely shows M1/E2 character, indicating no parity change for the levels involved. Of the possible spin combinations J+J-1 is preferred over J+J due to the more reasonable mixing ratio ( $\delta^2=0.04$  vs.  $\delta^2=0.20$ ). In the case of the 266.1 keV transition, its large negative  $A_2$  and vanishing  $A_4$  are similar to those belonging to E1 transitions in  $^{114,116}\text{Te}$  (c.f. Tables 4.1 and 4.2), although the 266.1 keV distribution is best fit by a J+J-1 M1/E2. As seen in its coincidence gate, this transition is a doublet with roughly 20% contamination, which depending on the contaminant anisotropy could affect the angular distribution somewhat. Thus a 266.1 keV J+J-1 E1 is also possible; however, a J+J M1/E2 is less plausible. The accuracy of the 91.5 keV  $\gamma$  ray distribution is also not certain, since the corrections for absorption in the target backing are quite large at that energy and are a function of angle. Nevertheless the possibility of a significant E2 component can be ruled out by the absence of any lifetimes greater than 2 nanoseconds, as shown by the results of the  $\gamma$ - $\gamma$ -TAC experiment. This transition is also unresolved from a  $\gamma$  ray in another nuclide, but the amount of contamination is about 15% and could not change the transition assignment to pure E1 or E2. Even so, the option of degenerate 3362 keV levels creates the possibility of two 91.5 keV  $\gamma$  rays in  $^{112}\text{Te}$  connecting the 3453.2 and 3362 keV levels. This widens the range of reasonable  $A_2$  and  $A_4$  values possible from a given

set of level spins and parities, but certain spin and parity combinations can still be ruled out, as outlined below.

A detailed analysis of all possible level structures above the 3362 keV state is quite tedious; a few options, however, should be reviewed, assuming 1)  $8^+$ , and  $7^+$ , or 2)  $8^+$  and  $7^-$  3362 keV levels, while remaining consistent with coincidence and angular distribution information presented thus far.

1) Treating the 266.1 keV transition as M1/E2  $J+J-1$  results in a  $7^+-8^+-9^+$  or  $7^+-7^+-8^+$  3362(non-yrast)-3453.2-3627.8 keV set of levels, depending on whether the 266.1 keV  $\gamma$  ray is chosen to feed the  $8^+$  or  $7^+$  3362 keV level respectively. Based on the coincidence data, in both cases this creates an even-spin positive-parity band built on a non-yrast  $8^+$  state, which band is strongly fed from above but does not connect at all to the yrast even-spin positive-parity band. In view of the fact that the  $12^+$  yrast state is seen to decay to the previously-established  $10^+$  states at 4116.7 and 4319.6 keV, the absence of any such interconnections would be extremely unlikely. In  $^{114}\text{Te}$  cross-transitions are evident for well-populated states. As well, this option results in a complete lack of negative-parity states, rather disconcerting in light of the negative-parity structures seen in  $A > 112$  Te isotopes.

Assuming E1 character for the 266.1 keV transition produces a  $7^+-8^--9^-$  or  $7^+-7^--8^-$  set of levels, again depend-

ing on whether the 266.1 keV  $\gamma$  ray feeds the  $8^+$  or  $7^+$  3362 keV level. In both of these cases the 91.5 keV angular distribution would not fit, unless the experimental numbers are virtually ignored. However, in order to make that plausible the intensities of the two 1064 keV  $\gamma$  rays would be such that the resulting angular distribution  $A_k$  coefficients could not match the well-determined experimental values.

2) Allowing  $8^+$  and  $7^-$  degenerate 3362 keV states, and assuming the 266.1 keV transition is M1/E2  $J \rightarrow J-1$  results in a  $7^- - 8^+ - 9^+$  or  $7^- - 7^- - 8^-$  scheme. The first option would produce an  $8^+ - 10^+ - \dots$  group with no connection at all to the yrast even-spin positive-parity band, as is the case with the  $7^+ - 8^+ - 9^+$  and  $7^+ - 7^+ - 8^+$  scenarios which did not seem plausible. As well, to come close to the 91.5 keV angular distribution the  $8_2^+ + 8_1^+$  (vs. the  $8^+ + 7^-$ ) transition would be strongest, with the result that the  $7^-$  3362 keV level would not be fed sufficiently strongly to change the 1064 keV distribution away from pure  $8^+ + 6^+$  E2 as much as was measured experimentally. The  $7^- - 7^- - 8^-$  option would have some trouble explaining the 91.5 keV angular distribution, and would actually result in two 91.5 keV  $7_2^- + 7_1^-$  and  $7_2^- + 8^+$   $\gamma$  rays in order to come close to fitting the experimental coincidence intensities. The absence of a  $7_2^- + 6^+$  transition is also quite disturbing, in light of the  $\sim 2 \times 10^3 E_1 E_Y^3$  factor favouring a  $7_2^- + 6^+$  over a  $7_2^- + 8^+$   $\gamma$  ray.

Taking the 266.1 keV transition to be E1 in nature and feeding an  $8^+$  or  $7^-$  3362 keV state leads to  $7^-8^-9^-$  and  $7^-7^+8^+$  solutions for the 3362(non-yrast)-3453.2-3627.8 keV set of levels. The latter choice once again creates an even-spin positive-parity band with no observable connection at all to the yrast band, and also fails to result in any negative-parity bands. Finally, a  $7^-8^-9^-$  scheme explains the angular distributions and coincidence intensities reasonably well; better, in fact, than any of the other options, with the possible exception of the 266.1 keV distribution data. Furthermore, this option a) does not produce levels which normally would decay to other established states but are not observed to do so, b) does not require or prefer two 91.5 keV  $\gamma$  rays, and c) results in negative-parity structures, the absence of which would have been questionable. Taking into account all of the factors considered up to this point, spins and parities of  $7^{(-)}8^{(-)}9^{(-)}$  were assigned to the 3362(non-yrast)-3453.2-3627.8 keV group of levels.

Concerning the 1064 keV  $\gamma$  ray doublet, this choice leads to an E2 + E1 combination. Using the average  $A_2$  coefficient from the other strong E2 yrast distributions,  $A_2^{E2} = 0.36(3)$ , and the average  $A_2$  from the four E1 distributions in  $^{114,116}\text{Te}$ ,  $A_2^{E1} = -0.30(4)$ , the measured  $A_2$  of 0.18(2) results in a mixture of about 70% E2 and 30% E1. A similar calculation for the  $A_4$  coefficients agrees with this split within experimental uncertainty. An indicated 0.1 keV

difference between the two 1064 keV transition energies was measured using centroids of those peaks in the 266.1 keV vs. 863.7+601.0+713.0 keV coincidence gates, although this is quite a small discrepancy.

The middle portion of the  $^{112}\text{Te}$  level scheme resulting from this discussion is shown in Figure 4.25, and was incorporated into the overall level scheme (Figure 4.23).

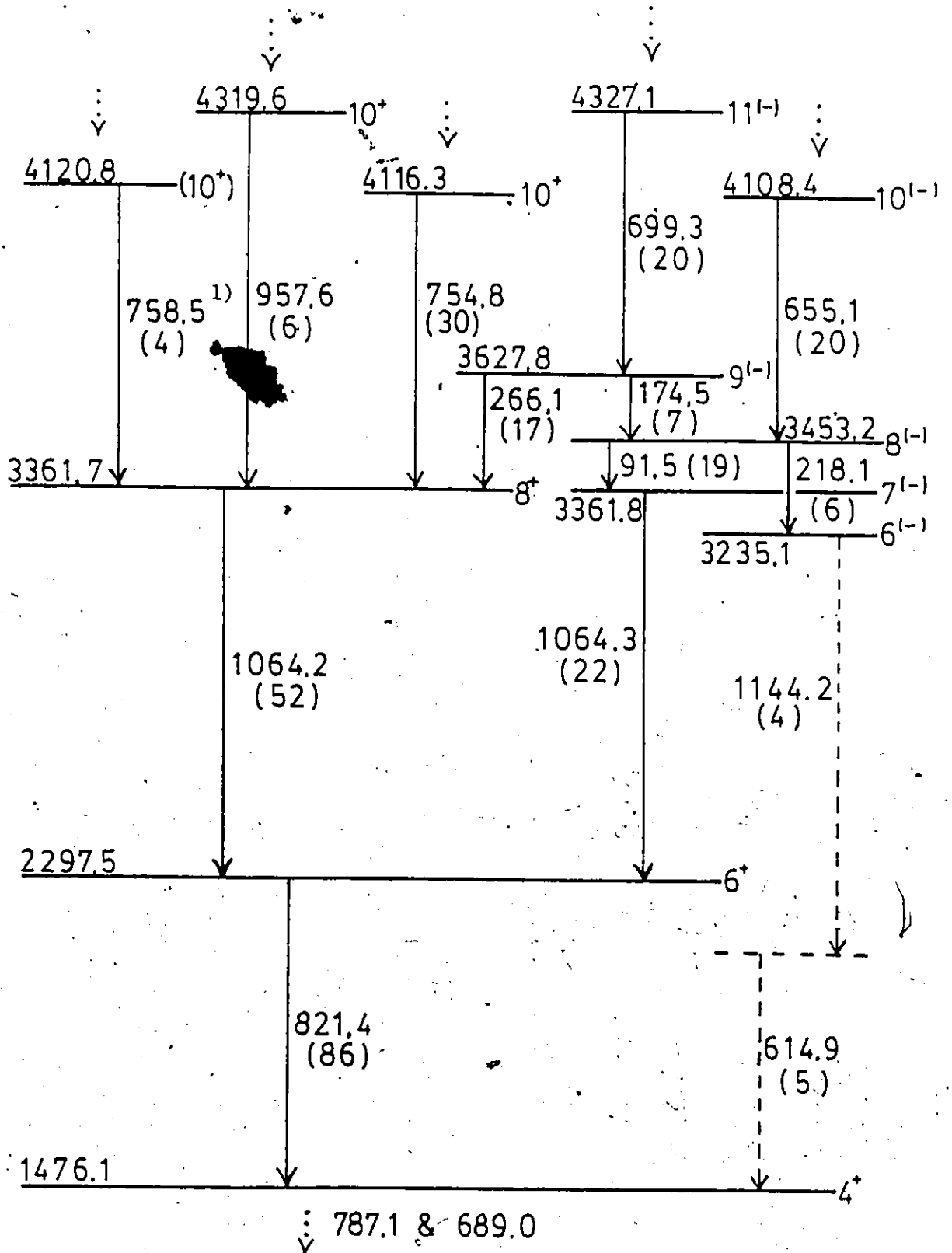
Based on the 218.1 keV angular distribution the level at 3235.2 keV was labelled as  $6^{(-)}$ . Peaks at 1144.2 and 614.9 keV are not seen clearly in all the gates corresponding to  $\gamma$  rays which feed into the 3453.3 keV state, and so those two transitions are only tentatively placed connecting the  $6^{(-)}$  and  $4^+$  levels. As well, the order of those two transitions is not definite. It is somewhat puzzling that a clear path de-exciting the  $6^{(-)}$  state having roughly the same intensity as the 218.1 keV  $\gamma$  ray was not observed; perhaps the intensity is split up into multiple paths at that point.

The 699.3, 795.0 and 750.6 keV members of the previously-mentioned cascade feeding the 3627.8 keV level display angular distributions with E2 character, leading to the  $9^{(-)}$ (3627.8 keV)- $11^{(-)}$ - $13^{(-)}$ - $15^{(-)}$  structure shown in Figure 4.23. A 1076.2 keV transition feeds into the top of that band; it is too weak to extract a meaningful distribution and a (16,17) spin assignment for the 6948.9 keV level is a reasonable conjecture.

Figure 4.25

Partial  $^{112}\text{Te}$  level scheme determined from coincidence plus angular distribution data.

- 1) Placement of the 758.5-(751.8) keV pair of  $\gamma$  rays is uncertain: they could feed the  $7^{(-)}$  instead of the  $8^{+}$  level.



A 655.1-755.5-567.4-1006.8 keV group entering the 3453.2 keV  $8^{(-)}$  level appear to be made up of all E2 transitions, thus establishing an  $8^{(-)}-10^{(-)}-12^{(-)}-14^{(-)}-16^{(-)}$  band. However, the weaker 465.0 keV  $\gamma$  ray feeding that structure appears to be M1/E2 in character, resulting in a  $(17^-)$  assignment to the 6903.1 keV state.

Placement of the 758.5-(751.8) keV pair of  $\gamma$  rays above the  $8^+$  level is not definite. Due to the existence of degenerate  $7^{(-)}$  and  $8^+$  levels, the spin of the 4121 keV level could be either  $10^+$  or  $9^{(-)}$ .

One feature of this  $7^{(-)}-8^{(-)}-9^{(-)}$  option is a  $9^{(-)}-11^{(-)}-13^{(-)}$  ... band which is actually yrast in the spin range  $9^{(-)}$  to (16,17) yet is not populated as strongly as the E2 positive-parity band, a behaviour which certainly goes against the norm. However, if changes in transition intensities are compared the story is quite the reverse. The "E2 group" intensities are almost exactly equal between spins  $16^+$  and  $8^+$ , the very spin range over which the  $9^{(-)}-11^{(-)}$  ... band is picking up strength. So above spin (16,17) the positive-parity band is being fed and seems to be yrast, but then from  $16^+$  (16,17) down to  $8^+$  ( $9^{(-)}$ ) the  $9^{(-)}-11^{(-)}$  ... structure appears more yrast-like in terms of the feeding pattern.

As is the case for the previous two  $^{116,114}\text{Te}$  isotopes, the  $^{112}\text{Te}$  negative-parity assignments are not absolutely definitive; nevertheless, the evidence is strongly in favour of that conclusion.

## Chapter Five - Discussion

### Introduction

Clearly there are many similarities between level structures of the  $^{112}\text{Te}$ ,  $^{114}\text{Te}$  and  $^{116}\text{Te}$  nuclei under consideration in the present work, and so this chapter discusses the experimental results for all three nuclides as a whole rather than on an individual basis. The discussion is presented within the context of (i) the theoretical models outlined in Chapter Two, (ii) data available for the heavier  $A > 118$  Te isotopes, and (iii) transitional nuclei in other mass regions, specifically  $(Z < 50, N > 50)$  and  $(N > 82, Z < 64)$ .

Systematics of the yrast levels in even-even  $^{112-124}\text{Te}$  isotopes are presented in Section 5.1. Then, following the outline of Chapter Two, Section 5.2 discusses the results in terms of a shell-model description, while Section 5.3 compares the simple collective vibrational model to the observed positive-parity levels. These two different views are combined in a discussion of the results in terms of the pairing-plus-quadrupole model in Section 5.4. The Interacting Boson Approximation predictions are examined in Section 5.5, while Section 5.6 provides a comparison of the

phenomenological Variable Moment of Inertia and Variable Anharmonic Vibrator Model results with experimental observations. Finally, the behaviour of high-spin states is considered in Section 5.7.

### 5.1 Systematics of Even-even $^{112-126}\text{Te}$ Isotopes

Figure 5.1 shows the level systematics of  $^{112,114,116}\text{Te}$ , taken from the present work, and the previously-known results for even-even  $^{118-126}\text{Te}$  nuclides. In order to show the overall picture, only yrast positive-parity states up to spin  $18^+$  and  $5^-$ ,  $7^-$ ,  $8^-$  and  $9^-$  negative-parity states are shown. Note that for the sake of this discussion states labelled as  $7^{(-)}$ ,  $8^{(-)}$ , ... in Chapter Four will be treated here as having negative parity.

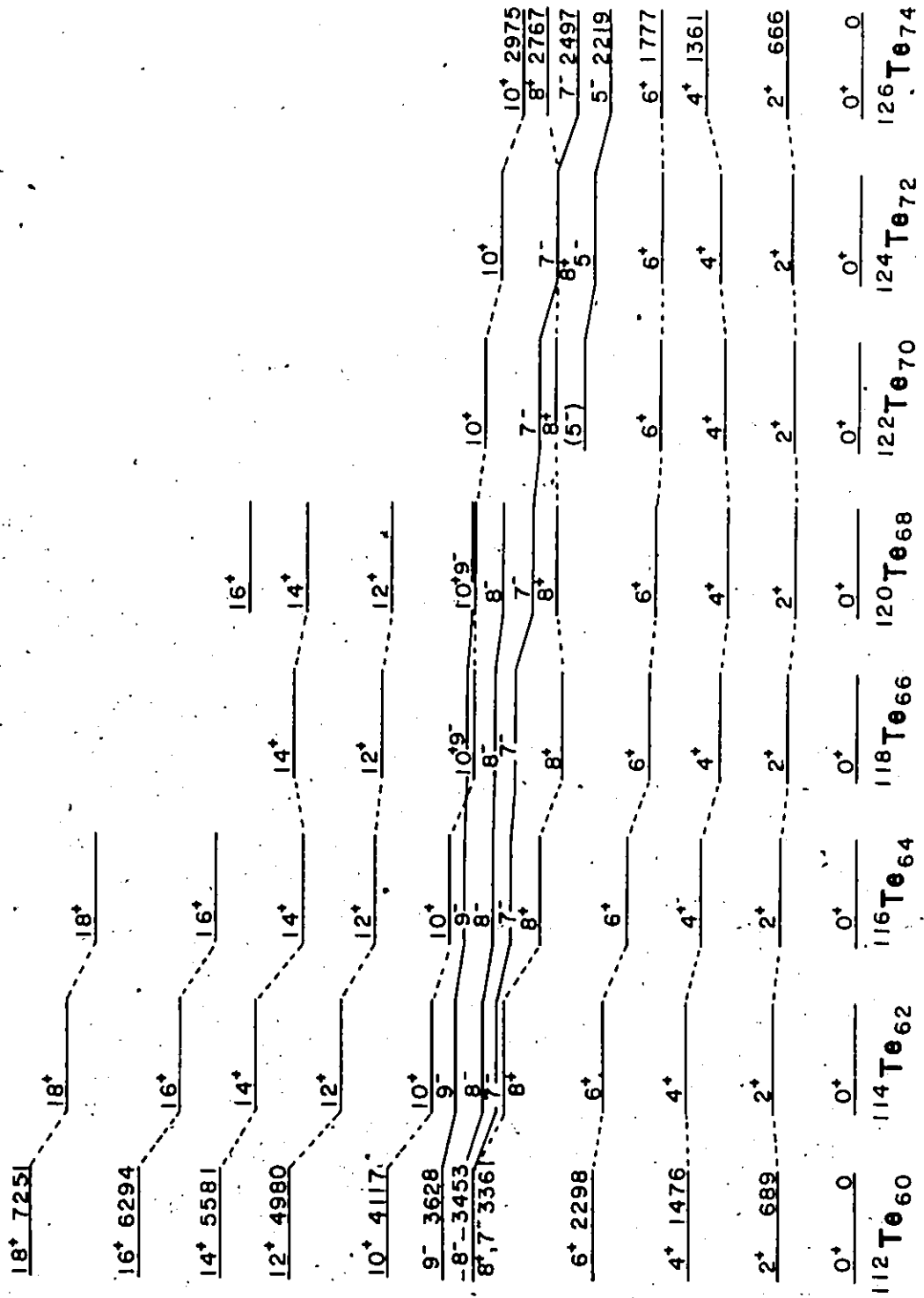
There are a number of general trends worth noting.

#### 5.1.1 Positive-parity Levels

The  $2^+$  and  $4^+$  states are lowest in energy near the middle of the neutron  $50 < N < 82$  shell,  $E(2^+) = 560$  keV at  $^{120}\text{Te}_{68}$ , and rise at the beginning and end of the shell. This tendency, as well as the observation of  $2_2^+$  and sometimes  $0_2^+$  members of the 2-phonon vibrational triplet levels near the  $4^+$  level in  $^{118-130}\text{Te}$ , plus the consistency of the  $R_4 = E(4^+)/E(2^+)$  ratios over a wide range of isotopes ( $1.95 < R_4 < 2.14$  for  $^{112-130}\text{Te}$ ) is indicative of collective vibrational effects. By contrast, in  $^{134}\text{Te}_{82}$ , which nucleus

Figure 5.1

Level systematics of even-even  $^{112-126}\text{Te}$ . For  $^{112-116}\text{Te}$  states above spin  $18^+$  are not shown. The data are taken from the present work ( $^{112-116}\text{Te}$ ), Ch82 and Va82 ( $^{118-122}\text{Te}$ ) and LS78 ( $^{124-126}\text{Te}$ ).



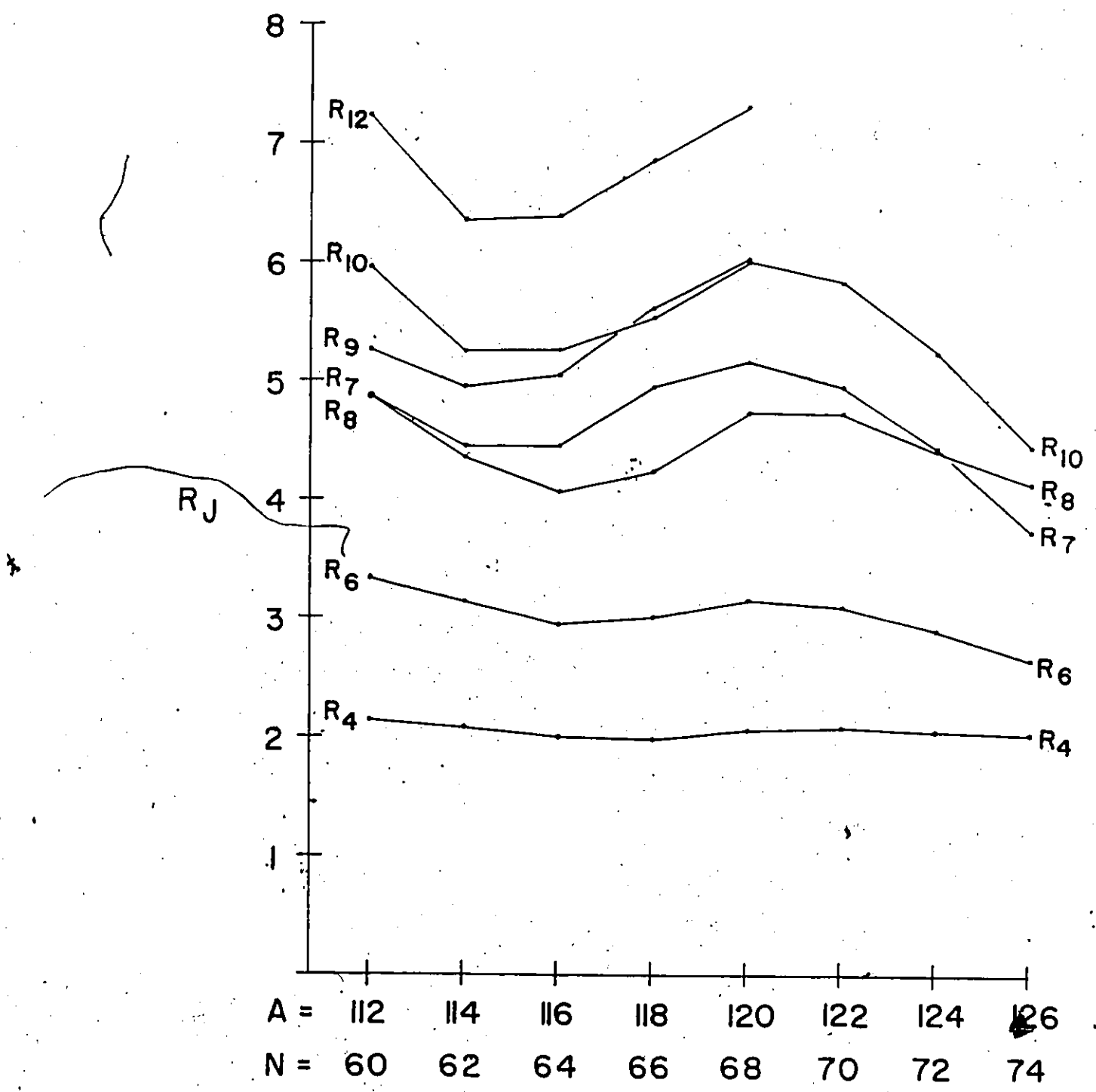
marks the end of the major neutron shell, the  $2^+$  state occurs at an energy of 1.279 MeV. The  $2^+$  and  $4^+$  energies decrease slightly from  $^{114}\text{Te}_{62}$  to  $^{112}\text{Te}_{60}$ , and this again is related to the nearby subshell closure at  $N=64$  due to the filling of the neutron  $1g_{7/2}$  and  $2d_{5/2}$  orbitals.

Two identical particles in a  $(g_{7/2}^2)$  or  $(g_{7/2}, d_{5/2})$  configuration can couple to a maximum spin of  $6^+$ . Already in  $^{126}\text{Te}_{74}$  the  $6^+-4^+$  spacing is less than in the middle of the shell, and certainly in  $^{134}_{52}\text{Te}_{82}$  the  $0^+-2^+-4^+-6^+$  spacing is what one would expect for two interacting  $g_{7/2}$  valence protons outside a  $Z=50, N=82$  inert core. In that isotope the  $6^+_1 \rightarrow 4^+_1$   $\gamma$  ray has an energy of only 115 keV, and the lifetime of the  $6^+$  state is 160 nanoseconds. However in the middle of the shell the  $0^+-2^+-4^+-6^+$  spacing is much more regular and vibrational-looking. Notwithstanding this collective behaviour, in general the  $6^+-8^+$  spacing is significantly larger than the average spacing below spin  $6^+$ , a difference which can be ascribed to a shell effect. Above the previously-mentioned  $(g_{7/2}^2)_{6^+}$  state the next two-particle positive-parity combinations are likely to be the  $(\nu h_{11/2}^2)_{8^+, 10^+}$  states. These are expected to occur significantly higher in energy (c.f. Section 5.2), giving rise to such a  $6^+-8^+$  gap.

Such shell effects may be seen more clearly by looking at energy ratios. In Figure 5.2 the  $R_J$ 's,  $R_J = E(J^+)/E(2^+)$ , are plotted for  $^{112-126}\text{Te}$ . The influence of

Figure 5.2

Excited-state energy ratios,  $R_J = E_J/E_{2^+}$ , for  $^{112-126}\text{Te}$ . The data are taken from the present work and references as noted in the caption for Figure 5.1.



the neutron sub-shell closure at  $N=64$  is seen in the pronounced minima near that neutron number. At  $^{126}\text{Te}$  features such as the proximity of  $R_8$  and  $R_{10}$  signal the onset of purer shell-model configurations.

The positive-parity states with spins  $10^+$  to  $16^+$  exhibit spacings similar to those of the  $0^+$  to  $6^+$  states, with another gap between the  $16^+$  and  $18^+$  levels. Since  $16^+$  is the highest spin attainable with either a  $(\nu h_{11/2}^2) \otimes (\pi g_{7/2}^2)$  or  $(\nu h_{11/2}^4)$  configuration, the  $10^+$  to  $16^+$  states may be expected to contain significant four-quasiparticle strength.

The  $10^+$  level energy is seen to decrease with increasing neutron number  $N$ , a tendency which would confirm the  $(\nu h_{11/2}^2)$  nature since the neutron Fermi level is getting closer to the  $\nu h_{11/2}$  orbital energy as  $N$  the number of neutrons increases. In contrast, the behaviour of the  $8^+$  level is generally more like that of the  $4^+$ . However in  $^{126}\text{Te}_{74}$  the  $8^+$  and  $10^+$  levels are only 208 keV apart, and their proximity supports the interpretation of both states having large  $(\nu h_{11/2}^2)$  components, although the  $B(E2)$  value for the connecting  $\gamma$ -ray transition is enhanced slightly over the two-neutron estimate (Ke71), indicating some collective or four-particle contribution. Theoretically,  $8^+$ ,  $10^+$ , ... levels in  $^{128-134}\text{Te}$ , closer to the end of the neutron shell, could well be purer shell-model states but they have not yet been observed experimentally.

There are a number of duplicate positive-parity states seen in the even-even Te isotopes (c.f. Figures 4.11, 4.18 and 4.26). These include non-yrast  $^{112,116}\text{Te}$   $10^+$  as well as  $^{114}\text{Te}$   $6^+$ ,  $8^+$  and  $10^+$  levels. Similar situations exist in  $^{118-122}\text{Te}$ . Spins of  $8^+$  and  $10^+$  have been tentatively assigned to weakly-fed states within 300 keV of each other in  $^{120,122}\text{Te}$ , for example, and identified with  $(\nu h_{11/2}^2)_{8^+,10^+}$  configurations (Ch82). Duplicate  $6^+$ ,  $8^+$  and  $10^+$  states in  $^{118,120}\text{Te}$ , which seem to have counterparts in  $^{114}\text{Te}$  but were not observed in  $^{112,116}\text{Te}$ , have been taken by Van Ruyven et al. (Va82) to indicate the coexistence of quadrupole and quasiparticle excitations.

The  $8_2^+$  and  $10_2^+$  states in  $^{114}\text{Te}$  are 412 keV apart, and considering the E2 transition rate  $E_\gamma^5$  factor the  $10_2^+ \rightarrow 8_2^+$  B(E2) is a factor of  $24 \pm 5$  larger than that for the  $10_2^+ \rightarrow 8_1^+$  832 keV  $\gamma$  ray. As well, the 596 keV  $12^+ \rightarrow 10_2^+$  transition is highly favoured over its 793 keV  $12^+ \rightarrow 10_1^+$  counterpart. It is surprising that with two competing structures producing close-lying levels with identical spin they are not mixed to a greater degree than that observed.

### 5.1.2 Negative-parity States

In this mass region only the  $1h_{11/2}$  "intruder" orbital has negative parity, and so any odd-parity levels may be expected to contain  $h_{11/2}$  strength. The  $^{112-126}\text{Te}$   $5^-$ ,  $7^-$ ,  $8^-$  and  $9^-$  levels show a gradual decrease in energy with

increasing neutron number instead of the minimum in the middle of the major shell displayed by the  $2^+$  states. Such behaviour indicates a non-collective character for these states, which can be formed by broken-pair  $(h_{11/2}, g_{7/2})9^- \dots 2^-$ ,  $(h_{11/2}, d_{5/2}^{-1})8^- \dots 3^-$ ,  $(h_{11/2}, d_{3/2})7^- \dots 4^-$  and  $(h_{11/2}, s_{1/2})6^-, 5^-$  configurations. The neutron  $h_{11/2}$  orbital is expected to be closer to the Fermi level than its proton counterpart (see Section 5.2) so these configurations should be neutron excitations (Ke71).  $7^-$ ,  $8^-$  and  $9^-$  states with spacings very similar to those in  $^{112-116}\text{Te}$  have been observed in even Sn isotopes and interpreted in a similar manner (Va80).

The  $8^-$  and  $9^-$  levels have negative-parity  $10^-$ ,  $12^-$  and  $11^-$ ,  $13^-$  structures respectively built on them with spacings similar to those in the  $0^+ - 6^+$  groups. As well, in  $^{112}\text{Te}$  these structures extend up to about spin 17 and there are gaps above the  $14^-$  and  $15^-$  levels reminiscent of the  $6^+ - 8^+$  spacing, leading to a possible interpretation of the  $8^- - 10^- - 12^- - 14^-$  and the  $9^- - 11^- - 13^- - 15^-$  "bands" as having similar configurations to the  $0^+ - 2^+ - 4^+ - 6^+$  ground-state "band" built on  $\nu(h_{11/2}, d_{5/2})8^-$  and  $\nu(h_{11/2}, g_{7/2})9^-$  broken-pair excitations.

In  $^{114}\text{Te}$  and  $^{116}\text{Te}$  the negative-parity bands were not observed up to as high spins. The  $^{114}\text{Te}$  5259.5 keV ( $12^-, 14^-$ ) level probably has spin  $14^-$ , by analogy to the 5201.3 keV  $14^-$  level in  $^{116}\text{Te}$ , and the resulting two  $14^- \rightarrow 12^-$  transition

energies of 435 and 494 keV are lower than the usual 600-800 keV band spacings. Based on the tentative  $14^-$  assignment to the  $^{114}\text{Te}$  5259.5 keV level, the 5433.6 keV state would have spin  $15^-$ , and so the  $9^-$ - $11^-$ - $13^-$ -( $15^-$ ) and  $8^-$ - $10^-$ - $12^-$ -( $14^-$ ) groups look quite similar in the two isotopes. The lower energies of the transitions between  $12^-$  and ( $15^-$ ) could be indicative of stronger single-particle j-j coupling influence for these bands in  $^{114,116}\text{Te}$  than in  $^{112}\text{Te}$ . Above the ( $15^-$ ) level in  $^{114}\text{Te}$  there is a gap of roughly 1 MeV until the next observed state, a feature also seen in  $^{112}\text{Te}$ .

## 5.2 Shell-model Description

Possible shell-model origins for some of the excited states in the even Te systems have already been alluded to in the previous section, but an explicit calculation may be instructive. As described in Section 2.1, a simple two-neutron and two-proton calculation was performed using a surface-delta residual interaction. The results appear in Figure 5.3, where they are compared to the experimental observations for  $^{114}\text{Te}$ . Some calculated states appearing well above those of identical spin shown in the diagram have not been included.

A number of discrepancies between this simple theory and experiment can be seen quite clearly. Not surprisingly, the theoretical positive-parity yrast states have nowhere near the relatively even spacing of the experimental yrast

Figure 5.3

Calculated shell-model states for  $A \sim 114$  Te. The single-particle energies and interaction strength used are given in Table 2.1.



levels. A realistic treatment of configuration mixing for the whole configuration space would not bring that about, and clearly some completely different interaction is necessary to produce these characteristic spacings.

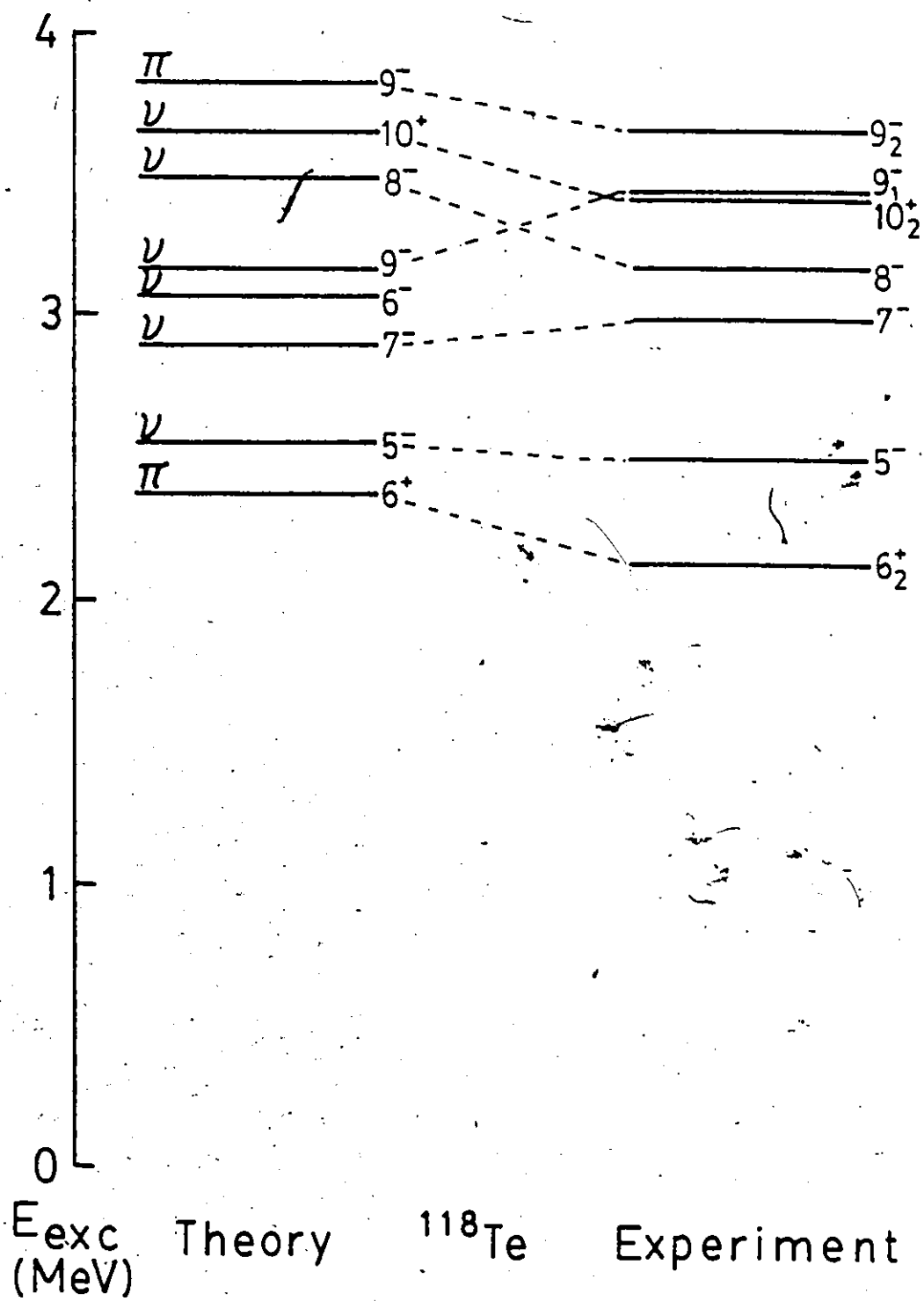
Secondly, neither the positions nor the relative order of the negative-parity  $7^-$ ,  $8^-$  and  $9^-$  states are reproduced well at all. Levels having virtually identical characteristics have been observed by Van Ruyven et al. (Va82) in  $^{118,120}\text{Te}$ , and interpreted as unpaired quasi-neutrons in predominantly either  $\nu(h_{11/2}, g_{7/2})$  or  $\nu(h_{11/2}, d_{5/2})$  configurations. However they were unable to obtain the correct  $7^-$ - $8^-$ - $9^-$  order, even using the more sophisticated approach of a Serber interaction within the number-projected two-quasiparticle model (c.f. Section 2.1). The results of that calculation, which include positive-parity two-quasiparticle states as well, are shown in Figure 5.4. The calculated  $9^-$  excitation energy is much lower than observed, while the theoretical  $8^-$  and  $7^-$  are too high. Also, the theoretical energies do not show the almost parallel decrease with increasing neutron number seen in  $^{112-118}\text{Te}$  and in the even Sn neutron analogues  $^{110-114}\text{Sn}$  (Va80).

The very simple formula of Chan et al. (Ch79) (see Equation [2.6]) for deriving excitation energies of two-particle states of maximum spin can be used to calculate some energies for expected shell-model states in Te nuclei.

Figure 5.4

Two-quasiparticle states in  $^{118}\text{Te}$  calculated by Van Ruyven et al. (Va82) using the P.B.C.S. model. The assigned configurations are:

$$\begin{aligned}6_2^+ &- \pi(g_{7/2}, d_{5/2}) \\5^- &- \nu(s_{1/2}, h_{11/2}) \\7^- &- \nu(d_{3/2}, h_{11/2}) \\6^- &- \nu(s_{1/2}, h_{11/2}) \\9_1^- &- \nu(g_{7/2}, h_{11/2}) \\8^- &- \nu(g_{7/2}, h_{11/2}) \\10_2^+ &- \nu(h_{11/2}^2) \\9_2^- &- \pi(g_{7/2}, h_{11/2})\end{aligned}$$



Unfortunately, information on the single-particle states in odd  $^{111-115}\text{Te}$  necessary for calculating neutron excitations is limited to the observation of  $7/2^+$ ,  $1/2^+$  and  $11/2^+$  states in  $^{115}\text{Te}$  (LS78). The excitation energy of the  $7/2^+$  relative to the  $1/2^+$  state (or visa versa) is not known, but they are quite close. Therefore using the energies given in Table 5.1, and based on the assumption that the  $7/2^+$ ,  $1/2^+$  and  $11/2^-$  states are basically  $\nu g_{7/2}$ ,  $\nu s_{1/2}$  and  $\nu h_{11/2}$  configurations, the excitation energies of the  $^{116}\text{Te}$   $\nu(h_{11/2}, g_{7/2})9^-$ ,  $\nu(h_{11/2}, s_{1/2})6^-$  and  $\nu(h_{11/2}^2)10^+$  states were calculated. Binding energies were taken from Wapstra and Bos (WB77). The experimental  $9^-$  and  $10^+$  energies, also listed in Table 5.1, are both closer to these results than S.D.I. energies (adjusted slightly for a  $^{114}\text{Te}$ - $^{116}\text{Te}$  shift in neutron Fermi level). This is not unexpected, since the previous shell-model calculation used single-particle energies appropriate for this region in general. A better method would be to use single-particle energies taken from suitable odd nuclei, however as has already been mentioned they are not always available for these neutron-deficient isotopes.

In the  $N > 82$  transitional region many of the states in  $^{148}_{64}\text{Gd}_{84}$  and  $^{150}_{66}\text{Dy}_{84}$  up to spin  $18^+$  have been assigned two- and four-quasiparticle configurations. Valence neutrons beyond the  $N=82$  closed shell play much the same role in that area as do valence protons beyond the  $Z=50$  closed shell in

Table 5.1

Shell-model calculation of two-particle states of maximum spin in  $^{116}\text{Te}$ , based on the formula of Chan et al. (Equation [2.6] Ch79).

Spin	Assumed Configuration	$^{116}\text{Te}$ Excitation Energy (MeV)		
		Eq'n. [2.6] Calculation	S.D.I.	Experiment
$10^+$	$\nu(h_{11/2}^2)$	3.28	4.52	3.58 <sup>a</sup>
$9^-$	$\nu(g_{7/2}, h_{11/2})$	3.00	2.46	3.43
$6^-$	$\nu(s_{1/2}, h_{11/2})$	3.00	4.50	<sup>a</sup>

The parameters used in Equation [2.6] are:

$$E_{\text{exc}}(^{115}\text{Te}; 7/2^+) = 0 \text{ MeV}$$

$$E_{\text{exc}}(^{115}\text{Te}; 1/2^+) = 0 \text{ "}$$

$$E_{\text{exc}}(^{115}\text{Te}; 11/2^-) = 0.28 \text{ "}$$

$$E_{\text{pair}} = 2.72 \text{ "}$$

<sup>a</sup> A  $6^-$  state was not observed in  $^{116}\text{Te}$ , but is seen in  $^{112}\text{Te}$  at an energy of 3.24 MeV.

the Sn region, evident by the collectivity induced by neutrons and protons respectively moving away from those two shell closures. Within that context  $^{148}_{64}\text{Gd}_{84}$  and  $^{150}_{66}\text{Dy}_{84}$  are analogous to  $^{116}_{52}\text{Te}_{64}$  and  $^{118}_{52}\text{Te}_{66}$ , but the Gd and Dy level spacings are more reminiscent of j-j coupling than are the more even spacings in the Te nuclei.

Figure 5.5 shows the states in  $^{148}\text{Gd}$  given shell-model assignments by Lunardi *et al.* (Lu79). The  $0^+ - 2^+ - 4^+ - 6^+$  and  $10^+ - 12^+ - 14^+ - 16^+$  level patterns are clearly different from their  $^{112,116}\text{Te}$  counterparts. As well, the availability of a  $j=9/2$  orbital in the Gd case ( $\nu h_{9/2}$ ) leads to  $(j_1=7/2, j_2=9/2)_8^+$  and  $(h_{11/2}^2) \otimes (j_1=7/2, j_2=9/2)_{18}^+$  combinations not possible for Te isotopes without the inclusion of the  $\pi g_{9/2}^{-1}$  hole in the configuration space, a step which is not indicated by the simple shell-model calculation undertaken in the present work.

### 5.3 Vibrational Model

As discussed in Section 2.2 the vibrational model in its simplest form predicts yrast states of spin  $0^+, 2^+, 4^+$  etc. spaced equidistant in energy, separated by the quadrupole vibrational phonon energy  $\hbar\omega_2$ . Such a spectrum is shown in Figure 5.6 compared to the positive-parity states observed in  $^{112}\text{Te}$ . The phonon energy was taken from the  $0^+ - 2^+ - 4^+$  spacings. An anharmonic vibrational spectrum is also shown

Figure 5.5

Shell-model configurations in  ${}^{148}_{64}\text{Gd}_{84}$ . Reproduced  
from Lunardi et al. (Lu79).



in the same Figure, using parameters derived from the  $^{112}\text{Te}$   $2^+$  and  $4^+$  levels, as in Equation [2.7].

Clearly this very basic model can reproduce neither the somewhat uneven spacings between successive levels, nor the locations of the higher-spin states, using either a harmonic or an anharmonic approach. In spite of this, the positive-parity levels of  $^{112}\text{Te}$  may retain a degree of vibrational influence even at high spins, since the level spacings remain fairly large ( $> 600$  keV) and do not show either clear-cut rotational tendencies or purely single-particle characteristics.

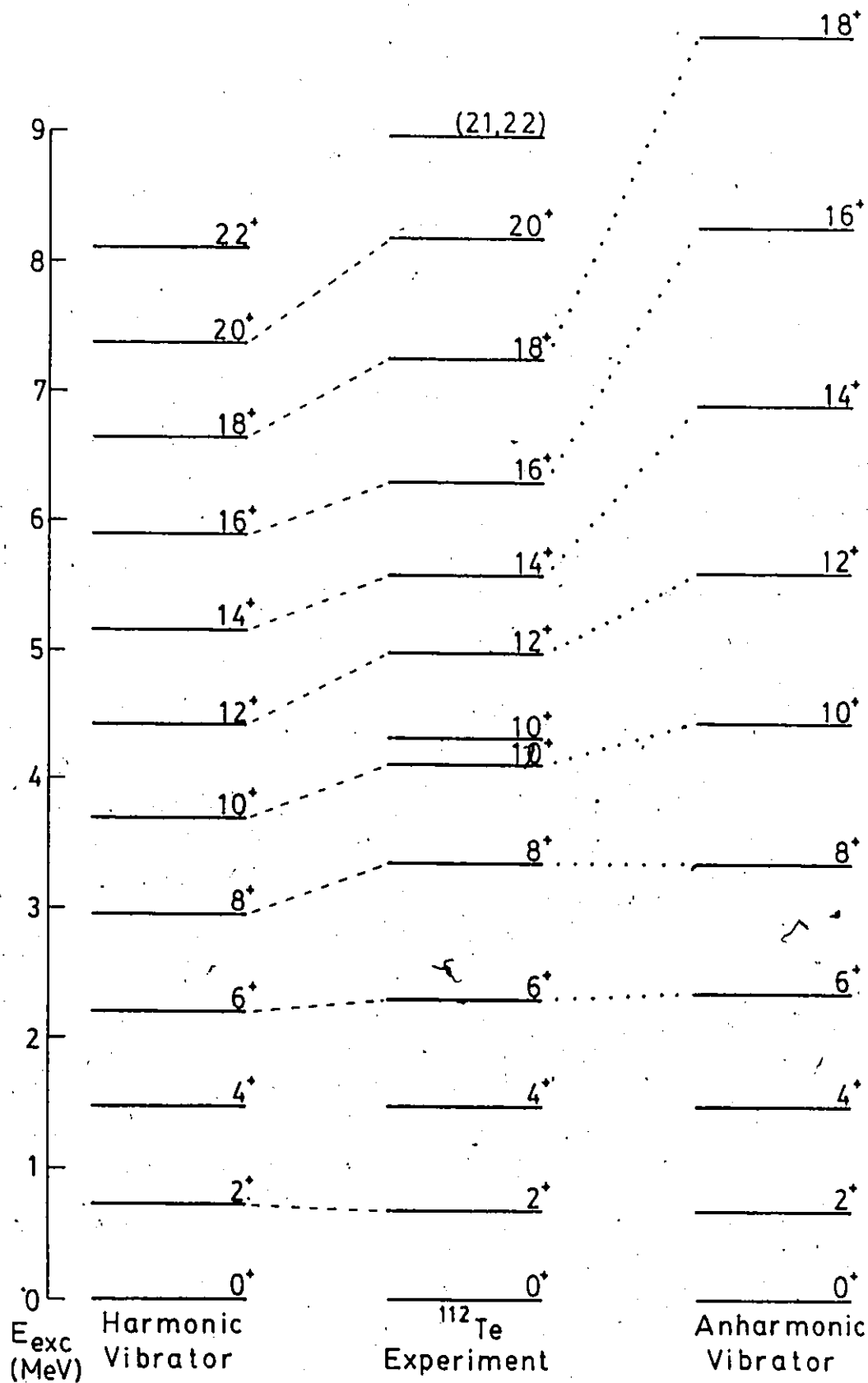
Although comparisons for  $^{114,116}\text{Te}$  similar to those in Figure 5.6 are not shown, the same general comments apply. The data for  $^{114}\text{Te}$ , though on the average fitting a harmonic vibrational pattern better than  $^{112}\text{Te}$ , contain irregularities and duplicate  $6^+$ ,  $8^+$  and  $10^+$  states, features the simple picture is incapable of reproducing.

#### 5.4 Pairing-plus-Quadrupole Model

As discussed in the previous sections, the level schemes of even-even Te isotopes systematically exhibit shell-model as well as collective vibrational influences. These excitation degrees of freedom are both included in the pairing-plus-quadrupole model covered in Section 2.3, involving two valence protons in  $50 < Z < 82$  single-particle

Figure 5.6

Vibrational model predictions compared to the  
experimental  $^{112}\text{Te}$  positive-parity level scheme:



orbitals coupled to the collective vibrational motion of the core.

Lopac has calculated (Lo70) a number of properties for some of the Te nuclides, and obtained fairly good agreement with experiment for level energies, quadrupole moments of the  $2^+$  states and some electromagnetic transition probabilities. Details of Lopac's procedure, including parameters, are given in Section 2.3. It should be noted that the calculation was performed using identical single-particle energies, vibrational phonon energies and pairing strengths for a range of nuclei, allowing only the particle-phonon coupling parameter  $a_2$  to vary as a genuine free parameter.

Both that calculation and the similar theoretical treatment by Degrieck and Vanden Berghe (DV74) only considered proton pair single-particle excitations coupled to the core vibrational motion in the description of positive-parity states up to medium spin. This is quite reasonable, in view of the following:

1) The systematics of Te low-spin excitations vary only slowly with neutron number, and near the neutron closed shell appear to be fairly pure proton shell-model states.

2) Low-spin states in  $^{122,124}\text{Te}$  were observed by Aublé and Ball (AB72) using the  $^{121,123}\text{Sb}(^3\text{He},d)$  reactions, which are expected to populate levels having significant two-proton strength. Degrieck and Vanden Berghe obtained good agreement

for spectroscopic strengths between the experimental data and their two-proton core vibration coupling model.

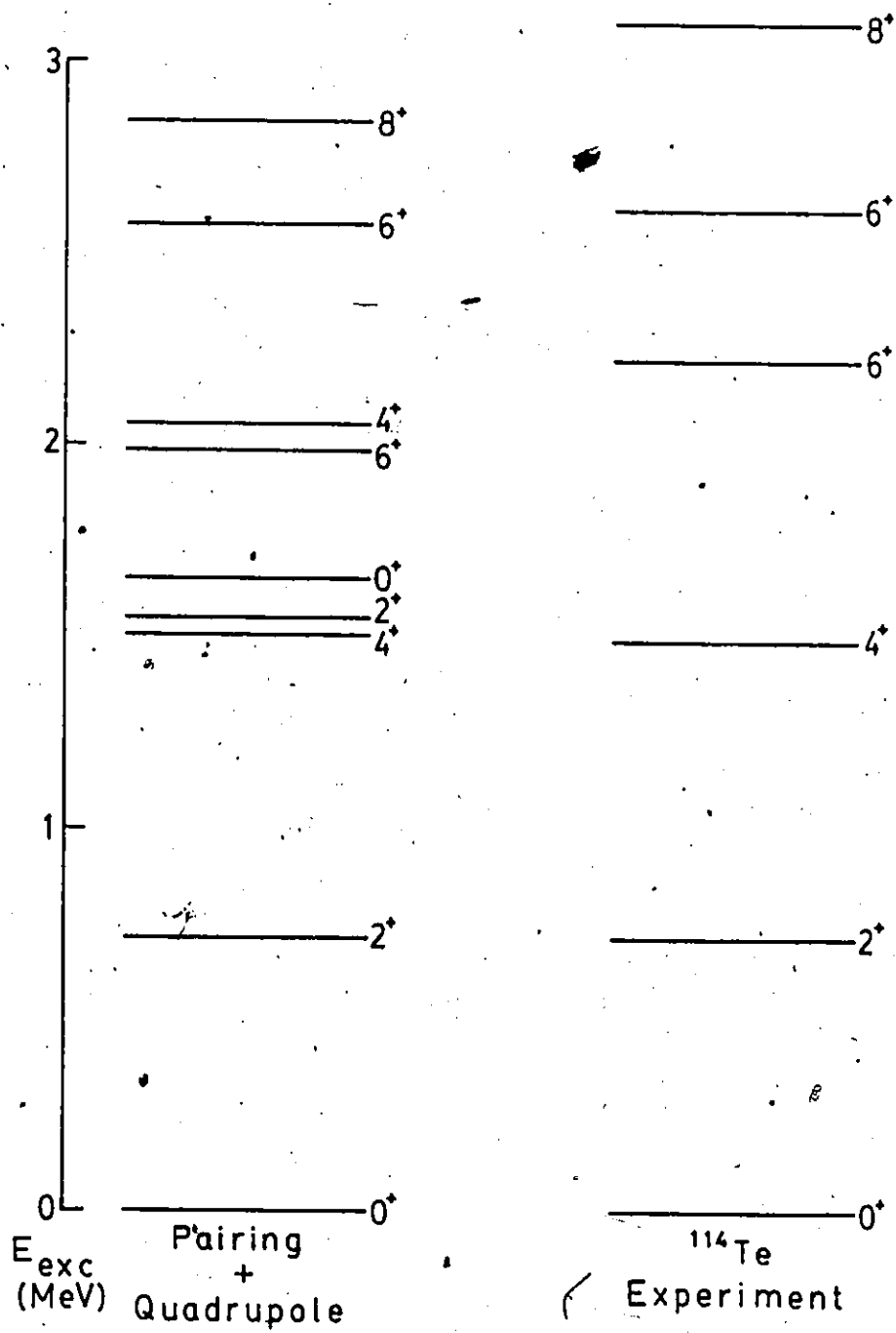
3) Lopac has calculated quadrupole moments using wavefunctions constructed of linear combinations of phonon and single-particle wavefunctions, and found that the negative sign of  $Q(2^+)$  was explained by significant contributions due to various proton orbitals.

The results of Lopac's calculation, corresponding to  $a_2 = 0.5$  MeV, are shown in Figure 5.7, along with the low-spin part of the  $^{114}\text{Te}$  level scheme. Lopac's results do not extend to high spins, and in fact the model as outlined cannot be expected to explain the structure at higher energies due to its lack of neutron single-particle excitation degrees of freedom. Since calculations of this type were not carried out in the present work, detailed differences between the  $^{112-116}\text{Te}$  isotopes which could be related to single-particle energy adjustments, for example, are not addressed here. Nevertheless some important features emerge from this basic comparison:

1) The model predicts that the  $6^+-8^+$  energy difference should be larger than the  $6^+-4^+$ ,  $4^+-2^+$  and  $2^+-0^+$  spacings, an effect which is seen in all the even-even Te nuclides. This is in fact slightly over-emphasized by the calculation, resulting in a  $6^+-4^+$  spacing more like that in  $^{126}\text{Te}$  than in the neutron-deficient  $^{112-116}\text{Te}$  isotopes.

Figure 5.7

Pairing-plus-quadrupole level scheme due to Lopac  
(Lo71) compared to experimental states up to  $8^+$  in  
 $^{114}\text{Te}$ .



2) The duplicate low-spin states seen in some nuclides, for example  $6^+$  states in  $^{114}\text{Te}$ , are reproduced by the model, although not precisely at the observed energies.

3) Wavefunctions extracted by Lopac show the  $0^+$  ground state and  $6^+$  level as being dominated by two-particle configurations, while for the  $2^+$  and  $4^+$  states collective components are more important. This description agrees with the systematic behaviour of these levels.

In the case of  $^{124}\text{Te}$  quadrupole moments for the yrast  $2^+$ ,  $4^+$ ,  $6^+$  and  $8^+$  levels were calculated by Lopac and found to be consistently large and negative.. As well, the calculated E2 matrix elements for transitions within this group were found to be significantly greater than for those proceeding to non-yrast levels, resulting in band-type structures. Based on these considerations, Lopac raised the possibility of a stable deformation, indicating that the particle-cluster vibration coupling may produce a transitional situation between spherical and well-deformed nuclei.

The pairing-plus-quadrupole type of model, with its inclusion of single-particle as well as collective degrees of freedom, seems to be a reasonable way of explaining the properties of many even-even Te isotopes at low spins ( $<8^+$ ) and therefore at excitation energies up to about 3 MeV. Due to the absence of neutron single-particle excitations the following are neglected:

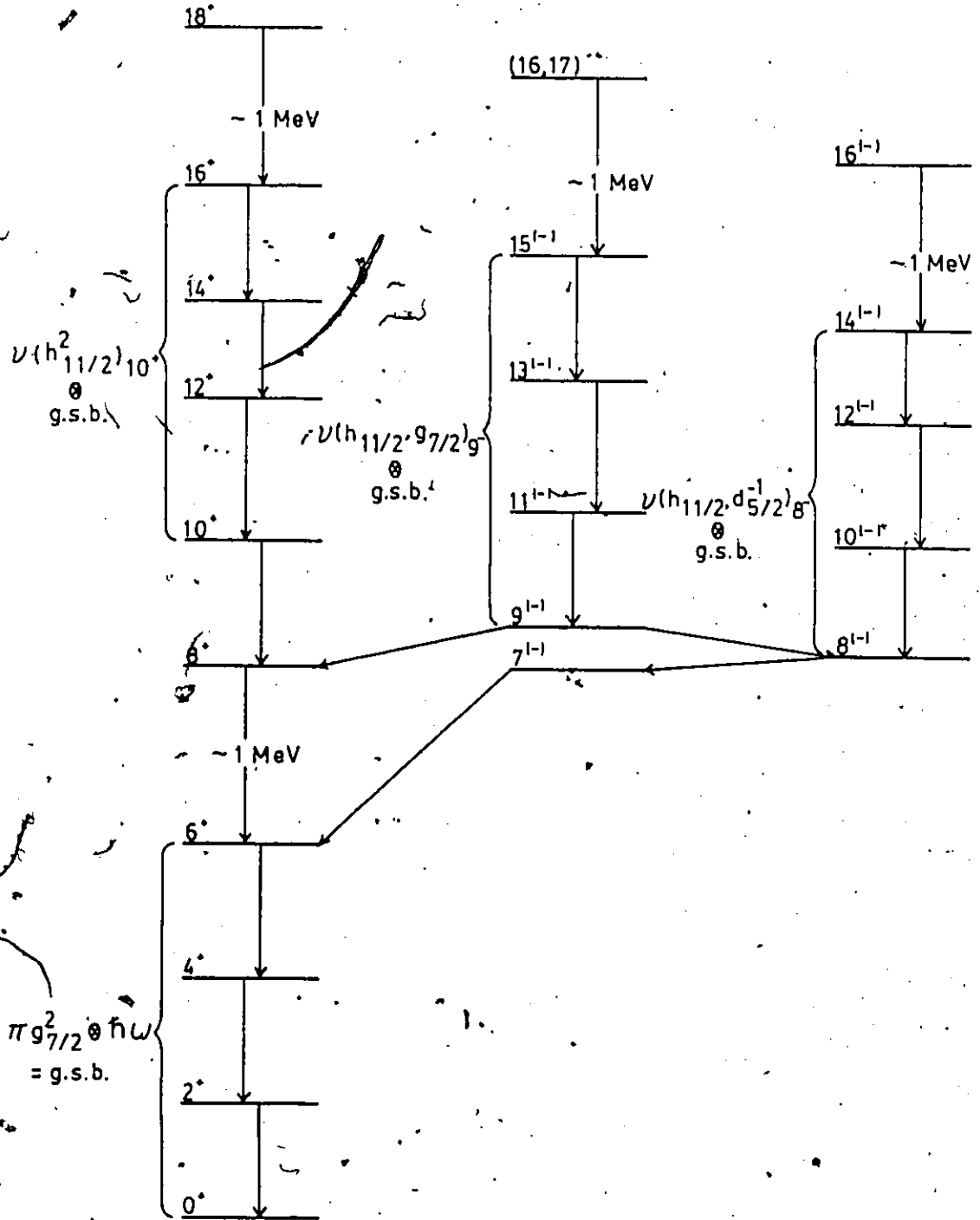
(i) yrast negative-parity states such as  $\nu(h_{11/2}, g_{7/2})_9^-$ , and:

(ii) positive-parity configurations such as  $\nu(h_{11/2}^2)_10^+$ , both of which should be favoured as yrast over the analogous proton configurations. However the higher-spin structure could well be due to neutron pair configurations coupled to the pairing-plus-quadrupole excitations responsible for low-spin structure. In the simplest picture this would result in band-type structures with spacing similar to the  $0^+-2^+-4^+-6^+$  "bands", built on states having configurations such as  $\nu(h_{11/2}, g_{7/2})_9^-$ ,  $\nu(h_{11/2}, d_{5/2}^{-1})_8^-$  and  $\nu(h_{11/2}^2)_10^+$ . In fact this type of effect can be seen in the level schemes of the  $^{112}, ^{114}, ^{116}\text{Te}$  nuclei studied in the present work. The pattern is perhaps clearest in  $^{112}\text{Te}$ ; the pertinent parts of its level structure within this interpretation are shown in Figure 5.8.

Within such a framework the  $0^+-2^+-4^+-6^+$  group of states has a  $\pi(g_{7/2}^2) \otimes h\omega$  configuration, while the  $10^+-12^+-14^+-16^+$  group has the same structure but based on the  $\nu(h_{11/2}^2)_10^+$  state, i.e.  $\nu(h_{11/2}^2)_10^+ \otimes \{\pi(g_{7/2}^2) \otimes h\omega\}$ . Similarly, the  $8^--10^--12^--14^--$  and  $9^--11^--13^--15^--$  quasi-bands can be thought of as  $\nu(h_{11/2}, d_{5/2}^{-1})_8^- \otimes \{\pi(g_{7/2}^2) \otimes h\omega\}$  and  $\nu(h_{11/2}, g_{7/2})_9^- \otimes \{\pi(g_{7/2}^2) \otimes h\omega\}$  configurations respectively. Gaps above the  $6^+$ ,  $16^+$ ,  $14^-$  and  $15^-$  states are due to an inability to generate more spin from the appropriate single-particle configurations, and are thus predominantly shell effects.

Figure 5.8

Interpretation of  $^{112}\text{Te}$  level scheme in terms of pairing-plus-quadrupole and neutron excitations.



### 5.5 Interacting Boson Approximation

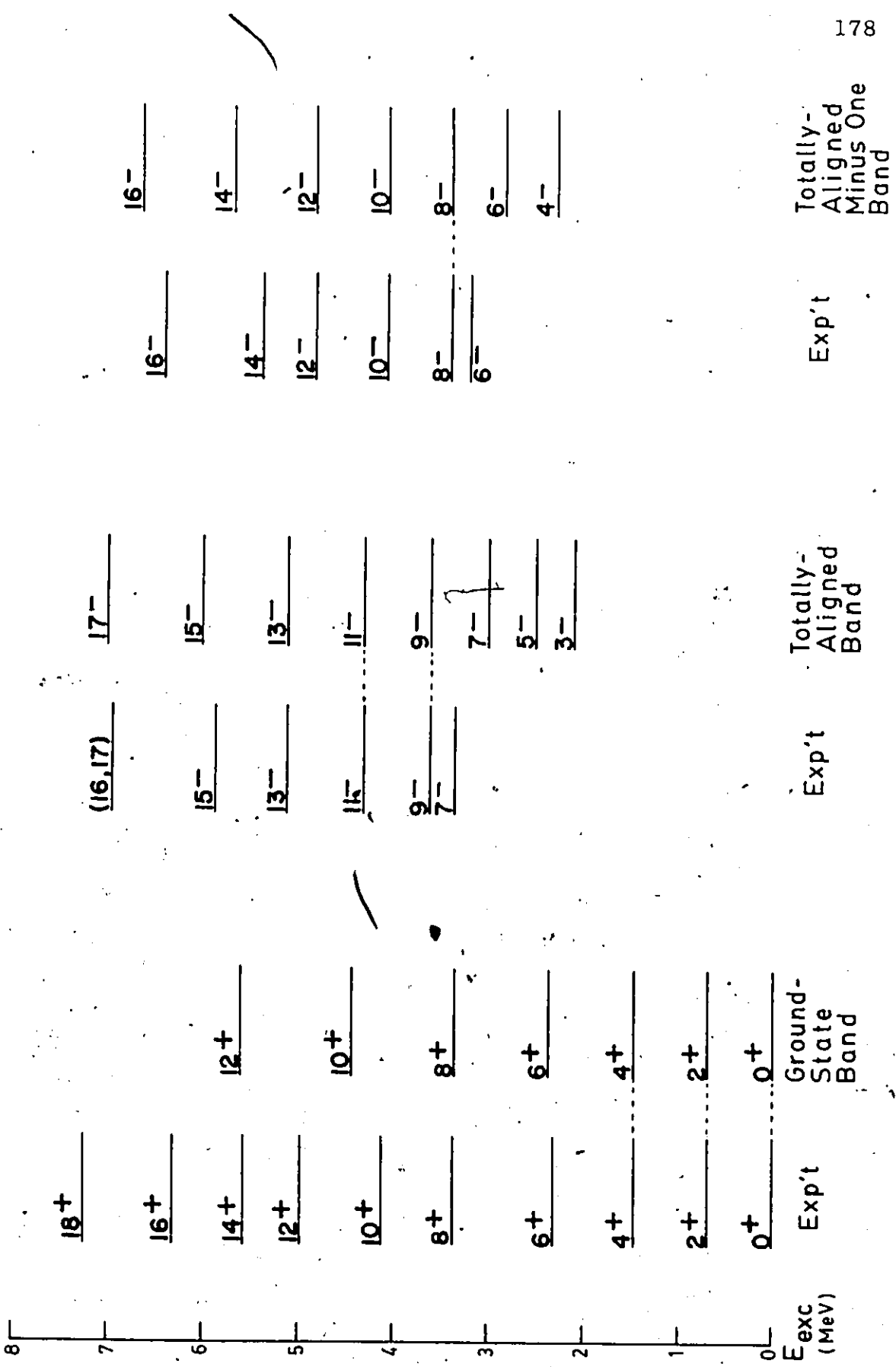
The vibrational SU(5) limit of the I.B.A., discussed in Section 2.4, results in some very simple expressions for energy levels and transition probability ratios, given by Equations [2.16] to [2.21]. As mentioned previously the ground-state band energies are identical to those of an anharmonic vibrator. Parameters for energies of the "totally-aligned" and "totally-aligned minus one" bands were obtained for  $^{112}\text{Te}$  by identifying the  $9^-$ ,  $11^-$  and  $8^-$  states as members of those respective bands. The resulting calculated level scheme is shown in Figure 5.9, together with the experimentally-observed states.

Positive-parity states produced by the anharmonic vibrator expression corresponding to the ground-state band energies in this picture clearly diverge from the experimental results above spin  $8^+$ , and for  $^{114,116}\text{Te}$  the disagreement is obvious even at lower spins.

Concerning negative-parity states, above the  $9^-$ - $11^-$  and  $8^-$  levels used to fit the model the band spacings are not too dissimilar, although the tendency will be for spacings to increase steadily with spin; so the drastic divergence seen in the ground-state band may just not be apparent yet in the others. That point aside, the calculated  $9^-$ - $7^-$  and  $8^-$ - $6^-$  energies do not agree with experiment at all, emphasizing the uniqueness of the observed  $9^-$  and  $8^-$  states as bandheads of some sort.

Figure 5.9

Calculated I.B.A. level scheme for  $^{112}\text{Te}$  compared to the experimental results. Levels used to determine the band parameters are connected with dashed lines.



Totally-  
Aligned  
Minus One  
Band

Exp't

Totally-  
Aligned  
Band

Exp't

Ground-  
State  
Band

Exp't

$E_{exc}$   
(MeV)

The transition probability ratio described by Equation [2.20], relating E2 transitions within the totally-aligned band to those E1 crossing transitions to the ground-state band, varies only as  $(n+1)/n$ , where  $J=2n$  for the g.s.b. Thus:

$$R_{tg}(9^-) \equiv \frac{\text{Rate}(9^- \rightarrow 8^+)}{\text{Rate}(9^- \rightarrow 7^-)} = K(9^-) \frac{B(E1; 9^- \rightarrow 8^+)}{B(E2; 9^- \rightarrow 7^-)} = K(9^-) \frac{4}{3} c \quad [5.1]$$

and:

$$R_{tg}(11^-) \equiv \frac{\text{Rate}(11^- \rightarrow 10^+)}{\text{Rate}(11^- \rightarrow 9^+)} = K(11^-) \frac{B(E1; 11^- \rightarrow 10^+)}{B(E2; 11^- \rightarrow 9^-)} = K(11^-) \frac{5}{4} c \quad [5.2]$$

where the K's contain the  $\gamma$ -ray energy and multipolarity dependence, and c is a constant for a given nucleus. Using the appropriate  $\gamma$  rays in  $^{112}\text{Te}$ :

$$\begin{aligned} \frac{K(9^-)}{K(11^-)} &= \left( \frac{E_{9^- \rightarrow 8^+}}{E_{11^- \rightarrow 10^+}} \right)^3 \left( \frac{E_{9^- \rightarrow 7^-}}{E_{11^- \rightarrow 9^-}} \right)^5 \\ &= 294 \end{aligned} \quad [5.3]$$

Therefore:

$$\frac{R_{tg}(9^-)}{R_{tg}(11^-)} = \frac{K(9^-)}{K(11^-)} \frac{4}{3} \frac{4}{5} = 315 \quad [5.4]$$

Experimentally, assigning reasonable limits to the lowest intensity observable:

$$R_{tg}(9^-) > 8.5$$

$$R_{tg}(11^-) < 0.1$$

[5.5]

and thus:

$$\frac{R_{tg}(9^-)}{R_{tg}(11^-)} > 85$$

[5.6]

which certainly includes the I.B.A. ratio [5.4]. Similar values can be calculated for  $^{114,116}\text{Te}$  and are shown in Table 5.2. The end result is that since some  $\gamma$ -ray intensities are below the experimental detection limit, these ratios cannot conclusively condemn or confirm the model, although the experimental and theoretical ratios for  $^{114}\text{Te}$  are clearly contradictory.

Van Ruyven et al. reported fairly good agreement between ground-state band excitation energies and their I.B.A.-2 calculations for  $^{118,120}\text{Te}$  up to spins  $14^+$  and  $12^+$  respectively; clearly better agreement than can be obtained from the basic SU(5) limit. However, they noted that the experimental excitation energies have irregularities which cannot be reproduced by a collective quadrupole treatment alone, reiterating the need for two-quasiparticle-core coupling in order to fully explain the observed level spacings. In addition, the problem of termination at high spins is still present.

Table 5.2

Experimental vs. I.B.A.  $\gamma$ -ray transition ratios.

Nucleus	$R_{tg}(9^-)/R_{tg}(11^-)$	
	Experiment	I.B.A.
$^{116}\text{Te}$	> 23	28
$^{114}\text{Te}$	> 83	21
$^{112}\text{Te}$	> 85	315

## 5.6 Variable Moment-of-Inertia and Variable Anharmonic Vibrator Models

These two very similar models, described in Section 2.5, are phenomenological in origin and in that sense are more an indication of a nucleus's symptoms rather than an underlying cause for its behaviour. As mentioned in Section 5.4, pairing-plus-quadrupole calculations in some heavier Te isotopes (eg. Lo70) point towards a  $0^+-2^+-4^+-6^+-8^+$  quasi-band, a situation in which the V.M.I. and V.A.V.M. could well be applicable.

Given starting values of  $\mathcal{J}_0$  and C obtained from nearby nuclei, V.M.I. Equations [2.23] and [2.25] were used in an iterative manner to arrive at parameters for  $^{112-116}\text{Te}$ , as listed in Table 5.3. The theoretical  $2^+$  and  $4^+$  energies only were matched to experimental values, in keeping with the philosophy that in these models the ground-state band behaviour should be determined by the characteristics of the nucleus at low spin. In the case of the V.A.V.M.,  $R_6 = E(6^+) / E(2^+)$  for  $^{114}\text{Te}$  and  $^{116}\text{Te}$  were both lower than the range of validity for the model and so Equations [2.30] and [2.31] were solved iteratively for  $^{112}\text{Te}$  alone, to obtain values for  $a$ ,  $\theta_0$  and C as seen in Table 5.3. Also included in the Table are parameters for the nearby transitional  $^{110}\text{Cd}$  and  $^{116}\text{Xe}$  nuclides, as well as for  $^{180}\text{Hf}$ , considered to be a good rotor.

Table 5.3

V.M.I. and V.A.V.M. parameters for  $^{112-116}\text{Te}$  and a few comparison nuclei.

Nucleus	$R_4$	$R_6$	$D_0$ ( $\text{MeV}^{-1}$ )	$C$ ( $10^{-3}\text{MeV}^{-3}$ )	$a$ ( $\text{MeV}$ )	$\theta_0$ ( $\text{MeV}^{-1}$ )	$C_{\text{VAVM}}$ ( $10^{-3}\text{MeV}^{-3}$ )
$^{112}_{52}\text{Te}_{60}$	2.14	3.34	-1.6	7.2	0.345	50.3	0.015
$^{114}_{52}\text{Te}_{62}$	2.09	3.13 <sup>1)</sup>	-3.1	6.1			
$^{116}_{52}\text{Te}_{64}$	2.00	2.95 <sup>1)</sup>	-8.7	3.0			
$^{110}_{48}\text{Cd}_{62}$	2.34	3.77	1.0	12.1			
$^{116}_{54}\text{Xe}_{62}$	2.33	3.90	1.5	2.8			
$^{180}_{\text{Hf}}^{2)}$	3.31	6.87	32.0	13.8	0.047	65.1	1.9

1) These values of  $R_6$  are outside the V.A.V.M. range of validity.

2) Parameters for  $^{180}\text{Hf}$  are best-fit values taken from Sc76 (V.M.I.) and BK84 (V.A.V.M.)

Using these values energy levels for higher spins were calculated, and are shown in Figure 5.10 along with the yrast positive-parity levels of  $^{112-116}\text{Te}$ . Both theoretical models exhibit gradually-increasing level spacings as a function of spin, the V.M.I. model certainly more so, even in the case of  $^{116}\text{Te}$  where  $R_4=2.00$ , the value for a vibrational  $E=n\hbar\omega$  nucleus. The V.M.I. clearly diverges substantially from experiment at spins as low as  $6^+$ . A fit to all the experimental ground-state band levels would cut down on the divergence but not address the fundamental disagreement between the form of V.M.I.-type solutions and the more irregular observed level energies. The V.A.V.M. does better in the only valid case of  $^{112}\text{Te}$ , but the same comment applies.

The variable moment-of-inertia model and its generalized derivatives (c.f. BK84) do a much better job describing nearby transitional Cd ( $Z=48$ ) and Pd ( $Z=46$ ) nuclei, where  $R_4$  values are typically in the vicinity of 2.3. As shown in Figure 5.11, the structure of these nuclei have been broken down (eg. Si80) into bands displaying V.M.I.-like spacings, based on  $0^+$  (g.s.),  $10^+$ ,  $9^-$  and  $8^-$  band-heads. Using the theoretical model of Flaum and Cline (FC76) a more fundamental description of these bands by Samuelson et al. (Sa79) characterizes them as Coriolis-decoupled rotational bands based on zero-quasiparticle ( $0^+$ ) and neutron two-quasiparticle ( $10^+$ ,  $9^-$  and  $8^-$ ) states, as labelled in the Figure. Recent lifetime measurements of  $\gamma$ -ray transition

Figure 5.10

Calculated V.M.I. and V.A.V.M. ground-state bands  
for  $^{112-116}\text{Te}$ . Levels used to determine the band  
parameters are connected with dashed lines.



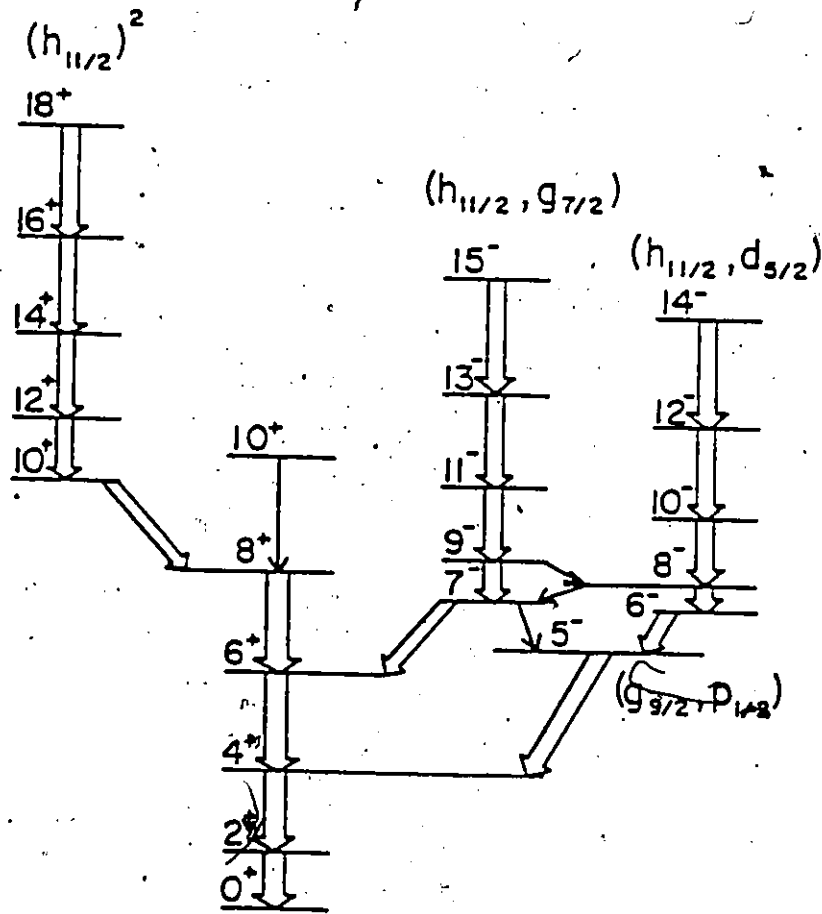
v

6	16*	14*	16*	14*	16*
5	12*	12*	14*	12*	14*
4	10*	10*	12*	10*	12*
3	8*	8*	8*	8*	8*
2	6*	6*	6*	6*	6*
1	4*	4*	4*	4*	4*

0	0*	0*	0*	0*	0*
E <sub>exc.</sub> (MeV)		V.A.V.M.		V.M.I.	
		112Te		114Te	
		Exp't		Exp't	
		V.M.I.		V.M.I.	

Figure 5.11

Typical slightly-deformed rotor spectrum for even-even transitional  $Z < 50$  nuclei, taken from Simms et al. (Si80).



strengths (An85) confirm this picture, and have led to the more specific classification of the negative-parity structures as  $9^-$ - $11^-$ -... completely-aligned  $\nu(h_{11/2}, g_{7/2})$  and  $8^-$ - $10^-$ -... semi-decoupled  $\nu(h_{11/2}, d_{5/2})$  bands.

The groups into which the level structure of Figure 5.11 has been partitioned are strikingly similar to those identified in  $^{112-116}\text{Te}$  (c.f. Figure 5.8), based on band-heads of identical spin, viz.  $0^+$ (g.s.),  $10^+$ ,  $9^-$  and  $8^-$ . However the energy level spacings are clearly not the same and the rotational picture cannot be extended to the  $Z=52$  Te transition region.

### 5.7 High-spin States

Although there are no clear-cut collective rotational bands in  $^{112-116}\text{Te}$ , bands having some rotational character based on 4p-2h excited  $0^+$  states may be indicated by the presence of  $(g_{9/2}^{-1})$  proton-hole excitations in Sb ( $Z=51$ ) and I ( $Z=53$ ) nuclei (eg. Sh79, Sh82, Ga82), as well as by the observation of 2p-2h bands in even-even Sn ( $Z=50$ ) isotopes (Br79). The moments of inertia extracted using the  $E=(\hbar^2/2J)J(J+1)$  formula from yrast  $8^+$ - $12^+$  spacings for  $^{112-120}\text{Te}$ , the only isotopes for which this information is available, are shown in Table 5.4. It can be seen that the  $^{116,118}\text{Te}$  values are similar to analogous moments taken from  $^{114,116}\text{Sn}$ , also appearing in that Table, as Chowdhury *et al.* have pointed out (Ch82). However, there is worse agreement in the cases of

Table 5.4

Moments of inertia obtained from  $8^+ - 12^+$  level spacings.

Nuclide	$2J/n^2$ (MeV <sup>-1</sup> )
<sup>112</sup> Te	51.9
<sup>110</sup> Sn	1)
<sup>114</sup> Te	58.5
<sup>112</sup> Sn	52.3
<sup>116</sup> Te	53.4
<sup>114</sup> Sn	50.1
<sup>118</sup> Te	52.6
<sup>116</sup> Sn	50.1
<sup>120</sup> Te	58.3
<sup>118</sup> Sn	49.8

1) The 2p-2h band is not seen in <sup>110</sup>Sn (Va80), presumably because the negative-parity states become clearly yrast at that neutron number.

$^{114}\text{Te}$  vs.  $^{112}\text{Sn}$  and  $^{120}\text{Te}$  vs.  $^{118}\text{Sn}$ , leading to some doubt as to whether the Te yrast  $8^+$  and  $12^+$  states can in general be interpreted as having significant rotational character. The 4p-2h band picture is supported in  $^{120}\text{Te}$  and  $^{122}\text{Te}$  by the existence of non-yrast  $0^+$ ,  $(2^+)$ ,  $4^+$ ,  $6^+$  and  $4^+$ ,  $6^+$  levels in those respective isotopes, with smaller spacings than higher spin, and also weakly-fed extra  $(8^+)$  and  $(10^+)$  levels lying within 300 keV of each other. These latter pairs of states were taken to be largely  $\nu(h_{11/2}^2)_{8^+,10^+}$  in nature by Chowdhury et al., indicating that the yrast  $8^+$  states could well have a more rotational character. Nevertheless duplicate states could be just as well explained, in a similarly qualitative manner at least, by the pairing-plus-quadrupole picture, where single-particle spins plus vibrational spins can add in more than one combination to produce a given spin, as shown in Figure 5.7.

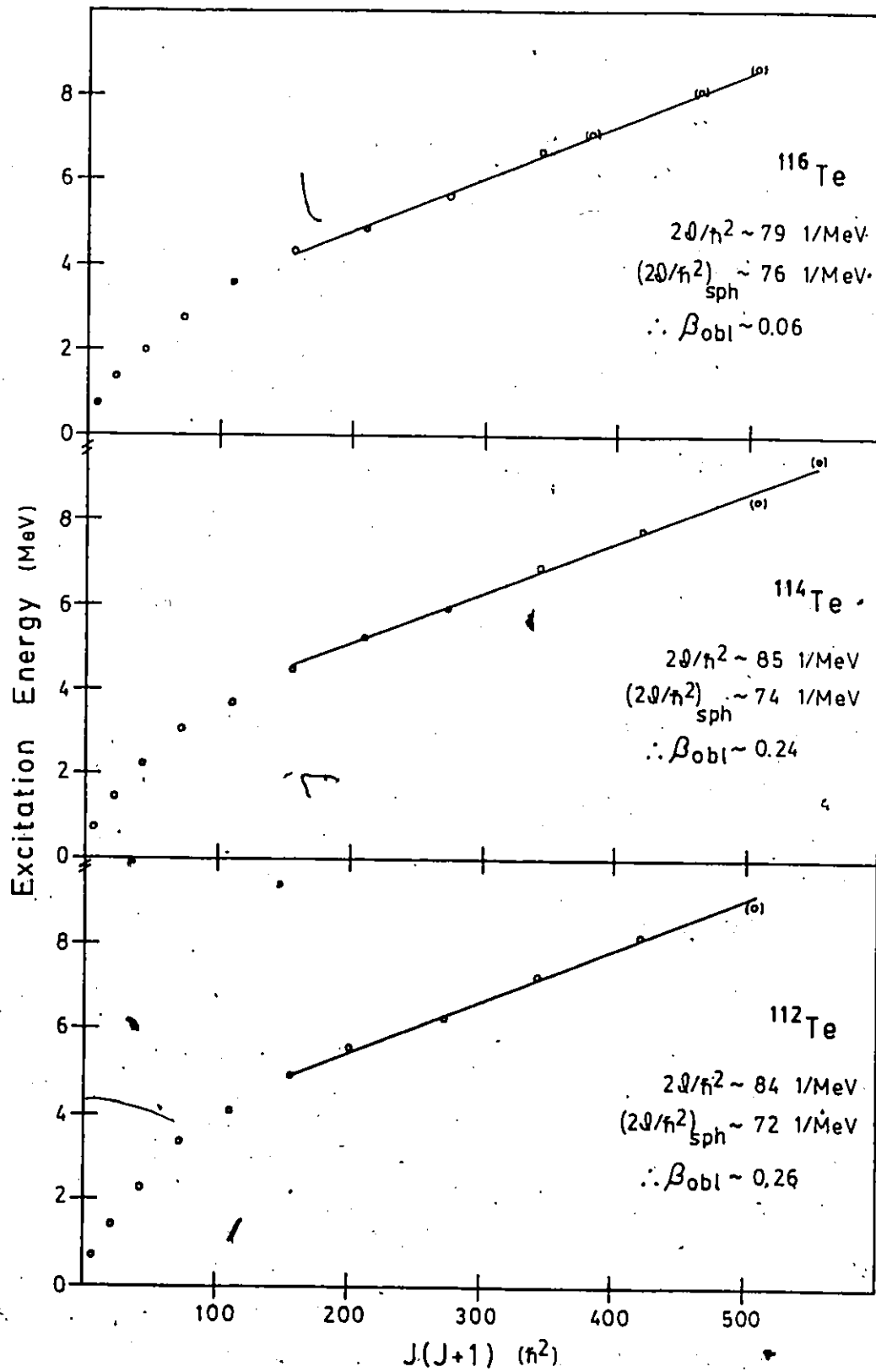
It is possible that the duplicate states seen in  $^{112}\text{Te}$  ( $10_2^+$ ),  $^{114}\text{Te}$  ( $6_2^+$ ,  $8_2^+$ ,  $10_2^+$ ) and  $^{116}\text{Te}$  ( $10_2^+$ ) arise from the competition between (a) single-particle states and states having large collective components, and/or (b) two different groups of states, both of the quasiparticle-plus-collective type. In order to analyse effectively a situation such as that in  $^{114}\text{Te}$ , where the  $12^+ \rightarrow 10_2^+ \rightarrow 8_2^+$  transitions are highly favoured over those corresponding to the normally more intense  $12^+ \rightarrow 10_1^+ \rightarrow 8_1^+$  yrast route, a more comprehensive

theoretical treatment which considers these situations is required.

At higher spins the shape changes and possible rotational effects discussed in Section 2.6 become applicable. Certainly the strikingly irregular transition energies seen in other nuclei exhibiting single-particle alignment about a symmetry axis (c.f.  $^{152}\text{Dy}$  (Kh78)) are not observed in  $^{112,114,116}\text{Te}$ . The question of yrast traps, also expected in this rotational picture, is still open, but upper limits of approximately 2 nanoseconds in  $^{112}\text{Te}$  and 20 ns in  $^{114,116}\text{Te}$  can be placed on yrast state lifetimes up to spins of about 20. The second limit is an estimate based on the non-observation of attenuated angular distribution coefficients in the yrast cascades of those nuclei: the coincidence resolving time results in a greater limit of roughly 50 ns. In the neighbouring  $^{118,120}\text{Te}$  isotopes only one isomer was detected by Van Ruyven et al. (Va82), that being the  $^{118}\text{Te}$  3189 keV  $8^-$  state which decays via a 189 keV  $\gamma$  ray to the  $7^-$  state, with a 0.23 ns lifetime. On the other hand, in the  $^{112-116}\text{Te}$  level schemes there does seem to be, on the average, a tendency for  $\Delta E/\Delta J$  to increase as a function of spin above  $J=12$  or so. Plots of excitation energy  $E_{\text{exc}}$  vs.  $J(J+1)$  for the positive-parity states, shown in Figure 5.12, can be fit by straight lines over the latter part of the data, as has been done for other nuclei suspected of this type of behaviour (eg. Kh78). (These high-spin data can also

Figure 5.12

Excitation energy vs.  $J(J+1)$  for high-spin states in  $^{112-116}\text{Te}$ . Points corresponding to levels having uncertain spin assignments have been placed in parentheses. Best-fit lines corresponding to  $E_{\text{exc}} \propto J(J+1)$  for  $J > 12$  have been drawn in.



be compared to an  $E_{\text{exc}} = \hbar\omega J/2$  vibrational-type function, although the fits as judged by the sum of squares of errors are overall a factor of two worse.) The slope of such an  $E_{\text{exc}}$  vs.  $J(J+1)$  plot, described by Equation [2.35], is just  $\hbar^2/2\mathcal{J}_{\text{rig}}$ , where  $\mathcal{J}_{\text{rig}}$  is the rigid-body moment of inertia for an oblate shape ( $\gamma=60^\circ$ ). The extracted  $2\mathcal{J}/\hbar^2$  values are also listed in Figure 5.12; and using Equation [2.40] and [2.34] were compared with rigid-body spherical values, resulting in  $\beta$ -deformation parameters of about 0.06 for  $^{116}\text{Te}$  and 0.25 for  $^{112,114}\text{Te}$ . The latter number is fairly large: the calculation by Andersson et al. (An76) described in Section 2.6 predicts  $\beta \sim 0.17$  for  $J=20$  in  $^{114,116}\text{Te}$ .

Simon et al. (Si79) have studied continuum  $\gamma$ -ray spectra at even higher spins following  $^{110}\text{Pd}(^{12}\text{C}, xn)\text{Te}$  and  $^{82}\text{Se}(^{40}\text{Ar}, xn)\text{Te}$  reactions over a range of beam energies, and concluded that  $^{118}\text{Te}$  exhibits non-rotational characteristics for  $J < 30$  and collective rotational behaviour above spin 40. The switch to collective rotation was inferred from the appearance of a significant E2 "bump" in the spectra as the input angular momentum was increased by raising the beam energy. This structural change is reproduced by the calculation of Bengtsson and Ragnarsson (BR85) as discussed in Section 2.6. Given the observed lack of low-energy transitions and clear isomers, no hard conclusions can really be made as to significant oblate deformations resulting from single-particle alignment at high spin in these nuclei. More

information over a larger range of spins, and accompanying measurements of lifetimes, and any possible static quadrupole moments (which are more sensitive to deformation (Ha84)) would be of interest.

## Chapter Six - Summary

In the present work high-spin states in the even-even transitional  $^{112}_{52}\text{Te}_{60}$ ,  $^{114}_{52}\text{Te}_{62}$  and  $^{116}_{52}\text{Te}_{64}$  nuclides have been observed following (H.I.,xnyp $\alpha$ ) reactions. Ground-state bands in  $^{114}\text{Te}$  and  $^{116}\text{Te}$ , previously known to spin ( $8^+$ ) and ( $12^+$ ) respectively, have been extended up to spins of (22,23) and ( $22^+$ ) respectively. As well, the ground-state band in  $^{112}\text{Te}$  has been identified in-beam for the first time, and established as far as spin  $20^+$ . Below about 7 MeV in excitation energy these positive-parity bands are all found to decay by means of stretched E2  $\gamma$  rays, although this could not be conclusively determined in  $^{116}\text{Te}$  due to the unresolved nature of the 511.4 keV ( $14^+$ )  $\rightarrow$   $12^+$  transition.

In addition, previously unknown  $7^{(-)}$ ,  $8^{(-)}$  and  $9^{(-)}$  states lying within 400 keV of each other have been observed in all three isotopes at excitation energies of approximately 4 MeV, similar to level triplets with identical spins and parity found in the Cd (Z=48) and Sn (Z=50) isotones. Bands built on the  $8^{(-)}$  and  $9^{(-)}$  states have been established, de-excited predominantly by stretched E2 transitions. The negative-parity states are more weakly fed than the positive-parity structures built on the ground state, although in the lightest isotope,  $^{112}\text{Te}$ , the  $9^{(-)}$  band is actually yrast in the spin range  $9^{(-)}$  to (16,17). Clearly

for these level structures definitive measurements of the  $7^{(-)}$ ,  $8^{(-)}$  and  $9^{(-)}$  parities, obtained from either electron conversion or  $\gamma$ -ray polarization studies, would be helpful. It was not possible to carry out those types of experiments during the present work.

As well as the nuclear structure information obtained in this study, the characteristics of some (H.I.,xnypza) reactions leading to a number of residual nuclei in this region have been examined and compared to the results of theoretical calculations from the statistical fusion-evaporation code ALICE82 (BB82). Generally the predictions of the code were not accurate and so were used only as a guide to probable exit channels.

In addition, a computer program for the deconvolution of complicated  $\gamma$ -ray spectra was developed and used as part of this project, and is described in the Appendix. The performance of SANDRA was compared to those of some other commonly-used data analysis methods, and the code has been found to be quite useful.

The spectroscopic results outlined in the present work represent a significant increase in the knowledge of level structures in the neutron-deficient Te nuclei. Together with the level schemes of  $^{118-122}\text{Te}$  deduced by Van Ruyven et al. (Va82) and Chowdhury et al. (Ch82) up to spin 14 or so, they provide a systematic picture of the yrast and

near-yrast level structures of these,  $Z > 50$  transitional nuclei. As indicated in the previous chapter a comprehensive theoretical treatment is still lacking; however, several features can be explained quite simply.

Collective quadrupole excitations play a major role in the structure of these nuclei, as shown by the  $^{112-130}\text{Te}$   $E_4^+/E_2^+$  values of 1.95 to 2.14, close to the harmonic vibrator limit. Although the strictly regular level spacings of the harmonic or the anharmonic vibrational model are not observed at higher spins, that does not preclude a significant degree of collective vibrational influence even up to approximately spin  $16^+$ . This conjecture is supported by the  $\gamma$ -ray transition energies, virtually all of which remain greater than 600 keV in both the positive- and the negative-parity bands.

The necessity of including quasiparticle excitations based on shell-model pair configurations is made evident by 1) consistently larger-than-average energy gaps in the band structures above spins corresponding to the maximum spins possible in reasonable shell-model configurations, 2) the clear distinction of the  $8^{(-)}$  and  $9^{(-)}$  states as band-heads, and 3) additional positive-parity levels which have different feeding patterns from those belonging to band members.

The pairing-plus-quadrupole model, incorporating collective harmonic vibrational as well as shell-model pairing interactions has been used by Lopac (Lo70) and Degrieck

and Vanden Berghe (DV74) in order to describe a broad range of  $A > 118$  Te isotopes, and their results for states up to spin  $8^+$  indicate  $\pi(g_{7/2}^2)$  configurations can explain energy level systematics, quadrupole moments and spectroscopic strengths in a semi-quantitative manner. However, specific calculations for  $^{112, 114, 116}\text{Te}$  have not been performed and their models do not incorporate the neutron particle configurations necessary to treat high-spin and negative-parity states. Van Ruyven et al. (Va82) obtained reasonable agreement with experimental ground-state band energies in the  $^{118, 120}\text{Te}$  cases by using the Interacting (Neutron-Proton) Boson Approximation (I.B.A.-2). Two-quasiparticle excitations were treated by the broken-pair B.C.S. model. They too noted that a proper explanation of the level structures should involve coupling of the quasiparticle to the collective degrees of freedom, a calculation which has not yet been attempted.

An interpretation of the major level structures in the neutron-deficient Te isotopes consisting of pairing-plus-quadrupole bands based on the  $0^+$  ground state and  $\nu(h_{11/2}^2)10^+$ ,  $\nu(h_{11/2}, d_{5/2}^{-1})8^-$  and  $\nu(h_{11/2}, g_{7/2})9^-$  neutron pair excitations has been advanced in Section 5.4. This simple picture contains the collective as well as the single-particle degrees of freedom which are obviously necessary to characterize nuclides in this transitional region.

An apparent trend toward a constant moment of inertia

at high spins, indicated by plotting excitation energy vs.  $J(J+1)$  at spins  $J > 12^+$ , has led to the additional consideration of "rotational" effects due to single-particle spin alignment. The lack of (i) clear data above spin 20, and (ii) obvious signatures such as isomeric transitions, prevents definite conclusions being drawn concerning high-spin structure.

From an experimental point of view, a distinction between collective and single-particle (quasiparticle) states is often made by examining the  $\gamma$ -ray transition rates obtained from lifetimes. The  $\gamma$ - $\gamma$ -TAC experiment undertaken in this work was only sensitive to lifetimes greater than 2 nanoseconds. Recoil distance "plunger" measurements would be required to extract lifetimes in the  $10^{-10}$ - $10^{-13}$  second range appropriate to rates for the E2 and E1 transitions. The data from such experiments would be quite helpful in understanding level structures in these isotopes, and also in making quantitative comparisons among the various models which are available. A comprehensive understanding of the different transitional regions, some of which have been mentioned in this report, is not yet realistic. Nevertheless, results such as those presented in this work together with more extensive lifetime measurements and core-particle calculations (eg. Fa82) are gradually providing us with a better framework for describing these interesting nuclei.

## Appendix

### A Numerical Method for Gamma-Ray Spectrum Deconvolution

The extraction of energy and intensity information from gamma-ray spectra is of considerable importance to experiments such as those described in the present work. Many nuclear physics spectra are characterized by large numbers of peaks, typically hundreds, residing on an appreciable background, and sophisticated analysis is often required to remove the effects of finite instrument resolution, as well as to estimate and correct for the background continuum. There are three methods commonly used to obtain peak areas and centroids.

- 1) A short region of the spectrum is manually selected for analysis, and chosen background channels are fitted with a polynomial function. The counts between chosen area channels are then integrated and the contribution due to the calculated background subtracted to obtain the final result. This may be convenient for small numbers of isolated peaks, and is easily implemented on most multi-channel analyzers and data acquisition systems. Selection of appropriate background and area markers is entirely manual and clearly requires considerable input from an

operator. The amount of computer time required is negligible.

- 2) A few suitable peaks are selected as samples of an analytical function representing the instrument response function, and a range of the spectrum automatically searched for peaks and background channels. A polynomial background is fitted under the identified peaks and finally a least-squares fit to those peaks is performed using the derived response function. Least-squares fitting is undoubtedly the most common procedure and there are a number of widely-used codes such as SAMPO80 (Ko81a, Ko81b) which employ various response functions, usually modified Gaussians, and which contain peak search routines designed to minimize operator intervention. It should be noted that many of these programs were developed for use with neutron activation or other  $\beta$ -decay gamma-ray sources and so contain certain inherent assumptions regarding data characteristics, as will be discussed later. Generally the peak-finding results have to be checked manually and revisions made to ensure that doublets, triplets etc. are properly identified. Codes of this type require several seconds of CPU time per peak analyzed.
- 3) Use sample peaks as estimates of the response function, as in 2) but without fitting any function to them, estimate and strip off a spectrum-wide background and then unfold the data to produce, ideally, a spectrum consisting of

separated "peaks" only one-to-two channels wide. The identification of peaks in the initial data has no meaning here, but is accomplished using the unfolded spectrum. Once sample peaks have been selected and an overall background fit obtained, no operator intervention whatsoever is required. A number of different algorithms have been developed which ensure positive convergence without statistical noise amplification (eg. LK82, Ke78, and Ri72).

The amount of computation required is generally much greater than for least-squares fitting procedures. If the instrument response function is the same across the entire spectrum, i.e. the system is translationally invariant, the problem can be moved into the conjugate domain and solved using Fourier transforms. For virtually all gamma-ray data the response function is not invariant, so a slower iterative procedure must be used in the original data domain.

In an effort to develop a method for analyzing large numbers of complicated spectra with minimal operator intervention, a two-step process was devised:

Step 1: The background is estimated and removed using a procedure based on the method given by Tervo et al. (Te83), which locates sub-minima across the spectrum, shifts these points into the "middle" of the background based on a statistical offset, and generates cubic interpolations to produce a smoothly-varying continuum which

can then be subtracted from the original data. The background estimation differs from that of Tervo et al. in that the routine used in the present work allows the search for sub-minima to be carried out over a range of intervals relative to a given channel, rather than over a fixed interval.

Step 2: The resulting background-free spectrum is unfolded by SANDRA (Semi-Automated Nuclear Data Reduction & Analysis), a program written during this project specifically for use with such data, based on an algorithm devised by Habib and Labrie (HL75), later revised by Habib (Ha82b), and extended in this work to apply to  $\gamma$ -ray data.

As a further step, a program named OTTO was written to read the outputs from SANDRA runs on different spectra and produce angular distribution fits, after making appropriate corrections.

The iterative method first proposed by van Cittert (va31) involves making an estimate  $N(x)$  of the "true" spectrum, and then correcting that approximation by the difference between the measured data and the convolution of the response function with that estimate. Thus to obtain the  $(n+1)$ 'th iteration one would calculate:

$$N^{(n+1)}(x) = N^{(n)}(x) + [Y(x) - \int R(x-x')N^{(n)}(x')dx'] \quad [1]$$

where  $R(x')$  is the normalized response function,  $Y(x)$  the measured data, and the integral is limited to the width of the response function.

The algorithm used here treats the normalized data points of sample peaks as response functions, and interpolates for channels between the given sample peaks, providing a response function for every channel in the region to be analyzed. The correction in Equation [1] is reduced by a factor  $D > 1$  to ensure convergence, and for discrete spectra the prescription thus becomes:

$$\begin{aligned} N^{(n+1)}(i) &= N^{(n)}(i) + [Y(i) - \sum_{k=-m}^n R(k)N^{(n)}(i+k)]/D \\ &= N^{(n)}(i) + [Y(i) - Z^{(n)}(i)] \end{aligned} \quad [2]$$

$$\text{where } Z^{(n)}(i) = \sum_{k=-m}^n R(k)N^{(n)}(i+k) \quad [3]$$

The summation extends over the number of points included in the response function.  $Z(i)$  is the generated spectrum which should eventually become very close to the original data  $Y(i)$ , as the unfolded spectrum  $N(i)$  converges to the true signal.

The correction in Equation [2] compares  $Y(i)$  with  $Z(i)$  at only one point. A better fit is obtained if more points are included in the comparison, and using the total extent of the response function leads to:

$$N^{(n+1)}(i) = N^{(n)}(i) + \sum_{\ell=i-m}^{i+n} [Y(\ell) - Z^{(n)}(\ell)] / D' \quad [4]$$

Here  $D'$  is chosen to be larger than  $D$ , to reduce the possibility of over-correction. In practice the code starts with all of the  $N(i)=0$  and runs  $M$  iterations using a one-point comparison, then  $M$  iterations comparing three points, and finally  $M$  iterations using all of the points in the response function. The value of  $M$  is set at the start of the process by the user. A number of different combinations of iterations for the three stages were used, but keeping  $M$  identical at each stage seems to provide consistently more accurate convergence. If at any point the procedure results in negative values of  $N(i)$  they are set to zero.

Habib has shown (Ha84b) that the result of such an algorithm is a unique solution, an important consideration if one is to have confidence in the method. In order to test its repeatability the program was run a number of times for two different cases under the same initial set of starting conditions, giving identical results each time.

The resulting approximation to the true spectrum is  $N^{(M)}(i)$ , which theoretically consists of peak "generators" of appropriate intensity in channels where a peak is centred, and zeroes elsewhere. However peak centroids will rarely match that of the response function peak, and statistical effects may result in data with less than ideal peak shapes,

so two to three adjacent generators would be considered as an acceptable unfolded peak. As the final step, adjacent generators are grouped together, a group being defined by zeroes on both sides, and labelled as peaks. Centroids and areas are calculated from the generator distributions, based on the response functions' parameters. Area uncertainties are derived using:

$$\Delta \text{Area} = [(\text{Area} + \text{Background}) + \text{Background} + \Delta F]^{1/2} \quad 5)$$

where  $\Delta F$  is the discrepancy between fit and data over the extent of the peak. In fact for smaller peaks this error represents somewhat of an upper limit. The formation of peaks from multiple generators does tend to produce a slightly broader but lower shape than the original data. As pointed out by Habib and Labrie (HL75), this may lead to some slight overestimation of peak areas. The effect becomes more important if the peaks being analyzed are quite narrow.

In order to make some kind of quantitative comparison of the new unfolding procedure with more conventional methods, a representative gamma-ray spectrum was chosen for analysis using four different procedures:

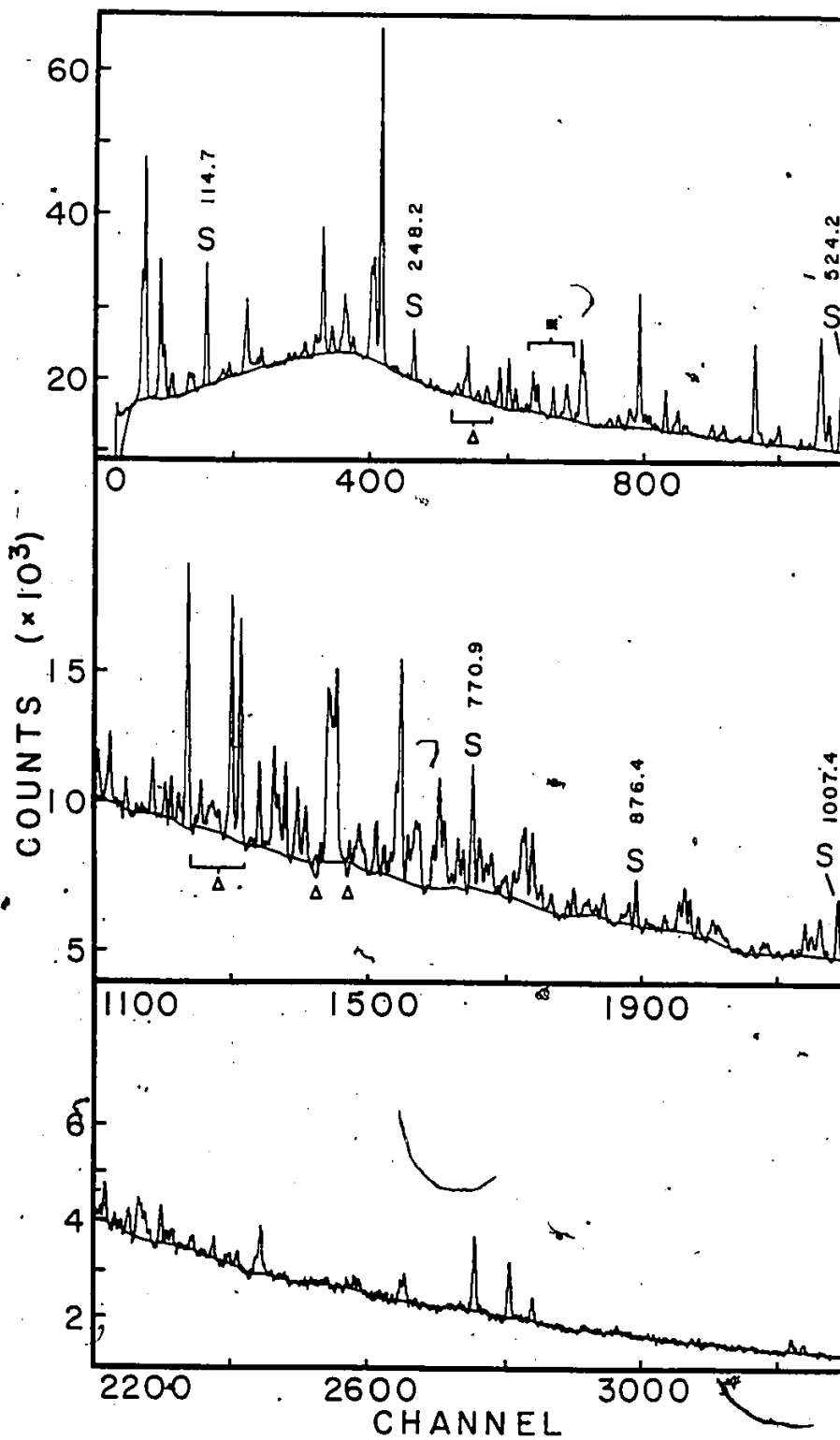
- a) Method 1 - Background and area markers were chosen by hand, and the simple area routines available on our XSYS data handling system employed.

- b) Method 2 - The program SAMPOMIN, modified from the National Research Council version of SAMPO80 by A.M. Kobos, D. Moss crop et al. (K084), became available during the latter stages of this work. SAMPOMIN facilitates the addition of peaks originally ignored by the search routine and uses the CERN-MINUIT minimization package (JR75), which allows the peak positions to be optimized during fitting.
- c) Method 2 (revised) - SAMPOMIN also permits one to use a spectrum-wide background with the data, which was accomplished with the prescription already described as Step 1, instead of SAMPO80's internal local background choices.
- d) Method 3 - The same "global" background fit as in procedure c) was used with the unfolding code SANDRA.

Figure A-1 shows the relevant portion of a  $\gamma$ -ray spectrum from the  $^{92}\text{Mo}(^{27}\text{Al}, \text{xnp}\alpha)$  reaction at 114 MeV, acquired using a 25% relative efficiency Ge detector. The global background fit is shown as well. There are approximately 270 peaks in the region 70 to 1500 keV with intensities ranging from = 600 to 190,000 counts. Very small peaks with large uncertainties were ignored. In all four cases the same linear energy calibration was used, and centroid comparisons were made in keV - the dispersion is 0.44 keV/channel. The

Figure A-1

$^{92}\text{Mo}(^{27}\text{Al}, \text{xnp}\alpha)$  projection spectrum together with the global background fit. Irregularities in that fit, marked by  $\Delta$ , occurred in the vicinities of channels 550 and 1300 (continuum slightly high) as well as at channels 1423 and 1470 (sharp dips). The latter feature seems to occur beside unusually broad, high multiplets such as the quadruplet between those two channels. Sample peaks are marked by S and labelled with their energies in keV. The region marked with a \* was selected for a comparison of the various fitting procedures.



Same six sample peaks, marked S on the spectrum, were used for b) - d).

SAMPOMIN will fit whole spectra but in this case the 3350 channels of interest were split up into five regions, to facilitate the required checks of peak identification and fitting. SAMPOMIN's default input file parameters were used: they differ somewhat from those of SAMPO80, mainly in that the acceptance of peaks is encouraged. The code identified 211 peaks in all, 16 of which turned out to be quite small with excessive uncertainties, leaving 195 "good" peaks. After comparing those with the original data, the locations of 66 additional peaks were entered and the locations of 8 others shifted slightly, leading to 261 good peaks being fit. The total CPU time on our VAX 11/750 using the code's own local background calculation was slightly over 37 minutes, or 8.6 seconds/peak.

The global background procedure, implemented in a program called XFIT, requires as input a number of interval lengths over which it searches for suitable background "nodes". If some of these lengths are too great the fit will not follow genuine irregularities: if some are too small the resulting "background" will be influenced by local minima within groups of peaks. Generally the same set of interval lengths could be used for most 4096-channel spectra having ~ 1500 to 2200 keV full scale. The background fit was checked on a display to ensure that questionable features of the

continuum were minimized. Places where those questionable features were judged to have occurred are marked with a  $\Delta$  in Figure A-1. XFIT required a few seconds of CPU time to produce a 4096-channel continuum.

When the global background was employed with SAMPOMIN, the peak identification procedure remained the same but the fitting time required dropped to just over 15 minutes (3.5 seconds/peak).

SANDRA unfolded the 3350 channels in 60 CPU minutes, performing 1000 iterations during each of the three stages, and located 324 peaks, 49 of which were judged to be insignificant, leaving 275 "good" peaks (13.1 seconds/peak). All of the peaks fitted using SAMPOMIN were identified by the unfolding process, although in sections exhibiting very complex structure there were some differences in the numbers and/or locations of peaks involved. One of SANDRA's virtues seems to be an ability to seek out peaks very effectively - in fact, the code may be slightly overzealous in that regard when the statistics are poor.

As the first step of the comparison centroids and areas of 31 singlet peaks were taken. The simple XSYS routine areas and centroids were used as reference values, not because the method is perceived to be intrinsically nearer to perfection, but it does represent a standard, fairly accurate means of extracting information from single peaks. Relative differences in the areas as well as centroid

3

differences between XSYS and the other three procedures were calculated and plotted with  $\Delta$ Centroid along the x-axis and  $\Delta$ Area along the y-axis, as shown in Figure A-2 for SAMPOMIN (internal background), SAMPOMIN (global background), and SANDRA respectively.

Means and standard deviations of the three  $\Delta$ Centroid and  $\Delta$ Area distributions were calculated and appear in Table A-1. These results indicate that the  $\Delta$ Centroid means and spreads from the three procedures are comparable and acceptable. The area differences, however, reveal that the mean and spread from SAMPOMIN (global background) and SANDRA are fairly close, although the mean area difference due to SANDRA is slightly higher, while those from SAMPOMIN (internal background) are larger by a factor of two or more.

If  $\Delta$ Area (SANDRA) is plotted against  $\Delta$ Area (SAMPOMIN (global background)) as in Figure A-3 a straight line can be fit to the distribution with a slope close to one and an intercept of nearly zero, indicating that the end results of the two procedures are comparable. Similar plots for SANDRA vs. SAMPOMIN (internal background) as well as SAMPOMIN (internal background) vs. SAMPOMIN (global background) reveal no such correlation. The implication is that the type of background calculation employed can be quite important, and the relative accuracy of the results casts some doubt on the validity of SAMPOMIN's internal background choices. Examination of these local background shapes shows that the para-

Figure A-2

Relative singlet peak area differences plotted versus centroid differences, with reference to XSYS values, for (i) SAMPOMIN (internal background), (ii) SAMPOMIN (global background), and (iii) SANDRA. Means and standard deviations for these distributions appear in Table A-1.

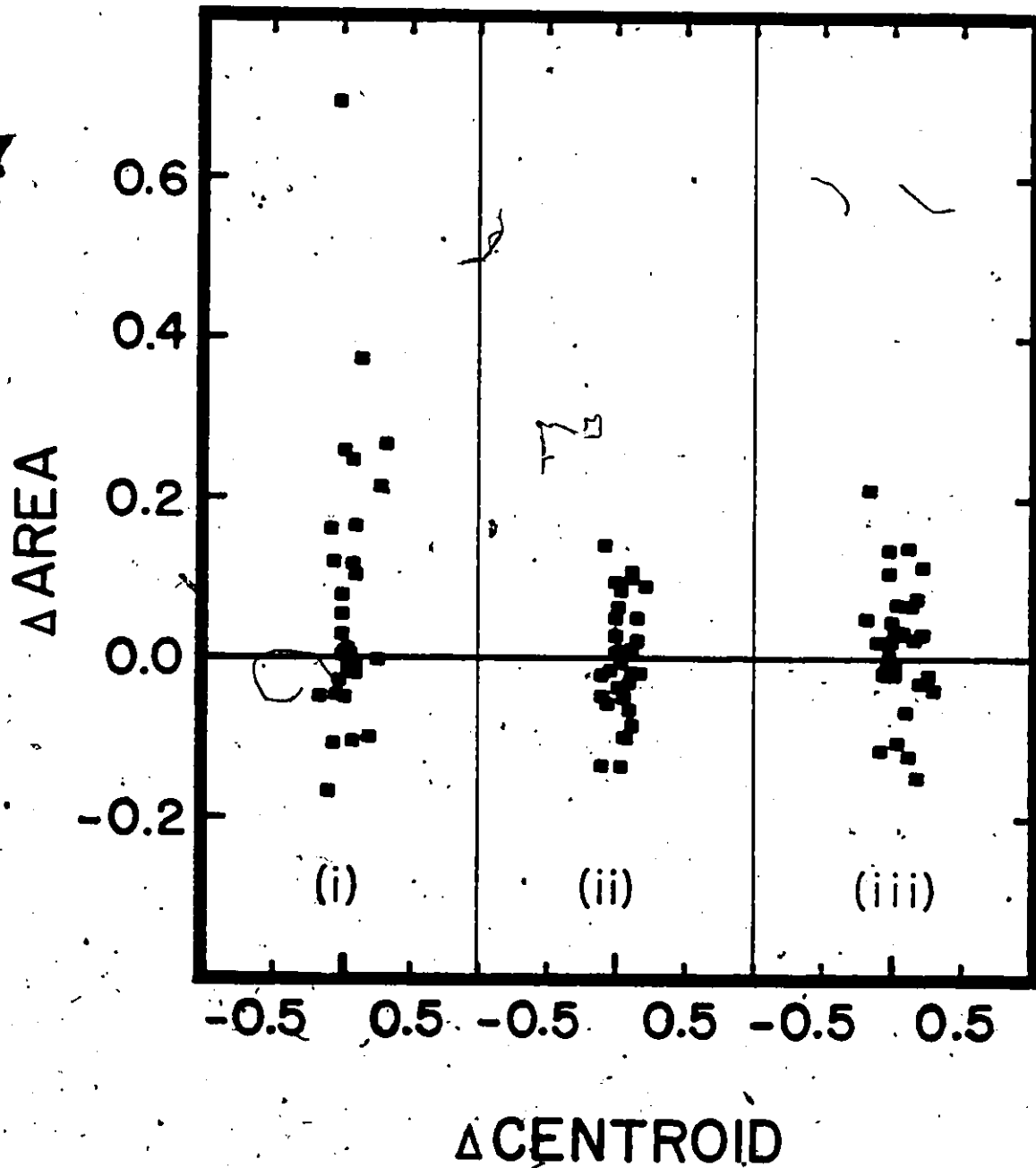
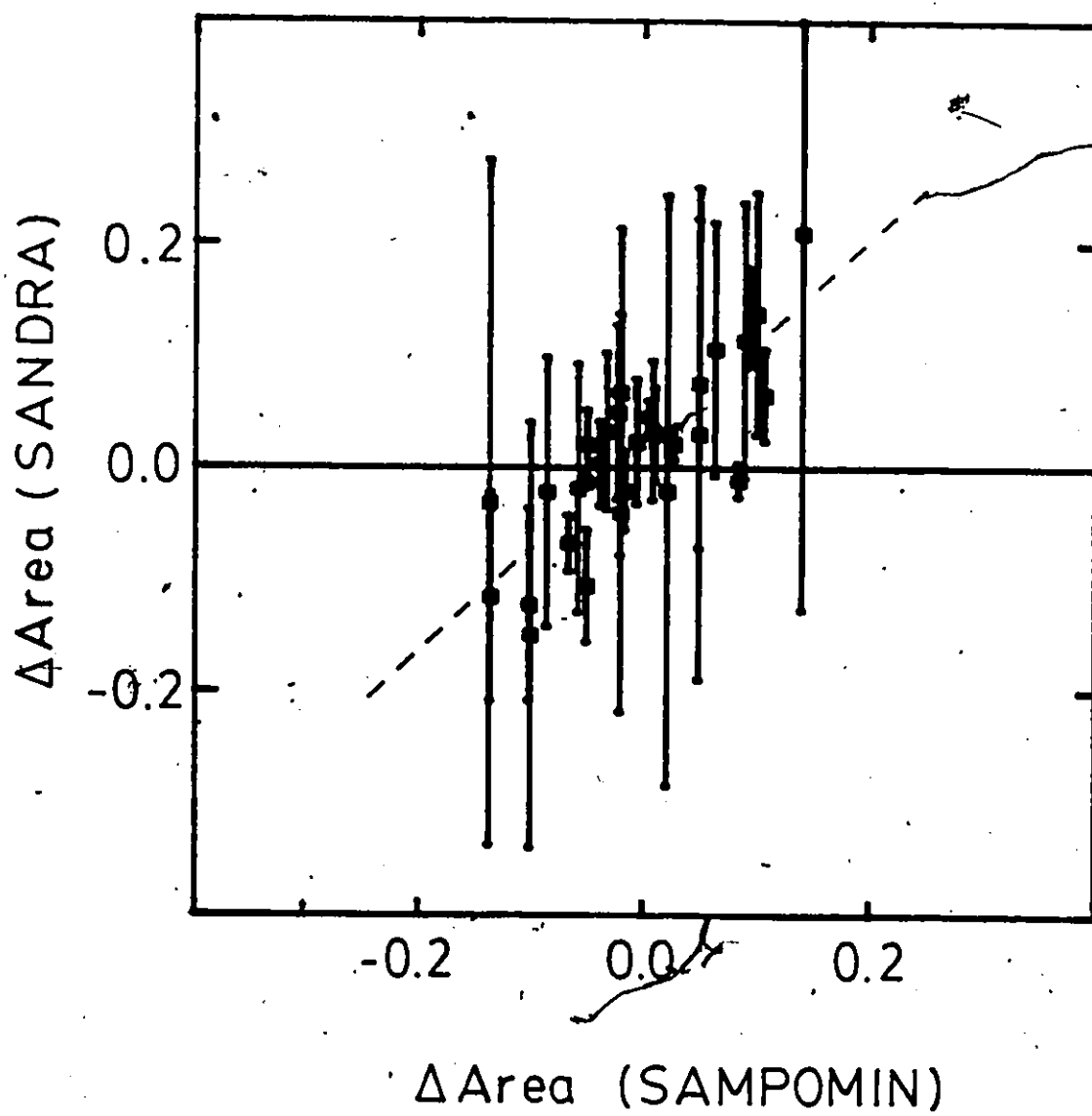


Table A-1: Comparison of differences in centroids and relative differences in areas for (i) simple XSYS versus SAMPOMIN (internal background), (ii) XSYS versus SAMPOMIN (global background) and (iii) XSYS versus SANDRA results.

Method Used	$\Delta$ Centroid (keV)		$\Delta$ Area (relative)	
	Average	Std. Dev.	Average	Std. Dev.
SAMPOMIN (internal background)	0.015	0.054	0.071	0.171
SAMPOMIN (global background)	0.014	0.043	-0.005	0.073
SANDRA	0.019	0.061	0.015	0.081

Figure A-3

Correlation between relative area differences for SANDRA and SAMPOMIN (global background). A best-fit line is indicated.

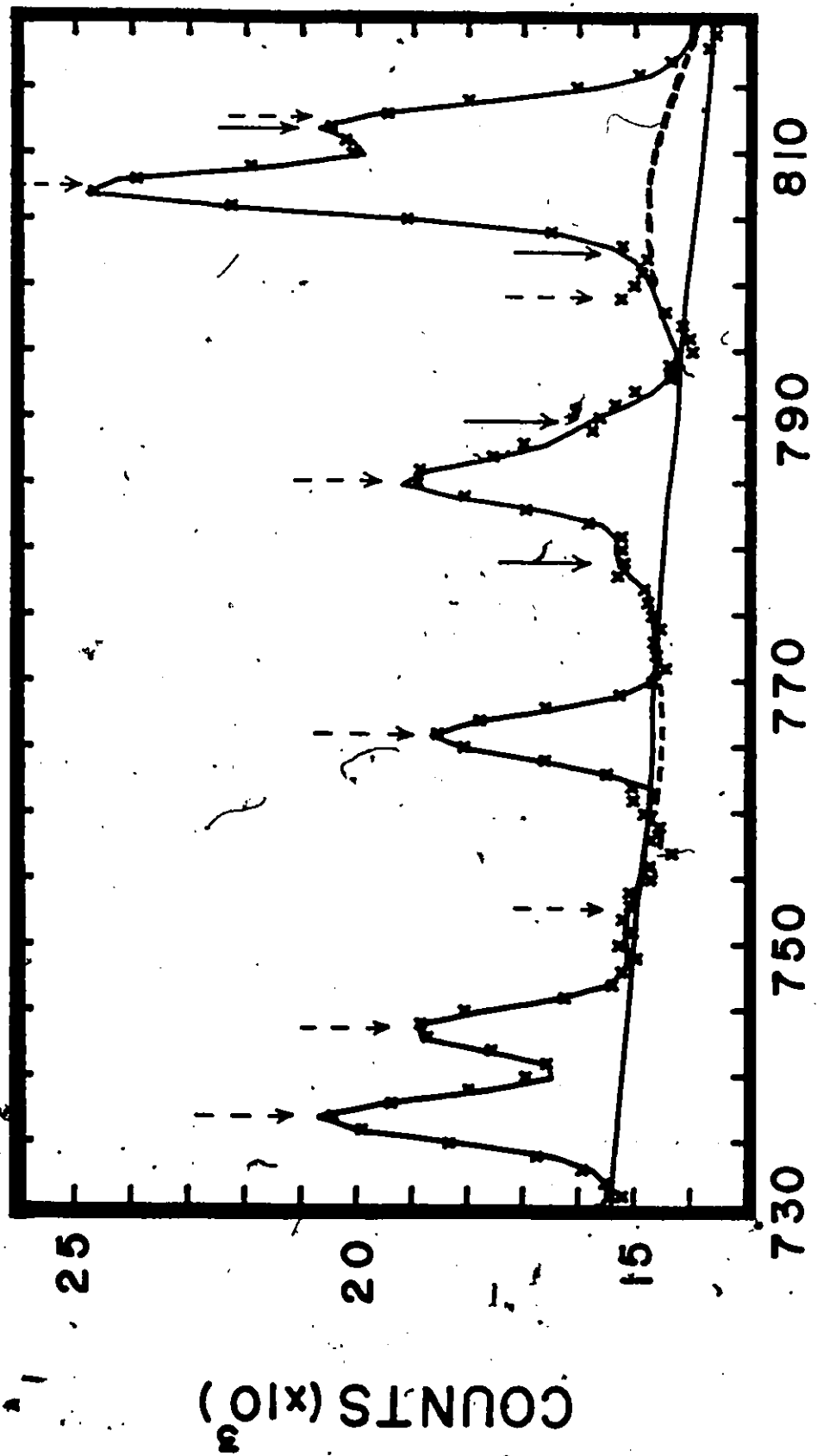


bolic fits produced by the code often exhibit curvatures markedly greater than either the global background or an eyeball estimate. This could frequently be traced to the mistaken choice of background channels which are close to the peak(s) being fitted but which are still part of complex non-background structure, an example of which can be found in the right hand group of peaks in Figure A-4. The effect may possibly be traced to the original intention of this code, which was to fit spectra usually containing fewer peaks and more regular background structure closer to the peaks.

The second step in this comparison involved examining the results of the two fitting procedures plus the unfolding method for a short section of the spectrum containing a number of multiplets. Figure A-4 shows channels 730 to 820 (321 to 361 keV) of the data with the SAMPOMIN (internal background) fit drawn in, as well as the internal background and global background for comparison. Figure A-5 displays the same original data plus the SAMPOMIN (global background) fit, with the background as well, and Figure A-6 the result of the SANDRA unfolding process using the same global background. The unfolded generator spectrum showing the peak groupings appears in Figure A-7, below the original data. Table A-2 compares the final peak intensities and centroids. A discussion of the procedures and results follows.

Figure A-4

Expanded region of the spectrum showing the SAMPOMIN (internal background) fit and its background choices (dashed lines), as well as the global background (solid line) for reference. Peaks identified by the search routine are marked ↓, while those added or shifted during fitting are marked ↓.



CHANNEL

Figure A-5

Expanded region of the spectrum showing the SAMPOMIN fit with the global background. Peaks identified by the search routine are marked ↓, while those added or shifted during fitting are marked ↓.

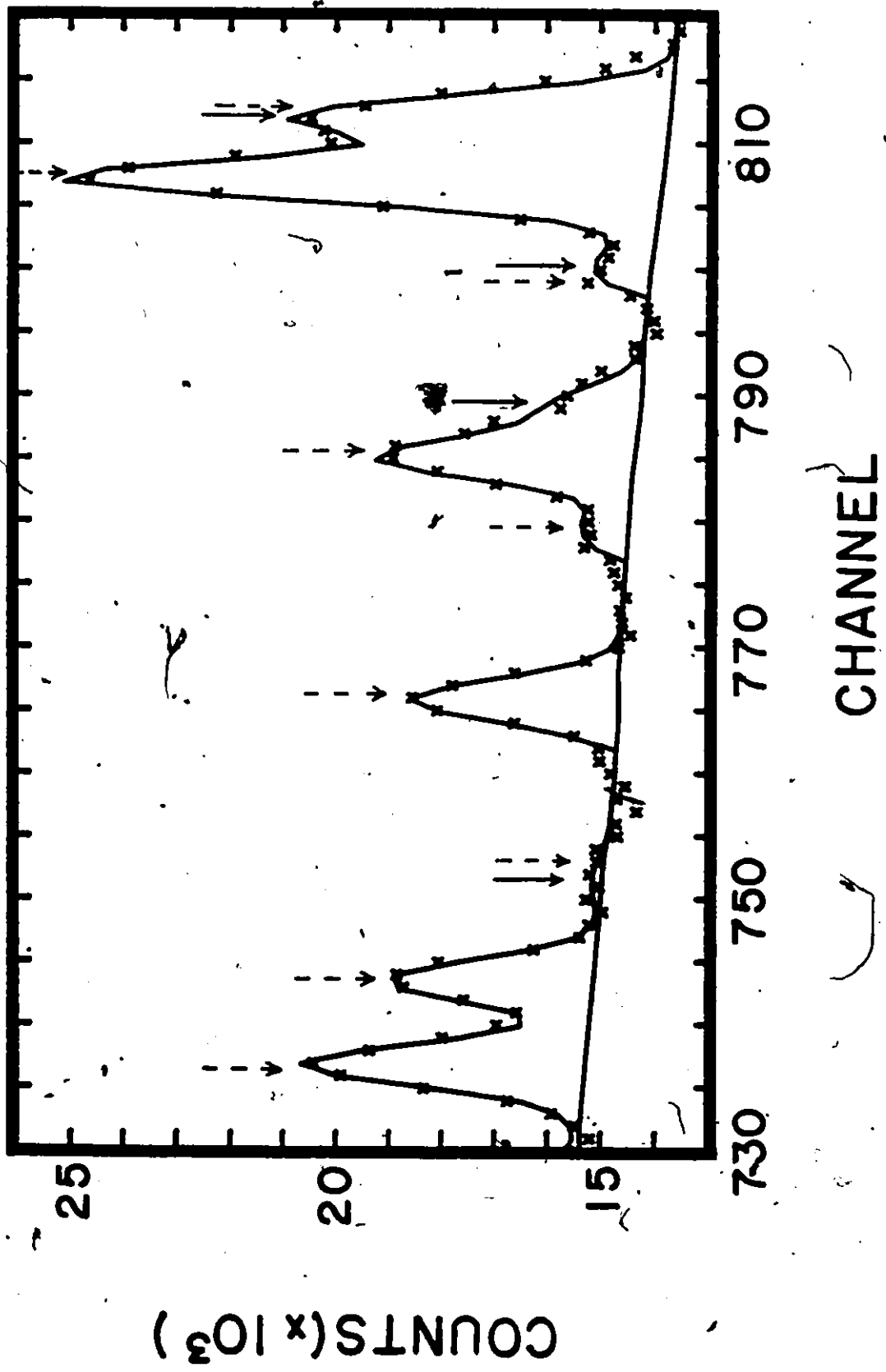
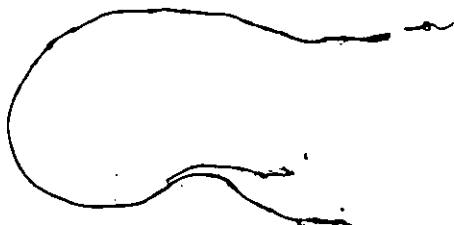
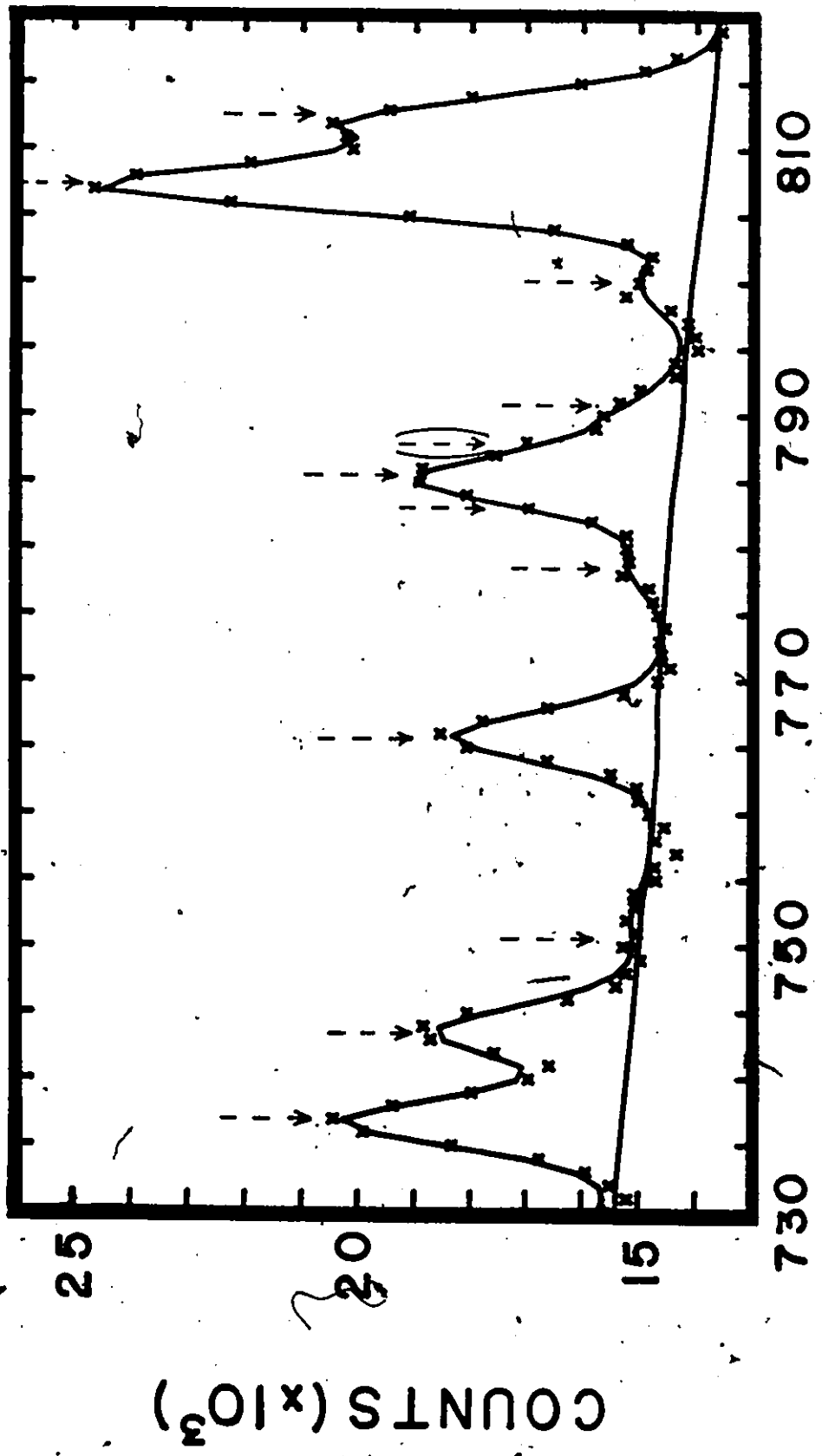


Figure A-6

Channels 730 to 820 showing the SANDRA fit and the global background used. Peaks identified after unfolding are marked ↓.

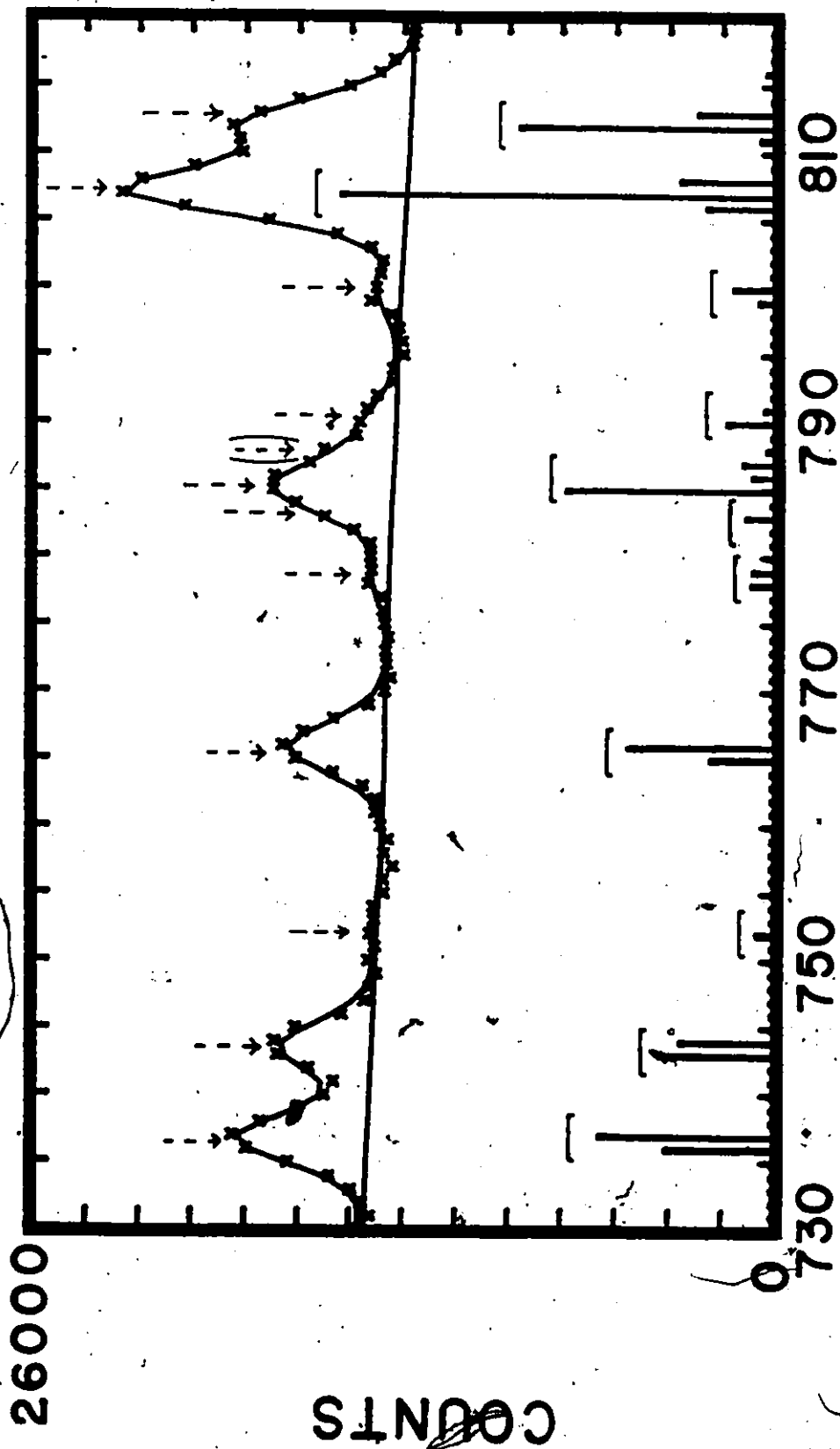




CHANNEL

Figure A-7

Channels 730 to 820 of the spectrum showing the groups of generators identified as peaks after unfolding by SANDRA. The resulting peak positions are marked ↓; the peak in brackets near channel 787 may be part of an unresolved doublet.



CHANNEL

COUNTS

26000

730

750

770

790

810

Table A-2: Comparison of peak centroids and intensities for channels 780-820 using SAMPOMIN (internal background), SAMPOMIN (global background) and SANDRA.

SAMPOMIN (internal background)			SAMPOMIN (global background)			SANDRA			
Centroid	Area	+/-	Centroid	Area	+/-	Centroid	Area	+/-	gen.
736.9	22,530	450	736.9	22,300	350	736.9	24,000	690	2
743.6	16,160	440	743.6	16,220	330	743.7	16,990	680	2
751.7	780	380	751.7	800	300	752.2	830	630	1
765.9	17,220	440	765.9	16,460	330	765.9	17,640	650	2
779.6	2,650	530	779.4	3,410	320	778.7	3,150	670	2
						783.2	2,100	650	1
785.1	19,330	630	785.2	20,170	420	785.6	21,970	700	4
789.2	6,000	550	789.3	6,760	400	790.4	4,380	660	2
			800.3	4,290	270	800.0	4,290	670	2
802.7	190	1,060							
807.3	42,220	490	807.2	47,510	400	807.3	51,110	720	3
812.2	24,910	440	812.2	29,760	370	812.4	29,010	720	3

SAMPOMIN (internal background)

PEAKFIND, the routine responsible for peak searching, located 8 peaks which have been marked ↓ on Figure A-4. The file containing this information was moved into a display region and compared with the data, and the code instructed to add peaks near channels 779 and 790. After fitting this region, however, SAMPOMIN rejected the peak it had at first identified at channel 799, and tried to fit two peaks at channels 810.6 and 812.8, where it had originally placed one peak at channel 812.9. It was found that to induce the code to fit three peaks to what was perceived as a clear triplet, this very short section had to be fit separately, and even then the small peak near channel 800 was not analyzed reasonably. Based on the  $\chi^2$  figures, as shown in Table A-3, the overall fit actually compared favourably with that of SAMPOMIN (global background). However, this is a bit misleading because the internal background allows somewhat more flexibility due to its reliance on data points very close to peaks, while the global background is forced to consider non-local continuum behaviour.

SAMPOMIN (global background)

The type of background fit does not affect the peak search routine, and the same set of peaks have been marked ↓ on Figure A-5. Again peaks near channels 779 and 790 were added. No revisions after the first fitting were required.

Table A-3:  $\chi^2$  results from the analysis of channels 730-820 using SAMPOMIN (internal background), SAMPOMIN (global background) and SANDRA.

Channels	SAMPOMIN (internal background)	SAMPOMIN (global background)	SANDRA
----------	-----------------------------------	---------------------------------	--------

730-774	100	93	166
775-795	57	78	27
796-820	129	252	41

730-820	286	423	234
---------	-----	-----	-----

SANDRA

Generator groups in Figure A-7 have been identified and labelled as peaks, with their centroids marked  $\downarrow$  in Figures A-6 and A-7. These groupings all occupy one, two or three channels, except for four adjacent generators centred at channel 785.6 in which the fourth generator is quite small.  $\chi^2$  comes out to be the lowest of the three results, which is to be expected: an unfolding procedure can be thought of as having more free parameters than most least-squares analyses.

Channels 775 to 795 are interpreted by the unfolding process as containing four and perhaps even five peaks, if one wishes to imagine the group of four generators as an unresolved doublet. The fit is certainly better than the least-squares solutions and none of the peaks identified are statistically insignificant. The main component centred at channel 786 is definitely wider than the singlet at channel 766, although the smaller peaks to each side contribute to this width. Without further information this is a moot point.

A comparison of the three fits is somewhat subjective; nevertheless, a few salient points can be made. Channels 730 to 779, where SANDRA produces lower and broader peak shapes than the data, appear to be better treated by the least-squares procedures, while the remainder of the section is better fit by the unfolding process. This is borne out by the  $\chi^2$  results. It appears that if SANDRA needs to put two

generators of similar intensity side-by-side, in order to position a peak correctly, then the resultant peak shape ends up being slightly distorted. The slightly higher areas given by SANDRA for peaks at channels 737, 744 and 766 could well be due to this effect.

Channels 775 to 795 are reproduced much more accurately by SANDRA than by SAMPOMIN in either of its versions. It is entirely possible that this "triplet" centred at ~ channel 786 is actually made up of four or even five peaks. SAMPOMIN (global background) could be told to fit five peaks there but distributed them somewhat differently than SANDRA, while the internal background version chose such an awkward continuum when asked to analyse that short section alone, that its results proved meaningless.

Channels 796 to 820 are not satisfactorily analysed by SAMPOMIN (internal background), as it seems to sacrifice the small peak at channel 800 in order to produce an extremely convex background, in the process installing an insignificant peak in the tail of the middle component.

#### Summary

A survey of 31 singlet peaks across the sample spectrum revealed that intensities and centroids produced by SANDRA and SAMPOMIN (global background) were reasonably consistent with simple XSYS integration and background

subtraction results, while those due to SAMPOMIN (internal background) showed poorer agreement, often due to faulty local background reconstruction.

Analysis of a more complicated part of the data resulted in fair agreement between SANDRA and SAMPOMIN (global background) for much of the section, with some ambiguity regarding interpretation of the multiplet between channels 775 and 795. A tendency to slightly overestimate (by  $< 5\%$ ) areas of peaks formed with adjacent generators of similar intensities could possibly be minimized by a more sophisticated area calculation in SANDRA. The global and internal background versions of SAMPOMIN produced areas which agreed within the given uncertainties except for the last multiplet in the section, underneath which the internal background was unsuitable.

The extraction of information from an entire spectrum emphasized a number of differences between the various methods. SAMPOMIN in either of its versions required extensive corrections to the results of its peak identification process, while the internal background option frequently produced inappropriate results. In addition, the necessity of refitting short sections with this version is somewhat unsettling. The global background option would seem to be preferable, and also requires only one-half the CPU time. SANDRA takes sample peak shapes directly from the experimental data, and does not assume any functional form. In

cases where, for example, small drifts occur during data acquisition and make the validity of an analytic shape questionable this may be preferable. The program takes roughly twice as long to run as the standard internal background version of SAMPOMIN; but requires no operator intervention at all and is amenable to (i) batch processing, and (ii) further automated data analysis, as in the case of the angular distribution analysis program OTTO. These can be considerable advantages in the many cases where computer time is more readily available than operator time.

### References

- AB72 R.L. Auble and J.B. Ball, Nucl. Phys. A179 (1972) 353.
- AI75a A. Arima and F. Iachello, Phys. Lett. 57B (1975) 39.
- AI75b A. Arima and F. Iachello, Phys. Rev. Lett. 35 (1975) 1069.
- An76 C.G. Andersson, S.E. Larsson, G. Leander, P. Möller, S.G. Nilsson, I. Ragnarsson, S. Åberg, R. Bengtsson, J. Dudek, B. Nerlo-Pomorska, K. Pomorski and Z. Szymański, Nucl. Phys. A268 (1976) 205.
- An78 C.G. Andersson, Hellström, G. Leander, I. Ragnarsson, S. Åberg, J. Krumlinde, S.G. Nilsson and Z. Szymański, Nucl. Phys. A309 (1978) 141.
- An81 E. Andersson, P. Herges, H.V. Klapdor and I.N. Wischniewski, Z. Phys. A299 (1981) 105.
- An85 W. Andrejtscheff, L.K. Kostov, H. Rotter, H. Prade, F. Stary, M. Senba, N. Tsoupas, Z.Z. Ding and P. Raghavan, Nucl. Phys. A347 (1985) 167.
- Ar77 A. Arima, T. Otsuka, F. Iachello and I. Talmi, Phys. Lett. 66B (1977) 205.
- As83 P. Ashbaugh, private communication (1983).
- Au80 G. Auger, G. Albouy, C. Roulet, H. Sergolle, A. Kerek and Th. Lindblad, Z. Phys. A296 (1980) 319.
- Ba80 R. Bass, "Nuclear Reactions with Heavy Ions", Springer-Verlag, Berlin, Heidelberg (1980).
- BB82 M. Blann and J. Bisplinghoff, Code ALICE/LIVERMORE 82, Lawrence Livermore Nuclear Laboratory Report UCID-19614 (1982-unpublished).
- BK84 D. Bonatsos and A. Klein, At. Nucl. Data Tables 30 (1984) 27.
- BM69 A. Bohr and B.R. Mottelson, Nuclear Structure Vol. I, W.A. Benjamin, Inc., New York (1969).
- BM74 A. Bohr and B.R. Mottelson, Phys. Scr. 10A (1974) 13.

- BM75 A. Bohr and B.R. Mottelson, Nuclear Structure Vol. II, W.A. Benjamin Inc., Reading, Mass. (1975).
- Bo74 D.D. Bogdanov, V.A. Karnankhov and L.A. Petrov, *Yad. Fiz.* 18 (1973) 3; *Sov. J. Nucl. Phys.* 18 (1974) 1.
- Bo80 J. Borggreen, S. Björnholm, O. Christensen, A. Del Zoppo, B. Herskind, J. Pederson, G. Sletten, F. Folkmann and R.S. Simon, *Z. Phys.* A294 (1980) 113.
- Br79 J. Bron, W.H.A. Hesselink, A. Van Poelgeest, J.J.A. Zalmstra, M.J. Uitzinger, H. Verheul, K. Heyde, M. Waroquier, H. Vincx and P. Van Isacker, *Nucl. Phys.* A318 (1979) 335.
- BR85 T. Bengtsson and I. Ragnarsson, *Nucl. Phys.* A436 (1985) 14.
- BS69 D.R. Bès and R.A. Sorensen, *Adv. Nucl. Phys.* 2 (1969) 129.
- BW52 J.M. Blatt and V.F. Weisskopf, Theoretical Nuclear Physics, John Wiley and Sons, New York (1952) 627.
- Ch79 Tsan Ung Chan, M. Agard, J.F. Bruandet and C. Morand, *Phys. Rev.* C19 (1979) 244.
- Ch82 P. Chowdhury, W.F. Piel, Jr. and D.B. Fossan, *Phys. Rev.* C25 (1982) 813.
- Da70 T.K. Das, R.M. Dreizler and A. Klein, *Phys. Rev.* C2 (1970) 632.
- Di66 R.M. Diamond, E. Matthias, J.O. Newton and F.S. Stephens, *Phys. Rev. Letters* 26 (1966) 1205.
- de83 M.J.A. de Voigt, J. Dudek and Z. Szymanski, *Rev. Mod. Phys.* 55 No. 4 (1983) 949.
- DV74 E. Degrieck and G. Vanden Berghe, *Nucl. Phys.* A231 (1974) 141.
- Fa82 A. Faessler, *Rep. Prog. Phys.* 45 (1982) 653.
- FC76 C. Flaum and D. Cline, *Phys. Rev.* C14 (1976) 1224.
- Ga82 M. Gai, D.M. Gordon, R.E. Shroy, D.B. Fossan and A.K. Gaigalas, *Phys. Rev.* C26 (1982) 1101.
- Ga84 W. Gast, U. Kaup, H. Hanewinkel, R. Reinhardt, K. Schiffer, K.P. Schmittgen, K.O. Zell, J. Wrzesinski,

- A. Gelberg and P.v. Brentano, Z. Phys. A318 (1984) 123.
- GH79 J.D. Garrett and B. Herskind in The Study of Nuclei far from Stability: Proc. of the Daresbury Study Weekend, DL/NUC/R20 (1979) 31.
- Gi81 A. Gizon, J. Genevy, J. Gizon, V. Barci, A. Plochocki, T. Batsch, J. Zylicz, A. Charvet and G. Marguier, Z. Phys. A302 (1981) 79.
- Ha82 O. Häusser, H.E. Mahnke, T.K. Alexander, H.R. Andrews, J.F. Sharpey-Schafer, M.L. Swanson, D. Ward, P. Taras and J. Keinonen, Nucl. Phys. A379 (1982) 287.
- Ha82b E.E. Habib, private communication (1982).
- Ha84 M. Hass, E. Dafni, H.H. Bertschat, C. Broude, F.D. Davidovsky, G. Goldring and P.M.S. Lesser, Nucl. Phys. A414 (1984) 316.
- Ha84b E.E. Habib, private communication (1984).
- He76 K. Heyde, M. Waroquier, H. Vincx and P. Van Isacker, Phys. Lett. 64B (1976) 125.
- He82 K. Heyde, P. Van Isacker, M. Waroquier, G. Wenes and M. Sambataro, Phys. Rev. C25 (1982) 3160.
- HL75 E.E. Habib and J.P. Labrie, Nucl. Instr. Methods 130 (1975) 199.
- HT77 J. Heinemeier and P. Tykesson, Revue de Physique Appliquée 12 (1977) 1471.
- IA74 F. Iachello and A. Arima, Phys. Lett. 53B (1974) 309.
- Ja84 V.P. Janzen, J.C. Waddington, J.A. Cameron, A.J. Larabee and D. Rajnauth, McMaster Accelerator Laboratory Annual Report (1984) 54.
- Ja85 V.P. Janzen, J.C. Waddington, J.A. Cameron, J. Johansson, M. Simpson, D. Viggars and H. Taylor, unpublished data (1985).
- JR75 F. James and M. Roos, Comp. Phys. Comm. 10 (1975) 343.
- Ka76 R. Kamermans, H.W. Jongsma, T.J. Ketel, R. Van der Wey and H. Verheul, Nucl. Phys. A266 (1976) 346.
- KC83 J. Kitching and J. Crawford, unpublished data (1983).

- Ke71 A. Kerek, Nucl. Phys. A176 (1971) 466.
- Ke78 T.J. Kennett, P.M. Brewster, W.V. Prestwich and A. Robertson, Nucl. Instr. Methods 153 (1978) 125.
- Ke84 A. Kerek, T. Lönnroth, K. Honkanen, E. der Mateosian and P. Thieberger, Z. Phys. A317 (1984) 169.
- Kh78 T.L. Khoo, R.K. Smither, B. Haas, O. Häusser, H.R. Andrews, D. Horn and D. Ward, Phys. Rev. Lett. 41 (1978) 1027.
- Kh79 T.L. Khoo, Proc. Symp. on High-spin Phen. in Nucl., Argonne, ANL/PHY-79-4 (1979) 95.
- Ki77 R. Kirchner, O. Klepper, G. Nyman, W. Reisdorf, E. Roeckl, D. Schardt, N. Kaffrell, P. Peuser and K. Schneeweiss, Phys. Lett. 70B (1977) 150.
- K179 P. Kleinheinz, Proc. Symp. on High-Spin Phen. in Nucl., Argonne, ANL/PHY-79-4 (1979) 125.
- K180 A. Klein, Phys. Lett. 93B (1980) 1.
- Ko81a M.J. Koskelo, P.A. Aarnio and J.T. Routti, Comp. Phys. Comm. 24 (1981) 11.
- Ko81b M.J. Koskelo, P. A. Aarnio and J.T. Routti, Nucl. Instr. Methods 190 (1981) 89.
- Ko84 A.M. Kobos et al., McMaster University Tandem Accelerator Laboratory internal communication (1984).
- Kr72 K.S. Krane, Nucl. Instr. Meth. 98 (1972) 205.
- KW76 H.V. Klapdor and H. Willmes, Phys. Lett. 62B (1976) 395.
- La80 R.D. Lawson, Theory of the Nuclear Shell Model, Clarendon Press, Oxford (1980).
- Le78 G. Leander, Proc. XVI Winter School on Selected Topics in Nuclear Structure, Bielsko Biela (1978) 621.
- Lh79 G. Lhersonneau in The Study of Nuclei far from Stability: Proc. of the Daresbury Study Weekend, DL/NUC/R20 (1979) 6.
- LK82 D.J. Lindstrom and R.L. Korotev, J. Radioan. Chem. 70 No. 1-2 (1982) 439.

- Lo70 V. Lopac, Nucl. Phys. A155 (1970) 513.
- LS78 C.M. Lederer and V.S. Shirley, Table of Isotopes (1978) 7th edition.
- Lu79 S. Lunardi, M. Ogawa, M.R. Maier and P. Kleinheinz, Proc. Symp. on High-Spin Phen. in Nuclei, Argonne, ANL/PHY-79-4 (1979) 393.
- LW80 A.J. Larabee and J.C. Waddington, McMaster Accelerator Laboratory Annual Report (1980) 46.
- Ma69 M.A.J. Mariscotti, G. Scharff-Goldhaber and B. Buck, Phys. Rev. 178 (1969) 1864.
- Mi77 R. Middleton, Revue de Physique Appliquée 12 (1977) 1435.
- MJ55 M.G. Mayer and J.H.D. Jensen, Elementary Theory of Nuclear Shell Structure, John Wiley and Sons, Inc., New York (1955).
- Mo80 M. Moshinski, Nucl. Phys. A338 (1980) 156.
- Mo81 I. Morrison, A. Faessler and C. Lima, Nucl. Phys. A372 13.
- MS67 W.D. Myers and W.J. Swiatecki, Ark. Fys. 36 (1967) 343.
- Ne69 J.O. Newton, Prog. in Nucl. Phys. vol. 2, Ed. by D.M. Brink and J.H. Mulvey, Pergamon Press, Oxford (1969) 53.
- No85 P.J. Nolan, A. Kirwan, D.J.G. Love, A.H. Nelson, D.J. Unwin and P.J. Twin, J. Phys. G11 (1985) L17.
- Ot78 T. Otsuka, A. Arima and F. Iachello, Nucl. Phys. A309 (1978) 1.
- Ot78a T. Otsuka, A. Arima, F. Iachello and I. Talmi, Phys. Lett. 76B (1978) 139.
- Pa56 S.P. Pandya, Phys. Rev. 103 (1956) 956.
- PB75 M.A. Preston and R.K. Bhaduri, Structure of the Nucleus, Addison-Wesley, Reading, Mass. (1975).
- Pe77 J. Pederson, B.B. Back, F.M. Bernthal, S. Björnholm, O. Christensen, F. Folkmann, B. Herskind, T.L. Khoo,

- M. Neiman, F. Pühlhofer and G. Sletten, Phys. Rev. Lett 39 (1977)-990.
- PW85 G. Palameta and J.C. Waddington, Nucl. Instr. Methods A234 (1985) 476.
- Re79 W. Reisdorf, in: Proc. of the VIIth Int. Workshop on Gross Properties of Nuclei and Nucl. Excitation, Hirschegg, INKA-Conf.-79-001-069 (1979) 93.
- Ri72 W.H. Richardson, J. Opt. Soc. Am. 62 (1972) 55.
- Ro59 M. Rotenberg, R. Bivins, N. Metropolis and J.K. Wooten, Jr., the 3-j and 6-j symbols, Technology Press, M.I.T., Cambridge, Mass. (1959).
- Ro80 E. Roeckl, G.M. Gowdy, R. Kirchner, O. Klepper, A. Piotrowski, A. Plochocki, W. Reisdorf, P. Tidemand-Petersson, J. Zylicz, D. Schardt, G. Nyman and W. Lindenzweig, Z. Phys. A309 (1980) 221.
- RS80 P. Ring and P. Schuck, The Nuclear Many-Body Problem, Springer-Verlag New York Inc. (1980).
- Sa78 L.E. Samuelson, F.A. Rickey, J.A. Grau, S.I. Popik and P.C. Simms, Nucl. Phys. A301 (1978) 159.
- Sa79 L.E. Samuelson, J.A. Grau, S.I. Popik, F.A. Rickey and P.C. Simms, Phys. Rev. C19 (1979) 73.
- Sa83 J. Sau, K. Heyde and J. Van Maldeghem, Nucl. Phys. A410 (1983) 14.
- Sc74 G. Scharff-Goldhaber, J. Phys. A7 (1974) L121.
- Sc76 G. Scharff-Goldhaber, C.B. Dover and A.L. Goodman, Ann. Rev. Nucl. Sci. 26 (1976) 239.
- Sc80 O. Scholten, Ph.D. Thesis, Univ. of Groningen (1980).
- Sc81 D. Schardt, T. Batch, R. Kirchner, O. Klepper, W. Kurewicz, E. Roeckl and P. Tidemand-Petersson, Nucl. Phys. A368 (1981) 153.
- SG70 G. Scharff-Goldhaber and A. Goldhaber, Phys. Rev. Lett. 24 (1970) 1349.
- Sh79 R.E. Shroy, A.K. Gaigalas, G. Schatz and D.B. Fossan, Phys. Rev. C19 (1979) 1324.

- Sh82 R.E. Shroy, D.M. Gordon, M. Gai, D.B. Fossan and A.K. Gaigalas, Phys. Rev. C26 (1982) 1089.
- Si79 R.S. Simon, R.M. Diamond, Y. El Masri, J.O. Newton, P. Sawa and F.S. Stephens, Nucl. Phys. A313 (1979) 209.
- Si80 P.C. Simms, F.A. Rickey and R.K. Popli, Nucl. Phys. A347 (1980) 205.
- SS72 F.S. Stephens and R.S. Simon, Nucl. Phys. A183 (1972) 257.
- St68 V.M. Strutinski, Nucl. Phys. A122 (1968) 1.
- Sz83 Z. Szymański, Fast Nuclear Rotation, Clarendon Press, Oxford (1983).
- Te83 R. J. Tervo, T. J. Kennett and W.V. Prestwich, Nucl. Instr. Methods 216 (1983) 205.
- Ti80 P. Tidemand-Petersson, R. Kirchner, O. Klepper, E. Roëckl, A. Plochocki, J. Zylicz and D. Schardt, Gesellschaft für Schwerionen-forschung (GSI) Scientific Report 1980 ISSN 0174-0814 p.56.
- Tr82 J. Tréherne, J. Genevy, A. Gizon, J. Gizon; R. Béraud, A. Charvet, R. Duffait, A. Emsallem, and M. Meyer, Z. Phys. A309 (1982) 135.
- Va74 W.F. Van Gunsteren, E. Boeker and K. Allaart, Z. Phys. A267 (1974) 87.
- Va80 A. Van Poelgeest, J. Bron, W.H.A. Hesselink, K. Allaart, J.J.A. Zalmstra, M.J. Uitzinger and H. Verheul, Nucl. Phys A346 (1980) 70.
- Va82 J.J. Van Ruyven, W.H.A. Hesselink, J. Akkermans, P. Van Nes and H. Verheul, Nucl. Phys. A380 (1982) 125.
- WB77 A.H. Wapstra and K. Bos, At. Nucl. Data Tables 19 (1977) 175.
- WD70 R.A. Warner and J.E. Draper, Phys. Rev. C1 (1970) 1069.
- WD73 W.J. Wyckoff and J.E. Draper, Phys. Rev. C8 (1973) 796.
- Ya67 T. Yamazaki, Nucl. Data, Section A, vol. 3 #1 (1967) 1.